MATERIALS PROCESSING
FUNDAMENTALS 2023

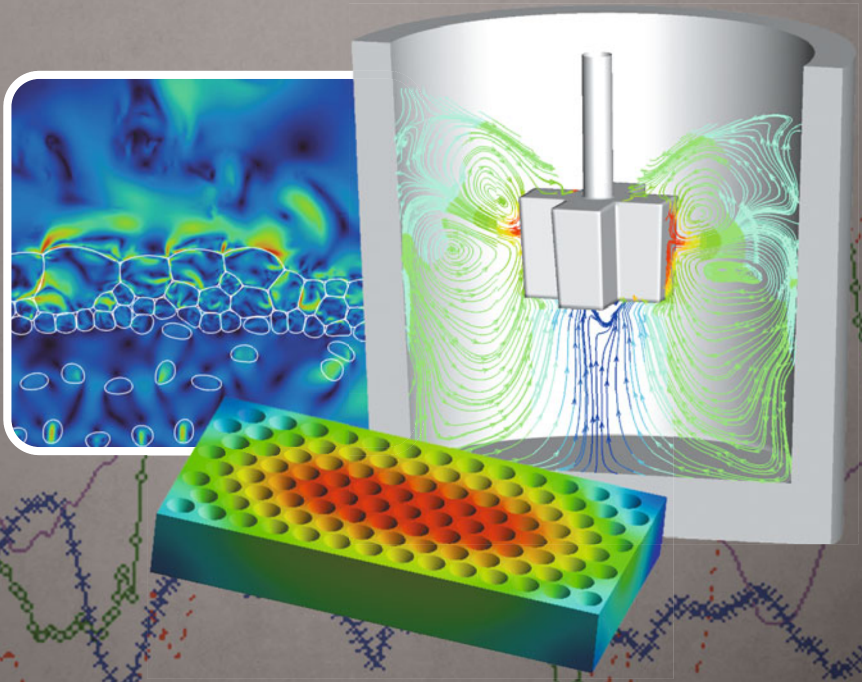

EDITED BY
Samuel Wagstaff
Alexandra Anderson
Adrian S. Sabau

TMS

Springer

The Minerals, Metals & Materials Series

Samuel Wagstaff · Alexandra Anderson ·
Adrian S. Sabau
Editors

Materials Processing Fundamentals 2023

TMS

Springer

Editors
Samuel Wagstaff
Oculatus Consulting
Marietta, GA, USA

Alexandra Anderson
Gopher Resource
Tampa, FL, USA

Adrian S. Sabau
Oak Ridge National Laboratory
Oak Ridge, TN, USA

ISSN 2367-1181 ISSN 2367-1696 (electronic)
The Minerals, Metals & Materials Series
ISBN 978-3-031-22656-4 ISBN 978-3-031-22657-1 (eBook)
https://doi.org/10.1007/978-3-031-22657-1

Cover Illustration: Left: From Chapter "Toward Meso-scale Modelling of Slag Foaming Phenomena in Pyrometallurgy", Quinn G. Reynolds et al., Figure 5: Dispersed-phase marker phases and velocities for ug = 0.02 m/s case. https://doi.org/10.1007/978-3-031-22657-1_10. Right: From Chapter "Effect of Wearing Impellers on Multiphase Flow and Desulfurization During KR Mechanical Stirring Process", Wei Chen et al., Figure 3: Effect of the number of employed heats of the impeller on the distribution of flow pattern, a initial state, b after employed 120 heats, c after employed 220 heats. https://doi.org/10.1007/978-3-031-22657-1_2. Bottom: From Chapter "Simulation of Ferroalloy Casting in Copper Moulds", Haifei An et al., Figure 8: Temperature field of the mould at 50 s before demoulding. https://doi.org/10.1007/978-3-031-22657-1_18.

This Springer imprint is published by the registered company Springer Nature Switzerland AG
The registered company address is: Gewerbestrasse 11, 6330 Cham, Switzerland

Preface

The symposium Materials Processing Fundamentals is hosted at the Annual Meeting of The Minerals, Metals & Materials Society (TMS) as the flagship symposium of the Process Technology and Modeling Committee. It is a unique opportunity for interdisciplinary presentations and discussions about, among others, processing, sensing, modeling, multi-physics, computational fluid dynamics, and thermodynamics.

The materials covered include ferrous and non-ferrous elements, and the processes range from mining unit operations to jointing and surface finishing of materials. Acknowledging that modern processes involve multi-physics, the symposium and its proceedings allow the reader to learn the methods and outcome of other fields' modeling practices, often enabling the development of practical solutions to common problems. Modeling of basic thermodynamic and physical properties plays a key role, along with computational fluid dynamics and multi-phase transport and interface modeling.

Contributions to the proceedings include applications such as steel processing, modeling of steel and non-ferrous alloys treatments for properties control, multi-physics, and computational fluid dynamics modeling for molten metal processes and properties measurement. Extractive, recovery, and recycling process modeling is also presented, completing a broad view of the field and practices of modeling in materials processing.

The engagement of TMS and committee members to chair sessions and review manuscripts makes this symposium and its proceedings possible. The editor and co-editors acknowledge the invaluable support and contribution of these volunteers as well as TMS staff members, in particular, Patricia Warren, Trudi Dunlap, and Matt Baker.

Samuel Wagstaff
Alexandra Anderson
Adrian S. Sabau

Contents

Part I Process Optimization

Part II Continuous Casting

Part III Slag and Ladle Treatment

Part IV New Processes and Insights

Part V Additive Manufacturing and Materials First Principles

Part VI Poster Session

About the Editors

Samuel Wagstaff is currently a partner at Oculatus Consulting, specializing in aluminum processing and product development. He holds degrees in Mechanical Engineering from Cornell University (B.S.) and Materials Science from MIT (M.S., Sc.D.). Previously as the Lead Scientist at Novelis, he led new product and process development for the entire R&D ecosystem across three continents. Currently, Dr. Wagstaff focuses on increasing profitability and productivities of non-ferrous products by process improvement and fundamental research. He has helped to design over 1 million tons of recycle capacity in the aluminum sector and is the author of over 35 patents. Sam is currently serving as the principal investigator on a $1M ReMADE grant to develop technology to improve the recyclability of organic laden aluminum scrap.

Alexandra Anderson Ph.D., PMP, is an R&D manager at Gopher Resource, LLC, an environmental solutions company specializing in lead battery recycling. Her work focuses on driving furnace productivity and efficiency initiatives through computational fluid dynamic (CFD) modeling and implementing novel equipment designs. Currently, she is also the principal investigator for a DOE HPC4Manufacturing partnership between Gopher Resource and Oak Ridge National Lab investigating high-fidelity multi-phase furnace modeling. Alexandra obtained her B.S. in Mechanical Engineering from Gonzaga University and her M.S. and Ph.D. in Metallurgical and Materials Engineering from the

Colorado School of Mines. Her dissertation investigated fluid flow and thermal profiles within secondary lead reverberatory furnaces using CFD techniques. Alexandra is active in The Minerals, Metals & Materials Society (TMS), where she serves as the vice-chair of the Process Technology and Modeling Committee; she was also the recipient of the 2021 TMS Extraction and Processing Division (EPD) Young Leader Award. Her scholarly activities include nine peer-reviewed publications, co-editorships of seven special topics for JOM, as well as several podium presentations at national conferences.

Adrian S. Sabau received an Engineer Diploma in Mechanical and Materials Processing from the University of Craiova, Romania, and a Ph.D. degree in Mechanical Engineering from Southern Methodist University in 1996. In 1999, Dr. Sabau joined Oak Ridge National Laboratory as a Research Staff Member of Materials Science and Technology, where he worked as a Senior Research Staff Member from 2008. Since 2018, Dr. Sabau has been a Computational Materials Scientist in the Computational Sciences & Engineering Division. Dr. Sabau seeks to advance the materials processing, metal casting, photonic processing, and materials for energy applications through the development of computational fluid dynamics and experimental methodologies for the property measurement, process analysis, and materials behavior in response to conditions experienced in service. Dr. Sabau is an ASME fellow, and ASM fellow, and the recipient of three R&D 100 awards in process sciences. He was granted 7 patents and has published 169 technical papers.

Part I
Process Optimization

Modeling of Macro-scale Reaction Effects in a Secondary Lead Reverberatory Furnace

Nicholas J. Walla, Emily A. Higley, Armin K. Silaen, Alexandra Anderson, Joseph Grogan, and Chenn Q. Zhou

Abstract A long-standing and effective way to recycle lead-acid battery materials is through processing of lead compounds into lead product within a reverberatory furnace. Exploration of process and design changes through unit modification can be costly, time-consuming, and potentially harmful to operational efficiency. Modeling of process behavior, including furnace heat transfer and material reduction/decomposition, can however be difficult. To this end, a method for reflecting the production capabilities of a lead reverberatory furnace under various operational conditions has been developed. Reactions of the lead compounds have been approximated within a steady-state computational fluid dynamics simulation by adding or removing heat from the domain depending on local thermal conditions. With this, process and design changes can be explored in the simulated environment before moving onto more-advanced stages of modeling or experimentation.

Keywords Reverberatory furnace · Lead recycling · Numerical modeling · Pyrometallurgy

---

N. J. Walla (✉) · E. A. Higley · A. K. Silaen · C. Q. Zhou
Center for Innovation through Visualization and Simulation, Purdue University Northwest, 2200 169th Street, Hammond, IN 46323, USA
e-mail: njwalla@pnw.edu

E. A. Higley
e-mail: ehigley@pnw.edu

A. K. Silaen
e-mail: asilaen@pnw.edu

C. Q. Zhou
e-mail: czhou@pnw.edu

A. Anderson · J. Grogan
Research and Development, Gopher Resource, 6505 Jewel Avenue, Tampa 33619, FL, USA
e-mail: Allie.Anderson@GopherResource.com

J. Grogan
e-mail: Joe.Grogan@GopherResource.com

S. Wagstaff et al. (eds.), *Materials Processing Fundamentals 2023*, The Minerals, Metals & Materials Series, https://doi.org/10.1007/978-3-031-22657-1_1

Introduction

Nearly 80% of lead produced within the United States comes from the recycling of scrap lead [1], with nearly half of global lead production being secondary lead produced from lead-acid battery recycling [2]. The dominant method for producing secondary lead is via pyrometallurgical processes in reverberatory furnaces, with 78% of secondary lead produced in the United States using reverberatory furnaces [3]. The growth of secondary lead production brings with it efforts to optimize the process and minimize any environmental impacts. For overall lead production (both primary and secondary), the smelting of secondary lead is a strong contributor to the global warming impact of the lead industry [4], hence the importance of optimization and energy reduction.

Research into reverberatory furnaces has been ongoing for decades using a variety of approaches. Experimental furnaces have been built to examine the specifics of operational behavior, such as the modular furnace design of King et al. [5]. Their modular furnace, in this case an aluminum reverberatory furnace, allowed for exploration of the material heat absorption based on surface area, the effects of combustion space volume changes, the impact of wall emissivity on overall heat flux, and various furnace input and output relationships. Kumar et al. [6] built an experimental furnace to explore the effect of flame impingement on the solid charged material, working to identify the effective heat transfer through the charge material under different furnace conditions. This effort was combined with a computational fluid dynamics (CFD) simulation of the furnace to further explore design and operation conditions.

Numerical modeling of pyrometallurgical furnaces is an attractive alternative to experimentation. Constructing and operating experimental furnaces can be prohibitively expensive or outright impossible in some instances. Experimentation on production furnaces risks damage, lost time, and negative impacts on unit productivity. Using numerical approaches such as CFD to model the multiphase reacting flow conditions offers the opportunity explore design and process decisions without risk and at drastically-lower costs.

Golchert et al. [7] created a CFD analysis of a secondary aluminum reverberatory furnace. The model focuses on the combustion gas space to simulate the fuel combustion, heat transfer, and pollutants/gas flow. Exploration of burner configuration using this model shows improvement to heat transfer when the burners were angled slightly downwards to counter the natural lift of the flame. Also focusing on the combustion gas space, Anderson et al. [8] performed simulations of a secondary lead reverberatory furnace to examine the potential impacts of the burden shape on potential productivity and refractory wear due to flame impingement, thus providing insight into charging behavior and burner positioning.

Numerical exploration of melting and smelting presents inherent difficulties for pyrometallurgical furnaces. Simplifications are often made to ensure numerical stability or to reduce complexity for the sake of computational resources or compute time. Buchholz and Rodseth [9] implemented an artificial heat sink on the aluminum product within the simulation of an aluminum reverberatory furnace. This allowed for the approximation of the absorption of the heat of fusion that occurs in the actual process while allowing for both a steady-state process and a static domain (i.e. no material phase change from the melting product).

This work takes a similar approach to model a secondary lead reverberatory furnace. However, the methodology has been adapted for additional considerations needed to approximate the heat transfer of several melting/smelting reactions. Extending off the previous work of this author [10], mechanisms are implemented for the release of off-gases that occur during furnace operation. With these behaviors, a model of the furnace is created that allows for exploration of design decisions and their impact on productivity while still modeling only the combustion gas space.

Methodology

The simulation model is created in ANSYS Fluent 2022R1 as a 3D, multiphase, steady-state simulation. Turbulence behavior is captured using the SST k-omega RANS turbulence model. The burners are directly modeled, with combustion occurring via the finite-rate/eddy-dissipation concept. Radiative heat transfer is considered using the P1 radiation model. In addition to its use in combustion, the species transport model is used for the off-gassing portion of the pseudo-reaction modeling. As mentioned above, no melting model is considered in this study and only the combustion gas space is included. Combustion of the natural gas fuel was modeled as a two-step reaction, with burner inputs taken from furnace operational conditions corresponding to the temperature and flue gas data used for model tuning.

Currently, not all the information needed to directly model the melting/smelting reactions of the charged material is known. Thus, the primary focus of this work is on the application of a "pseudo-reaction" condition that approximates a few macro-scale behaviors that occur during these reactions. Specifically, the model seeks to replicate the significant temperature changes and off-gas generation that occur.

Domain

With the simulation isolated to the combustion gas space alone, the numerical model consists of mass flow inlets within the burners and a single pressure outlet at the flue duct. The lead and slag tap holes are excluded from this study. A diagram of the furnace domain in this study is shown in Fig. 1. The furnace front contains the burners, the pile of charged burden material, and a small amount of slag/bath surface. The rear of the furnace has the slag/bath surface and the flue. All sides excluding the openings and bottom surfaces are composed of refractory bricks. These bricks are modeled as flat surfaces with thicknesses and convective heat losses defined within the simulation.

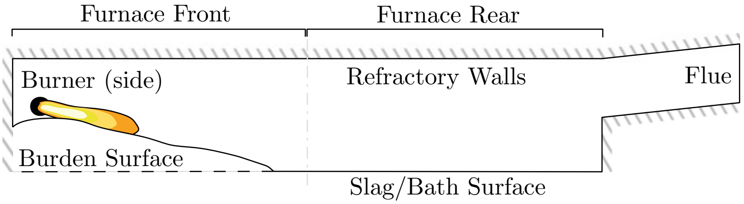

Fig. 1 Side view of furnace CFD domain

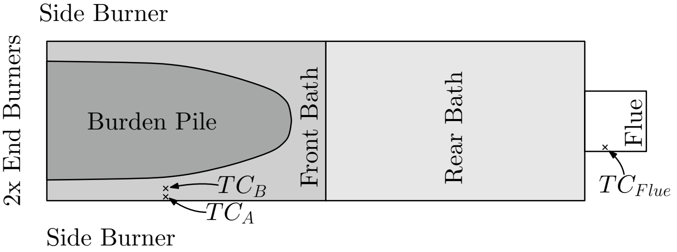

Fig. 2 Top-down view of domain lower surfaces and thermocouple locations

The bottom surface comprises three areas: the burden, the front bath, and the rear bath. The transition from front bath to rear bath occurs at roughly halfway down the length of the furnace. The diagram in Fig. 2 shows the extent of these regions. The burden pile is the portion of charged material that is not submerged within the bath, the shape of which is replicated from measurements of side slope angles, heights of the "spine" along the central axis, and distance from the side walls at several points. Also seen in the diagram are the locations of the three thermocouples used for tuning the behavior the model.

The numerical grid consists of roughly six million polyhedral cells. The cell zone for the combustion space within the furnace is divided into four zones: the overall area combustion gas space of the furnace and a zone for each of the three lower surfaces made by isolating the first three cells neighboring those respective surfaces. These isolated cell zones are used for applying the pseudo-reaction source terms within the simulation, allowing each zone to be treated separately (a necessary consideration due to differences in their behavior).

Heat Transfer Subroutine

The pseudo-reaction methodology consists of using user-defined subroutines to modify the behavior of a base simulation such that the impacts of smelting and melting reactions are included without the direct modeling of said reactions. For the study of the reverberatory furnace, the two primary factors missed by not modeling the

Table 1 Charge material reactions and pseudo-reaction coefficients

i	Reaction	A_i (kJK)	B_i (kJ)	T_{ref} (K)
1	$PbCO_3 \rightarrow PbO(s) + CO_2$ (g)	−0.084	39.01	588
2	$PbSO_4 + 2C \rightarrow PbS + 2CO_2$ (g)	−0.111	21.25	923
3	$Pb(OH)_2 \rightarrow PbO + H_2O$ (g)	0.035	55.51	373
4	$2 PbO + PbS \rightarrow 3 Pb + SO_2$ (g)	−0.294	237.7	1073
5	$2 PbO + C \rightarrow 2 Pb + CO_2$ (g)	−0.156	43.94	873

reactions directly are the exo- and endo-thermic temperature changes caused by the reactions and the off-gases produced by said reactions. The approximation of energy changes within the model was explored by the authors in their previous work [10], wherein surface conditions on the burden and bath were adjusted such that temperatures within the simulation matched measurements taken from furnace operations.

In short, the approach uses artificial heat sinks defined within the simulation using user-defined functions (UDFs) as energy source terms. Each zone has separately-defined heat sinks based on the expected physical behavior of the zone. For the burden, the enthalpy changes and reaction temperatures for each of the five reactions (seen in Table 1) are used to determine the strength of these heat sinks. These are used to generate an approximate linear rate of enthalpy changes across a range of temperatures. Within the UDF, the cell's temperature is compared against each reaction temperature, adding to the sum total of enthalpy change expected within that cell for each matching condition. The equation of this is shown in Eqs. 1, where α_{sink} is a constant that is used to globally tune this behavior.

The rear bath does not have any reactions, thus its condition is a much-simpler linear behavior based on the difference between the cell temperature and the lead liquidus temperature (and also with a scaling factor k_{sink} for adjustment) as seen in Eq. 2. The front bath uses a blend of these two conditions to reflect the submerged pile to the sides and front, with the front or rear behavior "fading" in based on cell position, as seen in Eqs. 3 and 4.

$$q_{\alpha_{\text{sink}}}(T) = -\alpha_{\text{sink}} \cdot \sum_{i=1}^{5} A_i(T - T_{\text{ref}_i}) + B_i \tag{1}$$

$$q_k(T_{\text{adj}}) = -k_{\text{sink}} \cdot (T - T_{\text{liq}}) \tag{2}$$

$$q_{\alpha_{\text{sink,front}}} = q_{\alpha_{\text{sink}}}(T) \cdot \max\left[\left(-\left(\frac{\bar{x} - \bar{x}_{\max}}{\bar{x}_{\max}}\right)^3 + 1\right), 0\right] \tag{3}$$

$$q_{k_{\text{sink,front}}} = q_{k_{\text{sink}}}(T) \cdot \max\left[\left(-\left(\frac{\bar{x}_{\max} - \bar{x}}{\bar{x}_{\max}}\right)^3 + 1\right), 0\right] \tag{4}$$

With the above behavior, the simulation of the reverberatory furnace can be given different burner inputs and result in different temperature profiles on the lower surface due to cells no longer meeting the requirements to “react”. However, upon analyzing the resulting heat balance of the model, an issue was noticed. The relative amount of heat leaving the furnace via the flue gas was far lower than expected. Further analysis showed that the amount of mass leaving the flue was far less than what was measured. While the pseudo-reaction heat condition could alter temperatures, it was not generating the significant gaseous byproducts of the reactions.

Off-Gas Subroutine

To overcome this limitation, a new feature was implemented into the pseudo-reaction code. Taking a similar approach as the heat-changing subroutine, off-gas generation subroutine would use the temperature data of marked cells (this time only above the burden pile) to determine if material needs to be generated. For each cell, the cell temperature is compared to the reaction temperatures of the reactions in Table 1. If the required condition is met, an amount of the resulting gas would be marked for generation. There were only three species to consider for this: CO_2 from reactions 1, 2, and 5, H_2O from reaction 3, and SO_2 from reaction 4. The SO_2 species is unique in that it will only generate within the domain due to the burden reactions, as the other two are also byproducts of the burner combustion.

As with the temperature data tuning via comparison with thermocouples, flue gas measurements allowed for tuning of the off-gas condition. However, while the temperature condition required only two tuning coefficients (α and k), the species condition required four: β_c for CO_2, β_h for H_2O, β_s for SO_2, and γ for the amount of mass generated. The β values are used to adjust the amount of species “generated” within the marked cells, as without the consideration of material consumption or reaction rates there is no way to quantify the relative differences in reactant quantity. With these β terms, each of the three separate off-gas species can be individually adjusted as needed.

In ANSYS Fluent, defining a source term for a species forces a species fraction but does not generate mass to match. Therefore, after determining how much of each species is generated within a particular cell, a *DEFINE_ADJUST* subroutine is executed to calculate a total amount of mass to be generated within the cell. This value is multiplied by the γ constant to scale the mass generation up or down as needed to match the known flue gas flow rate. A diagram of the UDF logic is shown in Fig. 3.

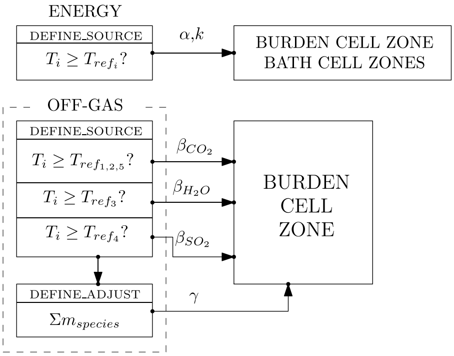

Fig. 3 UDF procedure for energy and off-gas behaviors

Results

As mentioned earlier, the pseudo-reaction behavior is tuned relative to data gathered from operation of the reverberatory furnace. The energy-adjustment subroutine is tuned such that temperature measurements within the simulation match measured values from three thermocouples (two near the burden pile and one within the flue). The previous efforts using only the energy-adjusting behavior [10] required tuning of the α and k terms to match the thermocouples. The relationship between the temperatures within the model and those parameters (mostly α) was nearly linear.

However, upon adding the off-gas generation behavior, differences were noted in both the temperature profiles of the system and the simulation's response to the tuning coefficients. The two systems (energy and off-gas) are inherently linked; a change in temperature results in an altered distribution/concentration of off-gasses which in turn affect the thermal properties of the combustion gas thus affecting the movement of heat within the domain. This leads to a more-difficult balancing act between the coefficients and the target values.

Figure 4 shows contours of temperature (normalized relative to global minimum and maximum values) on the lower surfaces of the furnace. Colder regions can be seen in the back of the burden pile and in the front of the pile that is only indirectly exposed to the heat from the burners. The spine of the burden pile is also at a slightly-lower temperature. The highest temperatures can be seen on the sides of the pile directly where the flames of the side burners impinge upon the burden material.

Plotting the strength of the pseudo-reaction's energy removal, an interesting pattern appears. Due to the nature of the enthalpy-based coefficients for each reaction, the regions with the highest temperatures do not correspond to the areas with the strongest degree of heat removal. As seen in Fig. 5, two "rings" of high energy removal exist near the peripheries of the burner impingement zones. With the exception of the third reaction (which remains endothermic), the reactions transition from endothermic behavior to exothermic behavior at various temperatures. At a temperature of approximately 1600 K a transition point is reached where the endothermic

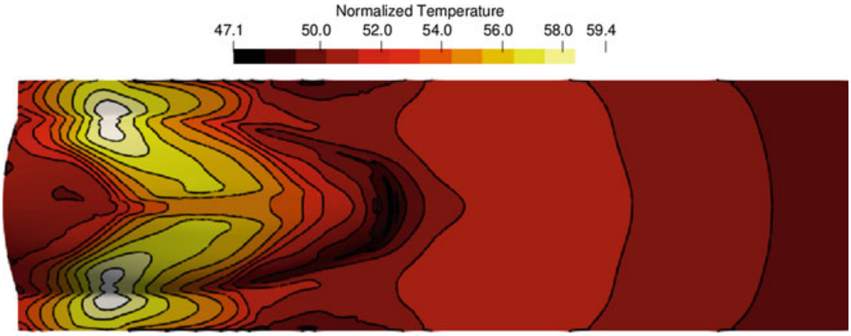

Fig. 4 Locally-scaled contours of normalized temperatures on lower surfaces

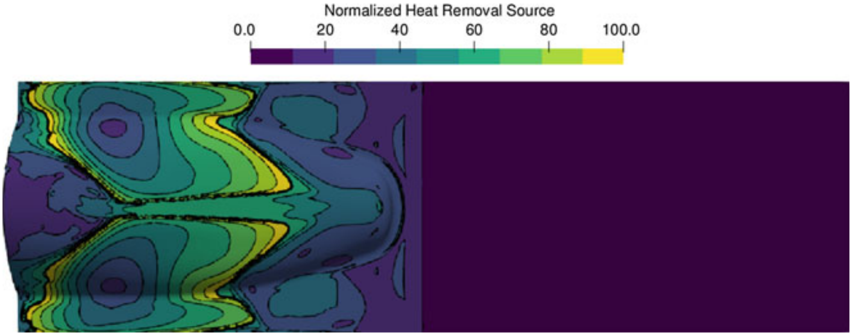

Fig. 5 Contours of pseudo-reaction energy source term on lower surfaces

and exothermic behaviors of all five reactions cancel each other out. This leads to a natural balancing effect in some regions of the burden pile.

As the SO_2 in the system is only sourced from the pseudo-reaction source term, contours of SO_2 concentration along the center plane of the domain provide some insight into the behavior approximated reactions. Figure 6 shows the off-gassing of the SO_2 from the burden surface, with the gas flow of the furnace driving the emissions towards the flue. The rear of the burden pile produces very little SO_2, likely due to the lower temperatures as the reaction which produces the SO_2 has the highest reaction temperature of the five reactions in the model.

The resulting composition of the flue gas after tuning the coefficients was within desired ranges for both the concentration of the target species as well as for the overall mass flow rate. Table 2 shows the resulting error in the model results relative to the measured data from furnace operations. The highest error seen is for the oxygen content of the flue versus the simulation. One aspect of the reactions that is not currently considered is the consumption of oxygen by the coke in Reaction 5. In operational measurements, flue gas volume of oxygen was found to be between

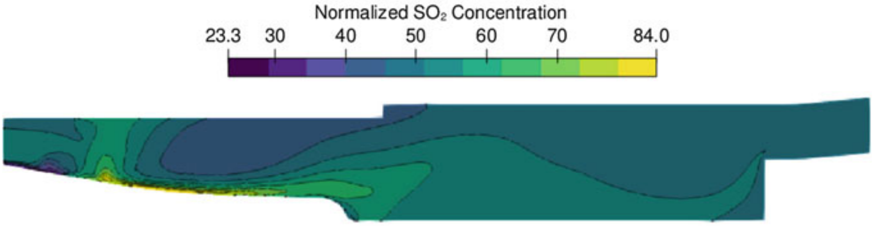

Fig. 6 Side view center plane contours of normalized SO_2 concentration

Table 2 Flue gas composition and flow rate error relative to operations

	H_2O	CO_2	O_2	SO_2	$\dot{m}_{\text{flue}}$
Error %	9%	7%	69%+	3%	5%

Table 3 Heat balance error relative to operations

Case	Reactions (%)	Walls (%)	Cooling (%)	Flue (%)	Total (%)
No Off-Gas	+65	−70	−57	−45	+7
Off-Gas	<1	−33	−54	−9	+7

Table 4 Thermocouple temperature error relative to operations

Case	TC_A (%)	TC_B (%)	TC_F (%)
No off-gas	1	2	1
Off-gas	0	2	11

0–4% (averaged to 2% for this analysis) while the simulation shows roughly 5% of flue output being oxygen.

Looking at the resulting heat removal within the furnace, Table 3 shows the impact of the off-gas inclusion in the pseudo-reaction model. It is estimated that 30–40% of the heat from the combustion sources is consumed by the melting and smelting processes. Comparing the previous pseudo-reaction simulation (without off-gassing) to a heat balance of the operating furnace, reactions and super-heating of the bath went from an over-prediction of roughly 65% (62% of combustion input) to nearly matching the estimation. The accuracy of heat removal via the walls also improved, though the error in heat removed via cooling elements remained unchanged. The heat removal via flue gasses is still slightly under-predicted but is much improved over the simulation without off-gas consideration.

One noticeable impact of the off-gas inclusion was an increased sensitivity to the adjustment of the α_{sink} value for the burden and bath energy removal. Previously, the α_{sink} term was found to have an almost-linear impact on the temperatures at the front and rear of the furnace. However, the addition of the off-gas species resulted in much greater changes at the front area of the furnace (at the two burden-adjacent thermocouples) versus the rear (flue thermocouple) region, with flue temperatures remaining close to the target value but front values plummeting at higher values of α_{sink}.

While the energy loss-only study used an α_{sink} of 70 to obtain a temperature match to the thermocouple data, the off-gas study required a lowering of the value to 40. Even then, Table 4 shows errors in temperature measurements increased from between 1–2% error up to as much as 11% error, with flue temperatures being much higher. This behavior is currently being investigated by the authors, but may be due to the "doubling-up" of heat removal via the source term and generation of new mass in the cell, wherein added mass alters the impact of the energy source term as applied by ANSYS Fluent as well as the increased heat capacity of the species-laden gas convecting more heat away from the burden region.

Interestingly, the error for overall heat losses within the furnace remained the same between the two simulations, indicating that the heat previously removed by the energy subroutine is now being transported by the generated species to exit at the flue.

Conclusions

In this work, a numerical subroutine was developed and applied to the steady-state simulation of a secondary lead reverberatory furnace. Aiming to replicate the macro-behaviors of the melting and smelting reactions from the conversion of the charge materials into liquid lead, a pseudo-reaction was used to alter the heat balance within the furnace as well as generate off-gasses that would occur during the process. The current model has been adjusted to match the measured behaviors of the operational furnace, with further work underway to validate and explore the model. Once validated, the simplifications made within this model will allow for faster modeling of furnace conditions, including exploration of furnace design and burner set points.

Acknowledgements This work was funded by Research Award No. W911NF1920108 from the Army Research Laboratories of the Department of Defense and the Worcester Polytechnic Institute. The authors would also like to extend their gratitude for Gopher Resource in providing information on design, operational conditions, measurement data, and process insight.

References

1. U.S. Geological Survey: Mineral commodity summaries 2021. Technical report, U.S. Geological Survey, Reston, VA (2021). https://doi.org/10.3133/mcs2021. https://pubs.er.usgs.gov/publication/mcs2021
2. Gottesfeld P, Pokhrel AK (2011) Review: lead exposure in battery manufacturing and recycling in developing countries and among children in nearby communities. J Occupat Environ Hyg 8(9):520–532

3. Queneau PB, Leiby R, Robinson R (2015) Recycling lead and zinc in the United States. World Metall ERZMETALL 68(3):149–162
4. Davidson AJ, Binks SP, Gediga J (2016) Lead industry life cycle studies: environmental impact and life cycle assessment of lead battery and architectural sheet production. Int J Life Cycle Assess 21(11):1624–1636
5. King PE, Hayes MC, Li T, Han Q, Hassan M, Golchert BM (2005) Design and operation of an experimental reverberatory aluminum furnace (2005)
6. Kumar A, Venuturumilli R, Kiss L, Walter G (2008) Experimental and numerical study of flame load heat transfer in an experimental furnace
7. Golchert BM, Zhou CQ, Quenette A, Han Q, King PE (2005) Combustion space modeling of an aluminum furnace, pp 887–892
8. Anderson A, Grogan J, Bogin G, Taylor P (2018) Computational Modeling of a secondary lead reverberatory furnace: effect of burden geometry. In: Davis BR, Moats MS, Wang S (eds) Extraction 2018. Springer, Ottawa, Ontario, Canada, pp 881–890. https://doi.org/10.1007/978-3-319-95022-8_70
9. Buchholz A, Rodseth J (2011) Investigation of heat transfer conditions in a reverberatory melting furnace by numerical modeling. Light Metals 2011:1179–1184
10. Walla NJ, Anisiuba V, Silaen AK, Anderson A, Grogan J, Zhou CQ (2022) Boundary conditions for modeling of a lead reverberatory furnace. In: ASME 2022 heat transfer summer conference, p. 8. American Society of Mechanical Engineers, Philadelphia, Pennsylvania, USA (2022). https://doi.org/10.1115/HT2022-81206. https://asmedigitalcollection.asme.org/HT/proceedings/HT2022/85796/V001T18A002/1146590

Effect of Wearing Impellers on Multiphase Flow and Desulfurization During KR Mechanical Stirring Process

Wei Chen, Yanyu Zhao, and Lifeng Zhang

Abstract It is of great significance to study the variation of the multiphase flow during the entire service process of an impeller to improve the dispersion of the desulfurizer and the desulfurization efficiency during the KR desulfurization process. In the current study, the key dimensions of an actual KR impeller during the service process were quantitatively measured first. Then, a three-dimensional model coupled with the k-ε turbulence model, VOF multiphase flow model, DPM model, UDS model, and unreacted core desulfurization model was established to predict the multiphase flow and desulfurization during the KR mechanical stirring process with different wearing impellers. The results show that with the increase of the wear degree of the impeller, the stirring effect was gradually weakened, resulting in a gradual weakening of the desulfurization efficiency. The desulfurization end sulfur content was 58.2 ppm after the impeller employed 220 heats, which was more than 4 times higher than the 13.0 ppm with a new impeller.

Keywords Wearing impellers · Multiphase flow · Desulfurization · KR process

Introduction

The KR mechanical stirring method has obvious advantages in the desulfurization effect and desulfurization cycle due to its superior kinetic conditions and is widely used in the hot metal pretreatment desulfurization process [1, 2]. Many researches about the fluid flow and desulfurization during the KR process have been published. Ji [3] used the Euler-granular model to study the mixing of the desulfurizer and

---

W. Chen
School of Mechanical Engineering, Yanshan University, Qinhuangdao 066004, China

Y. Zhao
Beijing Shougang Co., Ltd, Qianan, Hebei 064404, China

L. Zhang (✉)
School of Mechanical and Materials Engineering, North China University of Technology,
Beijing 100144, China
e-mail: zhanglifeng@ncut.edu.cn

S. Wagstaff et al. (eds.), *Materials Processing Fundamentals 2023*, The Minerals, Metals
& Materials Series, https://doi.org/10.1007/978-3-031-22657-1_2

high-sulfur hot metal under the variable-velocity stirring method. The effect of the impeller geometry on the fluid flow and particle volume fraction was investigated [4]. Li [5] developed a coupled k-ε model and VOF model to get insight into the flow pattern and interface behavior taking place during the KR desulfurization process. It shows that the interface profile and vortex depth strongly depend on the impeller dimension. Wang [6] established a transient-coupled three-dimensional numerical model to study the two-phase flow, heat transfer, desulfurizer motion, and desulfurization behavior during the KR hot metal treatment. He [7] studied the distribution and motion behavior of desulfurizers in a 170 t hot metal ladle with KR mechanical stirring using the Eulerian–Lagrangian approach. Nakaoka [8] investigated the fluid flow and particle transport accompanied by turbulent agglomeration using numerical simulation. It can be seen that most of the research was concerned with the fluid flow, vortex distribution, and particle dispersion. In addition, most of the published studies on the hot metal desulfurization were theoretical analyses and experimental observations applicable to special conditions [9, 10]. However, the desulfurization model with a wider scope needed to further couple the numerical simulation of the fluid flow and the desulfurization kinetic model, but this part of the research was still relatively few. The effect of the wear degree of the impeller on the flow field and desulfurization also needed further study [11].

In the current study, a three-dimensional model coupled with the k-ε turbulence model, VOF multiphase flow model, DPM model, UDS model, and unreacted core desulfurization model was established to investigate the effect of the impeller wear degree on the multiphase flow and desulfurization in a 250 t KR hot metal ladle.

Mathematical Model

A three-dimensional model based on a 250 t KR hot metal ladle was established, as shown in Fig. 1. The range of rotation speed and immersion depth of the impeller in the actual production process was 90–110 rpm and 1500–1700 mm, respectively. The upper and lower diameter of the hot metal ladle after removing the refractory part was 4066 mm and 3738 mm. The total number of grids of the current mold was about 0.5 million. Other specific model parameters and boundary conditions can be found in the previous study [12].

The upper and lower rotation diameter of the initial unused impeller in Fig. 1 were 1400 mm and 1300 mm, respectively. The height and width were 950 and 480 mm. As the stirring time increased, the employed impeller was gradually eroded by the hot metal and slag. In addition, the desulfurization slag also adhered to the impeller. Figure 2 shows the morphology of the same impeller with the initial state (left), after employed 120 heats (middle), and after employed 220 heats (right). The service life of the impeller was about 270 heats, and the results in Fig. 2 show that the impeller was severely eroded after employed 220 heats. Therefore, the above impellers were modeled and their effects on the flow field and desulfurization were investigated.

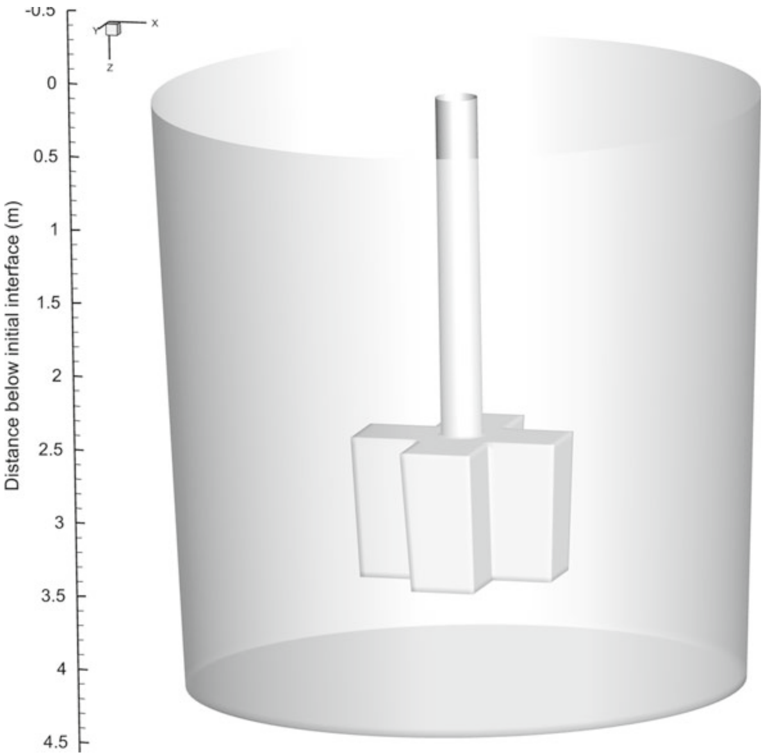

Fig. 1 Distribution of the computational domain

Fig. 2 Morphology of the same impeller with the initial state (left), after employed 120 heats (middle), and after employed 220 heats (right)

The VOF multiphase flow model was used to solve the volume fraction of the hot metal and air phases. The continuity equation and momentum equation for phase q are shown below.

$$\frac{\partial}{\partial t}\left(\alpha_q \rho_q\right) + \nabla \cdot \left(\alpha_q \rho_q \mathbf{u}_q\right) = 0 \tag{1}$$

$$\sum_{q=1}^{m} \alpha_q = 1 \tag{2}$$

$$\frac{\partial}{\partial t}(\rho \mathbf{u}) + \nabla \cdot (\rho \mathbf{u}\mathbf{u}) = -\nabla P + \nabla \cdot \left[\mu\left(\nabla \mathbf{u} + \nabla \mathbf{u}^{\mathrm{T}}\right)\right] + \rho \mathbf{g} + \mathbf{F} \tag{3}$$

where α_q is the volume fraction, ρ_q is the density in kg/m^3, and $\boldsymbol{F}$ is the momentum exchange between the phases due to interface force in kg/(m^2 s^2).

The turbulent flow inside the hot metal was solved using the standard k-ε model. The equation of turbulent kinetic energy k and its dissipation rate ε is calculated as:

$$\alpha_l \rho_l \left(\frac{\partial k}{\partial t} + \frac{\partial (k u_i)}{\partial x_i}\right) = \frac{\partial}{\partial x_j}\left[\alpha_l \left(\mu + \frac{\mu_{\mathrm{t}}}{\sigma_k}\right)\frac{\partial k}{\partial x_j}\right] + \alpha_l G_k - \alpha_l \rho_l \varepsilon \tag{4}$$

$$\begin{aligned} \alpha_l \rho_l \left(\frac{\partial \varepsilon}{\partial t} + \frac{\partial \varepsilon u_i}{\partial x_i}\right) = {} & \frac{\partial}{\partial x_j}\left[\alpha_l \left(\mu + \frac{\mu_{\mathrm{t}}}{\sigma_\varepsilon}\right)\frac{\partial \varepsilon}{\partial x_j}\right] \\ & + \alpha_l C_{1\varepsilon}\frac{\varepsilon}{k} G_k - \alpha_l C_{2\varepsilon} \rho_l \frac{\varepsilon^2}{k} \end{aligned} \tag{5}$$

where α_l is the volume fraction of hot metal; ρ_l is the density of hot metal, kg/m^3; μ_{t} is the turbulent viscosity, kg/(m s); The $C_{1\varepsilon} = 1.44$, $C_{2\varepsilon} = 1.92$, $\sigma_k = 1.0$, $\sigma_\varepsilon = 1.3$.

The trajectory of the desulfurizer particles was solved using the DPM as follows:

$$\begin{aligned} \frac{\mathrm{d}\mathbf{u}_{\boldsymbol{p}}}{\mathrm{d}t} = {} & \frac{\left(\rho_p - \rho_l\right)}{\rho_p}\mathbf{g} + \frac{3\mu C_{\mathrm{D}}\mathrm{Re}}{4\rho_p d_p^2}\left(\mathbf{u}_{\boldsymbol{l}} - \mathbf{u}_{\boldsymbol{p}}\right) \\ & + C_{\mathrm{VM}}\frac{\rho_l}{\rho_p}\frac{\mathrm{d}}{\mathrm{d}t}\left(\mathbf{u}_{\boldsymbol{l}} - \mathbf{u}_{\boldsymbol{p}}\right) + \frac{\rho_l}{\rho_p}\mathbf{u}_{\boldsymbol{p}}\nabla \cdot \mathbf{u}_{\boldsymbol{l}} \end{aligned} \tag{6}$$

where the four terms on the right side of the equation are gravity buoyancy force, drag force, pressure gradient force, and virtual mass force, respectively. The details can be found in the previous study [12].

A UDS transport equation was used for the convection and diffusion of the sulfur in the hot metal.

$$\frac{\partial}{\partial t}(\rho[\mathrm{S}]) + \nabla \cdot (\rho \mathbf{u}[\mathrm{S}]) = \nabla \cdot \left(\left(\rho D_{\mathrm{S}} + \frac{\mu_{\mathrm{t}}}{\mathrm{Sc}_{\mathrm{t}}}\right)\nabla \cdot [\mathrm{S}]\right) + \mathrm{S}_{\mathrm{CaO}} \tag{7}$$

where [S] is the mass fraction of sulfur in the hot metal; D_S is the diffusion coefficient m^2/s; Sc_t is the turbulent Schmidt number; S_{CaO} is the desulfurization source in kg/(m^3 s).

The desulfurization source S_{CaO} was calculated using the unreacted core model as follows [12]:

$$v_1 = \frac{4\pi r_0^2 \rho_l k_s}{100}([S] - [S]_e) \tag{8}$$

$$k_s = \frac{D_S}{d_p}\left(2.0 + 0.6\mathrm{Re}^{1/2}\mathrm{Sc}^{1/3}\right) \tag{9}$$

$$\mathrm{Sc} = \frac{\mu}{\rho_l D_S} \tag{10}$$

where each variable can be found in the previous study [12].

Multiphase Flow and Desulfurization in the Hot Metal Ladle

Figures 3 and 4 show the effect of the number of employed heats of the impeller on the distribution of flow pattern and volume fraction of hot metal, respectively. The rotation speed was 90 rpm, and the immersion depth was 1500 mm. It can be seen that with the increase of the number of employed heats of the impeller, the stirring effect on the hot metal gradually decreased and the overall velocity of the hot metal also decreased accordingly. As the number of impeller employed heats increased, two vortexes close to the shaft of the impeller gradually decreased and moved up until nearly disappearing after employed 220 heats.

Figures 5 and 6 show the effect of the number of employed heats of the impeller on the average sulfur content and desulfurization rate of the hot metal under the conditions of a rotating speed of 90 rpm and an immersion depth of 1500 mm. The desulfurization rate gradually decreased with the increase of the number impeller employed heats. With the same amount of desulfurizer added, the sulfur content at the desulfurization end increased from 13.0 ppm in the initial state of the impeller to 26.7 ppm and 58.2 ppm after the impeller employed 120 and 220 heats, respectively.

Conclusions

1. The key dimensions of an actual KR impeller with the initial state and after employed 120 and 220 heats were quantitatively measured. The effect of the number of employed heats of the impeller on the multiphase flow and desulfurization in a 250 t hot metal was numerically studied.

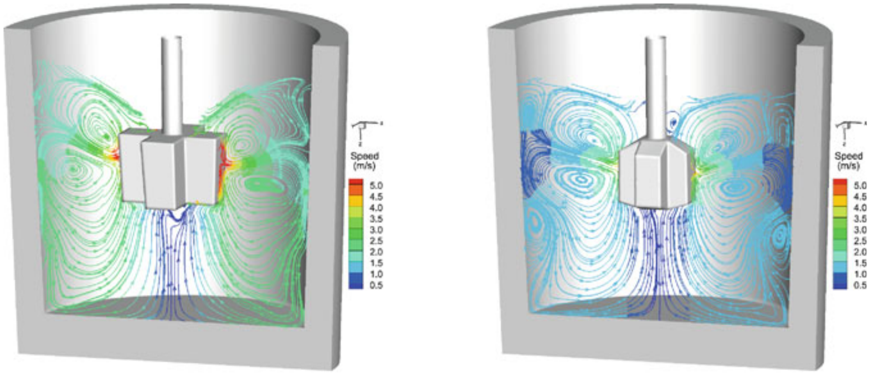

(a) Initial state (b) After employed 120 heats

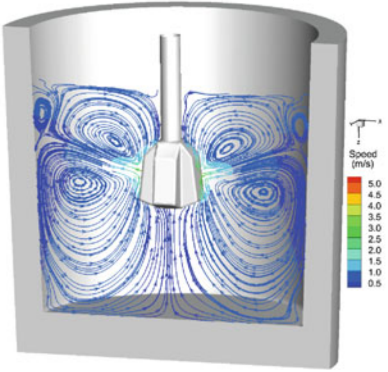

(c) After employed 220 heats

Fig. 3 Effect of the number of employed heats of the impeller on the distribution of flow pattern, **a** initial state, **b** after employed 120 heats, **c** after employed 220 heats

2. A three-dimensional model coupled with the k-ε turbulence model, VOF multiphase flow model, DPM model, UDS model, and unreacted core desulfurization model was successfully developed to predict the variation of the sulfur content and desulfurization rate.
3. The overall velocity of the hot metal significantly decreased with the increase of the number of employed heats of the impeller. The sulfur content at the desulfurization end increased from 13.0 ppm in the initial state of the impeller to 26.7 ppm and 58.2 ppm after the impeller employed 120 and 220 heats, respectively.

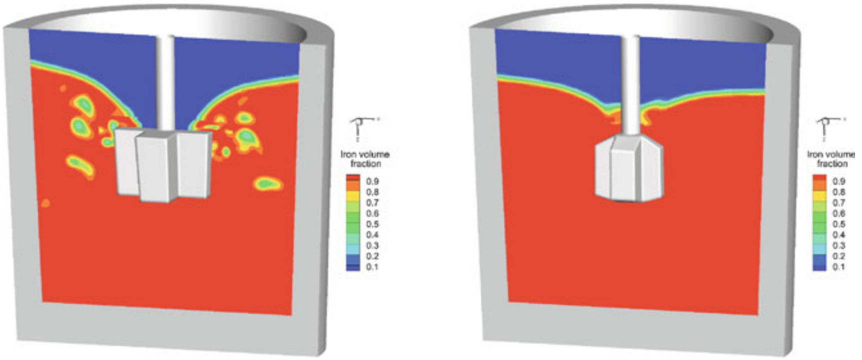

(a) Initial state (b) After employed 120 heats

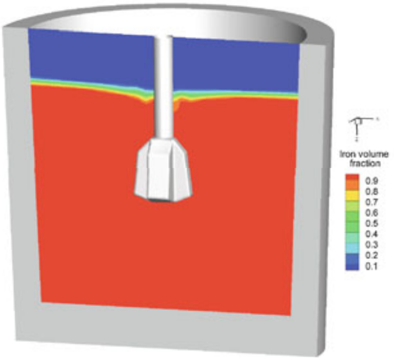

(c) After employed 220 heats

Fig. 4 Effect of the number of employed heats of the impeller on the distribution of hot metal volume fraction, **a** initial state, **b** after employed 120 heats, **c** after employed 220 heats

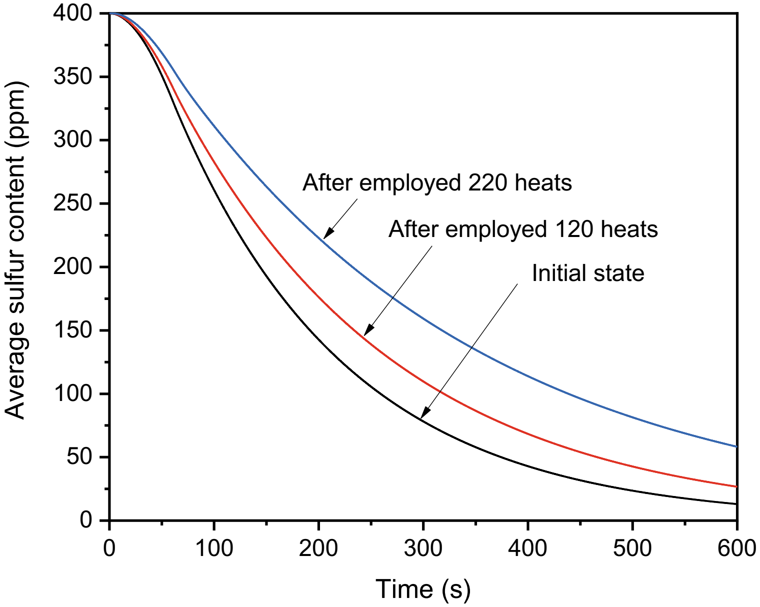

Fig. 5 Effect of the number of employed heats of the impeller on the sulfur content of hot metal

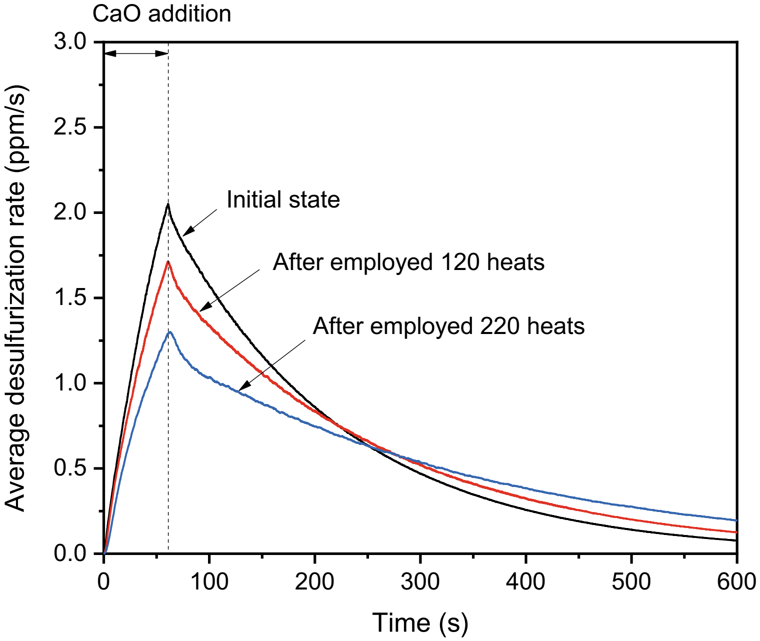

Fig. 6 Effect of the number of employed heats of the impeller on the desulfurization rate of hot metal

Acknowledgements The authors are grateful for the funding and support of the Science and Technology Project of Hebei Province (20311004D, 20591001D, 20311005D), High Steel Center of Yanshan University (HSC), and High Steel Center of North China University of Technology (HSC).

References

1. Nakai Y, Sumi I, Matsuno H, Kikuchi N, Kishimoto Y (2010) Effect of flux dispersion behavior on desulfurization of hot metal. ISIJ Int 50(3):403–410
2. Kurokawa N, Matsuo S, Jouguchi H, Yamada K, Watanabe Y (1993) Development in hot metal desulphurization process. Sumitomo Met 45(3):52–58
3. Ji J, Liang R, He J (2016) Simulation on mixing behavior of desulfurizer and high-sulfur hot metal based on variable-velocity stirring. ISIJ Int 56(5):794–802
4. Ji J, Du H, Jiang Y, Li D, Zhang S (2021) Effect of impellers on particle mixing behaviour in KR desulphurization process. Ironmaking Steelmaking 49(2):167–177
5. Li Q, Shen X, Guo S, Li M, Zou Z (2021) Computational investigation on effect of impeller dimension on fluid flow and interface behavior for kanbara reactor hot metal treatment. Steel Res Int 92(11)
6. Wang Q, Jia S, Tan F, Li G, Ouyang D, Zhu S, Sun W, He Z (2021) Numerical study on desulfurization behavior during kanbara reactor hot metal treatment. Metall Mater Trans B 52(2):1085–1094
7. He M, Wang N, Chen M, Chen M, Li C (2020) Distribution and motion behavior of desulfurizer particles in hot metal with mechanical stirring. Powder Technol 361:455–461
8. Nakaoka T, Taniguchi S, Matsumoto K, Johansen ST (2001) Particle-size-grouping method of inclusion agglomeration and its application to water model experiments. ISIJ Int 41(10):1103–1111
9. Nakai Y, Hino Y, Sumi I, Kikuchi N, Uchida Y, Miki Y (2015) Effect of flux addition method on hot metal desulfurization by mechanical stirring process. ISIJ Int 55(7):1398–1407
10. Jeong B-K, Bang G-H, Kang Y-B (2022) Role of liquid and solid particles in solid-liquid mixed fluxes on sulfur removal from molten iron under centrifugal stirring by an impeller. Powder Technol 396:1–12
11. Xiao L, Chen K, Dan B, Rong Z, Wang R (2016) Numerical study of flow field on molten iron desulfurization with mechanical stirring. Adv Mech Eng 8(7):1687814016649326
12. Zhao Y, Chen W, Cheng S, Zhang L (2022) Mathematical simulation of hot metal desulfurization during KR process coupled with an unreacted core model. Int J Miner Metall Mater 29(4):758–766

Post Processing Approach to Model Microsilica Formation

Kurian J. Vachaparambil, Kristian Etienne Einarsrud, Halvor Dalaker, and Stefan Andersson

Abstract In this work an OpenFOAM-based framework to simulate the evolution of microsilica, which is an important byproduct in the silicon/ferrosilicon industries, is proposed. The framework decouples the combustion reaction of CO and SiO from the microsilica generation based on the assumption that the combustion occurs in an oxygen rich environment - SiO_2 generated by combustion is much larger than its depletion due to particle evolution. The combustion of the reactants in the furnace hood is performed using rhoReactingBuoyantFoam, and its results are used as input to a population balance solver that simulates the particle nucleation and growth (due to mass transfer onto the particle surface) as well as depletion of SiO_2. The framework predicts particles of size around 30 nm at the outlet which is approximately in the smaller sizes of the particles observed in microsilica during experiments reported in literature.

Keywords Microsilica · CFD · OpenFOAM

Supplementary Information The online version contains supplementary material available at https://doi.org/10.1007/978-3-031-22657-1_3.

K. J. Vachaparambil (✉)
Process technology, SINTEF Industry, Trondheim, 7465, Norway
e-mail: kurian.vachaparambil@sintef.no

K. E. Einarsrud
Department of materials science and engineering, Norwegian University of Science and Technology (NTNU), Trondheim 7491, Norway
e-mail: kristian.e.einarsrud@ntnu.no

H. Dalaker · S. Andersson
Metal production and processing, SINTEF Industry, Trondheim 7465, Norway
e-mail: halvor.dalaker@sintef.no

S. Andersson
e-mail: stefan.andersson@sintef.no

S. Wagstaff et al. (eds.), *Materials Processing Fundamentals 2023*, The Minerals, Metals & Materials Series, https://doi.org/10.1007/978-3-031-22657-1_3

Introduction

During the production of silicon and ferrosilicon alloys, SiO reacts with oxygen (above the furnace hood) to form SiO_2 which nucleates to form particles which is referred to as microsilica. These are essentially amorphous silicon dioxide particles, typically around 0.1 μm in diameter (consisting of submicron and micron sized clusters), which has applications in cements [1–3]. As the quality and yield of microsilica are influenced by the conditions in the furnace, understanding how these particles evolve is critical.

In the best knowledge of the authors, the work by González-Fariña et al. [4] (and the associated doctoral thesis [5]) is the only one in literature to investigate the evolution of microsilica. In the doctoral work, [5], steady state simulation (using COMSOL) of the furnace hood (with a simplified 2D geometry) showed a narrow region in the furnace hood where the reactants and air mixed are the region where the microsilica was produced. Based on the simulation results of [4], [5] investigated the formation microsilica by the fully coupled transient model for a 1D case which investigated the phenomena when the reactants and air is well mixed and initially separated in addition to exploring the dynamics at two physical limits. The first limit: when O_2 is plentiful - the model (with particle evolution not coupled to the temperature and SiO_2 distribution) predicted the particle growing perpetually as SiO_2 is not depleted. The other limit: when the particle evolution is fully coupled to both the temperature field and SiO_2 field resulting in particles evolving until SiO_2 was depleted in addition to temperature being higher due to the heat released due to particle evolution that was hypothesized to cause the nucleation of more particles. The main drawback of [4] is that effect of velocity and turbulence was not treated in addition to the 1D simplification used. Additionally, the framework used by González-Fariña et al. [4] couples the particle growth (but not the particle nucleation) to the depletion of SiO_2.

In this work, inspired by González-Fariña et al. [4], we propose a OpenFOAM-based framework to model microsilica evolution in the furnace hood. The model assumes that the reactions occur in the oxygen rich environment to decouple the microsilica evolution from the combustion. The model accounts for the ceasing of the particle growth when SiO_2 reaches saturation. The model considers the microsilica evolution driven by just nucleation and growth by mass transfer to the surface, and that particle evolution does not impact the temperature field obtained from combustion reactions and that these particles do not agglomerate nor does it change the velocity field. Due to the high Reynolds number of the flow in the furnace hood [5], advection of the microsilica is treated and the flow is assumed to be dominated by turbulence.

Overview of the Proposed Framework

Modelling the Combustion of Gaseous Species

The main gaseous species found over the charge in the furnace react exothermically based on: $2CO + O_2 \leftrightharpoons 2CO_2$ and $2SiO + O_2 \leftrightharpoons 2SiO_2$ with N_2 assumed to be inert. This is in theory a multi-component mixture undergoing turbulent combustion which can be simulated using rhoReactingBuoyantFoam. The governing equations involving gaseous species in rhoReactingBuoyantFoam are the mass, momentum, energy, and species conservation:

$$
\begin{aligned}
&\frac{\partial \rho}{\partial t} + \nabla \cdot \left(\rho \vec{U}\right) = 0, \\
&\frac{\partial \rho \vec{U}}{\partial t} + \nabla \cdot \left(\rho \vec{U} \vec{U}\right) = -\nabla p_{rgh} - \vec{g} \cdot \vec{x} \nabla \rho + \nabla \cdot \tau, \\
&\frac{\partial \rho Y_i}{\partial t} + \nabla \cdot \left(\rho \vec{U} Y_i\right) + \nabla \cdot \vec{J_i} = \dot{w}_i, \\
&\frac{\partial \rho h_s}{\partial t} + \nabla \cdot \left(\rho \vec{U} h_s\right) + \frac{\partial \rho K}{\partial t} + \nabla \cdot \left(\rho \vec{U} K\right) - \frac{\partial p}{\partial t} + \nabla \cdot \vec{J_s} = \dot{Q}_r,
\end{aligned}
\tag{1}
$$

where ρ is the density of gaseous mixture, $\vec{U}$ is the velocity, p is the pressure, $p_{rgh} = p - \rho \vec{g} \cdot \vec{x}$, τ is the viscous stress tensor, Y_i is the mass fraction of ith species, h_s is the sensible enthalpy, and K is the specific kinetic energy. The diffusive flux of species, $\vec{J_i}$, is approximated based on Fick's 1^{st} law and the diffusion coefficient computed based on momentum diffusivity under the assumption of Schmidt number (Sc) is equal to one since turbulence is dominant. The heat flux, $\vec{J_s}$, is calculated based on conductive heat transfer and by ignoring the effect of species diffusion. The source terms in the energy equation, $\dot{Q}_r$ account for the heat production from the chemical reactions. It should be mentioned that we have ignored the impact of radiative heat transfer in this work. The source term in the species transport equation ($\dot{w}_i$), which takes into account the generation or consumption of species due to chemical reactions, is computed based on Eddy Dissipation Concept (EDC) model. Apart from the above conservation equations, there is governing equations related to modelling the turbulent nature of these gaseous flow which in this work is based on the $k - \omega$ SST model. The solver also treats the temperature dependent nature of transport and thermodynamic properties of species as well as the equation of state of the gas mixture (using perfect gas model).

Modelling Microsilica Evolution

To simulate the evolution of microsilica in the furnace hood, we employ quadrature method of moment (QMOM)-based population balance modelling approach (see [6]) to solve for the evolution of a particle size distribution function (PSD) or number density function (NDF), n. The QMOM approach uses moments which are defined as $m_k = \int_{L_{\min}}^{\infty} nL^k dL = \sum_{i=1}^{N} w_i L_i^k$ where $L_{\min}$ is the smallest possible size of the particles or the nucleation diameter for microsilica, w_i and L_i are the weight and abscissa of ith node of the QMOM, and N is the total number of nodes used in the quadrature approximation. It should be noted that the units of w_i and L_i are m^{-3} and m respectively. The average size of particle, also known as Sauter mean diameter, is computed as $d_{32} = m_3/m_2$. The governing equation for moments that describes microsilica evolution is

$$\frac{\partial m_k}{\partial t} + \nabla \cdot (\vec{U} m_k) = \nabla \cdot (D_p \nabla m_k) + L_{min}^k J + \sum_{i=1}^{N} k G w_i L_i^{k-1}. \qquad (2)$$

where $\vec{U}$ is the flow velocity (which is assumed to be steady field which is not impacted by the particle evolution), D_p is the effective diffusion coefficient of particles in the turbulent flow (in m^2/s), J is the nucleation rate computed in Eq. 3, and G is the growth rate of the microsilica particle size whose calculation is described in Eq. 5.

Nucleation Rate

When the local SiO_2 concentration reaches saturation, microsilica particles are nucleated in the bulk—homogeneous nucleation. The critical size for nucleation or $L_{\min}$ is calculated as $L_{\min} = \frac{4\gamma v_C}{k_B T \ln S}$ where S is the supersaturation ratio ($S = C_{\mathrm{SiO_2}/C_{\mathrm{sat}}}$), γ is the surface energy of SiO_2 molecule ($= 3.2 \times 10^{-2}$ J/m^2), v_C is the volume of a SiO_2 molecule ($= 4.536 \times 10^{-29}$ m^3), k_B is the Boltzmann's constant ($= 1.3806 \times 10^{-23}$ J/K), and T is the local temperature [4]. The nucleation rate (J), which describes the number of particles nucleated per unit volume per second, (based on [4]) is

$$J = 10^{25} \exp\left(-\frac{\Delta G}{k_B T}\right) = 10^{25} \exp\left(-\frac{16\pi \gamma^3 v_C^2}{3(k_B T)^3 (\ln S)^2}\right). \qquad (3)$$

Growth Rate

Once the microsilica particles nucleate, it essentially grows by mass transfer or condensation of the SiO_2 (which is in the gas phase) to the surface of the particle. The driving flux for the growth of these particle (which has units of mol/m^2-s) is given by

$$j = \left(D_{\mathrm{SiO_2,gas}} \frac{2 + 0.6\mathrm{Re}_p^{1/2} Sc^{1/3}}{L_i}\right)(C_{\mathrm{SiO_2}} - C_{\mathrm{sat}}), \qquad (4)$$

where C_{sat} is the saturation concentration of SiO_2, $C_{\mathrm{SiO_2}}$ is the local concentration SiO_2, Sc is the Schmidt number is set equal to one (due to the turbulent nature of the flow), $D_{\mathrm{SiO_2,gas}}$ is the diffusion coefficient of SiO_2 in the gas (which is approximated to be equal to the viscosity when $Sc = 1$), L_i is the abscissa of ith node, and Re_p is the Reynolds number of particle whose diameter is L_i. Using the driving flux for particle growth (j) defined in Eq. 4, particle growth rate (F) can be written as $F = j\pi L_i^2$ where πL_i^2 is the surface area of the particles assuming they are spherical. The corresponding growth rate of the particle volume is equal to $F\frac{M_{\mathrm{SiO_2}}}{\rho_p}$ where molar mass of SiO_2 is represented by $M_{\mathrm{SiO_2}}$ ($= 6.008 \times 10^{-2}$ kg/mol). The growth rate of the particle size, G, used in Eq. 2 is computed based on $\mathrm{d}L_i/\mathrm{d}t$ [4] as

$$G = \frac{\mathrm{d}L_i}{\mathrm{d}t} = 2j\frac{M_{\mathrm{SiO_2}}}{\rho_p}. \tag{5}$$

Coupling of Microsilica Evolution with Species Consumption

The evolution of microsilica is associated with the reduction of SiO_2 from the gaseous phase. If this coupling is not present, the microsilica particles grow perpetually. Since the microsilica formation is decoupled from the combustion simulation, we treat the SiO_2 solely as a species which gets depleted based on

$$\frac{\partial C_{\mathrm{SiO_2}}}{\partial t} + \nabla \cdot (\vec{U} C_{\mathrm{SiO_2}}) = \nabla \cdot (D \nabla C_{\mathrm{SiO_2}}) - J\frac{m_{\mathrm{SiO_2}}}{M_{\mathrm{SiO_2}}} - \sum_{i=1}^{N} j\pi w_i L_i^2, \tag{6}$$

where $C_{\mathrm{SiO_2}}$ is the concentration of SiO_2 (in units of mol/m^3), D is the effective diffusion coefficient of SiO_2 in the gas which is computed as equal to the sum of momentum and turbulent diffusivities (based on assumption that $Sc = 1$), $m_{\mathrm{SiO_2}}$ is the mass of a single SiO_2 molecule ($= 9.96 \times 10^{-26}$ kg [4]). The second last term in Eq. 6 takes into account the SiO_2 which is depleted as a result of nucleation of microsilica. The last term in Eq. 6 considers the depletion of SiO_2 due to growth of the microsilica particles which is computed from $\int_{L_{\min}}^{\infty} Fn\mathrm{d}L$.

Information on the implementation of the framework and its verification is available in Sections S-1 and S-2.

Simulation of Microsilica Evolution

Setup Description

The furnace hood, which is the region of interest in this work, is simplified to a two-dimensional geometry as shown in Fig. 1 similar to the setup used by [5] to test the proposed framework and get some preliminary insights into the process. The domain used for the simulation is meshed using 19600 hexahedral cells. The boundary conditions used in the combustion simulation are summarized in Tables S-1 and S-2.

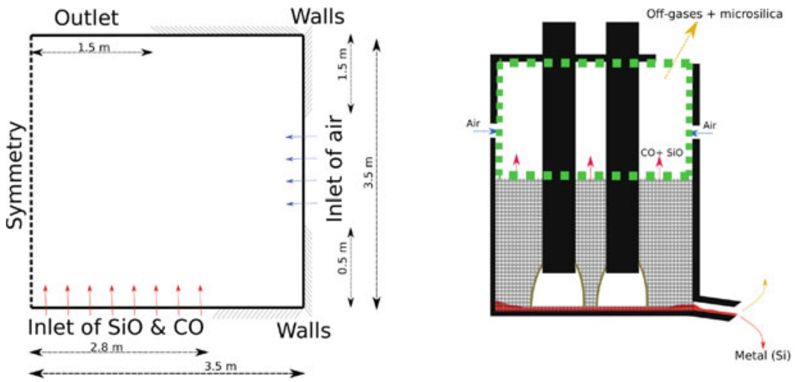

Fig. 1 Schematic of the simplified 2D geometry of the furnace hood (region within dashed green line in the schematic of furnace) used in the simulations

Based on the inlet flow rates used in the simulation, the reactions in the furnace hood occur in an oxygen rich environment. The species-specific thermophysical properties and the data used for the reaction kinetics parameters to describe the combustion of CO and SiO are set based on [7]. The inputs for the population balance simulations are obtained from [4] except for the C_{sat} which is set to value of 0.01 mol/m^3 (since it is expected to be in the range of 0–1 mol/m^3 according to [4]). The population balance solver is modelled with four moments as $N = 2$ is used for the simulations. The combustion simulation is assumed to be converged when the variation of the outflow of SiO_2 (at the outlet boundary) is less than 5% with time and bottom right region in the domain (qualitatively) reach a steady state. The combustion simulations are solved using a first order pseudo-transient time stepping approach, and spatial discretization is based on limited linear scheme (analogous to the setup used in [7]). For the microsilica evolution simulation, a first order implicit time stepping scheme along with second order spatial discretization scheme is used. Both these simulations are run with convergence criteria of 10^{-6}.

Results

The distribution of CO, CO_2, SiO, SiO_2, T and flow velocity obtained from the combustion simulations (at steady state) is plotted in Fig. S-4. The velocity streamlines show that flow in this simple domain is quite non-uniform. It is observed that reactions involving the reactants coming up from the charge surface and the colder air coming from the sides occur only in the rather small region where reactants come into contact with the oxygen due to the entrainment. Ensuing reactions results in locally high temperatures and high concentration of CO_2 and SiO_2. Also SiO seems to be depleted much quickly when compared to CO - due to faster reaction kinetics associated with SiO combustion, see [4, 7].

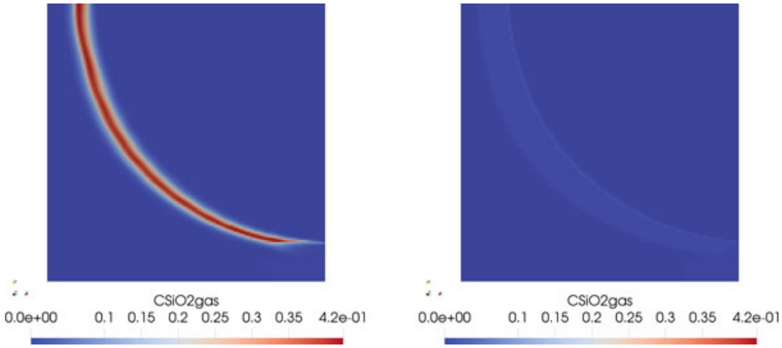

Fig. 2 Contour plots of the concentration of SiO_2 (in mol/m^3) at $t = 0$ s (left) and $t = 30$ μs (right) associated with the microsilica evolution

The depletion of SiO_2 due to the microsilica evolution is visualized in Fig. 2. The distribution of moments that describes the microsilica evolution is shown in Fig. S-5 and Fig. 3. As expected particles are generated in the high temperature where the combustion reaction generates SiO_2. The average particle size predicted by the framework, based on the peaks of m_3 and m_2 observed in Fig. 3, is calculated as $d_{32} = m_3/m_2$ to be around 30 nm. Interestingly the value of d_{32} obtained from the model is close to lower limit of the microsilica size (typically in the range of 10–500 nm with a mean size that is about 0.1 μm) reported in literature, see [1]. The work by Dingsøyr et al. [2] reported that the microsilica consists of submicron structures consisting of primary agglomerates (or clusters) of size varying from 0.05–1 μm and micron sized range of particles with diameter between 1–100 μm. Dingsøyr et al. [2] also reported that the number and size of the spheres (constituting clusters or primary agglomerates) depend on the production process and that these clusters consisted of particles stabilized by ‘material bridges’ whereas the larger micron sized particles are hypothesized to be formed by van der Waals forces. A later study, [3], investigated the structures in a densified silica fume (a process used to increase the density of the microsilica by increasing agglomeration [1]) and reported observing clusters made of spheres (whose sizes range between 0.03–0.16 μm) are ‘fused at points of contact’ due to sintering. Interestingly, lower size of these individual spheres observed in the experiments, which are in the range of tens of nanometers [2, 3], is around the same range at the particle size predicted by the framework.

Conclusion

In this work, we have presented a OpenFOAM-based framework to model microsilica in the furnace hood. The framework relies on a main assumption that the chemical reactions occur in an oxygen rich environment which allows us to decouple the combustion and microsilica evolution. The framework performs combustion simulation using rhoReactingBuoyantFoam solver in OpenFOAM whose results are used as an

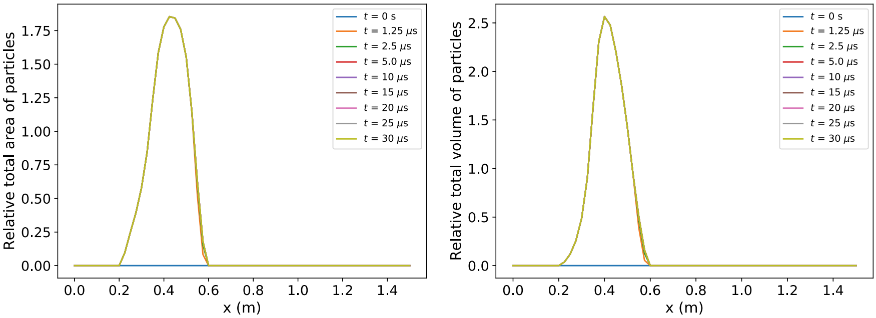

Fig. 3 Transient evolution of relative total area of particles (normalized second moment) or $\frac{m_2}{\overline{m}_0\overline{L}^2}$ (left) and relative total volume of particles (normalized third moment) or $\frac{m_3}{\overline{m}_0\overline{L}^3}$ (right) at the outlet boundary obtained from the population balance solver with $\overline{m}_0 = 10^{18}$ m^{-3} and $\overline{L} = 20 \times 10^{-9}$ m

input for the microsilica simulation based on population balance modelling based on QMOM. The proposed framework is used to simulate a simplified 2D model of the furnace hood. The results show that the SiO_2 is generated in a relatively narrow region where the reactants and oxygen mix due to entrainment. Despite the simplifications used in this work, the size of particles predicted by the framework (around 30 nm) seems to be in the lower limit of the particle sizes typically reported in literature. Source of this error is most likely due to the model not treating the particle sintering which has been reported in [2, 3] - which should be investigated in future works. Additionally, future works should include the impact of microsilica evolution on the temperature field as well as integrate the population balance model with the combustion model into a fully coupled solver.

Acknowledgements The current work has been funded by SFI Metal Production (Centre for Research-based Innovation, 237738). The authors gratefully acknowledge the financial support from the Research Council of Norway and partners of the center.

References

1. ACI 234R-96 (reapproved 2000): Guide for the use of silica fume in concrete. Technical report, American Concrete Institute (1996)
2. Dingsøyr E, Dåstøl E, Wedberg FRW, Kuntz M, Langtry R (1992) Particle size and particle size distribution of Elkem microsilica and its relevance to technical application. In: 5th European Symposium Particle Characterization, Nurnberg, Germany
3. Diamond S, Sahu S (2006) Densified silica fume: particle sizes and dispersion in concrete. Mater Struct 39(9):849–859
4. González-Fariña R, Münch A, Oliver JM, Van Gorder RA (2020) Modeling microsilica particle formation and growth due to the combustion reaction of silicon monoxide with oxygen. SIAM J Appl Math 80(2):1003–1033
5. González-Fariña, R.: Modelling the mechanisms of microsilica particle formation and growth. PhD thesis, University of Oxford (2021)

6. Passalacqua A, Heylmun J, Icardi M, Madadi E, Bachant P, Hu X (2019) OpenQBMM/OpenQBMM: OpenQBMM 5.0.1 for OpenFOAM 7. https://doi.org/10.5281/zenodo.3541425
7. Vachaparambil KJ, Panjwani B, Olsen JE (2022) Gassing during tapping of silicon. JOM 74:3990–3998

Thermodynamics and Kinetics of Coke Breeze Combustion Under Different Oxygen Content in the Sintering Process

Dongqing Wang, Wen Pan, Zhixing Zhao, and Yapeng Zhang

Abstract In order to investigate the influence of oxygen content in sintering flue gas on the heat generated by coke combustion and sintering flue gas, the thermodynamic calculation was carried out with FactSage software. Combustion kinetics under different oxygen content was studied with thermogravimetric analyzer. Thermodynamic research results showed that under the condition of sintering with iron ore fines, the oxygen content in the combustion-supporting air was abundant. When the oxygen content was more than 7%, the solid fuel in the sintered layer could meet the combustion conditions and release all the heat. Kinetic experiment results showed that the combustion rate of coke breeze in 5 min with 13% oxygen content in flue gas was equivalent to combustion rate of coke breeze in 2.75 min 21% oxygen content in flue gas. The research is helpful for energy recovery of sintering process and reducing carbon emission of blast furnace ironmaking.

Keywords Low-oxygen gas · Sinter · Coke breeze combustion · Thermodynamics and kinetics

Introduction

The sintering process is an important production link in the iron and steel industry, and its energy consumption accounts for about 11–16% of the total energy consumption of the industry, and the pollutants emitted by sintering account for about 50% of the total emissions of steel enterprises [1, 2]. In April 2019, the Ministry of Ecology and Environment of the People's Republic of China [2019] No. 35 "Opinions on Promoting the Implementation of Ultra-Low Emissions in the Iron and Steel Industry", the oxide emission limit of the sintering machine head flue gas, pellet roasting

---

D. Wang (✉) · W. Pan · Z. Zhao · Y. Zhang
Beijing Key Laboratory of Green Recyclable Process for Iron and Steel Production Technology, Beijing 100043, China
e-mail: wangdongqing1980@163.com

Institute of Iron and Steel Department, Research Institute of Technology, Shougang Group Corporation, Beijing 100043, China

S. Wagstaff et al. (eds.), *Materials Processing Fundamentals 2023*, The Minerals, Metals & Materials Series, https://doi.org/10.1007/978-3-031-22657-1_4

flue gas particulate matter, SO_2, and nitrogen was revised to 10, 35, and 50 mg/m^3, respectively, in order to achieve the ultra-low emission target of iron and steel enterprises [3]. Reusing part of the external exhaust gas can greatly reduce the emission of pollutants. Sintering flue gas is characterized by large amount, low oxygen, and high pollutant content. Typical atmospheric pollutants emitted include SO_2, NO_x, smoke dust, and dioxins. Many scholars have conducted researches on flue gas treatment and desulfurization and denitrification, which have a very positive effect on reducing pollutant emissions. Zhang et al. [4] studied the changes in the denitration performance of activated coke in the sintering flue gas purification system and its influence on the denitration rate of sintering flue gas. Yu et al. [5] proposed a multi-pollutant ultra-low emission technology system that implements source emission reduction, process control, and end treatment in the sintering process. Ye et al. [6] studied the generation mechanism of flue gas and pollutants and the relationship between flue gas volume and air leakage rate. Wang et al. [7] proposed a technology for synergistic removal of multiple pollutants in the sintering process. Hu et al. [8] proposed to reduce pollutant emissions through pre-reduction sintering. Zhang et al. [9] analyzed the influence of solid fuel combustion and iron-containing raw materials on the generation and emission of NO_x in sintering flue gas during the sintering process. Zhu et al. [10] studied the greenhouse gas CO_x emission law of iron ore sintering process. Cai [11] proposed to reduce air consumption and waste gas production to reduce the total emissions of pollutants and improve the regional atmospheric environment. Some scholars have found that: Adding an appropriate amount of Ca–Fe oxide in the sintering raw material can promote the reduction of sintering NO_x to a certain extent [12–14]. Xu et al. [15] carried out a numerical simulation on the flue gas distributor and the circulating fume hood of the flue gas circulation system and calculated the velocity field and temperature field of the sintering circulation system. Pei et al. [16] analyzed the reasonable selectivity of the sintering flue gas circulation process. Zhou et al. [17] optimized the flue gas temperature, the active control of flue gas dust, and the action time of flue gas by numerical simulation. Yang et al. [18] used FLUENT simulation software to simulate the flow field of the flue gas distributor, mixer, and circulation cover of the circulation system. Loo [19] proposed increasing the particle size of coke breeze to increase the thermal efficiency of the sinter bed. As is known, the mineralization characteristics of sintered ore at different positions of the sintering machine are not the same. Therefore, to develop sintering flue gas recycling technology, it is necessary to give full play to the characteristics of sintering flue gas at different stages to achieve energy saving, emission reduction, and improvement of sintering quality. In order to investigate the influence of the change of oxygen content in the sintering flue gas on the heat generated by the combustion of sintering flue gas and coke breeze, this paper studies the characteristics of the combustion of coke breeze under different oxygen content from both thermodynamics and kinetics, in order to provide technology for the recovery and utilization of flue gas.

Table 1 Compositions of coke breeze %

Sample	FCd	Vd	Ad	Ash			
				SiO_2	Al_2O_3	CaO	MgO
Coke breeze	84.90	1.10	14.00	45.00	30.00	4.00	0.60

Table 2 Gas parameters for thermogravimetric experiments (ml)

	Total gas flow rate	O_2	Ar
1	150	7.5	142.5
2	150	19.5	130.5
3	150	31.5	118.5

Research Methods

FactSage software was used to conduct thermodynamic research on flue gas combustion with different oxygen content, and FactPS is selected as the database. Kinetic experiments were conducted with the German Netzsch Simultaneous Thermal Analyzer STA449C. The first program by thermobalance chamber is maintained at 30 °C, subjected to vacuuming operation three times, and then, 5 mg (100 °C air drying oven for 2 h) breeze (see Table 1 for composition) was placed in a hot balance crucible. Purge the thermobalance with a flow rate of 50 mL/min argon. After the entire purge process was carried out for 20 min, the impurity gas in the reaction system was fully discharged. Then, an argon atmosphere (99.999% purity) at 20 °C/min temperature was raised to 1280 °C, lasting for 2 min, through a mixed gas (argon + oxygen) 150 ml (oxygen volume content accounting for the mixed gas: 5, 13, 21%), the experiment ended after 5 min. The specific experimental results are shown in Table 2.

Discussion

Distribution and Characteristics of the Combustion Zone

Pan et al. [20] tested the material bed temperature of a 198 m^2 sintering machine in a plant, and the results are shown in Fig. 1. It can be seen from Fig. 1 that the high temperature holding time of each layer of the combustion zone is different. The upper sinter combustion zone lasts for a short time, about 2 min; the lower sinter combustion zone lasts longer, close to 5 min; the middle combustion zone lasts in the middle. The highest temperature of the upper combustion zone is about 100 °C lower than that of the lower combustion zone, and its high temperature retention time above 1200 °C is about one third of that of the lower combustion zone. The reason is that the sintered material layer is self-storage, and the heat is gradually accumulated

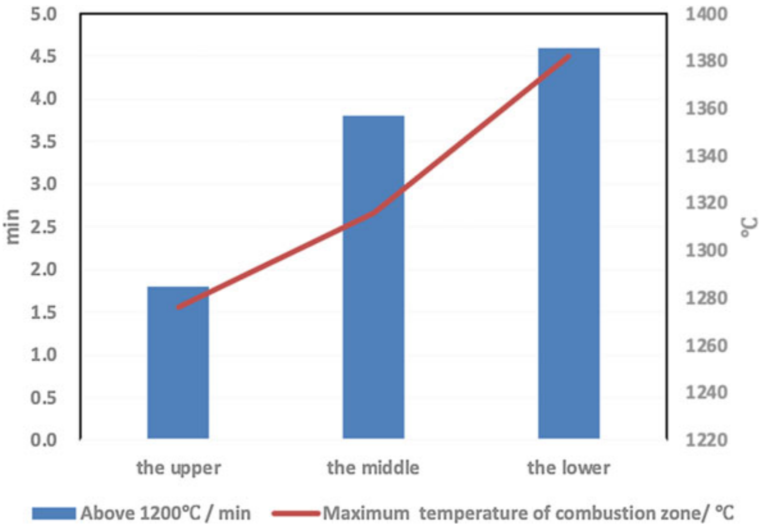

Fig. 1 Characteristics of combustion zone temperature

in the sintered material layer from top to bottom, resulting in less heat in the upper layer and more heat in the lower layer.

Thermodynamics of Combustion Flue Gases with Different Oxygen Contents

In order to investigate the influence of the change of oxygen content in the sintering flue gas on the heat, thermodynamic calculations were carried out with FactSage7.2 software. The calculation process refers to the ratio of coke breeze and flue gas in the actual sintering process. The calculation process of FactSage software is: 40 kg coke breeze and 1200 m^3 of 100 °C flue gas are mixed and burned, and the heat released by the reaction is used to heat the system (adiabatic process). Balance the thermodynamic parameters such as temperature and gas composition of the gas. The result calculated by FactSage software thermodynamics was substituted into the gas-specific heat capacity formula at constant pressure. Calculate the calorific value released when the gas temperature of the equilibrium system was cooled to 125 °C.

The oxygen content was increased from 3 to 21%, CO_2 was fixed at 3%, CO was fixed at 0.5%, and the nitrogen content was adjusted accordingly to ensure that the total volume percentage was 100%. It can be seen from Fig. 2 that as the oxygen content increases, the heat released by the gas first increases and then slightly decreases. The inflection point is that the oxygen content is 7%. Analyzing the reasons, it is believed that when the oxygen content is low, the coke breeze is incompletely burned and a large amount of CO is generated, so the combustion heat of the

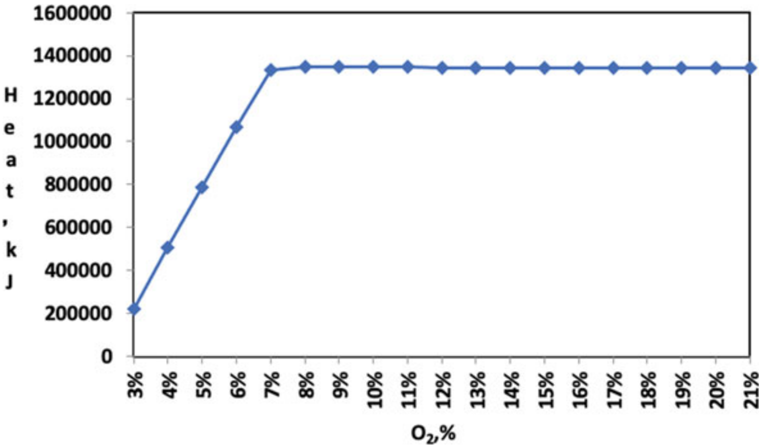

Fig. 2 Comparison of heat corresponding to the increase of oxygen content in flue gas (reduced to 125 °C)

system is low. As the oxygen content increases, the coke breeze is completely burned, CO disappears, all carbon becomes CO_2, and the heat generated by the combustion of the system remains basically unchanged.

Therefore, it can be considered from the perspective of thermodynamics that the oxygen content in the combustion-supporting air is a large amount of excess under the conditions of iron ore breeze sintering. When the oxygen content is greater than 7%, the solid fuel in the sintering layer can meet the requirements to complete the combustion.

Adequate thermodynamic conditions do not mean that the fuel in the low-oxygen content flue gas sinter layer can be completely burned. The fuel combustion process is greatly affected by the high temperature duration of the combustion zone, oxygen content, and moisture. Therefore, kinetics research is needed.

Kinetic Research

The thermogravimetry instrument automatically records the experimental data, obtains the W-t (time) curve, and calculates the combustion conversion rate of coke breeze using formula:

$$X = \Delta W / W_0 (1 - V_d - A_d) \quad (1)$$

ΔW—coal char participates in the gasification reaction and loses its quality; W_0—the initial quality of the sample; V_d—the volatile content in coke breeze; A_d—the ash content in coke breeze.

Table 3 Combustion conversion of coke breeze at different time

Time/minute	5% O_2	13% O_2	21% O_2
1.0	5.87	16.39	27.06
2.5	20.24	45.45	81.17
5.0	44.04	87.30	100.00

Table 4 Calculus expressions for common gas–solid reactions

Model	$f(\alpha)$	$G(\alpha)$
Homogeneous reaction model	$1-\alpha$	$-\ln(1-\alpha)$
Unreacted shrinking core model (sphere)	$2(1-\alpha)^{2/3}$	$1-(1-\alpha)^{1/3}$
Two-dimensional diffusion model	$-[\ln(1-\alpha)]^{-1}$	$\alpha+(1-\alpha)\ln(1-\alpha)$

The coal coke conversion rate is first-order differentiated from the corresponding gasification reaction time t, and the combustion conversion rate $\mathrm{d}x/\mathrm{d}t$ of coke breeze is obtained. The experiment was carried out for 1 min, 2.5 min, and 5 min. The data of the combustion conversion rate of coke dust is shown in Table 3. It can be seen from Table 4 that the higher the oxygen content in the atmosphere, the shorter the time required to reach the same combustion rate. Probably the main reason is that the decrease of oxygen volume fraction inhibits the diffusion between O_2 and coke breeze.

Figure 3 is a graph showing the influence of different oxygen content on the combustion conversion rate of coke breeze. It can be seen from Fig. 3 that at the beginning of the combustion reaction, the lower the oxygen content, the lower the combustion conversion rate of coke breeze.

For the typical gas–solid reaction of coal char gasification, the reaction process can be described by a homogeneous model, an unreacted shrinkage nucleus model, and a two-dimensional diffusion model [21]. The calculus expressions of common gas–solid reactions are shown in Table 4. If the model is selected appropriately, $G(\alpha)$ has a good linear relationship with t. According to statistical regression analysis, according to its maximum correlation coefficient, the appropriate response model $f(\alpha)$ can be determined. Linear correlation coefficient of different models with different oxygen content is shown in Table 5. Kinetic models of different reaction stages are shown in Table 6 (Fig. 4).

According to the above test results, the combustion rate of coke breeze in 5 min with 13% oxygen content in flue gas was equivalent to combustion rate of coke breeze in 2.75 min 21% oxygen content in flue gas. Therefore, if the combustion time is enough, the heat released by coke breeze combustion in low-oxygen flue gas is basically equal to that of high-oxygen flue gas, and low-oxygen flue gas with an oxygen content of 13% or above can also conform to the requirements of sintering production.

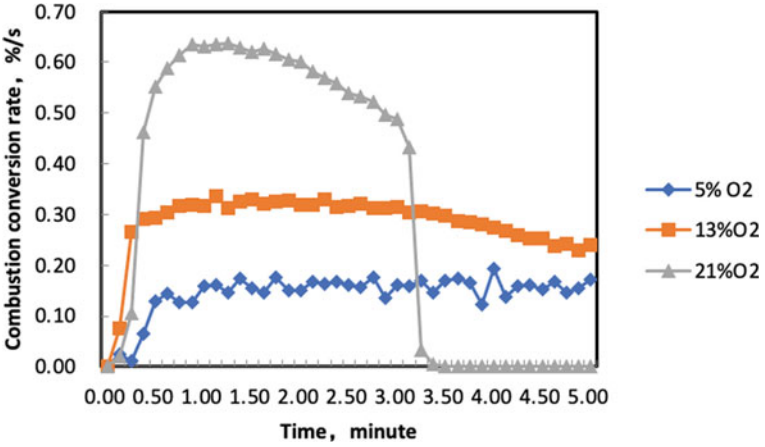

Fig. 3 Influence of different oxygen content at 1280 °C on the combustion conversion rate of coke breeze

Table 5 Linear correlation coefficient of different models with different oxygen content

O_2, %	Time/minute	Model	Correlation coefficient
5	$0.25 < t \leq 1.25$	Homogeneous reaction model	0.996
		Unreacted shrinking core model (sphere)	0.995
		Two-dimensional diffusion model	0.942
	$1.25 < t < 5$	Homogeneous reaction model	0.998
		Unreacted shrinking core model (sphere)	0.999
		Two-dimensional diffusion model	0.979
13	$0.25 < t \leq 1.75$	Homogeneous reaction model	0.999
		Unreacted shrinking core model (sphere)	0.998
		Two-dimensional diffusion model	0.968
	$1.75 < t < 5$	Homogeneous reaction model	0.985
		Unreacted shrinking core model (sphere)	0.995
		Two-dimensional diffusion model	0.985
21	$0.25 < t \leq 1.25$	Homogeneous reaction model	0.999
		Unreacted shrinking core model (sphere)	0.997
		Two-dimensional diffusion model	0.968
	$1.25 < t < 2.75$	Homogeneous reaction model	0.985
		Unreacted shrinking core model (sphere)	0.995
		Two-dimensional diffusion model	0.985

Table 6 Kinetic models of different reaction stages

O_2 (%)	Time, minute	Formula equation	Kinetic models	Correlation coefficient
5	$0.25 < t \leq 1.25$	$x = 1 - e^{0.022 – 0.082t}$	Homogeneous reaction model	0.996
13	$0.25 < t \leq 1.75$	$x = 1 - e^{0.035 – 0.218t}$		0.999
21	$0.25 < t \leq 1.25$	$x = 1 - e^{0.108 – 0.41\mathrm{t}}$		0.999
5	$1.25 < t < 5$	$x = 1 - (1.024 – 0.04t)^3$	Unreacted shrinking core model (sphere)	0.999
13	$1.75 < t < 5$	$x = 1 - (1.093 – 0.112t)^3$		0.995
21	$1.25 < t < 2.75$	$x = 1 - (1.195 – 0.254t)^3$		0.995

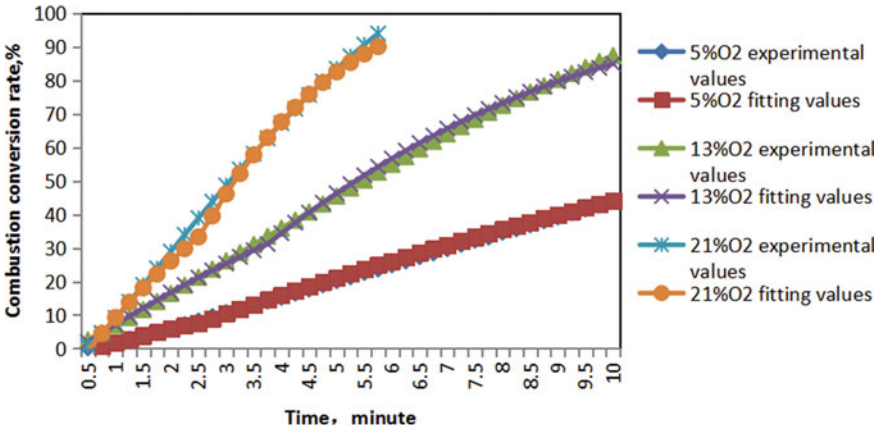

Fig. 4 Comparison of coke combustion rate and fitting curve value at 1280 °C with different oxygen content

Conclusions

From the perspective of thermodynamics, under the sintering condition of iron ore breeze, the oxygen content in the combustion-supporting air is abundant. When the oxygen content is greater than 7%, the solid fuel in the sintered material layer can meet the combustion conditions and release all the heat.

At the initial stage, the combustion reaction conforms to the characteristics of the kinetic model of homogeneous reaction. In the middle and late period of fuel combustion, the kinetic model is consistent with the characteristics of the unreacted shrinking nucleus model. Kinetic experiment results showed that the combustion rate of coke breeze in 5 min with 13% oxygen content in flue gas was equivalent to combustion rate of coke breeze in 2.75 min 21% oxygen content in flue gas. Therefore, as long as the combustion time is enough, the heat released by coke breeze combustion in low-oxygen flue gas is basically equal to that of high-oxygen flue gas, and the low-oxygen flue gas with an oxygen content of 13% or above can also conform to the requirements of sintering production.

References

1. Yan XM, Li YR, Zhu TY et al (2015) Review of emission and simultaneous control of multiple pollutants from iron-steel sintering flue gas. J Environ Eng Technol 5(2):85–90
2. Liu J, Ma XG, Xia TY et al (2019) Study and application of recycled desulfurization ash of sintering flue gas. Sinter Pelletizing 44(2):63–68
3. Ministry of Ecology and Environment of the People's Republic of China. Opinions on promoting the implementation of ultra low emissions in the steel industry [EB/OL]. [2019–04–28]. http://www.mee.gov.cn/xxgk2018/xxgk/xxgk03/201904/t20190429_701463.html
4. Zhang WL, Wu SL, Hu ZJ (2020) Analysis of affecting factors of activated coke denitration efficiency for sintering flue gas. Iron Steel 55(05):109–115
5. Yu Y, Zhu TY, Liu XL (2019) Progress of ultra-low emission technology for key processes of iron and steel industry in China. Iron Steel 54(9):1–11
6. Ye HD, Wang ZC, Liu Q et al (2019) Study on reduction technology of sintering flue gas and pollutants. Sinter Pelletizing 44(06):60–67
7. Wang XD, Hou CJ, Tian JL (2020) Application and practice of multi-pollutant cooperative control technology for flue gas in iron and steel industry. Chin J Process Eng 20(09):997–1007
8. Hu B, Gan M, Wang ZC (2017) Research status of pre-reduction sintering technology and development on the new technology. Sinter Pelletizing 42(06):22–26, 28
9. Zhang DB, Zhou MJ, Wang YF (2015) Emission reduction technology of NO_x process in sintering flue gas of baosteel. Ironmaking 34(6):47–51
10. Zhu DQ, He AP, Pan J et al (2006) Rule of greenhouse Gas CO_x emission in iron ore sintering process. Iron Steel 41(2):76–80
11. Cai JJ (2019) Air consumption and waste gas emission of steel industry. Iron Steel 54(04):1–11
12. Wu SL, Sugiyama T, Morioka K et al (1994) Elimination reaction of NO gas generated from coke combustion in iron ore sinter bed. Tetsu-to-Hagané 80(4):276–281
13. Koichi M, Shinichi I, Masakata S et al (2000) Primary application of the "in-bed-de NO_x" process using Ca–Fe oxides in iron ore sintering machines. ISIJ Int 40(3):280–285
14. Gan M, Fan XH, Lv W et al (2016) Fuel pre-granulation for reducing NO_x emissions from the iron ore sintering process. Breeze Technol 301:478–485
15. Xu Y, Mao R, Wang F et al (2020) Numerical simulation of sintering flue gas circulation system. 32(07):675–681
16. Pei YD, Zhang JJ, Qi CL (2019) Discussion on proper sintering flue gas recirculation process. Sinter Pelletizing 44(2):74–77
17. Zhou ZA, Su D, Zhang SP et al (2019) Research and application of efficientcy clicutilization technology of sintering residue energy. Sinter Pelletizing 44(2):69–73
18. Yang ZW, Wang ZC, Wen RY et al (2018) Simulation research of sintering flue gas recirculation system. Sinter Pelletizing 43(3):63–68
19. Loo CE (1991) Role of coke size in sintering of a hematite ore blend. Ironmaking Steelmaking 18:33
20. Pan W, Zhao ZX, Feng L et al (2020) Research on mineralization characteristic of sinter. Sinter Pelletizing 45(03):1–7, 12
21. Sun MM, Zhang JL et al (2018) Thermal and kinetic analysis on the co-combustion behaviors of anthracite and PVC. Metall Res Technol 1–9

Part II
Continuous Casting

Inverse Calculation of Time-Spatial Varying Mold Heat Flux During Continuous Casting from Fast Response Thermocouples

Haihui Zhang, Huiqiang Shen, and Pengcheng Xiao

Abstract This paper covers the determination of time-spatial varying mold heat flux using mold temperatures measured by fast response thermocouples at a frequency up to 60 Hz. A two-dimensional transient inverse heat conduction problem (2DIHCP) is established, where 2DIHCP is developed based on the sequential function specification method implemented with the spatial regularization terms to reduce the fluctuations in the estimated heat flux in both time and spatial domain. Then, the inverse problem was validated using a designed numeric test-problem. Finally, the inverse problem is applied to calculating the heat flux across the mold hot surface for a continuous casting trial using the mold simulator.

Keywords Modeling and simulation · Iron and steel · Process technology · Continuous casting

Nomenclature

c	Heat capacity (J/kg K)
$f(\partial\Omega_4, t)$	Temperature of the boundary $\partial\Omega_4$ (K)
$\boldsymbol{H}$	Spatial regularization matrix
$\mathbf{X}$	Sensitivity matrix
M	Numbers of the thermocouple in the calculated domain Ω
n_j	Number of heat flux components at the boundary $\partial\Omega_j$, $j = 1, 2, 3$.
N	$N = n_1 + n_2 + n_3$
q	Heat flux (W/m^2)

H. Zhang (✉) · H. Shen
Faculty of Materials Metallurgy and Chemistry, Jiangxi University of Science and Technology, Ganzhou 341000, China
e-mail: zhanghaihuiemail@gmail.com

P. Xiao
College of Metallurgy and Energy, North China University of Science and Technology University, Tangshan 063210, China

S. Wagstaff et al. (eds.), *Materials Processing Fundamentals 2023*, The Minerals, Metals & Materials Series, https://doi.org/10.1007/978-3-031-22657-1_5

r	Future time step (−)
s	Objective function
t, t_j	Time (s)
$\mathbf{T}$	Vector of estimated temperature (K)
T_m	Estimated temperatures at the measurement location (x_m, y_m) (K)
T_{ini}	Initial temperature (K)
x, y	Cartesian spatial coordinates (m)
$\mathbf{Y}$	Vector of the measured temperature (K)
Y_m	Measured temperature at the measurement location (x_m, y_m) (K)

Greek Symbols

α	Regularization parameters (K^2 m^4 W^4)
λ	Thermal conductivity (W m^{-1} K^{-1})
ρ	Density (kg m^{-3})
σ	Standard deviation of the measurements
ω	Random variable
Ω	Calculated domain
$\partial\Omega_1$, $\partial\Omega_2$, $\partial\Omega_3$, $\partial\Omega_4$	Boundary of the calculated domain Ω

Introduction

Many surface defects in final rolled steel products originate from the initial solidification of molten steel inside continuous casting molds. This has been found to be associated with the heat transfer behaviors of the mold itself [1–3]. The mold heat flux, especially at the mold meniscus area, is extremely complex due to the transient nature of the infiltration of lubricant liquid mold flux, intensive fluid flow, and mold oscillation, such that it would be very difficult to get a clear comprehensive understanding of all dynamics within the system [4–8].

The heat flux of the mold is a space–time varying variable [9]. Usually, the mold heat transfer is monitored by temperature sensors [10]. Hundreds of thermocouples/sensors are employed to monitor the mold temperature during the continuous casting process, with a temperature sampling rate of 1–65 Hz. The mold heat flux cannot be calculated directly from the measured temperatures because of the lack of information on the boundary conditions. Mathematically, the determination of the mold heat flux from measured temperatures is an inverse problem that means the solution is usually unstable, not unique or does not exist, and a small measured error in the temperatures will result in a large error of heat flux [11, 12].

The inverse problem method has a broad application prospect in determining the heat flux from measured temperatures. The principle of inverse problems for restructuring the heat flux is to find out a heat flux with the maximum probability making the sum of squared deviations between the calculated temperatures **T** and the measured temperatures **Y** to be minimum [13].

The development of the use of inverse problem methods to calculate continuous casting mold heat flux from temperature measurements can be traced back to the works by Brimacomb et al. [14], followed by Thomas et al. [15], Wang et al. [16–18], Griffiths [19], Rajaraman [20], and Talukdar et al. [21]. Those inverse problem methods could be classified as the gradient-based type methods, such as the function specification method [9], the Tikhonov regularization [22] and the conjugate gradient method [23, 24], and the stochastic-based type methods, such as the genetic algorithm and the neural network algorithm [25]. However, the major weakness of the inverse problem persists in that it is extremely sensitive to temperature measurement errors, particularly as the time step is made smaller [12, 26]. As continuous casting technology progresses, fast mold thermal monitoring systems are adopted that could provide a more accurate detection precision supervising the fluctuation of mold temperature [5, 6]. However, the faster temperature sampling rate of mold thermal monitoring systems is inevitably accompanied by a higher intensity of the error/noise in the measured temperatures [12]. As a result of the increase of the temperature sampling rate, the use of small-time step frequently introduces instabilities in the solution of the inverse heat conduction problem.

In the engineering community, the inverse problem of Beck's sequential function specification method is well-known and very successfully used in solving inverse heat conduction problems for over 50 years [27–31]. For Beck's sequential function specification method, the heat flux form is assumed to be a constant function or a linear function over several future time steps due to the fact that the temperature response is lagging with respect to the boundary heat flux [23], then the stabilization of the solution in the time domain can be improved by choosing an appropriate number of future time steps [24, 32]. However, a common issue raised is how to improve the stabilization of the solution in the time and spatial domain for extending the sequential function specification method to the two-dimensional heat transfer problem [33, 34].

Therefore, the purpose of this work is to establish a two-dimensional transient **i**nverse **h**eat **c**onduction **p**roblem (2DIHCP) for the estimation of the mold heat flux from fast-sampled temperature data. The inverse problem is developed where the function specification method with a spatial Tikhonov regularization [6, 35, 36] was used to improve the stabilization of the solution in time and spatial domains, respectively. Then, a numeric test-problem was designed to validate the inverse problem. Finally, the inverse problem is applied to calculating the mold heat flux during liquid steel casting.

The Experimental and Direct Problem Description

The continuous casting trial was conducted using a mold simulator. As Fig. 1 shows, the mold simulator applied to this study is an inverse type water-cooled copper mold (30 mm × 50 mm × 350 mm) with oscillation capability. A U-shaped type water-cooling groove with a diameter of 10 mm is manufactured along the center line of mold plate, 12.5 mm away from both ends and gets connected 20 mm above the bottom, where the water flows from one end to the other. The copper mold is equipped with an extractor that makes only one face of the mold exposed to the liquid melt. The temperatures in the mold are measured by T-type thermocouples at a frequency up to 60 Hz through a data acquisition system. The two columns of thermocouples are spaced 3 and 8 mm away from the mold surface, respectively, as shown in Fig. 1, the dots represent the locations of thermocouples. The arrangement allows the first column of thermocouples to catch the temperature history of the mold that will be used in the minimization of the objective function of the inverse problem. The second column of thermocouple inside the mold wall on $\partial\Omega_4$ (CD) is to provide the temperature boundary condition $f(t)$, where the temperature is interpolated linearly from two near measured temperatures for the nodes in between the two thermocouples at $\partial\Omega_4$. This arrangement of those thermocouples in the mold wall was chosen based on the study of Badri et al. [37] so as to improve the signal-to-noise ratio for the temperature measurements during the experiment. Then, the rectangular area **ABCD** with the height (**AB**) of H (= 21 mm) and the width (**BC**) of W (8 mm) is set as the heat transfer computational domain, which consists of four boundary conditions $\partial\Omega_1$ (DA), $\partial\Omega_2$ (AB), $\partial\Omega_3$ (BC), and $\partial\Omega_4$ (CD).

The experiment runs as follows: Step I The oscillating water-cooling copper mold and the extractor are dipped into the hot melt of liquid steel. After the mold and extractor reached the target depth, the mold flux level and the liquid steel level would be located in the mold thermocouple-measuring zone. Step II The mold and extractor were held for several seconds to form an initial shell on the water-cooled copper mold to ensure the initial shell is strong enough to prevent tearing during extraction. Step III The extractor withdrew the solidifying shell downward at a constant speed to simulate continuous casting. The mold moved upward at a certain speed to compensate for the rise of the mold level, so that the liquid level could be kept in the same position with respect to the mold. Step IV When the casting was completed for the desired length, the mold and extractor were withdrawn out of the furnace and then cooled in air.

By assuming the mold heat transfer is two-dimensional in the vertical section **ABCD** perpendicular to the mold hot surface. The heat transfer within the mold vertical section **ABCD** is assumed to be governed by Fourier partial differential equations. The direct problem, namely the problem of 2D heat transfer within the rectangular area **ABCD**, as shown in Fig. 1, is governed by the following equations.

$$c\rho\frac{\partial T}{\partial t} = \frac{\partial}{\partial x}\left(\lambda\frac{\partial T}{\partial x}\right) + \frac{\partial}{\partial y}\left(\lambda\frac{\partial T}{\partial y}\right), \text{ in domain } \Omega = [0, W] \times [0, H] \qquad (1a)$$

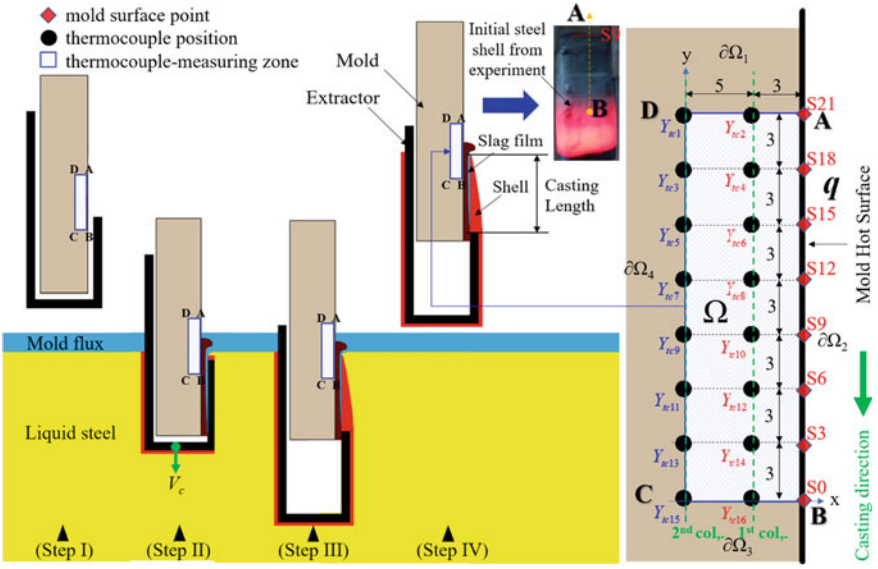

Fig. 1 Computational area of the mold and locations of thermocouples for the casting experiment

$$-\lambda\frac{\partial T(\partial\Omega_1 \cup \partial\Omega_2 \cup \partial\Omega_3, t)}{\partial \boldsymbol{n}} = \boldsymbol{q} \text{ to be estimated.} \tag{1b}$$

$$T(\partial\Omega_4, t) = f(t) \tag{1c}$$

$$T(x, y, 0) = T_{\text{ini}} \tag{1d}$$

where the symbol c represents the specific heat in J kg^{-1}, ρ is the density in kg m^{-3}, T is the temperature in K, t is the time in second, and λ is thermal conductivity in W m^{-1} K^{-1}, $\boldsymbol{q}$ (W m^{-2}) is the heat flux of boundary conditions $\partial\Omega_1$, $\partial\Omega_{2,}$ and $\partial\Omega_3$, $\boldsymbol{n}$ is the outer normal of boundary.

Inverse Problem Description

In this section, the inverse problem is developed based on the function specification method implemented by a spatial Tikhonov regularization [6, 35, 36]. The sequential function specification procedure is: (1) the heat fluxes are assumed to remain constant over the r future time steps, $\boldsymbol{q}^j = \boldsymbol{q}^{j+1} = \cdots = \boldsymbol{q}^{j+r}$, owing to the temperature response is lagging with respect to the boundary heat flux, and (2) By knowing the heat fluxes for $t < t_j$, namely $\tilde{\mathbf{q}}^1, \tilde{\mathbf{q}}^2, \ldots, \tilde{\mathbf{q}}^{j-1}$ are known, estimate $\mathbf{q}^j$ so that makes the sum of the squares of the deviations between the calculated temperatures $\mathbf{T}$ and the measured temperatures **Y** in the time interval $[t_j, t_{j+r-1}]$ to be minimized. Then, the inverse heat conduction problem could be converted into a problem that is to estimate $\mathbf{q}^j$ by making the following objective function to be minimum. Therefore, the definition of the inverse heat conduction problem is made as follows

$$s(\boldsymbol{q}^j) = \sum_{k=0}^{r-1} \sum_{m=1}^{M} \left[Y_m^{j+k} - T_m^{j+k}(\boldsymbol{q}^j)\right]^2 + \alpha R(\mathbf{q}^j) \tag{2}$$

where r is the number of future time steps. Y_m^j and T_m^j are the measured temperatures and the calculated temperatures at the time of t_j and the measured position m, respectively. M is the number of sensors. α is the spatial regularization parameter.

The finite difference method is used to solve the above direct problem, where the rectangular area **ABCD** (Ω) will be divided into grids, and the boundaries of $\partial\Omega_1$, $\partial\Omega_{2,}$ and $\partial\Omega_3$ will be split into n_1, n_2, and n_3 divisions, respectively. Then, $\boldsymbol{q}$ has N components, $N = n_1 + n_2 + n_3$, and q_k^j represents the kth component of heat flux $\boldsymbol{q}$ at the time of t_j.

$$\boldsymbol{q}^j = [\boldsymbol{q}_1^j, \boldsymbol{q}_2^j, \boldsymbol{q}_3^j]^{\mathrm{T}}, \boldsymbol{q}_1^j = \left[q_1^j, q_2^j, \ldots, q_{n_1}^j\right]^{\mathrm{T}},$$
$$\boldsymbol{q}_2^j = \left[q_{n_1+1}^j, q_{n_1+2}^j, \ldots, q_{n_1+n_2}^j\right]^{\mathrm{T}} \text{ and}$$
$$\boldsymbol{q}_3^j = \left[q_{n_1+n_2+1}^j, q_{n_1+n_2+2}^j, \ldots, q_N^j\right]^{\mathrm{T}}.$$

Besides, a first-order of spatial Tikhonov regularization term is added to the objective function Eq. (2) so as to improve the spatial stabilization of the solution. It should be mentioned that heat flux **q** might be subjected to discontinuity at the intersection points between two adjacent boundaries of $\partial\Omega_1$ and $\partial\Omega_2$ ($\partial\Omega_2$ and $\partial\Omega_3$). Thus, the spatial Tikhonov regularizations for the heat flux of the boundaries $\partial\Omega_1$, $\partial\Omega_{2,}$ and $\partial\Omega_3$ are described separately. That is

$$R(\mathbf{q}^j) = \sum_{n=1}^{n_1-1} (q_n^j - q_{n+1}^j)^2 + \sum_{n=n_1+1}^{n_1+n_2-1} (q_n^j - q_{n+1}^j)^2 + \sum_{n=n_1+n_2+1}^{N-1} (q_n^j - q_{n+1}^j)^2 \tag{3}$$

The estimated temperature $\mathbf{T}^j$ could be evaluated using a Taylor series expansion around the current solution $\tilde{\mathbf{q}}^j$.

$$\mathbf{T}^j = \tilde{\mathbf{T}}(\tilde{\mathbf{q}}^j) + \mathbf{X}_j(\mathbf{q}^j - \tilde{\mathbf{q}}^j). \tag{4}$$

$\tilde{\mathbf{T}}(\tilde{\mathbf{q}}^j)$ is the temperature calculated using the current solution $\tilde{\mathbf{q}}^j$. $\mathbf{X}_j$ is called as the $M \times N$ sensitivity coefficient matrix at time t_j and is defined as follows.

$$\mathbf{X}_j = \left[\frac{\partial \mathbf{T}(\mathbf{q}^j)}{\partial \mathbf{q}^j}\right]^{\mathrm{T}} = \begin{pmatrix} X_{1,1}^j & X_{1,2}^j & \cdots & X_{1,N}^j \\ X_{2,1}^j & X_{2,2}^j & \cdots & X_{2,N}^j \\ \vdots & \vdots & \ddots & \vdots \\ X_{M,1}^j & X_{M,2}^j & \cdots & X_{M,N}^j \end{pmatrix}, \text{ where}$$

$$X_{m,n}^j = \frac{\partial T_m^j}{\partial q_n^j}. \tag{5}$$

The least squares equation $s(\boldsymbol{q}^j)$ is minimized by differentiating it with respect to each component of unknown heat flux and setting the resulting expressions equal to zero, then a set of N equations is obtained for the estimation of heat flux.

$$\frac{\partial s(\boldsymbol{q}^j)}{\partial q_1^j} = 0, \frac{\partial s(\boldsymbol{q}^j)}{\partial q_2^j} = 0, \ldots, \frac{\partial s(\boldsymbol{q}^j)}{\partial q_N^j} = 0 \tag{6}$$

The above equations yield to a matrix system to estimate the increment for a new heat flux.

$$\Delta \mathbf{q}^j = \left(\sum_{i=1}^{r} \mathbf{X}_i^T \mathbf{X}_i + \alpha \boldsymbol{H}\right)^{-1} \left(\sum_{i=1}^{r} \mathbf{X}_i^T (\mathbf{Y}^{j+i-1} - \tilde{\mathbf{T}}^{j+i-1})\right) \tag{7}$$

where $\boldsymbol{H}$ is the $N \times N$ block diagonal regularization matrix. Both $\mathbf{Y}^j$ and $\mathbf{T}^j$ are $M \times 1$ vector, and M is the number of measurements.

$$\boldsymbol{Y}^j = [Y_1^j, Y_2^j, \ldots, Y_M^j]^{\mathrm{T}} \tag{8a}$$

$$\boldsymbol{T}^j = [T_1^j, T_2^j, \ldots, T_M^j]^{\mathrm{T}} \tag{8b}$$

$$\boldsymbol{H} = \mathrm{blkdiag}(\boldsymbol{H}_{n_1}, \boldsymbol{H}_{n_2}, \boldsymbol{H}_{n_3}) \tag{8c}$$

$$\boldsymbol{H}_{n_i} = \begin{bmatrix} 1 & -1 & & & \\ -1 & 2 & -1 & & \\ & \ddots & \ddots & \ddots & \\ & & -1 & 2 & -1 \\ & & & -1 & 1 \end{bmatrix}_{n_i \times n_i}. \tag{8d}$$

Sensitivity Coefficient Matrix

$X_{m,n}^{j}$ represents the temperature rise at the sensor location (x_m, y_m) for a unit step change in the surface heat flux at the point (x_n, y_n) of boundaries $\partial\Omega_1$, $\partial\Omega_2$, and $\partial\Omega_3$ and the time t_j. According to the definition of sensitivity coefficient [Eq. (5)], the sensitivity coefficient problem for calculating sensitivity coefficient matrix is obtained by taking the derivative of Eqs. [1a through 1d] with respect to a heat flux component q_n^j at the point (x_n, y_n) of boundaries $\partial\Omega_1$, $\partial\Omega_2$, and $\partial\Omega_3$, and n is 1, 2, …, N. The sensitivity coefficient problem governing the sensitivity coefficients $X_{m,n}^{j}$ is

$$c\rho\frac{\partial X_{,n}}{\partial t} = \frac{\partial}{\partial x}\left(\lambda\frac{\partial X_{,n}}{\partial x}\right) + \frac{\partial}{\partial y}\left(\lambda\frac{\partial X_{,n}}{\partial y}\right),\ 0 < t \le t_r$$
$$\text{in domain } \Omega = [0, W] \times [0, H] \tag{9a}$$

$$-\lambda\frac{\partial X_{,n}(\partial\Omega_1 \cup \partial\Omega_2 \cup \partial\Omega_3, t)}{\partial \boldsymbol{n}} = \begin{cases} 1, & (x, y) = (x_n, y_n) \\ 0, & \text{others} \end{cases} \tag{9b}$$

$$X_{,n}(\partial\Omega_4, t) = 0 \tag{9c}$$

$$X_{,n}(x, y, 0) = 0 \tag{9d}$$

The Determination of Regularization Parameter

The choice of the regularization parameter is required to balance the computational cost and the stability of the inverse problem solution algorithm. The L-curve method is adopted to optimize the regularization parameters α. L-curve criterion that plotted the curve of $\{\log(\|\mathbf{Y}-\mathbf{T}\|), \log(R(\mathbf{q}^j))\}$ often takes on a characteristic L shape, and the optimal regularization parameter was corresponding to the corner of maximum curvature in L-curve [38, 39]. However, many tests should be executed for the plot L-curve, which is very computationally expensive. Alternatively, we consider the use of Arcangeli's discrepancy principle to significantly speed up the selection of the optimal regularization parameter [40], that is

$$\|\mathbf{Y} - \mathbf{T}\| \approx \frac{\sigma}{\sqrt{\alpha}} \tag{10}$$

Stopping Criterion for the Iterative Procedure of Inverse Problem

The stopping criterion for Eq. (2) is given by

$$s \leq \varepsilon \tag{11}$$

As temperatures contain measurement error, the temperature residual could be approximated by

$$\varepsilon = (\mathbf{Y} - \mathbf{T})^{\mathrm{T}}(\mathbf{Y} - \mathbf{T}) \cong M\sigma^2 \tag{12}$$

where σ is the standard deviation of temperature measurement error.

Algorithm of Inverse Problem

As shown in Fig. 2, specify the number of future time steps r. **Step 1**, 2DIHCP is running with an initial guess heat flux $\boldsymbol{q}^j$ and a guess regularization parameter α. **Step 2**, solve the direct problem given by Eq. (1) with the estimated heat flux $\mathbf{q}^j$ for $\mathbf{T}$ during the time from t_j to t_{j+r}. **Step 3**, solve the sensitivity coefficient problem given by Eq. (9a–d) for the sensitivity coefficient matrix $\mathbf{X}$ in the time interval from 0 to t_r. **Step 4**, check the stopping criterion given by Eq. (11). If the stopping criterion Eq. (11) is satisfied, let $\alpha_{\text{old}} = \alpha$ and renew α using Eq. (10). Otherwise, the heat flux is updated using $\boldsymbol{q}^j = \boldsymbol{q}^j + \boldsymbol{\Delta q}$ and Eq. (7), and return to **Step 2**. **Step 5**, when $|\alpha - \alpha_{\text{old}}|/\alpha_{\text{old}} < 0.05$ is satisfied, $\mathbf{q}^j$ could be regarded as the estimated heat flux at time t_j, then set $j = j + 1$ and return to **Step 1** for the next time step calculation till the end of the time steps. Otherwise, the heat flux is updated using $\boldsymbol{q}^j = \boldsymbol{q}^j + \boldsymbol{\Delta q}$ and Eq. (7), and return to **Step 2**. The algorithm is achieved and programed using MATLAB$^{\text{TM}}$. All the partial differential equations are solved using the finite difference method.

Model Verification

Validation for Solving Partial Differential Equations by Numeric Solution

Partial differential equations of heat conduction problems Eqs. [1a through 1d] and the sensitivity coefficient problem given by Eqs. [9a through 9d] are solved using the **f**inite **d**ifference **m**ethod (**FDM**) with the classical Crank-Nicolson (**CN**) semi-implicit scheme. The **FDM** code must be validated to be effective for solving partial

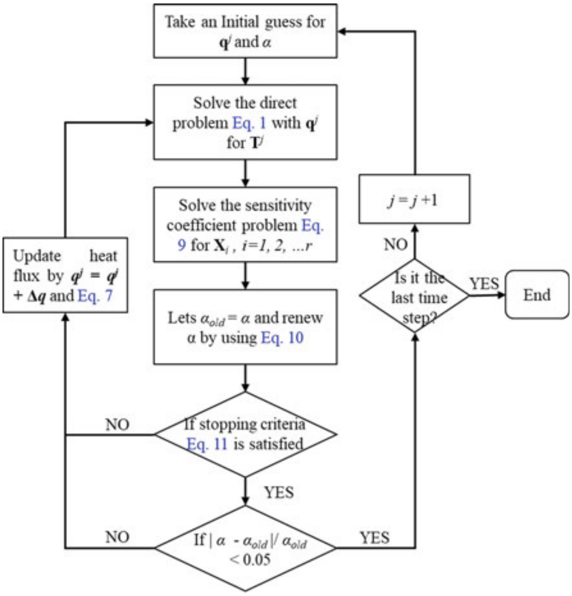

Fig. 2 Algorithm of the two-dimensional inverse heat conduction problem (2DIHCP)

differential equations before the run of the inverse calculation. Herein, the **FDM** code was also verified through comparison with the analytical solutions of the heat transfer in the solid from a classical textbook [41]. It was observed that the results of the **FDM** method were consistent with those analytic solutions, suggesting the **FDM** method can solve the heat conduction partial differential equation.

Validation for Algorithm of the Inverse Problem

The numeric test-problem is designed to verify the 2DIHCP. The direct problem is also a the rectangular area **ABCD** (made of copper, height H is 0.021 m and width W is 0.008 m, see Fig. 1) with the initial temperature of 273.15 K. The boundaries of $\partial\Omega_1$, $\partial\Omega_{3,}$ and $\partial\Omega_4$ are insulated boundaries, and the heat flux ***f(y, t)*** is applied to the $\partial\Omega_2$. The ***f(y, t)*** is

$$f(y,t) = \begin{cases} 1 \times 10^6, & 0 \le t < 5 \\ 1 \times 10^6\left(1 - \frac{1000}{21}y\right)\frac{t}{5} + 1 \times 10^6, & 5 \le t < 10 \\ 1 \times 10^6\left(1 - \frac{1000}{21}y\right) + 1 \times 10^6, & 10 \le t < 15\ . \\ 1 \times 10^6\left(1 - \frac{1000}{21}y\right)\frac{15-t}{5} + 1 \times 10^6, & 15 \le t \le 20 \\ 1 \times 10^6, & 20 \le t < 25 \end{cases} \tag{13}$$

The first column of eight virtual thermocouples was set 3 mm apart vertically from each other and 3 mm away from the mold hot surface; while the second column of other eight virtual thermocouples was spaced 3 mm apart vertically and 8 mm horizontally away from the hot face of the mold. The temperature measurement is taken every 0.1 s during the test-problem runs. The Gaussian noise signals $\sigma\omega$ ($T = T_{\text{ture}} + \sigma\omega$, σ is the standard deviation of noise and ω is a random variable and will be within -2.576 to 2.576 for the 99% confidence bounds) are added to the temperatures to mimic the thermocouple measurement error. Then, the measured temperatures are delivered to the 2DIHCP for the reconstruction of the heat flux in Ω_2. For the parameters used here, the number of future time steps is set as 15, the α is 1.71×10^{-6}, respectively. The estimation results of heat flux in Ω_2 with/without noise (Gaussian noise signals, $\sigma = 0.1$, to simulate the temperature measurement errors) and the exact value ***f(y, t)*** are shown in Fig. 3, where the heat fluxes at the locations of *y* at 0 mm, 3, 6, 9, 15, and 21 mm are listed, respectively. It was found that the heat fluxes calculated by 2DIHCP match well with the exact values, even for the situation that the measured temperature was contaminated by noise. This suggests that the 2DIHCP could reconstruct the boundary heat flux precisely and show the ability to resist measurement noises.

The results are compared with those values calculated by a robust one-dimensional **i**nverse **h**eat **c**onduction **p**roblem (1D-IHCP) developed by Beck et al. [12], where the future time step is 4. As shown in Fig. 3, although the heat fluxes obtained through 1D-IHCP show the same variation tendency with the exact value, the difference between the above two methods is obvious, especially when the measured temperature is contaminated with noise.

Application to Continuous Casting Mold

A continuous casting experiment of liquid steel ([C]: 0.200 wt%, [Si]: 0.230 wt%, [Mn]: 0.490 wt%, [P]: 0.012 wt%, and [S]: 0.03 wt%) was conducted, where the mold was oscillated with a frequency of 2.17 Hz that helps to separate the metal from the mold. With the progressive filling of the liquid steel (shown in Fig. 1), the responding copper mold wall temperatures were measured by thermocouples with a 60 Hz sampling rate, and the pouring temperature of steel was 1833 K. The calculation domain size and the distribution of the thermocouples are the same as the installation of the thermocouples in the numeric test-problem.

Figure 4 shows the measured in-mold temperature history of the first column thermocouples at different positions in the vertical. The responding temperature can be divided into two stages according to the process of the casting. In stage **I** (51.4–52.5 s), the responding temperatures increase quickly as the progressive filling of the liquid steel from the bottom to the top of the mold. After filling of the melt is completed, the liquid level corresponds to the location S9 with *y* is 9 mm, where the mold is exposed to air above this location ($y > 9$ mm). As it steps into stage **II** (52.5–58 s), the liquid steel is solidified against the surface of the water-cooled mold, the responding temperatures continue to increase and then keep relatively constant. It was found that the steady state temperature values for Y_{tc16} (*y* is 0 mm) and Y_{tc14}

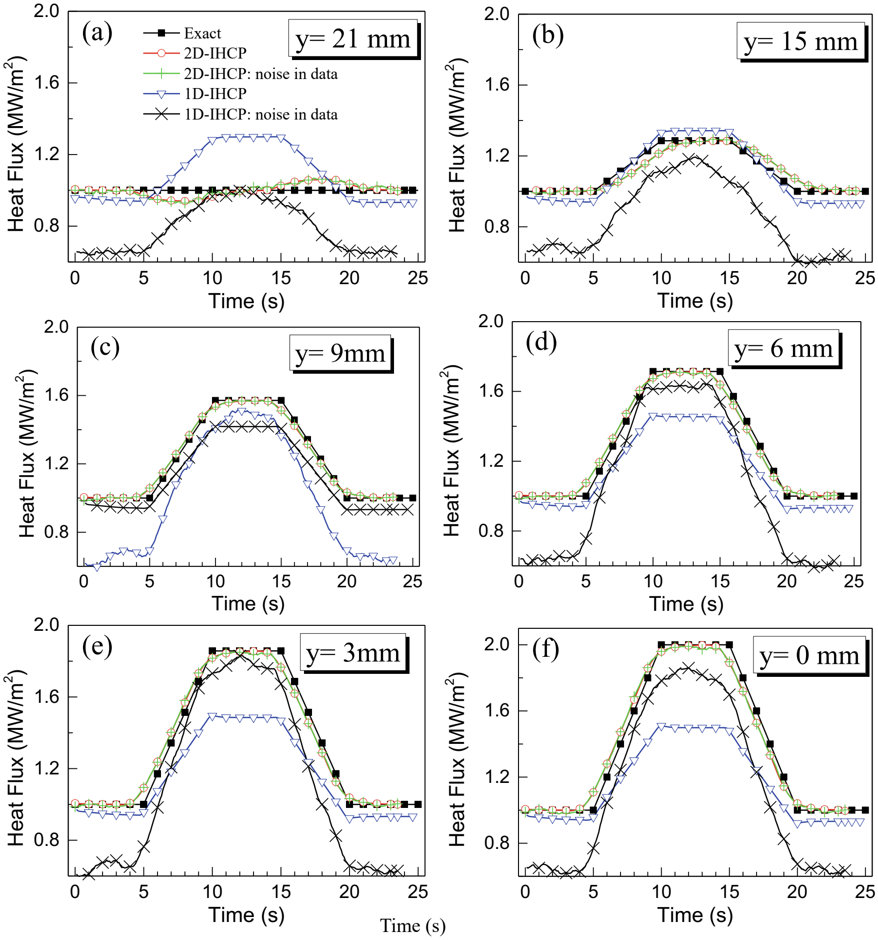

Fig. 3 Heat fluxes calculated by 2DIHCP and 1D-IHCP for the test-problem: **a** heat flux at y = 21 mm. **b** heat flux at y = 15 mm. **c** heat flux at y = 9 mm. **d** heat flux at y = 6 mm. **e** heat flux at y = 3 mm. **f** heat flux at y = 0 mm

(y is 3 mm) are the highest, followed by Y_{tc12} (y is 6 mm), Y_{tc10} (y is 9 mm), Y_{tc8} (y is 12 mm), Y_{tc6} (y is 15 mm), Y_{tc4} (y is 18 mm), and Y_{tc2} (y is 21 mm). It is suggested that the thermocouples corresponding to mold surface exposed to the air are cooler than those of thermocouples below the melt level.

Figure 5 shows the mold heat fluxes calculated by 2DIHCP from measured mold temperatures. For the 2DIHCP runs, the future time step is configured as 8, and α is 7×10^{-9}, respectively. During **stage I** of filling, it was found that the local heat fluxes increase rapidly and then reach their peak values and the highest value is around 1.03 MW/m², which is similar to industrial and other experimental results [3, 5–8]. During **stage II**, all the heat fluxes decrease rapidly at first due to the fast formation of

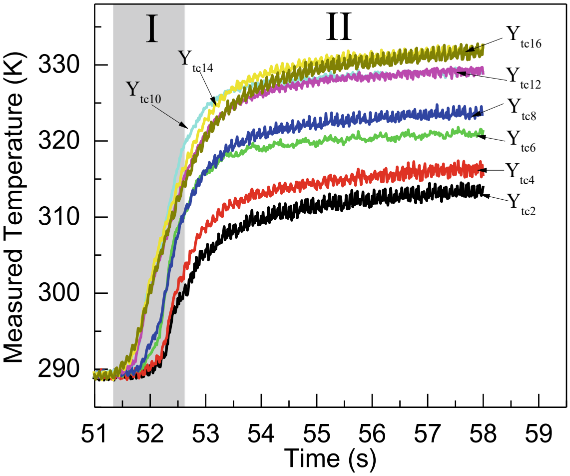

Fig. 4 Responding in-mold temperatures

the shell/mold air-gap, and then they continue to decrease gradually. From the above results, it could be suggested that during the initial filling of the liquid steel, the heat fluxes increased dramatically as the hot liquid directly contacted with the cold mold and the latent heat was released greatly with the increase of heat flux in **stage I**. Then, the initial shell is formed against the hot surface of the water-cooling mold; thus, the air gap in between the mold-metal interface is formed due to the solidification of liquid steel and consequently the interfacial thermal resistance increases dramatically, which explains the reason why the heat flux reduces intensively at the initial stage of **stage II**. With the further solidification of the liquid steel, the shell continues to grow and correspondingly the total thermal resistance across the solidified shell and mold-shell interface continues to increase. That is the reason why the heat fluxes were reduced gradually throughout the rest of **stage II**.

In the latter part of **stage II**, the other interesting phenomenon that was observed in this study is that the heat fluxes of locations at S3 (y is 3 mm) and S6 (y is 6 mm) are the highest, followed by S9 (y is 9 mm) and S0 (y is 0 mm), then S12 (y is 12 mm), S15 (y is 15 mm), S18 (y is 18 mm), and S21 (y is 21 mm). It might be explained that the location of S0 below the liquid steel level S9 (y is 9 mm) has a thicker shell thickness due to the longer solidification time, which resulted in a larger thermal resistance than the locations of S3 (y is 3 mm) and S6 (y is 6 mm), which the finding is consistent with other studies [5–8]. As for the position at the liquid level S9 (y is 9 mm), there exists significant vertical heat transfer upward to the top part of the mold, therefore, its heat flux is a little bit smaller than those of S3 and S6. As for the heat fluxes at S12 (y is 12 mm), S15 (y is 15 mm), S18 (y is 18 mm), and S21 (y is 21 mm), they are decreasing because they are far away from the liquid melt and the existing vertical heat transfer from the liquid to the upper mold. Therefore, the mold heat transfer is two-dimensional from the location 3 to 6 mm below the liquid melt vertically toward the upper part (may be a little downward) and horizontally to the inside of the mold.

Fig. 5 Mold heat flux calculated by 2DIHCP

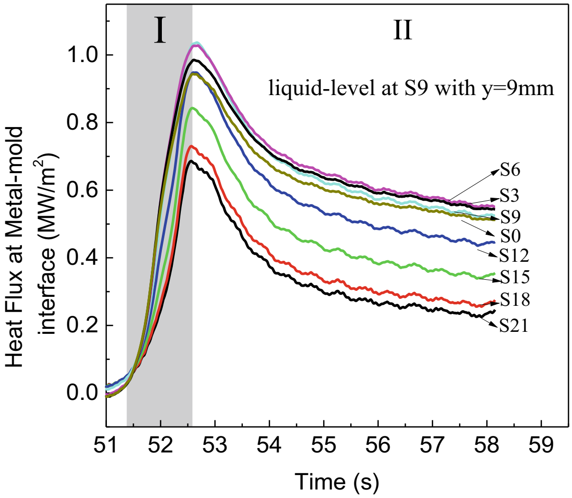

The mold wall temperature evolution during the casting process is reconstructed by 2DIHCP and shown in Fig. 6. The temperatures of the lower part of the mold wall are increased (turns to red) at first with the initial filling of the liquid steel, and then the hot red area expands both horizontally and vertically with the progressive filling of the liquid steel, which indicates the significant 2D heat transfer inside the mold as suggested above. It was noticed that there was no significant evolution of the temperature inside the mold after 54 s, which is consistent with Fig. 4, and the maximum temperature of the mold wall reaches as high as 335 K.

Conclusions

In this work, based on the function specification method with first-order spatial regularization, a two-dimensional transient inverse heat conduction problem (2DIHCP) is established for the determination of the mold heat flux using mold temperatures measured by fast response thermocouples at a frequency up to 60 Hz. The specific conclusions are summarized as:

1. The inverse problem of the function specification method implemented with the first-order spatial regularization could improve the temporal and spatial stabilization of recovered mold heat flux.
2. The built two-dimensional transient inverse heat conduction problem (2DIHCP) could reconstruct the boundary heat flux precisely and is capable of the ability to resist measurement noises. It could also provide more precise heat flux calculation than the one-dimensional **i**nverse **h**eat **c**onduction **p**roblem (1D-IHCP).

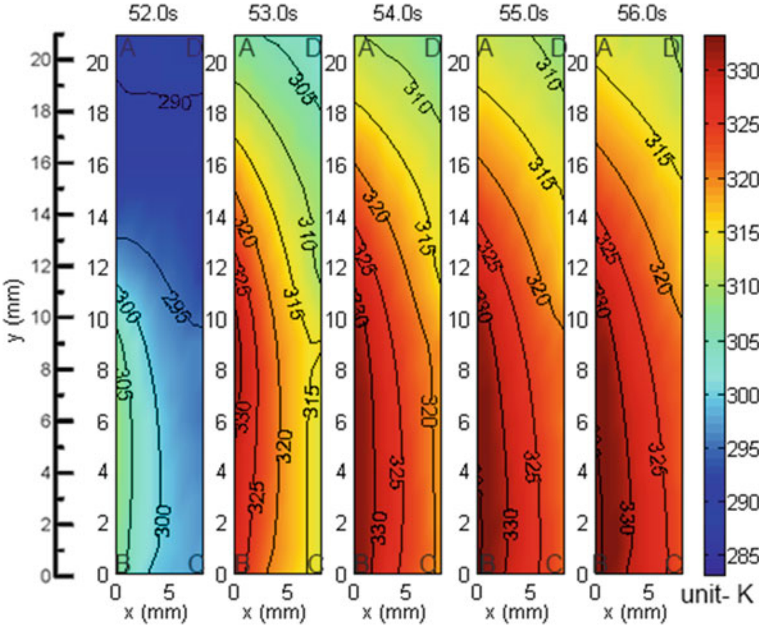

Fig. 6 Temperature evolution of the mold wall during the casting

Acknowledgements This work was partially supported by NSFC (No. 52074135, 51904107), the Natural Science Foundation of Jiangxi Province (No. 20202BAB214016), and the Youth Jinggang Scholars Program in Jiangxi Province (QNJG2020049).

Conflicts of Interest
The authors declare that they have no conflicts of interest.

References

1. Balogun D, Roman M, Gerald RE, Huang J, Bartlett L, O'Malley R (2022) Shell measurements and mold thermal mapping approach to characterize steel shell formation in peritectic grade steels. Steel Res Int 93(1):2100455
2. Niu Z, Cai Z, Zhu M (2020) Heat transfer behaviour of funnel mould copper plates during thin slab continuous casting and channel structure optimization. Ironmaking Steelmaking 47(10):1135–1147
3. Zhang H, Wang W (2017) Mold simulator study of heat transfer phenomenon during the initial solidification in continuous casting mold. Metall Mater Trans B 48(2):779–793
4. Badri A, Natarajan TT, Snyder CC, Powers KD, Mannion FJ, Byrne M, Cramb AW (2005) A mold simulator for continuous casting of steel: part II. The formation of oscillation marks during the continuous casting of low carbon steel. Metall Mater Trans B 36(3):373–383
5. Zhang H, Wang W (2016) Mold simulator study of the initial solidification of molten steel in continuous casting mold: part II. Effects of mold oscillation and mold level fluctuation. Metall Mater Trans B 47(2):920–931

6. Lyu P, Wang W, Zhang H (2017) Mold simulator study on the initial solidification of molten steel near the corner of continuous casting mold. Metall Mater Trans B 48(1):247–259
7. Zhang H, Wang W, Ma F, Zhou L (2015) Mold simulator study of the initial solidification of molten steel in continuous casting mold. Part I: experiment process and measurement. Metall Mater Trans B 46(5):2361–2373
8. Lopez PER, Mills KC, Lee PD, Santillana B (2012) A unified mechanism for the formation of oscillation marks. Metall Mater Trans B 43(1):109–122
9. Arunkumar S, Rao KS, Kumar TP (2008) Spatial variation of heat flux at the metal–mold interface due to mold filling effects in gravity die-casting. Int J Heat Mass Transf 51(11–12):2676–2685
10. Roman M, Balogun D, Zhuang Y, Gerald RE, Bartlett L, O'Malle RJ, Huang J (2020) A spatially distributed fiber-optic temperature sensor for applications in the steel industry. Sensors 20(14):3900
11. Cardiff M, Kitanidis PK (2008) Efficient solution of nonlinear, underdetermined inverse problems with a generalized PDE model. Comput Geosci 34(11):1480–1491
12. Beck JV, Blackwell B, Clair CR Jr (1985) Inverse heat conduction: Ill-posed problems. James Beck, New York
13. Yu Y, Luo X (2015) Estimation of heat transfer coefficients and heat flux on the billet surface by an integrated approach. Int J Heat Mass Transf 90:645–653
14. Pinheiro CAM, Samarasekera IV, Brimacomb JK, Walker BN (2000) Mould heat transfer and continuously cast billet quality with mould flux lubrication Part 1 Mould heat transfer. Ironmaking Steelmaking 27(1):37–54
15. Thomas BG, Wells MA, Li D (2011) Monitoring of meniscus thermal phenomena with thermocouples in continuous casting of steel. TC 216(416):8900
16. Wang X, Tang L, Zang X, Yao M (2012) Mold transient heat transfer behavior based on measurement and inverse analysis of slab continuous casting. J Mater Process Technol 212(9):1811–1818
17. Chang CW, Liu CH, Wang CC (2018) Review of computational schemes in inverse heat conduction problems. Smart Sci 6(1):94–103
18. Du F, Wang X, Fu J, Han X, Xu J, Yao M (2018) Inverse problem-based analysis on non-uniform thermo-mechanical behaviors of slab during continuous casting. Int J Adv Manufact Technol 94(1):1189–1196
19. Trovant M, Argyropoulos S (2000) Finding boundary conditions: a coupling strategy for the modeling of metal casting processes: part I. Experimental study and correlation development. Metall Mater Trans B 31(1):75–86
20. Griffiths WD (2000) Modelled heat transfer coefficients for Al–7 wt-% Si alloy castings unidirectionally solidified horizontally and vertically downwards. Mater Sci Technol 16(3):255–260
21. Chakraborty S, Ganguly S, Chacko EZ, Ajmani SK, Talukdar P (2017) Estimation of surface heat flux in continuous casting mould with limited measurement of temperature. Int J Therm Sci 118:435–447
22. Li Y, Wang G, Chen H (2015) Simultaneously estimation for surface heat fluxes of steel slab in a reheating furnace based on DMC predictive control. Appl Therm Eng 80:396–403
23. Zhang H, Wang W, Zhou L (2015) Calculation of heat flux across the hot surface of continuous casting mold through two-dimensional inverse heat conduction problem. Metall Mater Trans B 46(5):2137–2152
24. Özisik MN, Orlande HR (2018) Inverse heat transfer: fundamentals and applications. Routledge
25. Zhang L, Li L, Ju H, Zhu B (2010) Inverse identification of interfacial heat transfer coefficient between the casting and metal mold using neural network. Energy Convers Manage 51(10):1898–1904
26. Jayakrishna P, Chakraborty S, Ganguly S, Talukdar P (2021) Modelling of thermofluidic behaviour and mechanical deformation in thin slab continuous casting of steel: an overview. Can Metall Q 60(4):320–349

27. Argyropoulos SA, Carletti H (2008) Comparisons of the effects of air and helium on heat transfer at the metal-mold interface. Metall Mater Trans B 39(3):457–468
28. Kovačević L, Terek P, Kakaš D, Miletić A (2012) A correlation to describe interfacial heat transfer coefficient during solidification of Al–Si alloy casting. J Mater Process Technol 212(9):1856–1861
29. Sun Z, Hu H, Niu X (2011) Determination of heat transfer coefficients by extrapolation and numerical inverse methods in squeeze casting of magnesium alloy AM60. J Mater Process Technol 211(8):1432–1440
30. Rajaraman R, Velraj R (2008) Comparison of interfacial heat transfer coefficient estimated by two different techniques during solidification of cylindrical aluminum alloy casting. Heat Mass Transf 44(9):1025–1034
31. Coates B, Argyropoulos SA (2007) The effects of surface roughness and metal temperature on the heat-transfer coefficient at the metal mold interface. Metall Mater Trans B 38(2):243–255
32. Dour G, Dargusch M, Davidson C (2006) Recommendations and guidelines for the performance of accurate heat transfer measurements in rapid forming processes. Int J Heat Mass Transf 49(11–12):1773–1789
33. Blanc G, Raynaud M, Chau TH (1998) A guide for the use of the function specification method for 2D inverse heat conduction problems. Revue Générale Therm 37(1):17–30
34. Babu K, Prasanna Kumar TS (2010) Mathematical modeling of surface heat flux during quenching. Metall Mater Trans B 41(1):214–224
35. Wang W, Long X, Zhang H, Lyu P (2018) Mold simulator study of effect of mold oscillation frequency on heat transfer and lubrication of mold flux. ISIJ Int 58(9):1695–1704
36. Orlande HR (2012) Inverse problems in heat transfer: new trends on solution methodologies and applications. J Heat Transf 134(3)
37. Badri A, Natarajan TT, Snyder CC, Powers KD, Mannion FJ, Cramb AW (2005) A mold simulator for the continuous casting of steel: part I. The development of a simulator. Metall Mater Trans B 36(3):355–71
38. Aster RC, Borchers B, Thurber CH (2018) Parameter estimation and inverse problems. Elsevier, New York
39. Vogel CR (ed) (2002) Computational methods for inverse problems. Society for Industrial and Applied Mathematics, Philadelphia
40. George S, Thamban Nair M (1998) On a generalized Arcangeli's method for Tikhonov regularization with inexact data. Numer Funct Anal Optim 19(7–8):773–787
41. Özısık MN (ed) (1993) Heat conduction, 2nd edn. Wiley, New York, pp 62–75

Quality Prediction of Hot Rolled Products and Optimization of Continuous Casting Process Parameters Based on Big Data Mining

Zibing Hou, Zhiqiang Peng, Qian Liu, and Guanghua Wen

Abstract The continuous casting-rolling process is widely used due to the lower energy consumption and its compact process. However, the defect in continuous casting slab severely limits the development of the continuous casting-rolling technology. In this paper, based on big data mining technology, the quality prediction model for hot rolled coils and the corresponding optimization method for continuous casting parameters were proposed. Firstly, the GA (Genetic algorithm)-BP (Back-propagation) neural network prediction model with high accuracy was constructed according to the characteristics of actual production data. Then, the effect of continuous casting parameters on the probability of defects occurrence was investigated with the established model. The results show that the defects occurrence probability decreases firstly and then increases with the casting speed, as well as the temperature of molten steel, which are consistent with metallurgical theory. Meanwhile, the optimum casting speed and mold level are 1.3 m/min and 8200 mm, respectively. When the flow rate of argon blowing for stopper and nozzle are restricted to 8.5 and 8 L/min, the defects occurrence probability will be lower. Furthermore, the optimum critical values of temperature difference of mold cooling water and inlet temperature are 8 °C and 35 °C, respectively. This paper can provide the guidance for narrow range control of continuous casting parameters and contribute to the production of high-quality steel.

Keywords Continuous casting · Hot rolled coils · Surface defects · Data mining · Parameter optimization

---

Z. Hou (✉) · Z. Peng · Q. Liu · G. Wen
College of Materials Science and Engineering, Chongqing University, Chongqing 400044, People's Republic of China
e-mail: houzibing@cqu.edu.cn

Chongqing Key Laboratory of Vanadium-Titanium Metallurgy and New Materials, Chongqing University, Chongqing 400044, People's Republic of China

S. Wagstaff et al. (eds.), *Materials Processing Fundamentals 2023*, The Minerals, Metals & Materials Series, https://doi.org/10.1007/978-3-031-22657-1_6

Introduction

At present, the technology of continuous casting-rolling has been used widely due to the low energy consumption and compact process [1]. However, it is severe to avoid slab defects with current production conditions of continuous casting. These defects will be inherited into the rolled products and manifested as surface warp [2], inclusion [3], or crack [4], not only affecting the normal production process but also leading to additional energy consumption. Therefore, it is necessary to judge the slab's quality accurately and then adjust the continuous casting process parameters in advance. That will be conducive to the improvement of product's quality and save energy for steel industry.

The online defect recognition of slabs is mainly carried out from two aspects: physical detection and expert system. Methods of physical detection include CCD camera detection [5], eddy current detection [6], etc. However, the recognition accuracy of the physical detection is limited by iron oxide scale and harsh environment. Meanwhile, this detection equipment can only identify surface defects but is not suitable for internal defects. As for the expert system, experience accumulated from the actual production conditions is used for defect recognition [7], mainly based on sole parameter. Thus, it is difficult to meet the increasing demand for accurate judgement since the generation of slab defects is affected by multiple parameters. In recent years, technology of big data mining has been used in the prediction of product performance and quality in the industrial field [8, 9]. Nevertheless, there are few research on the prediction of slab quality due to lack of samples. With the development of information collection technology, the defects can be distinguished whether they are caused by the continuous casting process according to the quality information of rolled products. Actually, the rich quality information provided by the hot rolling mill is used for the traceability of some individual sample defects. At the same time, optimization of continuous casting parameters is mostly carried out through production experience or experimental research, which have problems such as high cost and long development period. Hence, it is meaningful to establish the quality prediction model for hot rolled coils based on the big data of production process and optimize process parameters.

In this paper, the methods of data preprocessing and quality prediction model based on BP (Backpropagation) neural network and GA (Genetic algorithm) were established with continuous casting parameters, as well as the quality information of hot rolled coils. Subsequently, the effect of parameters on surface defects of hot rolled coils was investigated. According to this study, it can provide guidance for the exact design of production process parameters, which is helpful to the fine control of continuous casting process.

Methods

Database Construction

25 parameters of continuous casting process, which involve ladle, tundish, and mold, were selected to establish the model. The parameters related to the second cooling were not considered for the reason that the defects of slabs are mainly generated in the initial solidification stage of the molten steel. Meanwhile, the production parameters, defect types, and the number of defects vary with steel grades. Thus, the data were classified into three categories, low carbon steel, peritectic steel, and medium carbon steel. For the quality information of hot rolled coils, the defective and normal samples are highly unbalanced, which will easily lead to the overfitting of the prediction model and poor performance for the class with small samples. Figure 1 shows the Pearson correlation coefficient among continuous casting parameters, and it can be seen that there is a certain correlation among some continuous casting parameters. The redundant data reduce the modeling efficiency of the prediction model, and it is easy to make the model overfitting.

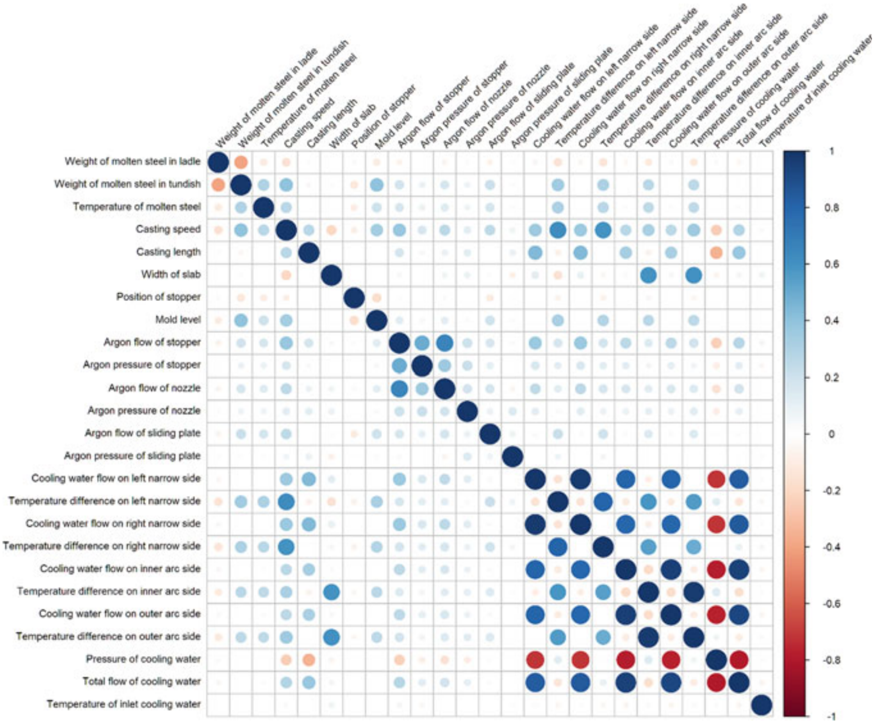

Fig. 1 Heat map of correlation coefficient among continuous casting parameters

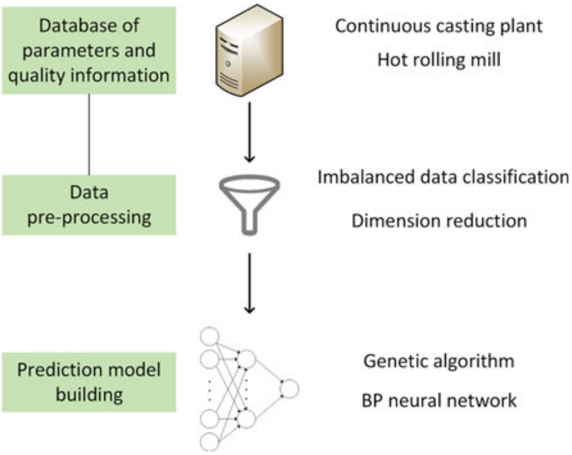

Fig. 2 Flow chart of quality prediction model for hot rolled coils

Quality Prediction Model

Based on the data characteristics of continuous casting parameters and quality information of hot rolled coils, the flow chart of prediction model was proposed, as shown in Fig. 2. Firstly, the samples attributed to the continuous casting responsibility were filtered from the database and merged with production data of continuous casting. Then, data preprocessing was performed on the above database, including classification for imbalanced data of defect information and data dimensionality reduction. For convenience of modeling, defective and normal samples were marked as 1 and 0, respectively. The preprocessed data were used as the input of the hot rolled coil quality prediction model, and the BP neural network algorithm was optimized with the genetic algorithm in order to achieve effective prediction.

Analysis Method for Influence of Parameters on Defects

The GA-BP neural network can be used to investigate the effect of continuous casting parameters on the defects of hot rolled coils. The prediction of new data can be achieved by saving the constructed neural network model, which means that the trained model is considered as a multivariable function. Thus, the values of dependent variables with different values of the independent variable can be calculated. In this paper, a certain continuous casting parameter was taken as the independent variable, the rest of the parameters were fixed, and the single parameter was adjusted to investigate the relationship between the possibility of defect occurrence and different parameters. Obviously, the probability of defects occurrence increases with the calculated value of the model. Therefore, the optimal value or operating interval of continuous casting parameters can be finally obtained.

Table 1 Prediction results of GA-BP model

Steel grade	MAE	MSE	RMSE	AR (%)	FAR (%)
Low carbon steel	0.1067	0.0445	0.210	94.7	82.5
Peritectic steel	0.1299	0.0521	0.2236	93.3	87.5
Medium carbon steel	0.3063	0.1465	0.3827	85.4	78.3

Results and Discussion

Model Evaluation

Mean absolute error (MAE), mean squared error (MSE), and root mean squared error (RMSE) were used to evaluate the performance of the prediction model. MAE is one of the comprehensive evaluation methods of error analysis, which can avoid the offset of positive and negative values. MSE is the mean absolute percentage error. The smaller the MSE, the higher the prediction accuracy. RMSE represents the dispersion degree of the predicted value, and lower value of which indicates higher prediction accuracy. To better describe the prediction results of the model on the quality of hot rolled coils, the accuracy rate for overall samples (AR) and defective samples (FAR) were introduced to evaluate the accuracy rate of different models.

Table 1 shows the calculation results of different means of model evaluation. From which, we can see that prediction model for medium carbon steel has the highest model evaluation indexes (MAE, MSE, and RMSE) and relatively lower accuracy rate compared to the other two steel grades, while the MAE, MSE, and RMSE values for low carbon steel are the lowest, which means that the model has a higher prediction accuracy. Meanwhile, it is also found that the prediction accuracy of the model varied with steel grades, which may be caused by the difference in sample size. Overall, the AR for each steel grade is larger than 85%, which indicates that the prediction models for different steel grades are accurate enough to investigate the influence of continuous casting parameters on the defects of hot rolled coils. Due to the largest sample size and the best prediction effect among all steel grades, data of low carbon steel was selected for further study.

Effect of Continuous Casting Parameters on Defects

Casting Speed, Temperature of Molten Steel, and Mold Level

Figure 3 shows the relationship between the quality of the hot rolled coils and three continuous casting parameters (casting speed, temperature of molten steel, and mold level). The horizontal axis represents the value of each continuous casting parameter, and the vertical axis represents the dimensionless output value calculated by

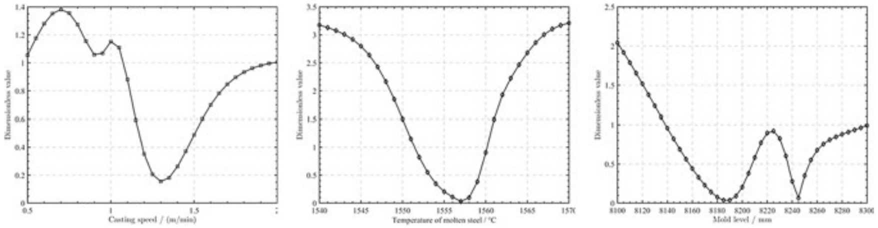

(a) (b) (c)

Fig. 3 Effect of **a** casting speed, **b** temperature tundish molten steel, and **c** mold level on possibility of defects

the constructed neural network. The probability of defects occurrence increases with dimensionless output value. As indicated in Fig. 3a, the possibility of defects occurrence first decreases and then gradually increases with casting speed. Meanwhile, the hot rolled coils are not prone to defects when the casting speed is 1.3 m/min. The reason for this result may be that the melting performance of the mold flux is poor when the casting speed is low, thus affecting the surface quality of the slab. High casting speed can cause the fluctuation of heat transfer on all sides of the mold, which aggravates the generation of surface cracks [10]. Previous research has shown that higher or lower casting speed may also lead to slag inclusions [11].

It can be seen from Fig. 3b that it is beneficial to the quality of the hot rolled coils when the temperature of molten steel is in the range of 1550 ~ 1560 °C. Higher temperature of molten steel leads to higher superheat, which causes thinner shell thus resulting in breakout or crack. Meanwhile, lower superheat is not conducive to the melting of slag [12], which will also lead to surface defects. Furthermore, the possibility of defects occurrence is greatly affected by the mold level from Fig. 3c. Mold level is an important parameter of the casting process, which can effectively reflect the clogging of the nozzle [13]. This result shows that the probability of defect occurrence is the lowest when the mold level is around 8200 mm, which is the setting value in the plant.

The effect of casting speed, temperature of molten steel, and mold level on the defects of hot rolled coils can be well explained by production experience and metallurgical theory, which shows the feasibility of using neural networks to investigate the effect of parameters on product defects. Moreover, argon blowing and the heat transfer of the mold were also investigated.

Argon Blowing

Figure 4 shows the relationship between parameters of argon blowing and the possibility of defects occurrence. It can be seen from Fig. 4a–c that the effects of argon flow on defects of the hot rolled coils are nonlinear, and all of which have the same trend of increasing first, then decreasing, and finally increasing again with flow rate. The best value for stopper and nozzle is about 8.5 L/min and 8 L/min, respectively.

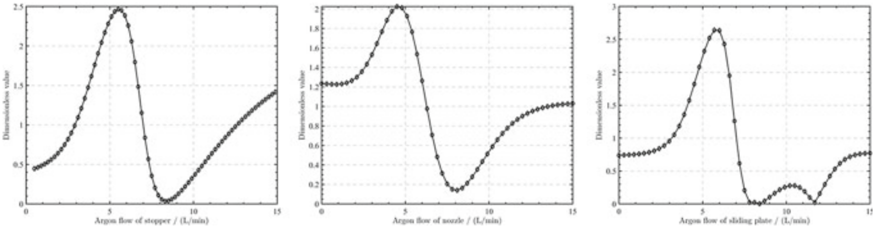

(a) (b) (c)

Fig. 4 Effect of on probability of defects: **a** argon flow of stopper; **b** argon flow of nozzle; **c** argon flow of sliding plate

Higher or lower flow rate of argon blowing will easily lead to defects caused by large fluctuation of mold level.

Heat Transfer of Mold

Figure 5 shows the relationship between the heat transfer parameters of mold and the possibility of defects occurrence. From Fig. 5a–d, it can be seen that the influence of cooling water flow at different positions on the possibility of defects is similar. With the increase of water flow, it shows a trend of decreasing first, then increasing, then decreasing, and finally increasing again, which indicates that the influence of cooling water flow on slab defects is relatively complex. The results of Fig. 5e–h show that the possibility of defects occurrence decreases first and then increases with the temperature difference of cooling water. When the temperature difference is in the range of 7–9 °C, the possibility of defects is relatively low, and it is recommended to control the temperature difference to about 8 °C in actual production. From Fig. 5i–k, it can be seen that optimum control values inlet water pressure and temperature of the mold are around 1.08 Mpa and 35 °C, respectively. Within a certain range (8600–8700 L/min), probability of defects occurrence decreases with increasing total cooling water flow rate, which may be due to less fluctuations in heat transfer.

Conclusions

Based on the features of production data from the plant, the data preprocessing method and the quality prediction model for hot rolled coils were firstly proposed. Then, the relationships between product defects and continuous casting parameters were investigated. The model performed well on the testing set. The prediction accuracies of overall samples to low carbon steel, peritectic steel, and medium carbon steel were 94.7%, 93.3%, and 85.4%, respectively. As for the defective samples, prediction accuracies for different steel grades were 82.8%, 87.5%, and 87.3%, respectively.

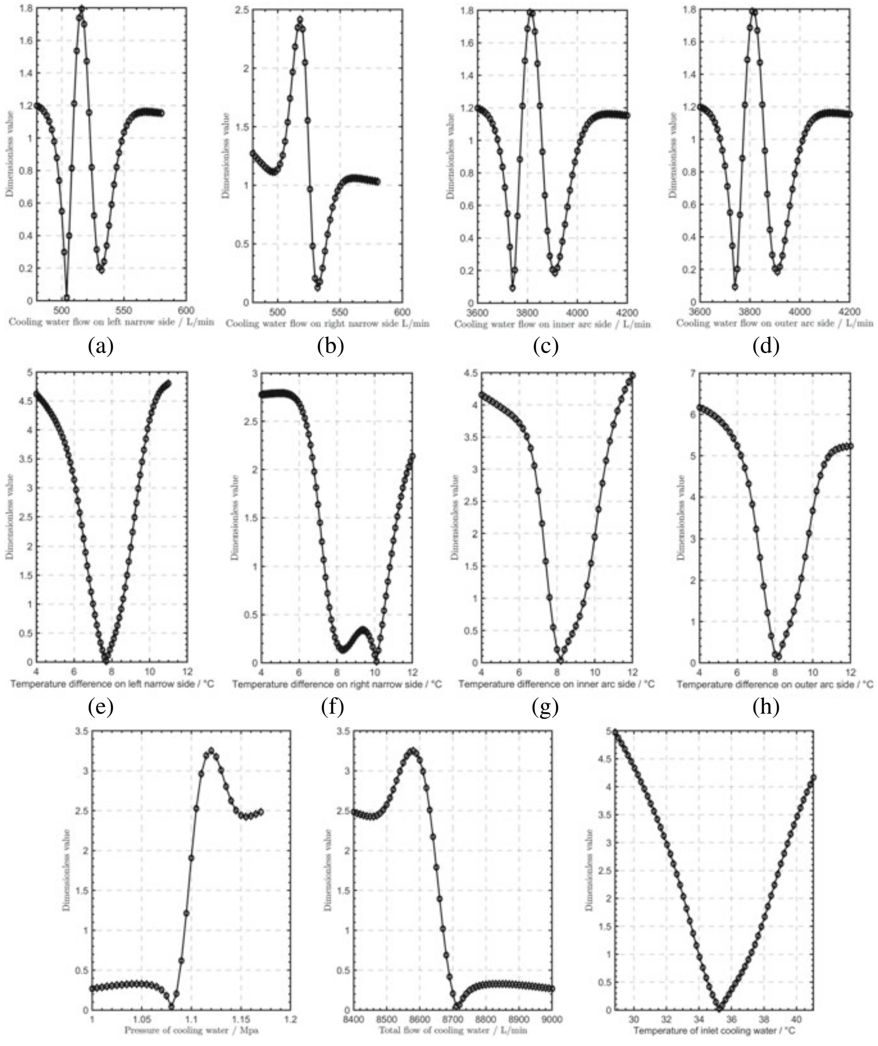

(a) (b) (c) (d)

(e) (f) (g) (h)

(i) (j) (k)

Fig. 5 Effect of the heat transfer of the mold on the probability of defects: **a** cooling water flow on left narrow side; **b** cooling water flow on right narrow side; **c** cooling water flow on inner arc side; **d** cooling water flow on outer arc side; **e** temperature difference on left narrow side; **f** temperature difference on right narrow side; **g** temperature difference on inner arc side; **h** temperature difference on outer arc side; **i** pressure of cooling water; **j** total flow of cooling water; **k** temperature of inlet cooling water

Moreover, the optimal operating values of some parameters were obtained according to the prediction model based on actual production data. For casting speed and mold level, the optimal operating values are 1.3 m/min and 8200 mm, respectively. The probability of defects occurrence is low when flow rate of argon blowing for stopper and nozzle are restricted to around 8.5 L/min and 8 L/min, respectively. As to the heat transfer of mold, the optimal temperature difference between inlet and outlet water is 8 °C, and the temperature of inlet water should be controlled to around 35 °C.

Acknowledgements The authors are very grateful for the support from National Natural Science Foundation of China (52274318).

References

1. Wang S, Zhao G, Bao S (2013) Surface cracks analysis on continuous casting slab Q345c during hot delivery and hot charging. Adv Mat Res 785:1081–1086
2. Kainz A, Ilie S, Parteder E (2008) From slab corner cracks to edge-defects in hot rolled strip—experimental and numerical investigations. Steel Res Int 79(11):861–867
3. Luo C, Stahlberg U (2001) Deformation of inclusions during hot rolling of steels. J Mater Process Tech 114(1):87–89
4. Ervasti E, Stahlberg U (1999) Behaviour of longitudinal surface cracks in the hot rolling of steel slabs. J Mater Process Tech 94(2–3):141–150
5. Zhao L, Qi O, Chen D, Zhang X (2011) CCD imaging definition controlling methods in continuous casting slab surface defects acquisition. Adv Mat Res 233:2490–2494
6. Qiu X, Wei C, Cui X, Wei J (2013) Real-time pre-processing of the pulsed eddy current signal from continuous casting slabs. Insight 55(3):136–141
7. Yan J, Bi X, Tian Z (2012) The on-line continuous casting slab surface quality prediction expert system. Int J Educ Manag Eng 2(1):54–58
8. Li H, Li X, Liu X, Bu X, Li H, Lyu Q (2022) Prediction of blast furnace parameters using feature engineering and stacking algorithm. Ironmak Steelmak 49(3):283–296
9. Shen C, Wang C, Wei X, Li Y, Zwaag S, Xu W (2019) Physical metallurgy-guided machine learning and artificial intelligent design of ultrahigh-strength stainless steel. Acta Mater 179:201–214
10. Wang X, Tang L, Zang X, Yao M (2012) Mold transient heat transfer behavior based on measurement and inverse analysis of slab continuous casting. J Mater Process Tech 212(9):1811–1818
11. Li S, Du X (2010) The effect of casting speed on slag-inclusion defects in 1050 × 200 mm ultra-low-carbon automobile steel slabs. Metall Res Technol 118(6):611
12. Sun Y, Ni Y, Wang H, Xu Z, Cai K (2010) Longitudinal surface cracks of thin slabs. Int J Miner Metall Mater 17(2):159–166
13. Nadif M, Lehmann J, Burty M, Domgin J (2007) Control of steel reoxidation and CC nozzle clogging: an overview. Metall Res Technol 104(10):493–500

Study on the Uniformity of Surface Temperature of Continuous Casting Slab Based on Solidification and Heat Transfer Simulations

Yadong Wang and Lifeng Zhang

Abstract In the current study, a two-dimension solidification and heat transfer model was developed based on the slab continuous casting (CC) process in a domestic steel plant. The layout of jet nozzles of segment 2 and segment 3 in secondary cooling zones was adjusted to optimize the distribution of temperature along the width direction. The following main findings indicate that the temperature was more uniform. In segment 2 and segment 3, middle jet nozzles were replaced by those in side positions, and the distribution of water flow rate and temperature along the width direction was more uniform. In the outlet of segment 2, except for the slab corner, the fluctuation range of the temperature along the width direction decreased from 39.7 to 14.1 °C. In the outlet of segment 3, except for the slab corner, the fluctuation range of the temperature along the width direction decreased from 40.4 to 17.3 °C.

Keywords Continuous casting slab · Solidification · Heat transfer · Simulation

Introduction

In the slab CC process, the uniformity of heat transfer in the secondary cooling zones has an important effect on the surface and internal quality of slabs. Transverse corner cracks had a close relationship to secondary cooling which was reported by many researchers [1–3]. At the bending and straightening segments during the CC process, an appropriate cooling method to prevent the temperature of the slab corner from avoiding the poor hot ductility temperature range is essential to avoid transverse corner cracks. A method of optimizing the uniformity of solidified shell in the transverse direction was introduced by Long et al. [4], and the center macro-segregation in steel slabs was mitigated. A two-dimension heat transfer model was developed for the optimization of cooling intensity along the transverse direction, which contributed to regular solidification end in the CC slab, and the center macro-segregation was significantly mitigated. Longitudinal cracks and serious shape defects originated

---

Y. Wang · L. Zhang (✉)
School of Mechanical and Materials Engineering, North China University of Technology,
Beijing 100144, China
e-mail: zhanglifeng@ncut.edu.cn

S. Wagstaff et al. (eds.), *Materials Processing Fundamentals 2023*, The Minerals, Metals
& Materials Series, https://doi.org/10.1007/978-3-031-22657-1_7

generally due to improper cooling patterns in the mold, but improper cooling in secondary cooling zones may contribute to defect propagation [5–7].

In the current study, to obtain the uniform distribution of temperature along the width direction, a two-dimension solidification and heat transfer model was established to optimize the distribution of water flow rate. The layout of jet nozzles of segment 2 and segment 3 in secondary cooling zones was adjusted, and the distribution of temperature along the width direction was optimized.

Mathematical Formulation

In the current study, a two-dimensional heat transfer and solidification model was established to calculate the thermal history of the CC slab. A detailed description of the two-dimensional heat transfer and solidification model can be found in the previous study [1]. In the current model, crystallizer heat transfer, water spray cooling, water evaporation cooling, roll contact cooling, and radiation cooling were considered. Governing equations of boundary conditions in mold zone and secondary cooling zones were given in the previous study [2]. Water spray cooling was the main factor governing heat transfer in secondary cooling zones. The distribution of water flow rate for all jet nozzles was measured, and the test equipment was given in the previous work [2]. The main parameters used in the current study are listed in Table 1. The content of the IF steel is listed in Table 2. Water flow in mold and secondary cooling zones is listed in Table 3. I represents the loose side of the wide face, and O represents the fixed side of the wide face. IO means that I and O each account for half of the water flow rate.

Table 1 Parameters of CC process

Parameters	Values
Cross section of the slab (mm^2)	240 × 1500
Effective mold length (mm)	800
Casting speed (m/min)	1.2
Pouring temperature (°C)	1555
Liquidus temperature of the steel (°C)	1530
Solidus temperature of the steel (°C)	1499

Table 2 Chemical compositions of IF steel

Elements	C	Mn	Si	S	P	Als	Cr	Ni	Cu	Nb	V	Ti
Content (%)	0.001	0.109	0.002	0.002	0.009	0.045	0.008	0.006	0.011	0.001	0.003	0.072

Table 3 Water flow in mold and secondary cooling zones

Cooling zones	Length (m)	Water flow (L/min)
Wide face of mold	0.8	5300
Narrow face of mold		480
Wide face of foot zone	0.24	478
Narrow face of foot zone	0.9	342
1IO	1.15	1018
2IO	2.435	1226.6
3I	1.849	302.4
3O		334.8
4I	3.71	345.6
4O		457.2
5I	3.99	205.2
5O		340.2
6I	2.0	61.2
6O		136.8
7I	4.24	88.4
7O		238
8I	6.3	59.2
8O		123.9

Solidification and Heat Transfer Simulation of CC Slabs

When the superheat is 25 °C and the casting speed is 1.2 m/min, the shell thickness and the temperature on the center of the loose side surface are shown in Fig. 1. With the distance from the meniscus increasing, the temperature at the loose side surface tended to decrease. At the inlet of each section, a temperature rise was generated due to the secondary cooling water flow decreasing along the casting direction. The shell thickness near the outlet of the mold was 18.0 mm, and the solidified end was located at 22.9 m from the meniscus.

The temperature distribution along the width direction at the outlet of different secondary cooling sections is shown in Fig. 2. In the foot zone and Sect. 1, the temperature distribution of the CC slab along the width direction was uniform. Entering Sect. 2, the temperature distribution became uneven. Near the outlet of Sect. 2, the maximum temperature was 842.3 °C which was located at about 520 mm from the slab center. Due to the two-dimensional cooling at the corner of the CC slab, the temperature at the slab corner was minimum, and it was about 674 °C. A local minimum point of temperature was 802.6 °C which was located at about 200 mm from the slab center. Near the outlet of Sect. 3, there were two higher temperature points, 808.5 °C, and 813.2 °C, and they were located at the slab center and 600 mm from the slab center, respectively. A relatively low temperature was 772.8 °C, and it was located about 250 mm from the slab center. Therefore, the layout of jet nozzles

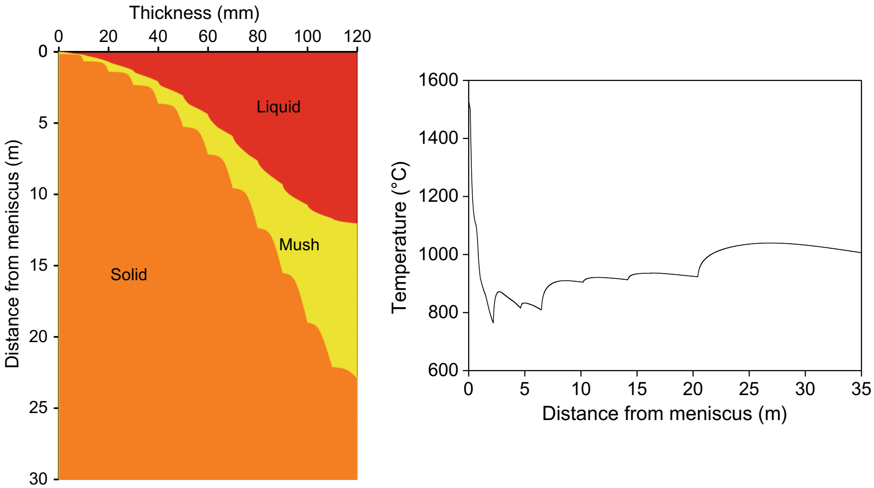

(a) Shell thickness

(b) Temperature at the center of the loose side surface

Fig. 1 Shell thickness and temperature at the center of the loose side surface

of segment 2 and segment 3 in secondary cooling zones should be adjusted to obtain more uniform distribution of temperature along the width direction.

Study on Optimizing the Distribution of Temperature Along Width Direction

To obtain the uniform distribution of temperature along the width direction, the layout of jet nozzles of segment 2 and segment 3 in secondary cooling zones should be adjusted. The measured distribution of the water flow rate of segment 2 under different gas pressure is shown in Fig. 3. For a jet nozzle in the middle, the distribution of water flow rate was approximately parabolic. With the gas pressure increasing, the water flow rate increased. For a jet nozzle in the sides, the distribution of water flow rate was relatively uniform. Within 100 mm from the nozzle center, the water flow rate was almost equal. When the distance from the nozzle center was higher than 100 mm, the water flow rate decreased.

To obtain uniform distribution of temperature along the width direction, the layout of jet nozzles should be adjusted. In the current study, middle jet nozzles were replaced by those in side positions. The measured distribution of the water flow rate of segment 2 in secondary cooling zones is shown in Fig. 4. Before optimization, there were severe fluctuations along the width direction, and the fluctuation range can reach 10 L/(m^2 s). After optimization, more uniform distribution of water flow rate was obtained, and the fluctuation range was within 5 L/(m^2 s). The measured

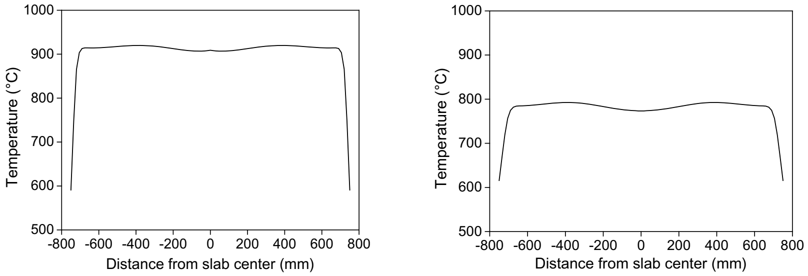

(a) Outlet of foot zone

(b) Outlet of section 1

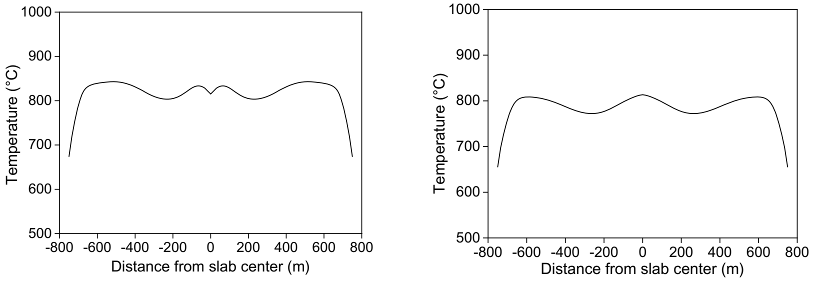

(c) Outlet of section 2

(d) Outlet of section 3

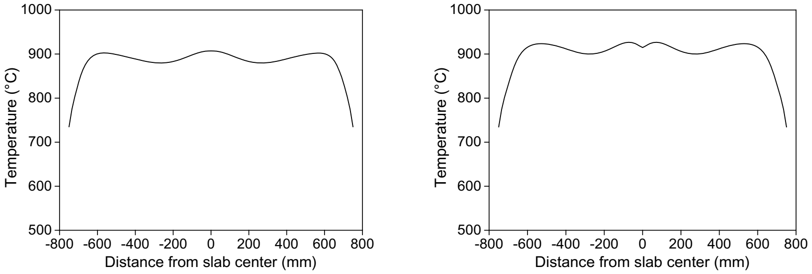

(e) Outlet of section 4

(f) Outlet of section 5

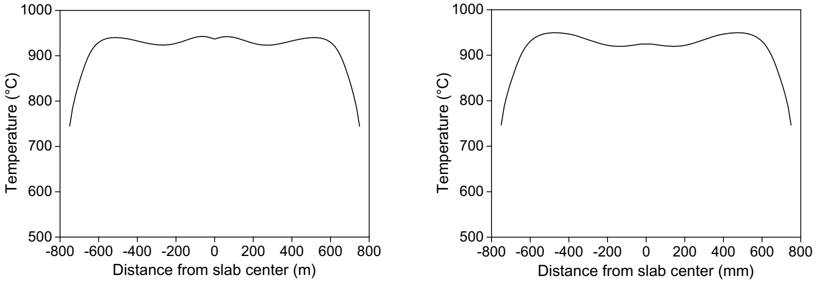

(g) Outlet of section 6

(h) Outlet of section 7

Fig. 2 Temperature distribution of the CC slab along the width direction

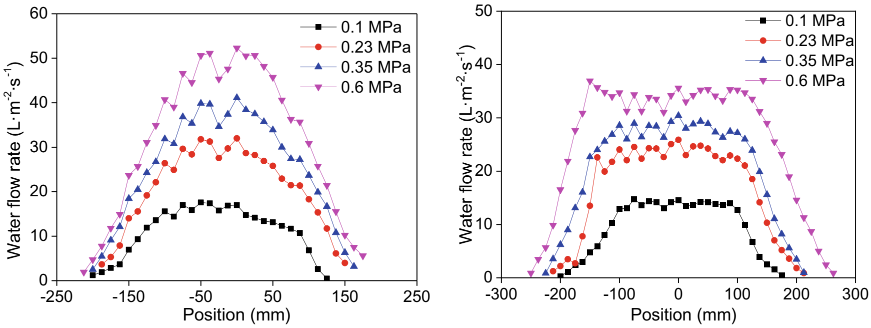

(a) Jet nozzles in the middle (b) Jet nozzles in side positions

Fig. 3 The measured distribution of water flow rate of segment 2 in secondary cooling zones

distribution of the water flow rate of segment 3 in secondary cooling zones is shown in Fig. 5. In the original condition, the fluctuation range can reach 10 L/(m^2 s). After optimization, the fluctuation range was within 3 L/(m^2 s).

After the layout of jet nozzles was adjusted, the temperature distribution of the CC slab along the width direction was more uniform, which is shown in Fig. 6. In the outlet of segment 2, except for the slab corner, the fluctuation range of the temperature along the width direction decreased from 39.7 to 14.1 °C. In the outlet of segment 3, except for the slab corner, the fluctuation range of the temperature along the width direction decreased from 40.4 to 17.3 °C.

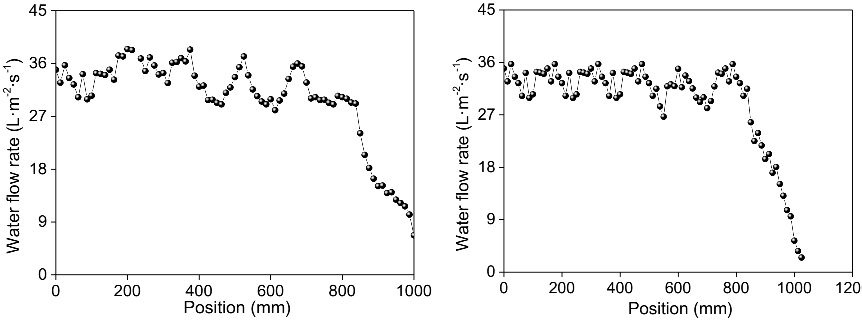

(a) Before optimization (b) After optimization

Fig. 4 The measured distribution of water flow rate of segment 2 in secondary cooling zones

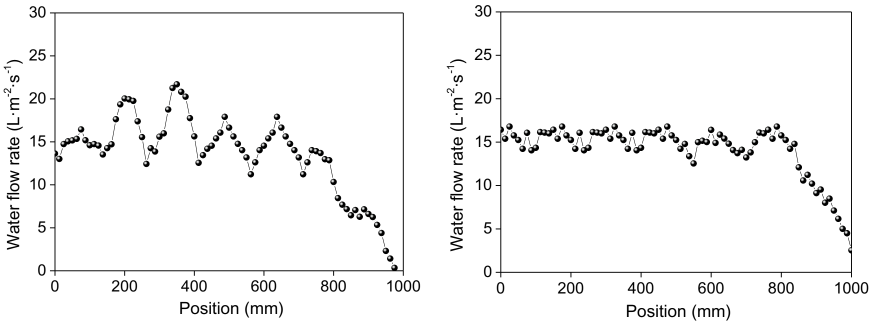

(a) Before optimization (b) After optimization

Fig. 5 The measured distribution of water flow rate of segment 3 in secondary cooling zones

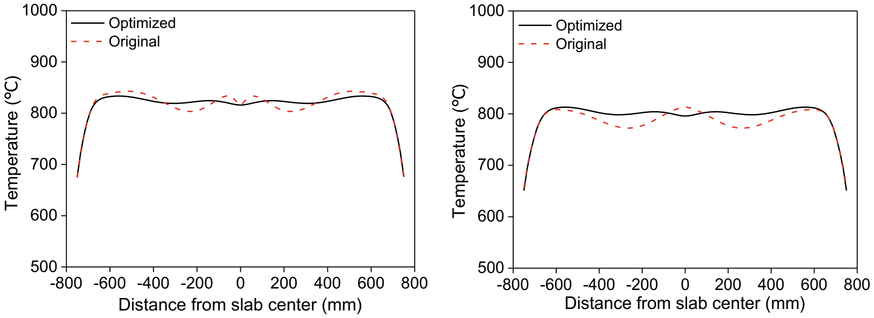

(a) Outlet of segement 2 (b) Outlet of segement 3

Fig. 6 Temperature distribution of the CC slab along the width direction

Conclusions

The layout of jet nozzles of segment 2 and segment 3 in secondary cooling zones was adjusted, and the distribution of temperature along the width direction was optimized. The following conclusions can be drawn:

1. In segment 2 and segment 3, middle jet nozzles were replaced by those in side positions, and the distribution of water flow rate and temperature along the width direction was more uniform.
2. In the outlet of segment 2, except for the slab corner, the fluctuation range of the temperature along the width direction decreased from 39.7 to 14.1 °C.
3. In the outlet of segment 3, except for the slab corner, the fluctuation range of the temperature along the width direction decreased from 40.4 to 17.3 °C.

Acknowledgements The authors are grateful for support from the National Natural Science Foundation of China (U22A20171, 52204333) and the High Steel Center (HSC) at North China University of Technology, China.

References

1. Zhang L, Yang X, Li S (2014) Control of transverse corner cracks on low-carbon steel slabs. JOM 66(9):1711–1720
2. Wang Y, Ren Q, Zhang L, Yang X, Yang W, Ren Y, Zhang H (2021) Formation and control of transverse corner cracks in the continuous casting slab of a microalloyed steel. Steel Res Int 92(6):2000649
3. Xing L, Zhang Z, Bao Y, Chen B, Zheng F, Wang M (2021) Causes of corner cracks in hypoperitectic microalloyed steel billets. Steel Res Int 92(7):2100035
4. Long M, Chen D (2011) Study on Mitigating center macro-segregation during steel continuous casting process. Steel Res Int 82(7):847–856
5. Camisani-Calzolari FR, Craig IK, Pistorius PC (1999) Control strategies for the secondary cooling zone in continuous casting. In: IEEE Africon, vol 1999, pp 1435–440
6. Wang P, Xiao H, Chen X, Li W, Yi B, Tang H, Zhang J (2022) Improved in-mold metallurgical behavior for slab casting of IF steels by a novel multi-poles electromagnetic stirring. Metall Mater Trans B 53(3):1691–1702
7. Zhang B, Xue Z, Liao Z, Wang S, Zheng H, Zhou J (2014) Analysis on surface longitudinal cracking of Q345D slab. J Iron Steel Res Int 21:108–112

How to Prevent Porosity Defects in Steel Casting Component

Izudin Dugic

Abstract The production of steel casting can in some cases be complicated and difficult. To produce quality castings, it requires the casting to be clean and free from any defects. One of the main casting defects is hot tearing, also known as a crack or shortness. This phenomenon represents the formation of an irreversible failure (crack) in the steel semisolid casting. The second defect that commonly occurs in casting is porosity. Porosity is often used to describe any void or hole found in a casting. To control the porosity, you need to understand its sources and causes. Porosity can occur either by gas formation, solidification shrinkage, or non-metallic compound formation, all while the metal is liquid. This experimental work is focused on reducing the porosity defects in steel casting components at a production scale. The produced casting component was strongly affected by porosity defects.

Keywords Steel casting · Gas porosity · Casting simulation · Solidification

Introduction

The production of quality castings requires the casting surface to be clean and free from any defects. Steel castings production can be a complicated and difficult process. There are different types of defects in steel casting produced in sand casting that can occur. A majority of these defects are caused due the evolution of gases [1]. Furthermore, these different types of porosity may present both at the micro- and macro-length scales.

Many authors have discussed the problem with gas porosity, and a lot of work have been done in the foundry industries to understand how to avoid gas porosity in the casting components [2–8]. An extensive review of the research in this area is provided by Lee et al. [9].

One of the most important parts of the casting manufacturing process is the gating system of the casting. They have an effective role in casting defects free. The gating

---

I. Dugic (✉)
Faculty of Technology, Department of Mechanical Engineering, Linnaeus University, 35195 Vaxjo, Sweden
e-mail: Izudin.dugic@lnu.se

S. Wagstaff et al. (eds.), *Materials Processing Fundamentals 2023*, The Minerals, Metals & Materials Series, https://doi.org/10.1007/978-3-031-22657-1_8

system's purpose is to provide a smooth, uniform, and complete filling of the mold with pure molten metal [10–12].

To give an increased knowledge of the gas porosity and the influence from different factors, a series of test casting at a production scale using the sand casting process were performed at the XY Foundry.

Experimental

Casting Component

In the experimental work, a typical casting component from production was selected, see Fig. 1. The length of the component is 430 mm, the width is 354 mm, and the weight is 93.80 kg. The material of the component is Cast steel, SS11-2225-24 (Steel for hardening and tempering).

Serial production in the last three months showed a 23% scrappage due to internal defects and parts not meeting standard requirements 6134K/12/E3. In series production, there are 4 models on the pattern and one feeder per detail is used, see Fig. 2. The circles in Fig. 2 show position for the feeders.

In order to investigate what types of defects occur in the casting component, a scrap casting component from the serial production was used. The casting component was sliced into small pieces to find any possible internal pores or other defects and its location, see Fig. 3. Figure 4 shows one of the pieces with defects.

Fig. 1 The casting component

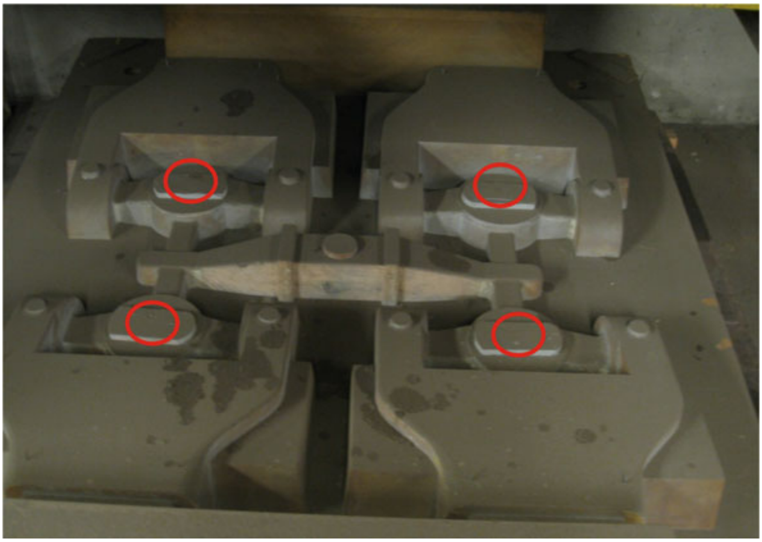

Fig. 2 The geometry of the pattern plate

Fig. 3 The sliced casting component

Casting Simulation

The whole casting process was simulated with the commercial software MagmaSoft®, in order to investigate the solidification characteristics as well as

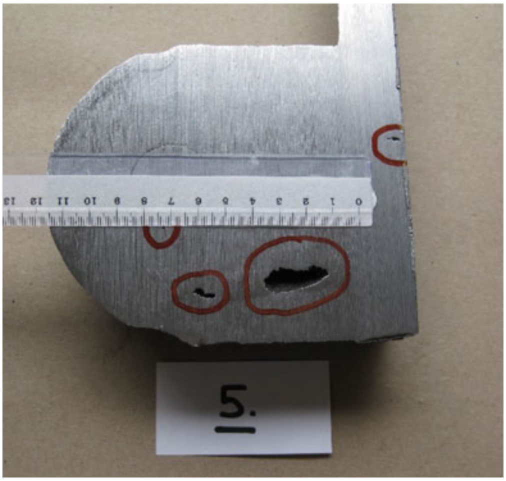

Fig. 4 The pieces with the defects

porosity formation in the casting studied. For this, a special module for cast steel was used. Figures 5 and 6 show some of the 3-D results from the simulation.

As a result, from the simulation, the gating system was changed by putting three extra feeders per detail, see Fig. 7. The circles in Fig. 7 show position for the extra feeders.

Figure 8 shows the geometry of the one of the four models with the feeders. The number 1 in Fig. 8 is the feeder that had used before changing the gating system. Numbers 2, 3, and 4 in Fig. 8 show the extra added feeders.

Fig. 5 3-D results from the simulation

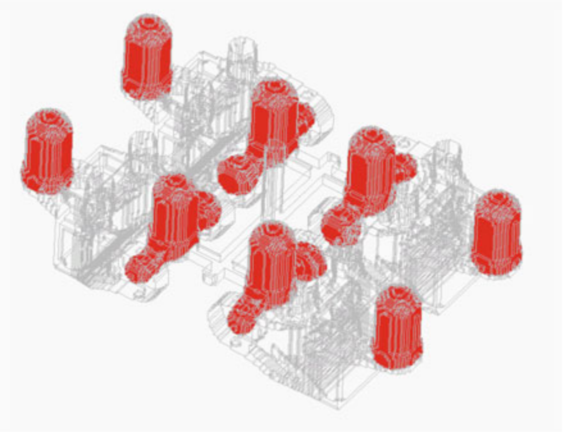

Fig. 6 3-D results from the simulation

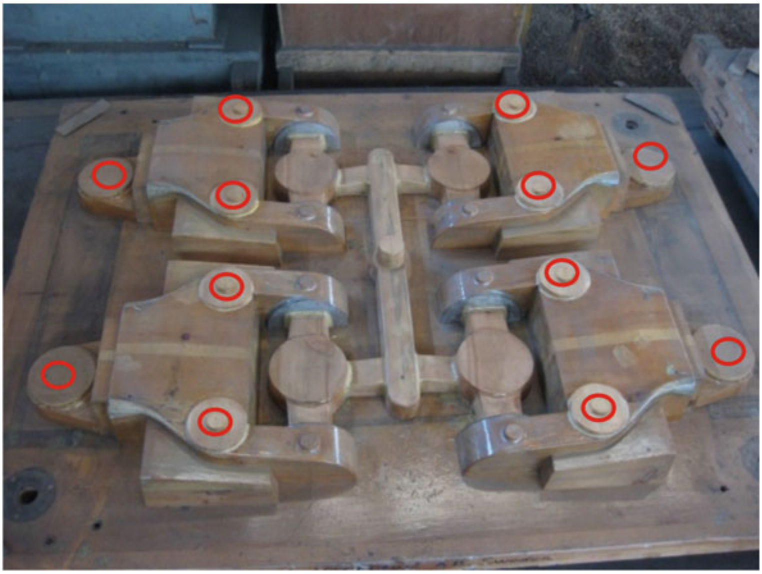

Fig. 7 The geometry of the pattern plate after changing

Alloys and Other Materials

Melting was done in a high frequency furnace. After melting, the melt is transported in a 1 ton pouring ladle to a production line. The light emission spectrometer—ARL 3460 was used to determine the chemical composition from cast coin specimens.

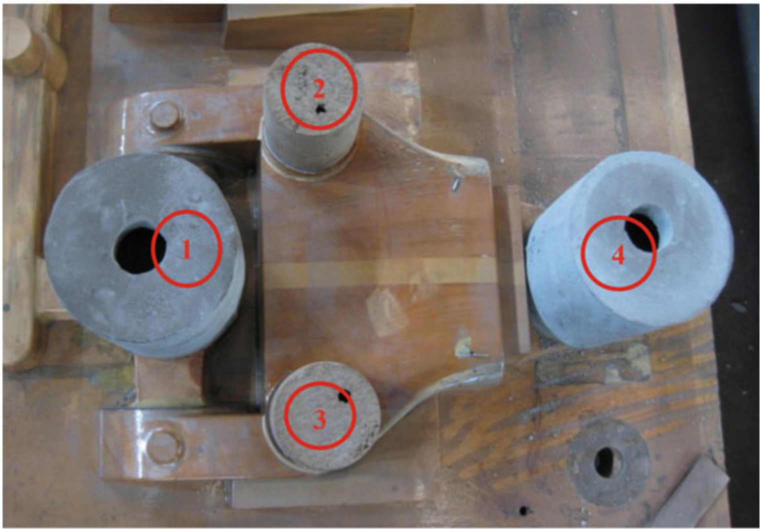

Fig. 8 The geometry of one of the four models with the feeders

The coins were cast immediately before the melt was poured into the molds. The chemical composition for the experiments is shown in Table 1.

Table 2 shows the pouring temperature and pouring time for the experiments.

The castings were made in furan sand molds. The cores are also made in furan sand. For the experiments, 4 flasks were molded and casted. This yields a total of

Table 1 The chemical composition of the melt

Molds	Element in wt %							
	C	Si	S	P	Mn	Cr	Ni	Mo
I	0.250	0.430	0.018	0.023	0.780	1.070	0.030	0.210
II	0.245	0.430	0.019	0.023	0.775	1.070	0.030	0.208
III	0.247	0.425	0.018	0.022	0.785	1.068	0.030	0.210
IV	0.248	0.435	0.019	0.023	0.780	1.070	0.029	0.212
Req. min	0.220	0.300	–	–	0.500	0.090	–	0.150
Req. max	0.290	0.600	0.035	0.035	0.800	1.200	0.300	0.250

Table 2 The pouring temperature and pouring time of the experiments

Molds	Pouring temperature, °C	Pouring time, sec
I	1620	23
II	1618	24
III	1622	23
IV	1620	25

Fig. 9 One of the lower casting mold with the cores

16 castings, thereby providing a statistical basis for the evaluation of the effect of changing gating systems on gas porosity. Figure 9 show one of the lower castings mold with the cores.

Results and Discussion

Castings Inspection

After sand blasting, all casting components were investigated by an ocular inspection. Only one casting (or 6.25%) was defected with castings defect, and it was sand erosion, see Fig. 10. This detail is scrapped because it could not be used but this detail is used for future mechanical measurements.

After ocular inspection, all castings are investigated by radiographic examination according to ASTM E446. Some of the radiographic measurements are shown in Appendix 1.

Measurements of Mechanical Properties

Four samples for tensile test and measurements of hardness were taken from the scrapped detail, see Fig. 11. The rectangles with the number in Fig. 11 show position for samples for the mechanical measurements. The test has been performed according to the SS-EN 10 002-1. The results are shown in Table 3.

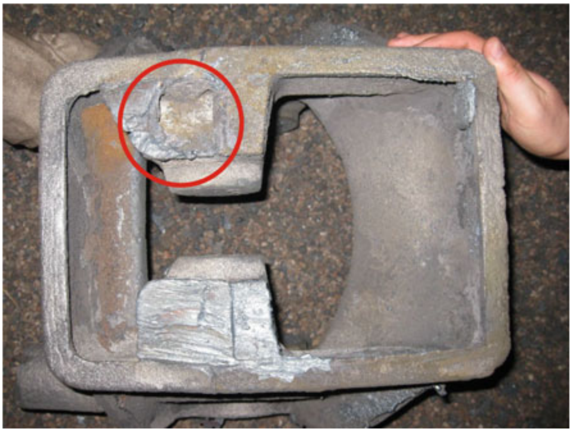

Fig. 10 The casting component with the defect

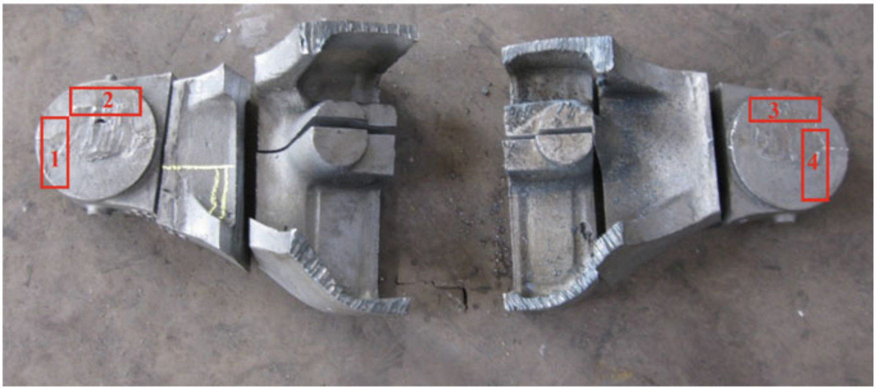

Fig. 11 The casting component used for the measurements of mechanical properties

Table 3 Results from mechanical measurements

Samples	Hardness (HB)	$R_{p0,2}$ (MPa)	R_m (Mpa)	A_5 (%)	Z (%)
1	265	762	875	16	52
2	261	743	869	14	50
3	267	755	872	13	51
4	265	760	870	14	50
Req. min	240	590	780	10	25
Req. max	290		930		

Hardness (HB) = Brinell hardness
$R_{p0,2}$ (MPa) = Proof stress
R_m (MPa) = Tensile strength
A (%) = Elongation after fracture
Z (%) = Reduction of area after fracture

Conclusions

After all the castings were inspected by an ocular inspection and investigated by radiographic examination, it can be concluded that the changing of the gating systems plays an important role in the formation of casting defects.

Of the 16 casting components, there was only one detail, or 6.25% that had casting defect and it was due to sand erosion. The same detail is used for the measurements of mechanical properties.

The measurements of the mechanical properties show that the casting meets the requirements according to the standard for the material.

The casting component simulation was performed to understand the problems in the casting. The feeder's location and the number have found out the results from the simulation. The simulation software increases the quality and applicability of the casting product.

Acknowledgements The author would like to thank Linnaeus University, Faculty of Technology, Department of Mechanical Engineering, Vaxjo, Sweden.

Appendix

See Fig. 12 and Tables 4 and 5.

Table 4 X-ray inspection report

Consign unit	MMV AB			Inspect unit		BF-ray department			
Part name	XXX	Part number	XXXX	Material		001, 122, 252	Quantity		15(Pc)
Radial type	XXQ-3205	FFD	600 mm	TS	2.2 × 2.2 mm	Image quality indicator			GB5618
Film type	AGFAC7	Film dimension	80 × 180 100 × 360	Add influence screen thickness front 0.03 mm back 0.13 mm					
Darkroom deal with	Hand work	Develop fixative temperature		20 °C		Inspect scale		100%	
Inspection standard	ASTM E446-98	Accept standard				ASTM E446 According to photo			

Table 5 Irradiation parameter and inspection results

Irradiation position number	Irradiation position thickness (mm)	Tube voltage (Kvp)	Tube current (Ma)	Irradiation time (Min)	FFD (mm)	Image quality indicator (mm)	Film density	Result (P/F)
1A	15	155	5.0	2.0	600	0.25	1.89	No find
1B	15	155	5.0	2.0	600	0.20	2.52	No find
1C	15	155	5.0	2.0	600	0.20	2.16	No find
1D	15	155	5.0	2.0	600	0.20	2.30	No find
2A	15	155	5.0	2.0	600	0.25	1.89	No find
2B	15	155	5.0	2.0	600	0.20	2.52	No find
2C	15	155	5.0	2.0	600	0.20	2.70	No find
2D	15	155	5.0	2.0	600	0.20	2.22	B1
3A	15	155	5.0	2.0	600	0.25	1.89	No find
3B	15	155	5.0	2.0	600	0.20	2.52	No find
3C	15	155	5.0	2.0	600	0.20	3.15	No find
3D	15	155	5.0	2.0	600	0.20	2.30	No find
4A	15	155	5.0	2.0	600	0.25	1.89	No find
4B	15	155	5.0	2.0	600	0.20	2.52	B1
4C	15	155	5.0	2.0	600	0.20	2.50	A1
4D	15	155	5.0	2.0	600	0.20	2.30	No find

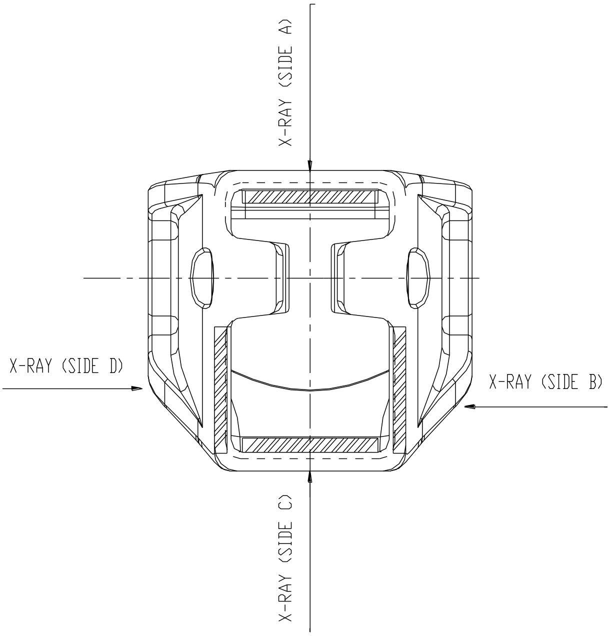

Fig. 12 Irradiation position drawing

References

1. Campbell J (2003) Castings, 2nd edn. Butterworth-Heineman, Oxford
2. Catalina AV, Leon-Torres JF, Stefanescu DM, Johnson ML (2007) Prediction of shrinkage-related defects in steel castings. In: Proceedings of the 5th decennial international conference on solidification processing, Sheffield
3. Desai J, Parikh V, Shah T (2013) Reducing porosity for alloy steel casting. Int J Eng Res Technol (IJERT) 2(11)
4. Carlson KD, Lin Z, Hardin R, Beckermann C (2002) Modeling of porosity formation and feeding flow in steel casting. In: Proceedings of the 56th SFSA technical and operating conference, Paper No. 4.4, Steel Founders' Society of America, Chicago, IL
5. Griffin JA, Bates CE (1991) Ladle treating, pouring and gating for the production of clean steel castings. In: Steel Founders' Society of America Research Report No. 104, Technical Steering Committee Report
6. Yang S-H, Lee Z-H (2006) A method for predicting nitrogen gas pores in nitrogen alloying stainless steels. Mater Sci Eng 417(1–2):307–314
7. Stefanescu DM (2005) Computer simulation of shrinkage related defects in metal castings—a review. Int J Cast Met Res 18(3):129–143. https://doi.org/10.1179/136404605225023018
8. Monroe R (2005) Porosity in castings. In: Paper 05–245(04).pdf, Page 1 of 28 AFS Transactions 2005 © American Foundry Society, Schaumburg, IL USA
9. Lee PD, Chirazi A, See D (2001) Modeling microporosity in aluminum–silicon alloys: a review. J Light Met 1(1):15–30
10. Ducic N, Cojbasic Z, Manasijevic S, Radisa R, Slavkovic R, Milicevic I (2016) Optimization of the gating system for sand casting using genetic algorithm. American Foundry Society, pp 1–11

11. Dmitriev VS, Kostyuchenko TG (2018) Design of the gating system for production of casting blanks for space device cases. Mater Sci Forum 1–7
12. Nandagopal M, Sivakumar K, Senthilkumar G, Sengottuvelan M (2017) Study of sand casting gating system. Int J Recent Eng Res Dev 2(11):1–8

Fluctuant Solidification Behavior in the Centerline of Continuous Casting Billets Based on Numerical Simulation

Dongwei Guo, Zihang Zeng, Kunhui Guo, and Zibing Hou

Abstract The fluctuant solidification behavior of the solute-enriched liquid phase in the centerline of the continuous casting billets, which is closely related to the centerline segregation defect, will significantly affect the central quality uniformity along the casting direction. Meantime, the fluctuation phenomenon of the solidification end point during the continuous casting process is still unclear. In this work, the solid fraction in the centerline of the billets was analyzed based on a three-dimensional numerical model, and the fluctuation characteristics of the centerline solid fraction were revealed. At the same time, through the analysis of the actual solidification structure, the fluctuation of the centerline local cooling rate was also investigated, which was associated to that of the solid fraction. On this basis, according to the periodic fluctuation characteristics of centerline solid fraction and local cooling rate, the periodic fluctuation mechanism of the solidification end point of continuous casting was proposed.

Keywords Continuous casting · Segregation · Fluctuation of centerline solid fraction · Fluctuation of local cooling rate · Fluctuation of solidification end point

---

D. Guo · Z. Zeng · K. Guo · Z. Hou (✉)
College of Materials Science and Engineering, Chongqing University, No. 174 Shazhengjie, Shapingba, Chongqing 400044, China
e-mail: houzibing@cqu.edu.cn

D. Guo
e-mail: guodongwei@cqu.edu.cn

Z. Zeng
e-mail: 202009131256@cqu.edu.cn

K. Guo
e-mail: guokunhui@cqu.edu.cn

Chongqing Key Laboratory of Vanadium-Titanium Metallurgy and New Materials, Chongqing University, Chongqing 400044, China

S. Wagstaff et al. (eds.), *Materials Processing Fundamentals 2023*, The Minerals, Metals & Materials Series, https://doi.org/10.1007/978-3-031-22657-1_9

Introduction

Nowadays, the steel industry is increasingly demanding the uniformity and stability of the internal quality of continuous casting billets [1, 2]. The centerline segregation defect formed by the enrichment of solute elements during the continuous casting process is a key factor affecting the central quality uniformity of billets [3]. The fluctuation of centerline segregation along the casting direction is closely related to the cooling process and solidification behavior of the solute-enriched liquid phase in the central area of the billets at the end of solidification. Although previous studies [4, 5] described the formation mechanism of centerline segregation, the continuous cooling process and solidification behavior of the solute-enriched liquid phase along the casting direction in the central area of the billets and its influence on the fluctuation of centerline segregation are still unclear.

On the other hand, the final electromagnetic stirring (F-EMS) [6] and the mechanical soft reduction (MSR) [7] are usually used during the actual continuous casting process to improve the uniformity of solute distribution in the central area of the billets and reduce the centerline segregation defect. During the application process of the F-EMS and MSR, it is required that the central solid fraction [8] and the molten pool width [9] of billets should be kept in a specific range. At this time, the fluctuation of the solidification end point of continuous casting will lead to the fluctuation of central solid fraction or molten pool width of billets, thus affecting the effect of the F-EMS and MSR on centerline segregation. However, due to the high temperature and "black box" characteristics of the continuous casting process, the fluctuation characteristic of the solidification end point of continuous casting still needs to be investigated.

Based on the above literature review, the typical medium-carbon steel continuous casting billets were selected as the research object in this work. The main chemical composition (mass %) is C 0.40, Si 0.25, Mn 0.7, Cr 0.95, Mo 0.18, and Fe balance. Firstly, the fluctuation characteristic of solid fraction in the centerline of billets was obtained through the three-dimensional numerical model of the continuous casting process. Subsequently, based on the actual solidification structure on the longitudinal section of selected billets, the fluctuation characteristic of the local cooling rate in the centerline was also analyzed. On this basis, the periodic fluctuation mechanism of the solidification end point during continuous casting was proposed combined with the periodic fluctuation of centerline solid fraction and local cooling rate. This paper can provide a theoretical reference for the cooling process and solidification behavior of molten steel in the central area of continuous casting billets and the fluctuation mechanism of the solidification end point of continuous casting.

Experiment Method

Three-Dimensional Numerical Simulation of Continuous Casting Process

In this paper, the fluctuation characteristics of solid fraction and local cooling rate in the centerline of billets were used to reflect the continuous cooling process and solidification behavior of the solute-enriched liquid phase in the centerline area. However, the fluctuation of the centerline solid fraction cannot be obtained through the actual solidification structure characteristics. Therefore, COMSOL Multiphysics 5.6 was used to model the solidification process of the selected continuous casting billets under two sets of process parameters, and the fluctuation characteristic of the centerline solid fraction along the direction was calculated. The computational domain of the modeling process is shown in Fig. 1, and the specific continuous casting process parameters are shown in Table 1.

Governing Equations

Based on the above-mentioned description and assumptions of the model, the flow and solidification process of molten steel in billets is simulated by solving the continuity equation, Navier–Stokes equation, energy equation, and other supplementary equations. The turbulent characteristic of the molten steel flow is defined by the k-ε model, where k is the turbulent kinetic energy, m^2/s^2; ε is the turbulent dissipation rate, m^2/s^3. The equations are expressed as follows:

$$\rho \nabla u = 0 \tag{1}$$

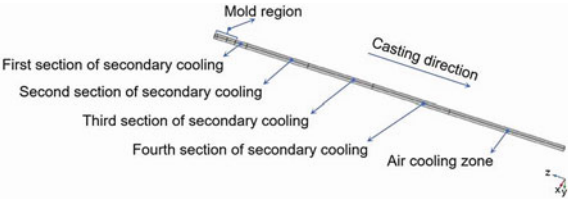

Fig. 1 Calculation domain of three-dimensional solidification model of selected continuous casting billets

Table 1 Main production parameters of selected continuous casting billets

Sample No	Superheat, °C	Casting speed, m/min	Specific water amount, L/kg
1	42	1.8	0.68
2	40	2.1	0.68

$$\rho(u \cdot \nabla)u = -\nabla p + \nabla\left[\mu_{\text{eff}}(\nabla u + (\nabla u)^t\right] + F + (\rho - \rho_{\text{ref}})g \tag{2}$$

where ρ is the density, kg/m^3; u is the vector velocity of molten steel, m/s; p is pressure, Pa; F is volume force, N/m^3; μ_{eff} is the effective viscosity of molten steel, kg/(m s); ρ_{ref} is the reference density of molten steel, kg/m^3; is the acceleration of gravity, m/s^2.

The effective viscosity of molten steel can be expressed as:

$$\mu_{\text{eff}} = \mu + \mu_t \tag{3}$$

$$\mu_{\text{t}} = \rho C_\mu \frac{k^2}{\varepsilon} \tag{4}$$

where μ is the laminar viscosity, kg/(m s); μ_{t} is the turbulent viscosity, kg/(m s); and C_μ is a constant of 0.09.

The turbulence kinetic energy, k, and the turbulent dissipation rate, ε, are given as follows:

$$\rho(u.\nabla)k = \nabla \cdot \left[\left(\mu + \frac{\mu_t}{\sigma_k}\right)\nabla k\right] + P_k - \rho\varepsilon \tag{5}$$

$$\rho(u \cdot \nabla)\varepsilon = \nabla \cdot \left[\left(\mu + \frac{\mu_t}{\sigma_\varepsilon}\right)\nabla \varepsilon\right] + C_{\varepsilon 1}\frac{\varepsilon}{k}P_k - C_{\varepsilon 2}\rho\frac{\varepsilon^2}{k} \tag{6}$$

$$P_k = \mu_{\text{t}}\left[\frac{\nabla u}{\nabla u + (\nabla u)^t}\right] \tag{7}$$

where σ_k, σ_ε, $C_{\varepsilon 1}$, and $C_{\varepsilon 2}$ are empirical constants and the values are 1.0, 1.3, 1.44, and 1.92, respectively.

The energy conservation equation can be described as follows:

$$\rho C_{\text{p}} u \cdot \nabla t + \nabla \cdot q = Q + Q_{\text{p}} + Q_{\text{vd}} \tag{8}$$

$$q = -\lambda \nabla t \tag{9}$$

where C_{p} is the heat capacity at constant pressure, J/(kg °C); λ is the thermal conductivity, W/(m °C); Q is the external heat source; Q_{p} is the heat source by pressure works; Q_{vd} is the heat source by viscous dissipation.

During the solidification process, the physical parameters of molten steel in the mushy zone, such as density, heat capacity, and thermal conductivity, are not constant but are dependent on the temperature and/or solid fraction of the mushy zone. These physical parameters can be calculated according to Eqs. (11)–(14).

$$\rho = \theta\rho_1 + (1 - \theta)\rho_2 \tag{10}$$

$$C_p = \frac{1}{\rho}[\theta\rho_1 C_{p,1} + (1-\theta)\rho_2 C_{p,2}] + L_{1\to 2}\frac{\partial \alpha_m}{\partial t} \tag{11}$$

$$\alpha_m = \frac{1}{2}\frac{(1-\theta)\rho_2 - \theta\rho_1}{\theta\rho_1 + (1-\theta)\rho_2} \tag{12}$$

$$\lambda = \theta\lambda_1 + (1-\theta)\lambda_2 \tag{13}$$

where ρ_1 and ρ_2 are the density of solid and liquid steel, and the values are 7600 kg/m^3 and 7020 kg/m^3, respectively; $C_{p,1}$ and $C_{p,2}$ are the heat capacity of solid and liquid steel, and the values are 710 J/(kg °C) and 880 J/(kg °C), respectively; λ_1 and λ_2 are the thermal conductivity of solid and liquid steel, and the values are set to be 118.8 W/(m °C) and 29.7 W/(m °C). During the calculation process, the solidus and liquidus temperatures of the selected medium-carbon steel were set to 1357 °C and 1497 °C, respectively.

Boundary and Initial Conditions

The size of the numerical model is 160 mm × 160 mm, which corresponds to the actual billets, and the length of the calculation domain is 15.9 m. The lengths, the boundary conditions, and the relevant formulas of mold, secondary cooling zone, and air cooling zone are shown in Table 2 [10–12], where q_m, q_k, and q_a are the heat flux of mold, secondary cooling zone, and air cooling zone, respectively, kW/m^2; δ_m is the holding time in the mold, s; β is a coefficient about the shape of the mold and the parameter of casting, kW/(m^2 s$^{1/2}$); h_k is the heat transfer coefficient of the secondary cooling zone, W/(m^2 °C); w is water flow rate, L/(m^2 min); η is the radiation coefficient; σ is the Stefan-Boltzmann constant; t_b, t_w, and t_a are the temperature of the billets surface, the water of secondary cooling zone, and the environment of air cooling zone, respectively, °C. The mold water flow rate is 114 m^3/h, according to the actual production condition of selected billets. At the beginning of the calculation, it is assumed that the calculation domain is filled with molten steel and the temperature is consistent with the casting temperature, which can be presented as:

$$t_\mathrm{in} = t_1 + t_\mathrm{sh} \tag{14}$$

where t_in is the casting temperature of molten steel, °C; t_1 is the liquidus temperatures of the selected medium-carbon steel, °C; t_sh is the superheat of the molten steel, °C. The straight bore type submerged entry nozzle is not considered in the established numerical model, so the velocity of molten steel flowing into the mold is equal to the casting speed, namely:

$$v_\mathrm{in} = v_c \tag{15}$$

where v_in is the velocity of molten steel flowing into the mold.

Table 2 Parameters and relevant computational formulas at different sections in calculation of three-dimensional model

Section	Length, m	Boundary condition	Computational formula
Mold	0.9	q_m	$q_m = (2.68 - \beta\sqrt{\delta_m}) \times 10^3$
First section of secondary cooling zone	0.5	$q_k = h_k(t_b - t_w)$	$h_k = 153.6(w/60)^{0.351}$
Second section of secondary cooling zone	2.7	$q_k = h_k(t_b - t_w)$	$h_k = 160 + 8.35w^{0.851}$
Third section of secondary cooling zone	2.9	$q_k = h_k(t_b - t_w)$	$h_k = 200 + 10.44w^{0.851}$
Fourth section of secondary cooling zone	3.5	$q_k = h_k(t_b - t_w)$	$h_k = 200 + 10.44w^{0.851}$
Air cooling zone	5.4	$q_a = \eta\sigma({t_b}^4 - {t_a}^4)$	$\eta = 0.8$

Acquisition of Solidification Structure in Billets

Billet samples produced by process parameters No. 1 and No. 2 were obtained during the actual continuous casting process. According to the method shown in Fig. 2a, two central longitudinal section samples of continuous casting billets under process parameters No. 1 and No. 2 were obtained, and the solidification structure on the central longitudinal section can be obtained by hot pickling experiment. During the experiment, the samples were etched with 1:1 warm hydrochloric acid–water solution for revealing the solidification structure more clearly. The temperature of the hydrochloric acid–water solution was 60–80 °C, and the pickling time was 25 min [13].

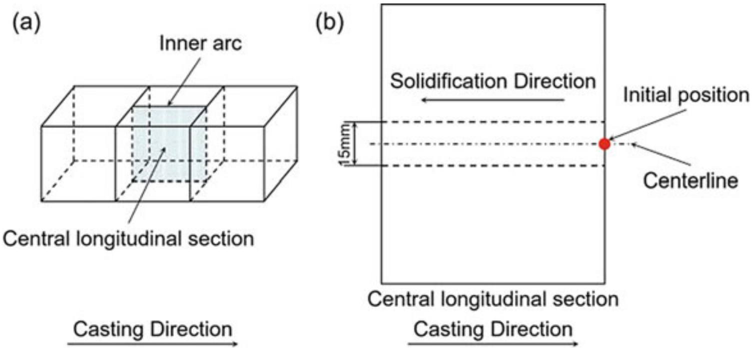

Fig. 2 Sampling method for central longitudinal section of selected continuous casting billets (**a**) and measurement position of secondary dendrite arm spacing of fine dendrites inside central segregation spot (**b**)

Results and Discussion

Fluctuation of Solid Fraction and Local Cooling Rate in the Centerline of Billets

Based on the three-dimensional numerical model presented, the solid fraction in the centerline of billets No. 1 and No. 2 can be obtained. In this work, the effect of molten steel solidification in the centerline of billets on centerline segregation defect was investigated, and the centerline segregation was formed at the end of solidification. Therefore, to reflect the solidification behavior at the end of solidification more intuitively, the change data of the centerline solid fraction of billets No. 1 and No. 2 from 90 to 100% are extracted, and the results are shown in Fig. 3. It can be seen that the centerline solid fraction gradually increases, but the increase process is fluctuating. Assuming that the actual continuous casting process is in an ideal state, that is, the position of the solidification end point and the shape of the liquid core are constant, the centerline solid fraction of billets should increase smoothly. Meantime, at the solidification end point, due to the stable centerline solid fraction, the centerline local cooling rate of the billets should also be constant under specific cooling conditions. At this time, the solute element distribution and solidification structure in the centerline will be relatively uniform. However, the fluctuation of the centerline solid fraction of the actual billets means that the cooling process and solidification behavior in the centerline are not uniform, which will aggravate the fluctuation of the centerline segregation along the casting direction.

To verify the above analysis, the centerline local cooling rate was calculated through the actual solidification structure of billets No. 1 and No. 2. Figure 4 shows

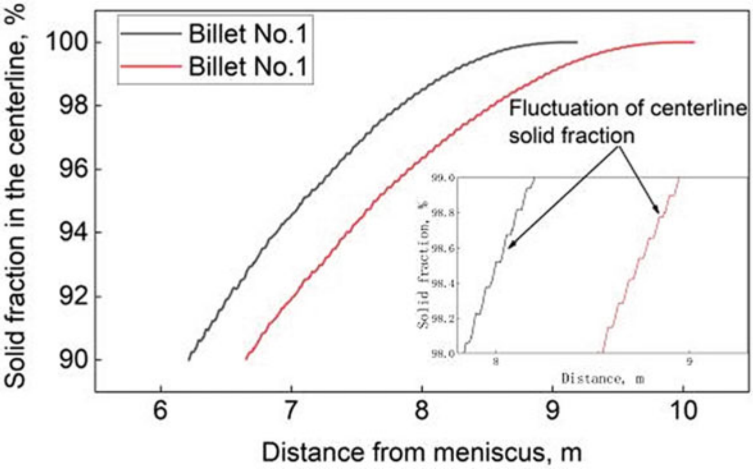

Fig. 3 Trend of solid fraction from 90 to 100% in the centerline of billets No. 1 and No. 2

the solidification structure in the central area on the longitudinal section of billets No. 1 and No. 2, and the spot segregation defect solidified by the enriched solute liquid phase between dendrites at the end of solidification [14, 15]. Due to the solidification characteristic of continuous billets from outside to inside, spot segregation in the central area can reflect the solidification behavior of molten steel in the final stage. Then, the central spot segregation defect on the longitudinal section of billets No. 1 and No. 2 was analyzed, and it was found that there were fine dendrites, different from the conventional solidification structure, in the spot segregation, as shown in Fig. 5. The secondary dendrite arm spacing (SDAS) can reflect the local cooling rate during the formation of dendrites. As the local cooling rate increases, the dendrites will be finer. Therefore, the fine dendritic structure inside the spot segregation can be used to intuitively reflect the local cooling rate at the final solidification of the central area of the billets.

According to the method shown in Fig. 1b, the SDAS of fine dendrites inside the spot segregation on the longitudinal section of billets No. 1 and No. 2 was measured. Starting from the initial position in Fig. 1b, the SDAS of the fine dendrites inside each spot segregation was measured along the solidification direction. When there

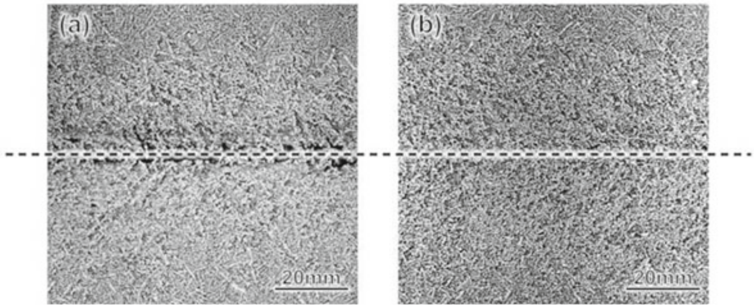

Fig. 4 Solidification structure in central area on the longitudinal section of billets No. 1 (**a**) and No. 2 (**b**)

Fig. 5 Fine dendrites inside spot segregation in central area on longitudinal section of billets No. 1 (**a**) and No. 2 (**b**)

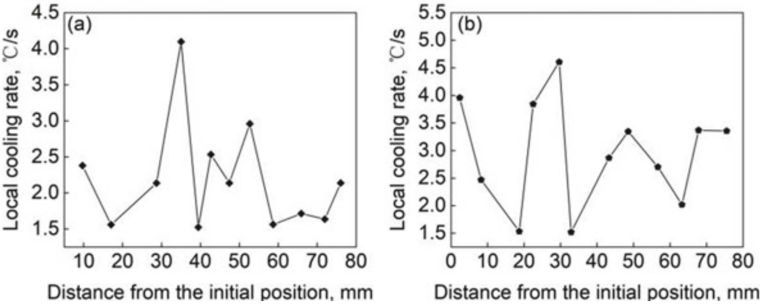

Fig. 6 Local cooling rate along the solidification direction in the centerline of billets No. 1 (**a**) and No. 2 (**b**)

were multiple fine dendrites inside the spot segregation, the measurement results were represented by the average SDAS of multiple fine dendrites. Then, the local cooling rate can be calculated by Eq. (16).

$$d_2 = \beta \cdot R^{-\alpha} \tag{16}$$

where is the SDAS of fine dendrites inside the centerline spot segregation of billets, μm; R is the local cooling rate at the fine dendrites, °C/s; α and β are coefficients. For the billet selected in this paper, α is 0.38 and β is usually 148 [16].

The calculated centerline local cooling rate along the solidification direction is shown in Fig. 6. It can be seen that during the final stage of the solidification process in billets, the local cooling rate along the solidification direction is fluctuating, which corresponds to the calculation result of the centerline solid fraction. In the actual continuous casting process, the fluctuation of the centerline solid fraction represents the volume fluctuation of the solute-enriched liquid phase, and the solidification of the solute-enriched liquid phase with different volumes will lead to the fluctuation of the centerline local cooling rate. The non-uniformity of the solidification process and cooling rate in the central area will finally lead to the fluctuation of centerline segregation and properties of the billets.

Fluctuation of Solidification End Point in Continuous Casting Process

According to the centerline solid fraction of billets No. 1 and No. 2 shown in Fig. 3, a relatively typical section is taken for analysis, and the results are shown in Fig. 7. It can be seen that the centerline solid fraction of the billets can be regarded as periodic fluctuation. In a single fluctuation period, the centerline solid fraction decreases first and then increases. Thus, the fluctuation period of the centerline solid fraction marked by the dotted line in Fig. 7 can be obtained. Since the centerline solid fraction is

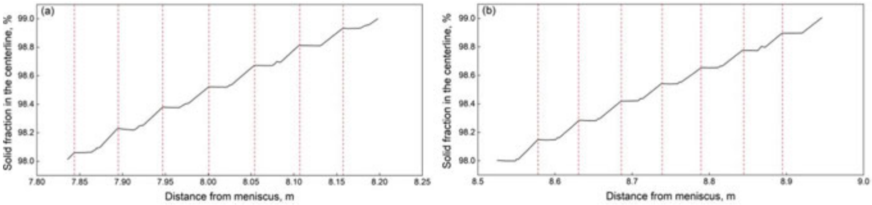

Fig. 7 Period of local solid fraction in centerline of billets No. 1 (**a**) and No. 2 (**b**)

related to the local cooling rate, the centerline local cooling rate should also fluctuate periodically.

Subsequently, the centerline local cooling rate of billets shown in Fig. 6 was analyzed, and it was found that the local cooling rate was also periodic along the solidification direction. According to the calculation results, the polynomial fittings of the different cooling rate periods along the solidification direction were carried out, and the results are shown as the blue curves in Fig. 8. It can be seen that the local cooling rate decreases first and then increases in one period along the solidification direction, where $T_{1\text{-}1}$ and $T_{1\text{-}2}$ are the periods of centerline local cooling rate of billet No. 1, $T_{2\text{-}1}$ and $T_{2\text{-}2}$ are the periods of centerline local cooling rate of billet No. 2. The common periodic fluctuation characteristic of the solid fraction and cooling rate in centerline represent that periodicity is the inherent characteristic of solidification and cooling in billets.

The centerline solid fraction and local cooling rate are the reflections of the final stage of billets solidification. When the solute-enriched liquid phase in the centerline is solidified under certain cooling rate, the solidification end point is formed. Combined with the periodic fluctuation of the solid fraction and local cooling rate in the centerline, it is speculated that the actual solidification end point of continuous casting also fluctuates periodically in a certain range. The periodic fluctuation process of centerline solid fraction, local cooling rate, and solidification end point of continuous casting billets is shown in Fig. 9. Firstly, the fluctuation characteristic of the macroscopic or microscopic flow of molten steel in the billets [17, 18] will

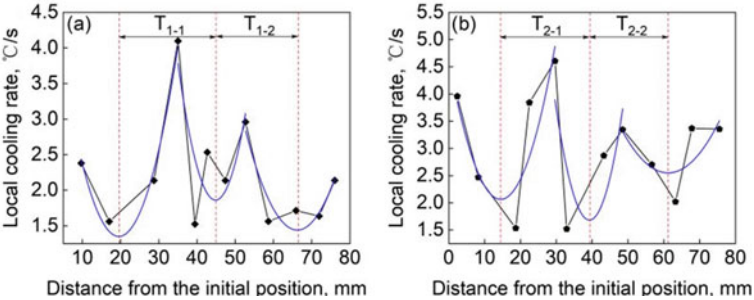

Fig. 8 Fitting period of local cooling rate in the centerline of billets No. 1 (**a**) and No. 2 (**b**)

affect the temperature distribution of molten steel in the liquid core, resulting in a periodic distribution of centerline solid fraction. With the movement of the billets, the fluctuating centerline solid fraction will complete the final solidification. For the cooling process ① in Fig. 9, the volume of the solute-enriched liquid phase increases with the decrease of the centerline solid fraction. Under certain cooling conditions, the cooling rate will decrease and the cooling time will increase. When the casting speed is constant, the increase of cooling time at the end of solidification makes the solidification end point move away from the meniscus, that is, the position marked by the dotted line e_2. As for the cooling process ②, the volume of the solute-enriched liquid phase decreases with the increase of the centerline solid fraction. Thus, the cooling rate will increase and the cooling time will decrease under certain cooling conditions, which will make the solidification end point move to the meniscus, that is, the position marked by the dotted line e_1. The cooling process ③ is roughly the same as the cooling process ①, and the solidification end point moves again to the position marked by the dotted line e_1.

In summary, the fluctuation characteristic of the centerline solid fraction in billets was found through the three-dimensional numerical model of medium-carbon steel billets. Subsequently, according to the solidification structure on the longitudinal section of selected billets, the fluctuation of the centerline local cooling rate was analyzed. During the continuous casting process, the fluctuation of the centerline solid fraction under certain cooling conditions will cause the fluctuation of the centerline local cooling rate. The common fluctuation characteristic of these two parameters reflects the uneven solidification behavior and cooling process along the casting direction at the end of solidification, which eventually leads to the uneven solidification structure and centerline segregation defect of the billets. On this basis, the fluctuation periodicity of the centerline solid fraction and local cooling rate was

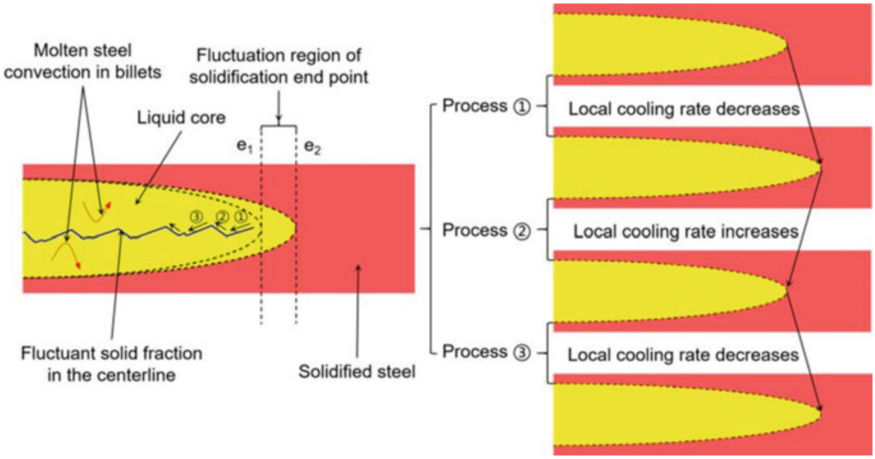

Fig. 9 Schematic diagram of periodic fluctuation process of solid fraction, local cooling rate in centerline, and solidification end point in continuous casting billets

analyzed, and the periodic fluctuation mechanism of the solidification end point of continuous casting was proposed based on this periodicity.

Conclusions

Based on the three-dimensional numerical model of medium-carbon steel billets, the fluctuation characteristic of the centerline solid fraction of billets was assessed. At the same time, the centerline local cooling rate was calculated through the actual solidification structure characteristics of billets, and the fluctuation characteristic corresponding to the solid fraction was shown. The fluctuation characteristic of the centerline solid fraction and local cooling rate results in the uneven cooling and solidification in the centerline of billets and aggravate the fluctuation of the centerline segregation along the casting direction.

The fluctuation periodicity of the centerline solid fraction and local cooling rate was analyzed. Based on this periodic characteristic, the periodic fluctuation mechanism of the solidification end point of continuous casting was proposed. This paper can provide a theoretical reference for the cooling process and solidification behavior of molten steel in the central area of continuous casting billets and the fluctuation mechanism of the solidification end point of continuous casting.

Acknowledgements The authors are very grateful for COMSOL Multiphysics 5.6 software and the support from National Natural Science Foundation of China (52274318).

References

1. Ai XG, Han D, Li SL, Zeng HB, Li HY (2020) Optimization of flow uniformity control device for six-stream continuous casting tundish. J Iron Steel Res Int 27(9):1035–1044
2. Zhou YJ, Xu K, He F, Zhang ZY (2022) Application of time series data anomaly detection based on deep learning in continuous casting process. ISIJ Int 62(4):689–698
3. Choudhary SK, Ganguly S (2007) Morphology and segregation in continuously cast high carbon steel billets. ISIJ Int 47(12):1759–1766
4. Chen HB, Long MJ, Chen DF, Liu T, Duan HM (2018) Numerical study on the characteristics of solute distribution and the formation of centerline segregation in continuous casting (CC) slab. Int J Heat Mass Transf 126:843–853
5. Jiang DB, Wang WL, Luo S, Ji C, Zhu MY (2018) Numerical simulation of slab centerline segregation with mechanical reduction during continuous casting process. Int J Heat Mass Transf 122:315–323
6. Wan Y, Li MH, Chen LJ, Wu YC, Li J, Pan HB (2019) Effect of final electromagnetic stirring parameters on central cross-sectional carbon concentration distribution of high-carbon square billet. Metals 9(6):665–681
7. Ji C, Luo S, Zhu MY (2014) Analysis and application of soft reduction amount for bloom continuous casting process. ISIJ Int 54(3):504–510

8. Zeng J, Chen WQ, Wang QX, Wang GS (2016) Improving inner quality in continuous casting rectangular billets: comparison between mechanical soft reduction and final electromagnetic stirring. Trans Indian Inst Met 69(8):1623–1632
9. Xiao C, Zhang JM, Luo YZ, Wei XD, Wu L, Wang SX (2013) Control of macrosegregation behavior by applying final electromagnetic stirring for continuously cast high carbon steel billet. J Iron Steel Res Int 20(11):13–20
10. Wang W, Hou ZB, Chang Y, Cao JH (2018) Effect of superheat on quality of central equiaxed grain zone of continuously cast bearing steel billet based on two-dimensional segregation ratio. J Iron Steel Res Int 25(1):9–18
11. Choudhary SK, Mazumdar D (1995) Mathematical modelling of fluid flow, heat-transfer and solidification phenomena in continuous-casting of steel. Res Int 66(5):199–205
12. Cai K, Yang J (1989) Investigation of heat transfer in the spray cooling in continuous casting. J Univ Sci Technol Beijing 11(6):510–515
13. Hou ZB, Guo ZA, Guo DW, Cao JH, Chang Y, Wen GH (2019) A new method for carbon content distribution based on grayscale image of casting blank macrostructure in carbon steel. J Iron Steel Res 31(7):620–627
14. Tsuchida Y, Nakada M, Sugawara I, Miyahara S, Murakami K, Tokushige S (1984) Behavior of semimacroscopic segregation in continuously cast slabs and technique for reducing the segregation. Trans Iron Steel Inst Jpn 24(11):899–906
15. Ji Y, Lan P, Geng H, He Q, Shang CJ, Zhang JQ (2018) Behavior of spot segregation in continuously cast blooms and the resulting segregated band in oil pipe steels. Steel Res Int 89(3):700331
16. ElBealy M, Thomas BG (1996) Prediction of dendrite arm spacing for low alloy steel casting processes. Metall Mater Trans B 27(4):689–693
17. Liu ZQ, Li BK, Jiang MF, Tsukihashi F (2013) Modeling of transient two-phase flow in a continuous casting mold using euler-euler large eddy simulation scheme. ISIJ Int 53(3):484–492
18. Li XL, Li BK, Liu ZQ, Niu R, Liu YQ, Zhao CL (2019) Large eddy simulation of multi-phase flow and slag entrapment in a continuous casting mold. Metals 9(1):7–20

Part III
Slag and Ladle Treatment

Toward Meso-scale Modelling of Slag Foaming Phenomena in Pyrometallurgy

Quinn G. Reynolds and Oliver F. Oxtoby

Abstract Dispersed multiphase fluid flows, in which one phase is distributed as small inclusions in another, occur in a wide range of chemical and process industries. In pyrometallurgical smelting, these may manifest in the form of decoupling of gases from one of the molten phases. This can cause slag foaming, which occurs when gas bubbles are unable to escape from the viscous slag rapidly enough and a low-density foam layer builds up at the surface of the slag pool. Although uncontrolled slag foaming can cause hazardous equipment failures, controlled foaming has the potential to significantly reduce energy consumption of many smelting processes. Improvements in the understanding of slag foaming are therefore of value both from health and safety as well as economic and environmental aspects. This paper presents the evaluation and application of the dynamic multi-marker (DMM) method, a novel meso-scale computational fluid dynamics algorithm for efficient modelling of dispersed-phase systems, for slag foaming problems. Foaming behaviour and gas–liquid decoupling are studied using numerical simulations of test systems, and the results are compared to established empirical relationships.

Keywords Slag foaming · Computational modelling · Pyrometallurgy

Introduction

The pyrometallurgical production of commodities such as iron and steel, ferroalloys, precious metals, and numerous others underpins much of modern industrialised society [1]. Pyrometallurgical smelting processes are frequently energy- and carbon-intense, and the drive to reduce direct and indirect emissions from heavy industry worldwide is placing considerable pressure on such plants to optimize their

Q. G. Reynolds (✉)
Pyrometallurgy Division, Mintek, Randburg, South Africa
e-mail: quinnr@mintek.co.za

Department of Process Engineering, University of Stellenbosch, Stellenbosch, South Africa

O. F. Oxtoby
ENGYS, London, UK

S. Wagstaff et al. (eds.), *Materials Processing Fundamentals 2023*, The Minerals, Metals & Materials Series, https://doi.org/10.1007/978-3-031-22657-1_10

existing operations while shifting toward cleaner and more efficient technologies for the future. Combined with the rapid growth in processing of complex secondary ores from recycling sources such as e-wastes and batteries, there is increasing demand for cross-cutting energy saving techniques which can be applied to pyrometallurgical furnaces of many types.

Most high-temperature reductive smelting and recycling processes operate with multiple immiscible molten phases inside the furnace vessel. Presence of a slag phase, typically a mixture of metal oxides and other refractory materials, is common. Due to the unique properties of molten slag such as high viscosity and surface tension, *slag foaming* is a phenomenon that occurs under certain conditions in many pyrometallurgical processes. As the name suggests such foams consist of many small bubbles of gas trapped together in a low-density layer, separated by thin films of liquid slag. The bubbles may originate either from external gas injection lances, or more commonly from solid carbonaceous reductants reacting with the process material to produce CO gas.

Slag foaming is frequently viewed as undesirable as it can lead to poor control of the process energy and metallurgical balances, and in extreme cases rapid uncontrolled slag foaming events may cause eruptions or explosions on the furnace vessel which are hazardous for operators working in the area. As shown in Fig. 1, controlled slag foaming does, however, have great potential for protecting the furnace walls, reducing consumption of (typically carbon-based) electrodes in electric furnaces, and improving process energy efficiency; the steel industry in particular has applied slag foaming to good effect in this regard [2].

The existing body of academic literature on slag foaming focuses predominantly on experimental tests conducted in laboratory and industrial environments, and the formulation of empirical correlations based on these data. The pioneering research of Fruehan and colleagues [3–5] dominates the field, and data from much of their work is frequently collated and re-analysed in reviews such as [6].

Empirical correlations developed for slag foaming are usually expressed in terms of dimensionless groups. Per the Buckingham π theorem any suitable set can be chosen, but in these applications it is preferred to use the Morton, Archimedes, and

Fig. 1 Arc furnace without (*l*) and with (*r*) an insulating slag foam layer, showing reduction in energy losses

Table 1 Dimensionless groups in slag foaming

N_Σ	$\frac{g\mu\Sigma}{\sigma}$
N_{Mo}	$\frac{g\mu^4}{\rho\sigma^3}$
N_{Ar}	$\frac{g\rho^2 d_{\mathrm{b}}^3}{\mu^2}$
N_{Ca}	$\frac{\mu u_{\mathrm{g}}}{\sigma}$

Capillary numbers as independent values, with the foam index number N_Σ as the dependent variable. Definitions of these numbers in terms of dimensioned parameters are given in Table 1, with g the normal acceleration due to gravity, μ the viscosity of the slag, σ the surface tension of the slag, ρ the density of the slag, d_{b} a representative diameter of the bubbles in the foam, and u_{g} a superficial gas velocity based on the volumetric gas flow rate and the surface area over which bubbles are being emitted into the slag. The foam index Σ is defined as the rate of change of the stable foam height with the superficial gas velocity and has the units of time. It should be noted that the expressions in Table 1 apply only in the simplified case of negligible minimum foaming velocity, and slag density much greater than gas density; interested readers are referred to Lotun and Pilon [6] for a more detailed treatment including these additional phenomena.

Using these quantities, researchers have developed many different empirical correlations to describe the available slag foaming data, several of which are shown below [3, 4, 6].

$$N_\Sigma = 359 N_{\mathrm{Mo}}^{0.5} \tag{1}$$

$$N_\Sigma = 900 N_{\mathrm{Mo}}^{0.4} N_{\mathrm{Ar}}^{-0.3} \tag{2}$$

$$N_\Sigma = 2617 N_{\mathrm{Mo}}^{0.067} N_{\mathrm{Ar}}^{-0.867} N_{\mathrm{Ca}}^{-0.2} \tag{3}$$

Some authors have questioned the inclusion of the bubble diameter d_{b} as an independent variable. Stadler et al. [7] conducted additional slag foaming experiments and concluded that there was no statistical justification for choosing between Eqs. (1) and (2) given the errors involved in such work. Lotun and Pilon [6] also raised doubts from a more theoretical standpoint, observing that well-established relationships of foam index to viscosity, density, and surface tension are only recovered from correlations such as Eq. (3) when the bubble diameter is assumed to be a function of the physical properties of the slag. Although bubble diameter has been retained as an independent variable in the current study, it is clear that this will require investigation in future work.

The application of numerical and computational models to dispersed-phase flows such as slag foaming is desirable as an alternative to the challenges of conducting experimental investigations at high temperatures but presents a number of challenges of its own. The primary problem is the very wide range of length scales involved; a typical industrial reactor or furnace may be tens of metres in size while the individual particles of the dispersed phase are of the order of centimetres or millimetres, and the thin films between adjacent particles may be down to micrometres or nanometres in thickness. A hierarchical approach is therefore advisable, with computational materials science models describing the properties of the film at atomistic level, meso-scale computational fluid dynamics (CFD) models describing the resolved flow patterns at the particle scale, and CFD models using simplified empirical closures to capture the bulk statistical effects of the dispersed phase at industrial scale. Many examples of industrial-scale models are already available in the literature, e.g. Sattar et al. [8], however, information required for the empirical closures needed to complete these models generally comes from limited experimental data or simplified theoretical treatments and is a significant source of error.

Computational modelling methods to address the micro- and meso-scales remain in their infancy but have the potential to serve as an extensive data source supporting the development of more robust engineering simulation tools via bottom-up numerical experimentation. With this in mind, this paper aims to evaluate the applicability of a novel algorithm for CFD modelling of dispersed multiphase flows at the meso-scale, the dynamic multiple marker (DMM) method, to the problem of slag foaming.

Model Description

The DMM method is based on the volume-of-fluids (VOF) technique for multiphase flows and makes use of dummy or marker phase fields to prevent any adjacent bubbles in a simulation from merging prematurely even when the thickness of the film of slag between them drops below the resolution limit of the mesh on which the problem is being solved. This is combined with a dynamic graph-based contact detection and phase reassignment algorithm which minimises the number of marker phases required at each time step in the simulation. In addition, a sub-grid model based on the Reynolds equation for film thickness evolution is activated when bubbles are in contact with one another and may be used to trigger film rupture and coalescence of bubbles. Detailed descriptions of the various components of the DMM algorithm may be found in [9, 10].

In the present work, the DMM solver and specialised inlet–outlet boundary conditions for the dispersed phase were implemented using the v2206 release build of the OpenFOAM® open-source computational mechanics platform [11]. Software automation tools written in Python 3.9 facilitated with pre- and post-processing of the data from the simulations [12]. Field visualisations were performed using ParaView 5.10 [13].

Results and Discussion

For the purposes of this paper, the choice was made to study the foaming problem in 2D planar geometries. Although the DMM method and OpenFOAM® software implementation extend trivially to three dimensions, the computational cost associated with such simulations is much higher. 3D studies are therefore best left to production simulations after the method has been more thoroughly tested and validated.

Based on the literature summaries of previous experimental work on slag foaming [6], a representative reference set of material property and numerical parameters was selected as shown in Table 2. These are used for all simulations presented here unless otherwise mentioned. h_{crit} indicates the thickness of the thin films between bubbles at which point rupture is assumed to occur—this has been observed to be of the order of 500 nm for silicic materials similar to metallurgical slags [14].

Readers will note that in real slag foaming problems the density of the gases involved is typically very low (< 1 kg/m^3). The elevated gas density used in this work is an approximation which greatly improves numerical stability of standard VOF multiphase flow solution algorithms in cases of high surface tension and low fluid density, by damping the effect of parasitic currents at the phase interfaces. The suitability of this choice will be examined in the following section.

Numerical Considerations

In this section, a single gas bubble was simulated as it rises from 0.05 m below the surface of a slag layer and subsequently ruptures into the bulk gas phase above. An example sequence showing the system behaviour over time is given in Fig. 2. The bubble deforms considerably as it rises, and the surface of the slag is pushed upward by the bubble before it settles. After a short period of time the slag film surrounding the bubble thins and ruptures.

Table 2 Reference parameter set for slag foaming simulations

Parameter	Value
Slag phase density, ρ	2750 kg/m^3
Slag phase viscosity, μ	0.5 Pa.s
Gas phase density, ρ_g	30 kg/m^3
Gas phase viscosity, μ_g	5×10^{-5} Pa.s
Interfacial tension, σ	0.35 N/m
Bubble diameter, d_b	0.01 m
Mesh resolution, δ_l	5×10^{-4} m
Critical film thickness, h_{crit}	5×10^{-7} m

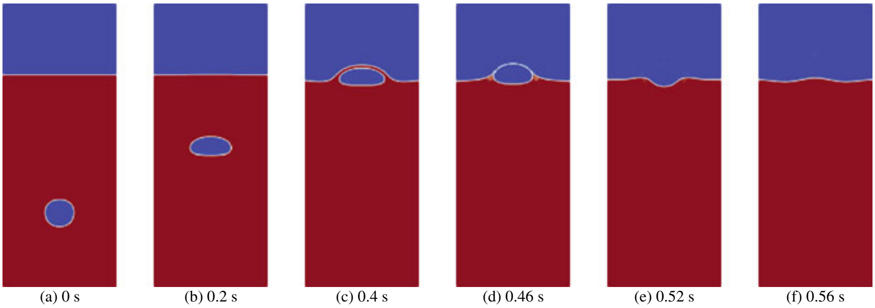
(a) 0 s (b) 0.2 s (c) 0.4 s (d) 0.46 s (e) 0.52 s (f) 0.56 s

Fig. 2 Phase fields at different times for bubble rise reference case ($\rho_g = 30$ kg/m^3, $\delta_l = 500$ um). Red is slag phase, blue is gas

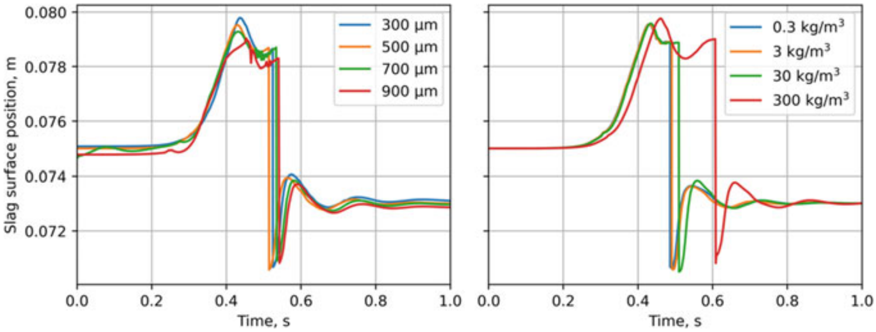

Fig. 3 Model dependence on mesh resolution (*l*) and gas phase density (*r*)

This simple test case was used to test the effect of both mesh resolution and gas density on the results. The position of the slag (or bubble) phase interface on the bubble centreline was monitored over time to give a quantitative indication of the dynamics. The results are shown in Fig. 3. Relatively low sensitivity to mesh resolution was observed, with all simulations showing similar behaviour in both the mesh-level (bubble rising and slag surface deformation) and sub-grid-level (film thinning and time to rupture) solutions. The choice of gas density was also seen to have relatively little impact on the bubble rising and rupturing behaviour provided the value was kept at 30 kg/m^3 or less.

Slag Foaming Case Study

Using the reference set of parameters in Table 2, slag foaming was simulated in a region 20 × 20 cm in size. The region was initialised with a layer of slag 0.05 m thick. The left and right boundaries of the region are cyclic and allow material to pass freely between them. The upper boundary is open to atmosphere, and the lower boundary is assumed to be a solid wall with 20 equally spaced inlets located along it. Bubbles are emitted continuously from the inlets, on which gas injection is timed to reproduce both the specified bubble diameter and superficial gas velocity. 20 s of model time was simulated, with the period of stable foam height (typically the final 12.5 s) being used for further analysis in each case. At each time step in the simulation the distribution of phase fields was sampled along vertical lines at five different positions in the region and used to measure both the upper and lower extent of the low-density foam layer. The results were then averaged to obtain an indicative foam height as a function of time.

Figures 4 and 5 show the evolution of the simulation at a superficial gas velocity of 0.02 m/s. During slag foaming new bubbles enter the base of the foam layer and travel slowly upward, occasionally merging with adjacent bubbles as they do so, before reaching the top of the layer and rupturing into the bulk gas phase. This leads to a distinct stratification of bubble sizes in the foam, with smaller bubbles at the bottom of the layer and the largest near the top surface.

The foam thickness in the simulation is shown as a function of time in Fig. 6. The general behaviour can be roughly divided into three periods. During the start-up phase, from time zero to approximately 0.5 s, the injected bubbles rise through the expanding slag layer. The growth phase, between 1.5 and 7.5 s, is characterised by the formation and increase in height of the foam layer. The stable foaming phase, from 7.5 s to the end of the simulation, shows an approach to a steady average foam

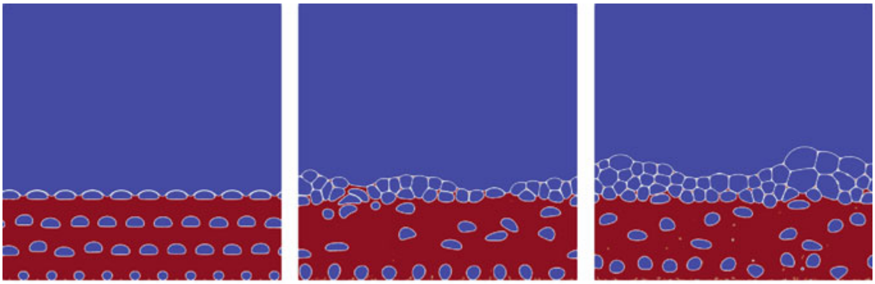

(a) 1 s (b) 2 s (c) 5 s

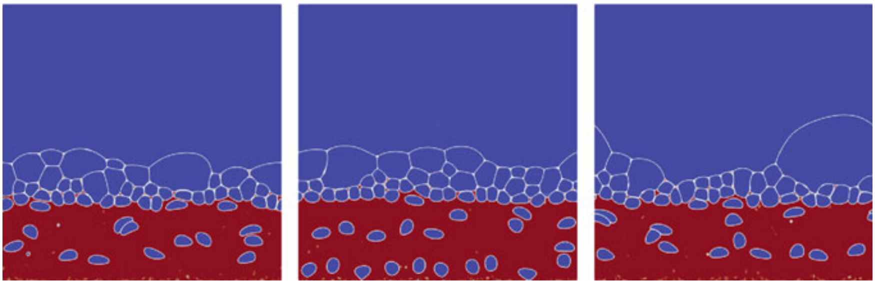

(d) 10 s (e) 15 s (f) 20 s

Fig. 4 Phase fields at different times for $u_g = 0.02$ m/s case. Red is slag phase, blue is gas

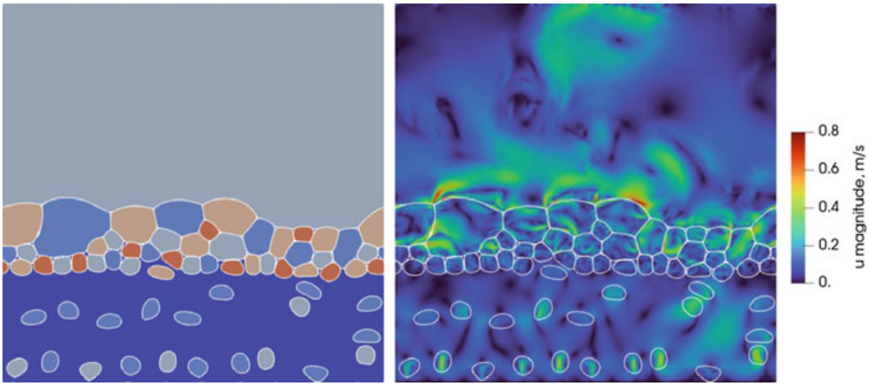

(a) Marker phases, 15 s (b) Velocities, 15 s

Fig. 5 Dispersed-phase marker phases and velocities for $u_g = 0.02$ m/s case

height as the rates of bubble addition and rupture in the layer begin to come into equilibrium.

Dividing the foam thickness during the final 12.5 s of the simulation by $u_g = 0.02$ m/s gives a crude estimate of the slag foaming index. The distribution of values so obtained has a mean of $\Sigma = 2.08$ s and a standard deviation of 0.48 s. 95% of the values therefore lie between 1.12 and 3.04 s, indicating considerable variability; longer simulation times are recommended to narrow this range in future work. The values obtained do nonetheless compare reasonably well with the predictions of correlation Eqs. (1), (2), and (3) which give 1.85 s, 1.42 s, and 1.84 s, respectively, using the reference parameters in Table 2.

A common test procedure in experimental slag foaming studies is the variation of u_g over a range. Additional simulations were therefore performed using superficial velocities of 0.01 and 0.03 m/s. The foam thickness evolution for all three simulations is shown in Fig. 7. It is immediately obvious that at low superficial velocities the

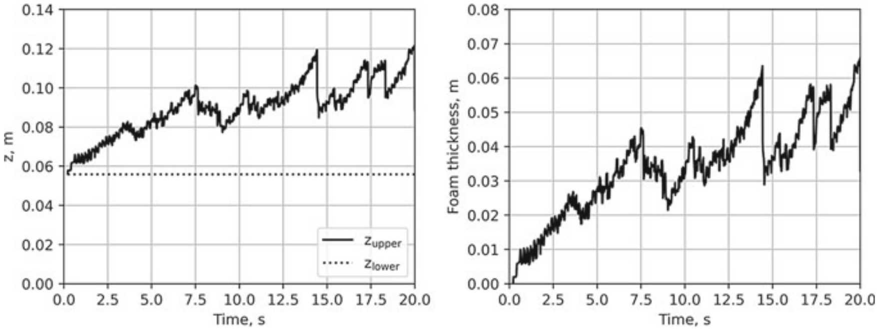

Fig. 6 Foam levels in reference case simulation for $u_g = 0.02$ m/s, (*l*) position of upper and lower boundaries of foam layer, (*r*) estimated foam thickness

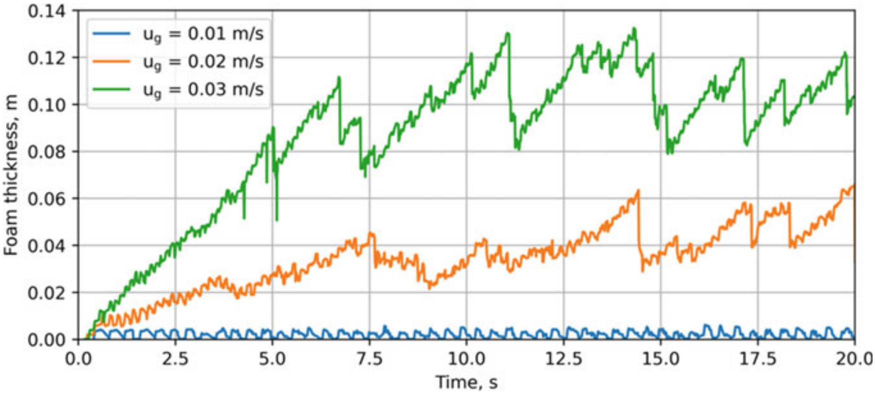

Fig. 7 Foam thickness results with increasing u_g

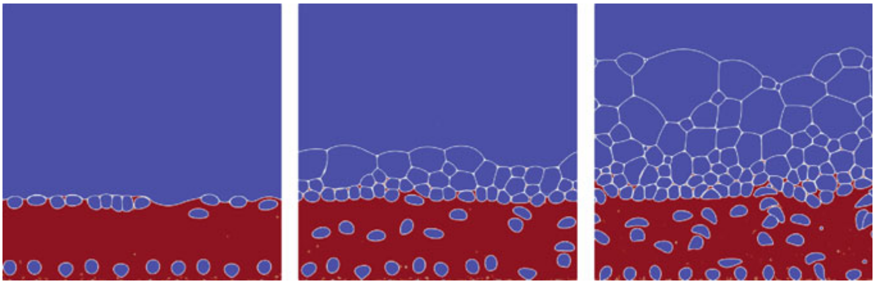
(a) 15 s, u_g = 0.01 m/s (b) 15 s, u_g = 0.02 m/s (c) 15 s, u_g = 0.03 m/s

Fig. 8 Phase fields during stable foaming for different superficial gas velocities

bubbles are not replenished at the surface of the slag faster than they burst, and no foam layer develops. This effect has been noted and discussed at length in [6] and others in terms of a minimum foaming velocity u_{g0}; in such work increasing the superficial velocity past the minimum value results in the formation of a foam layer roughly proportional to $u_g - u_{g0}$. A similar relationship is observed qualitatively in the present simulation results, although further work will be required to confirm this rigorously. Comparative visualisations of the phase fields during the stable foaming period at different superficial gas velocities are shown in Fig. 8, from which the differences in foam layer thickness are obvious.

Conclusions

Preliminary testing of the dynamic multiple marker method for applications in slag foaming studies was successfully conducted and indicates that the method shows promise for studying slag foaming problems at the meso-scale. Comparisons against empirical relationships from the literature showed reasonable agreement in the quantitative and qualitative trends, with similar foam indices obtained from the simulations and foam heights increasing at higher superficial gas velocities.

Although the model shows good mesh independence and low dependence on gas densities, more work is required to assess its sensitivity to the various numerical settings available in the DMM algorithm. In particular, a detailed investigation into the numerical performance of the sub-grid model for the evolution of the thin films between bubbles is currently underway. Additional challenges in the case of slag foaming include very high interfacial tension, a high-viscosity continuum phase, and a low-density dispersed phase, all of which exacerbate various numerical issues and instabilities in the underlying VOF algorithm on which the method is based. These will need to be addressed before numerical experimentation using this approach can be considered production-ready. Computational costs also remain a challenge with such high-resolution meso-scale models, despite the good efficiency and scalability obtained with the DMM approach. With the transition to 3D, which will be necessary to accurately capture foam topology and bubble size statistics, this will become even more significant and will need to be investigated further in future work.

In addition to the purely numerical issues, more work on revising and optimising the solver's implementation in OpenFOAM® is planned and can easily be combined with extensions to include heat transfer and other effects. Enhancement of the sub-grid film model to include additional physics related to ionic and metallic fluids will also be considered. Most importantly, a rigorous testing and validation programme is planned in which DMM simulations will be compared against cold-model experiments to more thoroughly demarcate its strengths and weaknesses.

Acknowledgements This paper is published by permission of Mintek. The authors acknowledge the Centre for High Performance Computing (CHPC), South Africa, for providing computational resources to this research project.

References

1. Pariser HH, Backeberg NR, Masson OCM, Bedder JCM (2018) Changing nickel and chromium stainless steel markets—a review. J S Afr Inst Min Metall 118(6):563–568. https://doi.org/10.17159/2411-9717/2018/v118n6a1
2. Luz AP, Tomba Martinez AG, López F, Bonadia P, Pandolfelli VC (2018) Slag foaming practice in the steelmaking process. Ceram Int 44(8):8727–8741. https://doi.org/10.1016/j.ceramint.2018.02.186
3. Jiang R, Fruehan RJ (1991) Slag foaming in bath smelting. MTB 22(4):481–489. https://doi.org/10.1007/BF02654286
4. Zhang Y, Fruehan RJ (1995) Effect of the bubble size and chemical reactions on slag foaming. MMTB 26(4):803–812. https://doi.org/10.1007/BF02651727
5. Matsuura H, Fruehan RJ (2009) Slag foaming in an electric arc furnace. ISIJ Int 49(10):1530–1535. https://doi.org/10.2355/isijinternational.49.1530

6. Lotun D, Pilon L (2005) Physical modeling of slag foaming for various operating conditions and slag compositions. ISIJ Int 45(6):835–840. https://doi.org/10.2355/isijinternational.45.835
7. Stadler SAC, Eksteen JJ, Aldrich C (2007) An experimental investigation of foaming in acidic, high FexO slags. Miner Eng 20(12):1121–1128. https://doi.org/10.1016/j.mineng.2007.01.013
8. Sattar MA, Naser J, Brooks G (2013) Numerical simulation of slag foaming in high temperature molten metal with population balance modeling. Procedia Eng 56:421–428. https://doi.org/10.1016/j.proeng.2013.03.142
9. Musehane NM, Oxtoby OF, Reddy BD (2018) Multi-scale simulation of droplet–droplet interaction and coalescence. J Comp Phys 373:924–939. https://doi.org/10.1016/j.jcp.2018.07.027
10. Reynolds QG, Oxtoby OF, Erwee MW, Bezuidenhout PJA (2021) An extension of the multiple marker algorithm for study of phase separation problems at the mesoscale. MATEC Web Conf 347:00025. https://doi.org/10.1051/matecconf/202134700025
11. ESI (2022) OpenFOAM v2206. https://www.openfoam.com/news/main-news/openfoam-v2206. Accessed 09 Dec 2022
12. Python Software Foundation, “Python,” (2022). https://www.python.org/. Accessed 09 Dec 2022
13. Kitware, “ParaView,” (2022). https://www.paraview.org/. Accessed 09 Dec 2022
14. Castro JM, Burgisser A, Schipper CI, Mancini S (2012) Mechanisms of bubble coalescence in silicic magmas. Bull Volcanol 74(10):2339–2352. https://doi.org/10.1007/s00445-012-0666-1

Simulation on the Slag Desulfurization During the LF Refining in a Gas-Blowing Ladle

Jujin Wang, Yuexin Zhang, Binyu Lyu, and Lifeng Zhang

Abstract A three-dimensional numerical model coupled the fluid-flow simulation and the reaction kinetics was established to study the evolution of the sulfur content in the molten steel. The VOF, k-ε, and DPM models were employed to simulate the fluid flow of three phases in the ladle furnace, including the steel, the slag, and the air. Reactions between the steel and the slag were considered in the simulation using a series of user defined functions. The steel-slag reactions had a significant effect on the sulfur content in the molten steel, resulting the continuous decrease of the sulfur content. The [S] content reduced from 0.077 wt% into 0.01 wt% in 50 min. The distribution of [S] in the molten steel was uneven, with the lowest near the steel-slag interface and the highest in the middle zone between the argon blowing point and the ladle wall.

Keywords Desulfurization · VOF-DPM · Gas-stirred ladle · Numerical model

Introduction

Sulfur is one of the detrimental impurities in the steel, which decreases dramatically the impact resistance [1] and weldability [2] of the steel products. The removal of the sulfur in the molten steel is usually produced in the KR process. For the steelmaking without the KR process, the ladle metallurgy plays an important role in the sulfur removal. During the secondary refining, the desulfurization reaction occurs between the steel and the slag, as expressed in Eq. (1). At the steel-slag interface, the sulfur reallocates according to the thermodynamic equilibrium [3, 4].

$$(\mathrm{CaO}) + [\mathrm{S}] = (\mathrm{CaS}) + [\mathrm{O}] \tag{1}$$

J. Wang · L. Zhang (✉)
School of Mechanical and Materials Engineering, North China University of Technology, Beijing 100144, China
e-mail: zhanglifeng@ncut.edu.cn

Y. Zhang · B. Lyu
School of Metallurgical and Ecological Engineering, University of Science and Technology Beijing (USTB), Beijing 100083, China

S. Wagstaff et al. (eds.), *Materials Processing Fundamentals 2023*, The Minerals, Metals & Materials Series, https://doi.org/10.1007/978-3-031-22657-1_11

The desulfurization mechanism of the synthetic slag is complex and affected by several factors including the composition and weight of the slag [5–7], the injected gas flow rate [8], the temperature [9], and the dissolved element in the steel. Sulfur capacity was often used to evaluate the desulfurization efficiency of the slag in thermodynamics. For convenience, the sulfur partition ratio, which expresses the ratio of sulfur in the slag to sulfur in the metal at the interface, was employed by mostly researchers to calculate the desulfurization thermodynamic instead of calculating the equilibrium directly [10].

The desulfurization efficiency is also determined by the flow field of the steel and slag, as the fluid flow at the steel-slag interface has a big effect on the mass transfer kinetic of the sulfur. In recent years, many researchers have employed computational fluid dynamics (CFD) to provide the flow field for the mass transfer. Wang et al. [10] established a transient three-dimensional coupled model and analyzed the desulfurization behavior during the VE-ESR process. Antonio et al. [11] coupled the fluid dynamics, thermal, and kinetic behaviors to study the steel desulfurization process in a gas-stirred ladle furnace. Jonsson et al. [12] used an axisymmetric-two-dimensional CFD model with a thermodynamic solver to analyze the desulfurization during the refining process. Andersson et al. developed a similar two-dimensional model as the Jonsson did for evaluating the desulfurization and reoxidation of the slag. Margareta et al. [13] proposed a two-dimensional fluid-flow model covering three phases (steel, slag, and gas), coupling the thermodynamic equation to study the desulfurization. Lou et al. [14–16] proposed a CFD-SRM coupled model to predict desulfurization efficiency in an 80 tons ladle.

However, though the numerical simulation has been widely studied, most of kinetic models simplified the solution for the interface equilibrium, such as using a constant distribution ratio at the interface instead of solving equilibrium equations [10, 14–16]. Therefore, in the current study, an accurate and real-time method for the kinetic process was proposed, where the equilibrium at the interface was solved by coupling the mass transfer and the thermodynamic based on the coupled reactions model [17–19]. The ion and molecular coexistence theory (IMCT) was employed to calculate the activity of CaO and CaS in the slag, and the associate model was used to calculate the activity of [Ca], [O], and [S] in the steel.

Model Description and Numerical Scheme

Model Schematic

Figure 1 shows the schematic of the current established model. The model consisted of two parts. One was the solver of the flow of the steel-slag-air three phases, which was solved using the Fluent 22.0. And another was the species transport, including the [Ca], [O], [S] in the steel phase, and the (CaO), (CaS) in the slag phase. The momentum source and the turbulent source were considered using user defined

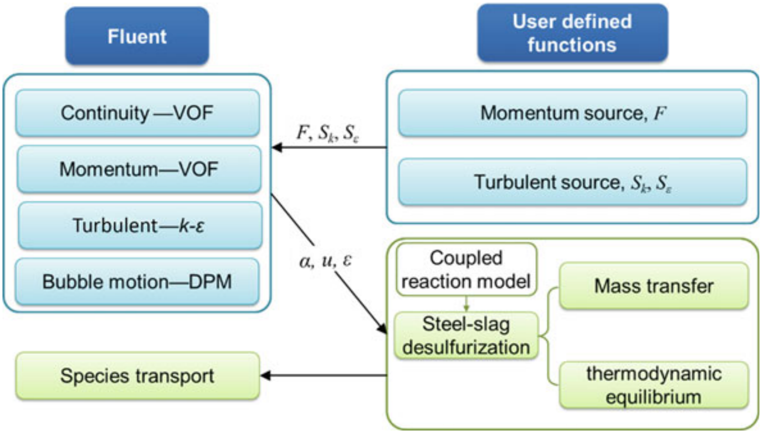

Fig. 1 Model schematic for the fluid flow and the desulfurization

functions (UDFs). Besides, the desulfurization at the steel-slag interface was realized using the coupled reaction model, which was also attached to the Fluent using UDFs.

Three-Dimensional Multiphase Fluid Flow

A coupled discrete particle model (DPM) and volume of fluid (VOF) model was applied to simulate the motion of injected argon bubbles and the fluid flow during the ladle furnace (LF) process. Besides, the turbulent flow was solved using the k-ε two-equation model. The detailed description and validation of these models could be find elsewhere [20–24], which would not be discussed here.

Continuity equation (VOF model):

$$\frac{\partial \alpha_q \rho_q}{\partial t} + \nabla \cdot \left(\alpha_q \rho_q \vec{u}_q\right) = 0 \tag{2}$$

Momentum conservation equation (VOF model):

$$\begin{aligned}\frac{\partial}{\partial t}(\rho_{\mathrm{M}}\vec{u}_{\mathrm{M}}) + \nabla \cdot (\rho_{\mathrm{M}}\vec{u}_{M}\vec{u}_{\mathrm{M}}) &= -\nabla p \\ &+ \nabla \cdot \left[\mu_{\mathrm{M}}\left(\nabla\vec{u}_{\mathrm{M}} + \nabla\vec{u}_{\mathrm{M}}^{T}\right)\right] + \rho_{\mathrm{M}}\vec{g} + \vec{F}\end{aligned} \tag{3}$$

Turbulence equations (k-ε two-equation model):

$$\frac{\partial \rho_{\mathrm{M}} k}{\partial t} + \nabla \cdot (\rho_{\mathrm{M}}\vec{u}_{\mathrm{M}} k) = \nabla \cdot \left[\left(\mu_{\mathrm{M}} + \frac{\mu_{t,\mathrm{M}}}{\sigma_k}\right)\nabla k\right] + G_k - \rho_{\mathrm{M}}\varepsilon + S_k \tag{4}$$

$$\frac{\partial \rho_{\mathrm{M}}\varepsilon}{\partial t} + \nabla \cdot (\rho_{\mathrm{M}}\vec{u}_{\mathrm{M}}\varepsilon) = \nabla \cdot \left[\left(\mu_{\mathrm{M}} + \frac{\mu_{t,\mathrm{M}}}{\sigma_{\varepsilon}}\right)\nabla\varepsilon\right] + \frac{\varepsilon}{k}(C_{1\varepsilon}G_k - C_{2\varepsilon}\rho_{\mathrm{M}}\varepsilon) + S_{\varepsilon} \quad (5)$$

The motion of argon bubbles (DPM):

$$\frac{\mathrm{d}\vec{u}_B}{\mathrm{d}t} = \vec{F}_D + \vec{F}_G + \vec{F}_B + \vec{F}_{\mathrm{VM}} + \vec{F}_P + \vec{F}_L \quad (6)$$

Species Transport for Components in the Steel and Slag

The concentration field of components in the steel and slag was simulated by solving the transport equation, as shown in Eqs. (7)–(8), where [Ca], [O], and [S] were considered to only transport in the steel phase and (CaO) and (CaS) only transport in the slag phase. Source terms in Eqs. (7)–(8) were indicated the composition change due to the desulfurization.

$$\frac{\partial}{\partial t}\left(\rho_{\mathrm{st}}c_{[i]}\right) + \nabla \cdot \left(\rho_{\mathrm{st}}\vec{u}c_{[i]}\right) = \nabla \cdot \left(\frac{\mu_{\mathrm{eff}}}{\mathrm{Sc_t}}\nabla c_{[i]}\right) + S_{c_{[i]}} \quad (7)$$

$$\frac{\partial}{\partial t}\left(\rho_{\mathrm{st}}c_{(i)}\right) + \nabla \cdot \left(\rho_{\mathrm{st}}\vec{u}c_{(i)}\right) = \nabla \cdot \left(\frac{\mu_{\mathrm{eff}}}{\mathrm{Sc_t}}\nabla c_{(i)}\right) + S_{c_{(i)}} \quad (8)$$

Kinetic Model for the Desulfurization at the Steel-Slag Interface

A kinetic model based on the coupled reaction model was established to calculate the desulfurization at the steel-slag interface. In practice, Fluent called the kinetic model using UDFs in cells with volume fraction of the steel phase larger than 0.1 and that of the slag phase larger than 0.1. The detail of the kinetic could be find in Refs. [17–19]. The variation of the sulfur in the steel and components in the slag were calculated using Eqs. (9)–(10). Source terms in Eqs. (7)–(8) were equal to the value of Eqs. (9)–(10) multiplied by the density of the steel and slag, respectively, which was carried out using UDFs.

$$\frac{\mathrm{d}[\%\mathrm{M}]}{\mathrm{d}t} = -\frac{A_{\mathrm{interface}} \cdot k_{\mathrm{M}}}{V_{\mathrm{steel}}}\left([\%\ \mathrm{M}]^{\mathrm{b}} - [\%\mathrm{M}]^{*}\right) \quad (9)$$

$$\frac{d(\%MO_n)}{dt} = -\frac{A_{\text{interface}} \cdot k_{MO_n}}{V_{\text{slag}}}\left[(\%MO_n)^{\text{b}} - (\%MO_n)^{*}\right] \tag{10}$$

where [%M] and $(\%MO_n)$ represent the content of components in the steel and slag, respectively, wt%; A is the area of the reaction interface, m^2; V is the volume of the phase, m^3; k is the mass transfer coefficient, m/s; the superscript "b" and "*" represent the bulk and equilibrium of the phase.

The IMCT was used to calculate the activity of the slag phase, while the associate model coupled with the UIPF model was employed to calculate the activity of the steel phase. The initial composition of the slag was 61.64%CaO-19.39%Al_2O_3-2.43%SiO_2-8.42%MgO-2.16%CaS-5.96%CaF_2, and that of the steel was 0.108%C-0.013%Si-0.764%Mn-0.077%S-0.003%O-0.028%Al-0.0004%Ca-Fe.

Simulation Results

Three-Dimensional Flow Field

The three-dimensional flow field of the steel-slag-air was solved employing the Fluent 22.0 on a working station equipped with two Intel Xeon Gold 6226R CPUs and 96 GB RAM. Figure 2 shows the stable flow field in a 230 tons ladle with bottom-blowing argon of 1200 NL/min. There were two circulating flows in the molten steel. A relatively obvious circulating flow was formed on the side far from the argon blowing point. Another was a less obvious circulating flow which was formed in the middle region between the argon blowing point and the ladle wall.

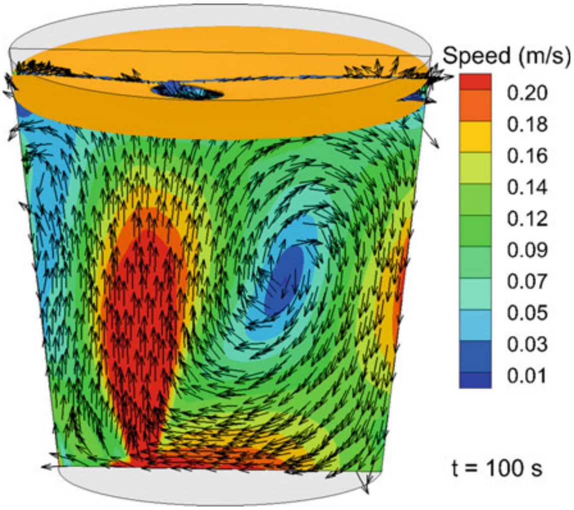

Fig. 2 Distribution of the velocity vector on the longitudinal section passing the argon blowing point of the molten steel in the ladle

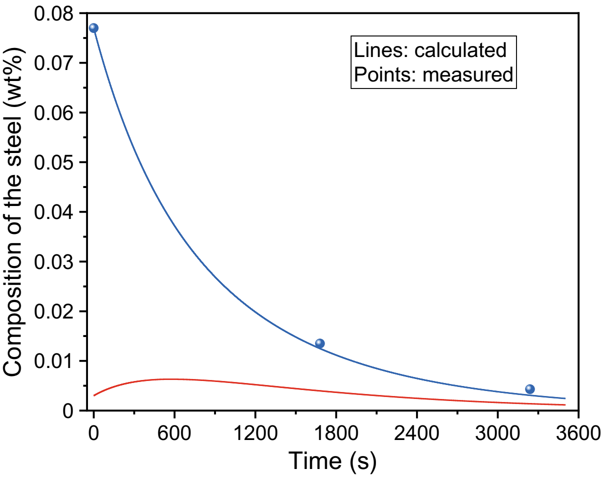

Fig. 3 Evaluation of the average content of [S] and [O] in the molten steel

Variation of the Sulfur Content in the Steel

Figure 3 shows the calculated variation of the average content of the dissolved [S] and [O] in the molten steel in several hundred seconds. The [S] content has a continued decrease during the refining process. At the beginning of the refining, the [S] content was about 0.077 wt%. Through the desulfurization reaction between the steel and the slag, the [S] content reduced to about 0.01% in 5 min. At the same time, the dissolved [O] had a little bit increase followed by a decrease. As the followed two reactions were considered in the current model, a positive direction of Eq. (11) and a negative direction of Eq. (12) could be figured out in the first 600 s.

$$[\mathrm{Ca}] + [\mathrm{S}] = (\mathrm{CaS}) \tag{11}$$

$$[\mathrm{Ca}] + [\mathrm{O}] = (\mathrm{CaO}) \tag{12}$$

Three-Dimensional Distribution of the Sulfur

Due to the desulfurization reaction occurred exclusively at the steel-slag interface, the [S] content near the steel-slag interface must be the lowest, as shown in Fig. 4. What's more, the steel and the slag kept flowing during the refining, so the [S] transferred from the interior to the interface. Therefore, the distribution of the [S] content showed an uneven state. In the zone in the middle between the argon blowing point and the ladle wall, the [S] content was the highest. This was owing to the low speed flow in this zone. The distribution tendency of the [S] was the same at different refining periods. The difference lied on that the overall [S] content kept decreasing when the refining was going on.

Conclusion and Summary

In the current study, a numerical model coupled with a kinetic model was proposed to evaluate the desulfurization of the slag during the refining process. The VOF model, k-ε model, and DPM model were employed to solve the three-dimensional flow of the steel-slag-air system. The thermodynamic equilibrium and the mass transfer at the steel-slag interface was coupled to solve the kinetic process. The following conclusion was obtained.

1. Two circulating flows in the molten steel were formed under the influence of argon blowing. A relatively obvious circulating flow was formed on the side far from the argon blowing point. Another was a less obvious circulating flow which was formed in the middle between the argon blowing point and the ladle wall.
2. On the condition of high initial [S] content, the slag with high content of CaO had an apparent desulfurization ability. The [S] content reduced from 0.077 wt% into 0.01 wt% in fifty minutes.
3. The distribution of the [S] content in the molten steel showed an uneven state with the lowest near the steel-slag interface and the highest in the middle zone between the argon blowing point and the ladle wall. The distribution tendency of the [S] was the same at different refining periods. The difference lied on that the overall [S] content kept decreasing when the refining was going on.

Fig. 4 Three-dimensional distribution of the sulfur in the molten steel at different times

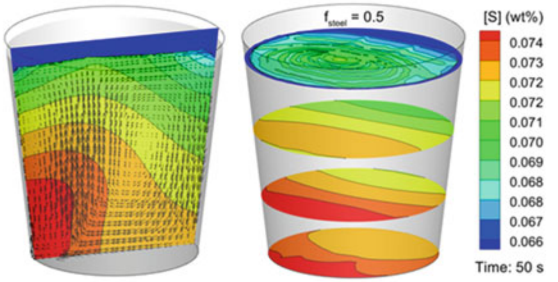

(a) 50 s

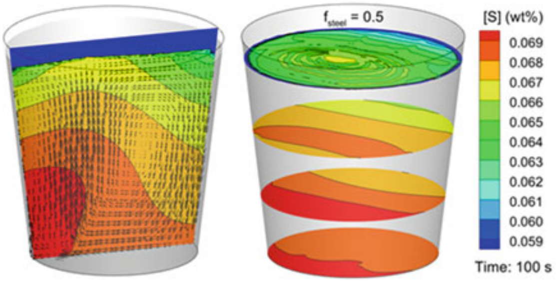

(b) 100 s

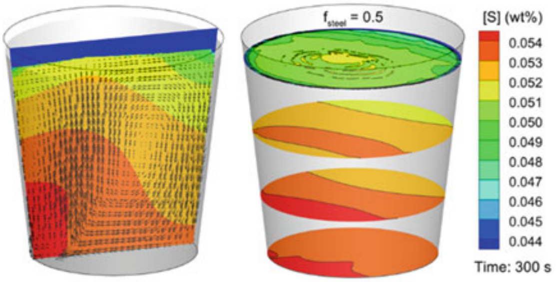

(c) 300 s

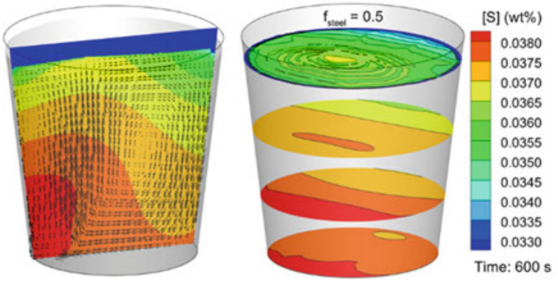

(d) 600 s

Acknowledgements The authors are grateful for support from the National Natural Science Foundation of China (Grant No. U1860206, No. 51725402, 51874031, 51874032), the S&T Program of Hebei (Grant No.20311004D), the High Steel Center (HSC) at North China University of Technology and the High Quality Steel Consortium (HQSC) at University of Science and Technology Beijing, China.

References

1. Maciejewski J (2015) The effects of sulfide inclusions on mechanical properties and failures of steel components. J Fail Anal Prev 15(2):169–178
2. Weider C, Pichard C (1991) Effects of sulphur and inclusion morphology in friction welding of structural steels. Weld Int 5(5):369–377
3. Shi C, Huang Y, Zhang J, Li J, Zheng X (2021) Review on desulfurization in electroslag remelting. Int J Miner Metall Mater 28(1):18–29
4. Visuri VV, Vuolio T, Haas T, Fabritius T (2020) A review of modeling hot metal desulfurization. Steel Res Int 91(4):1900454
5. Kang JG, Shin JH, Chung Y, Park JH (2017) Effect of slag chemistry on the desulfurization kinetics in secondary refining processes. Metall Mater Trans B 48(4):2123–2135
6. Takahashi K, Utagawa K, Shibata H, Kitamura S, Kikuchi N, Kishimoto Y (2012) Influence of solid CaO and liquid slag on hot metal desulfurization. ISIJ Int 52(1):10–17
7. Yang AF, Karasev A, Jönsson PG (2015) Characterization of metal droplets in slag after desulfurization of hot metal. ISIJ Int 55(3):570–577
8. Cao Q, Pitts A, Nastac L (2018) Numerical modelling of fluid flow and desulphurisation kinetics in an argon-stirred ladle furnace. Ironmaking Steelmaking 45(3):280–287
9. Fan W, Zhang J, Ao W, Huang J (2015) Effect of Al_2O_3 and CaF_2 on melting temperature of high calcium ladle desulfurization slag. Adv Mater Res 1094:325–328
10. Wang F, Tan J, Huang X, Wang Q, Liu Z, Baleta J, Li B (2022) Mathematical and numerical predictions of desulfurization behavior in the electromagnetically controlled vibrating-electrode electroslag remelting furnace. Metall Mater Trans B 53(3):1792–1805
11. Uriostegui Hernandez A, Garnica Gonzalez P, Ramos Banderas JA, Solorio Diaz G, Hernandez Bocanegra CA (2022) Desulphurization kinetic prediction into a steel ladle by coupling thermodynamic correlations, fluidynamics and heat transfer. ISIJ Int 62(6):1189–1198
12. Jonsson L, Sichen D, Jönsson P (1998) A new approach to model sulphur refining in a gas-stirred Ladle—a coupled CFD and thermodynamic model. ISIJ Int 38(3):260–267
13. Andersson AMT, Jonsson LTI, Josson PG (2003) A model of reoxidation from the top slag and the effect on sulphur refining during vacuum degassing. Scand J Metall 32(3):123–136
14. Lou W, Wang X, Liu Z, Luo S, Zhu M (2018) Numerical simulation of desulfurization behavior in ladle with bottom powder injection. ISIJ Int 58(11):2042–2051
15. Lou W, Zhu M (2015) Numerical simulation of slag-metal reactions and desulfurization efficiency in gas-stirred ladles with different thermodynamics and kinetics. ISIJ Int 55(5):961–969
16. Lou W, Zhu M (2014) numerical simulation of desulfurization behavior in gas-stirred systems based on computation fluid dynamics—simultaneous reaction model (CFDSRM) coupled model. Metall Mater Trans B 45(5):1706–1722
17. Zhang Y, Ren Y, Zhang L (2017) Modeling transient evolution of inclusion in Si-Mn-killed steels during the ladle mixing process. Metall Res Technol 114(3):308
18. Zhang Y, Ren Y, Zhang L (2018) Kinetic study on compositional variations of inclusions, steel and slag during refining process. Metall Res Technol 115(4):1–7
19. Wang J, Zhang L, Cheng G, Ren Q, Ren Y (2021) Dynamic mass variation and multiphase interaction among steel, slag, lining refractory and nonmetallic inclusions: laboratory experiments and mathematical prediction. Int J Miner Metall Mater 28(8):1298–1308

20. Luo Y, Liu C, Ren Y, Zhang L (2018) Modeling on the fluid flow and mixing phenomena in a RH steel degasser with oval down-leg snorkel. Steel Res Int 89(12):1800048
21. Liu C, Li S, Zhang L (2018) Simulation of gas-liquid two-phase flow and mixing phenomena during RH refining process. Acta Metall Sin 54(2):347–356
22. Duan H (2016) Simulation on multiphase flow and mixing phenomena during ladle metallurgy process. In: The eighth China-Korea joint symposium on advanced steel technology, Chongqing, China, pp 55–62
23. Duan H, Ren Y, Zhang L (2019) Fluid flow, thermal stratification, and inclusion motion during holding period in steel ladles. Metall Mater Trans B 50(3):1476–1489
24. Duan H, Zhang L, Thomas B, Conejo A (2018) Fluid flow, dissolution, and mixing phenomena in argon-stirred steel ladles. Metall Mater Trans B 49(5):2722–2743

A Modified Thermodynamic Software to Control the Composition of Inclusions During Calcium Treatment Process

Weijian Wang and Lifeng Zhang

Abstract Based on the minimum Gibbs free energy method, a modified thermodynamic model was established to predict the composition of inclusions during the calcium treatment process. Three types of phase were contained in the steel-inclusion system, including the molten steel phase, the liquid inclusions phase, and the solid inclusions phase. The Wanger model was applied to calculated activities of elements in the molten steel. Reported interaction parameters were evaluated and used to improve the accuracy of thermodynamic calculation results. The coexistence theory was applied to calculate activities of Al_2O_3 and CaO in liquid inclusions. According to the thermodynamic calculations, the effect of T.Ca content in the molten steel on the transformation of inclusions was discussed. Combining the established thermodynamic model and a calcium yield prediction model, a software for precise control of calcium treatment process was also developed.

Keywords Calcium treatment · Software · Calcium yield · Thermodynamic model

Introduction

Aluminum is widely used in steelmaking process due to its strong deoxidation ability. However, a large amount of Al_2O_3 inclusions were generated after the addition of aluminum in the molten steel, leading to nozzle clogging, and some product defects [1–6]. Calcium treatment technology was applied to modify solid Al_2O_3 inclusions into liquid calcium aluminates [7–10]. The optimal calcium addition to the molten steel was relative to the composition and temperature of the steel. Solid inclusions were hardly modified to liquid state if the calcium content was too low, while solid CaO and CaS were generated with the excessive calcium addition, which can also cause nozzle clogging easily [9, 11–13]. Moreover, it was difficult to control the yield of calcium stably due to its low solubility in the molten steel and low boiling

---

W. Wang · L. Zhang (✉)
School of Mechanical and Materials Engineering, North China University of Technology, Beijing 100144, China
e-mail: zhanglifeng@ncut.edu.cn

S. Wagstaff et al. (eds.), *Materials Processing Fundamentals 2023*, The Minerals, Metals & Materials Series, https://doi.org/10.1007/978-3-031-22657-1_12

temperature. Therefore, it was an important issue to realize the precise control of calcium treatment.

In the current study, a thermodynamic model was established to predict the composition of inclusions based on the minimum Gibbs free energy method during calcium treatment process. Next, a calcium yield prediction model was established through the neural network technology. Finally, a software was developed to achieve the online control of precise calcium treatment with the objective of precisely controlling of the inclusions composition. Combined with the calcium yield model, the precise length of the calcium wire required in the liquid steel could be reported online.

Prediction of Calcium Yield

The calcium yield, in other words, the efficiency of calcium recovery was calculated through Eq. (1). It was difficult to control the calcium yield precisely during calcium treatment process. The factors having influence on calcium yield during the calcium treatment process were numerous and complex including temperature, steel composition and steel grade, and so on. The solubility of calcium in the molten steel was affected by the temperature. The time for the calcium wire melting completely in the molten steel was shorten with the increase of temperature so that the position where the calcium wire completely melted became shallower at the same wire feeding speed, which had an adverse effect on the improvement of calcium yield. After entering the molten steel, calcium reacted with the dissolved oxygen to generate CaO, meaning that the high dissolved oxygen content in the molten steel was beneficial to the increase of calcium yield. The effect of the temperature and dissolved oxygen content in the molten steel on calcium yield is shown in Figs. 1 and 2.

$$\text{Calcium yield} = \frac{\%\ \text{Ca}_{\text{Final}} - \%\ \text{Ca}_{\text{Initial}}}{\%\ \text{Ca}_{\text{Addition}}} \tag{1}$$

Fig. 1 Relationship between the temperature and calcium yield [15]

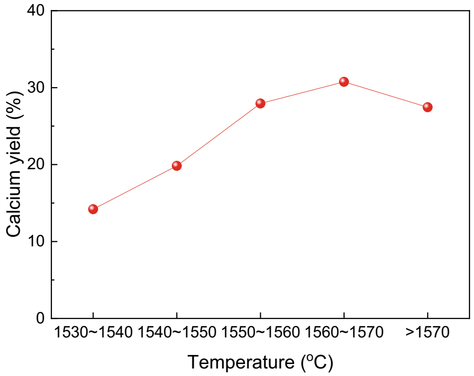

Fig. 2 Relationship between the dissolved oxygen content and calcium yield [16]

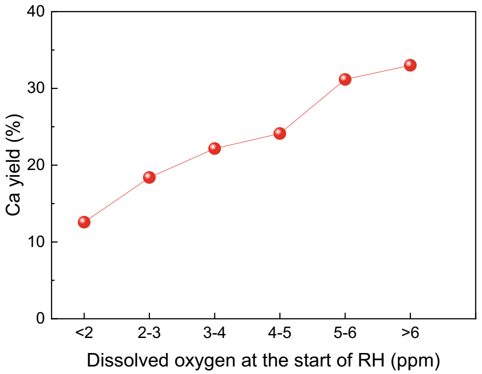

where $\%Ca_{Final}$ means the T.Ca content after calcium addition, %; $\%Ca_{Initial}$ means the initial T.Ca content before calcium addition, %; $\%Ca_{Addition}$ means the amount of calcium addition during calcium treatment process, %.

A calcium yield prediction model [14] that had been introduced elsewhere was established based on the neural network technology to predict and improve the calcium yield during steel refining process so that the required feeding length of the calcium wire could be calculated precisely and timely once the steel composition and temperature were determined. Three steps were contained for the calcium yield prediction by neural network technology. Firstly, the initial data was collected, analyzed, and preprocessed and the appropriate parameters were selected to construct the neural network model. Then, the constructed neural network was trained until the accurate calculation results were obtained. Finally, the trained neural network model could be applied to predict the calcium yield during the calcium treatment process. The comparison between predicted calcium yields using neural network model and the detected yields in industrial trials shows a good agreement with each other, as shown in Fig. 3. The composition, temperature of the molten steel, the amount of slag addition, and some operation parameters that had a great effect on the calcium yield were included in the dataset. There are totally 511 sets of data collected from a steel plant, while 461 sets of data were selected as teaching data to train the model. The input layer, middle layer, and output layer were included in the neural network model. The unit number of input layer was 22, and the unit number of output layer was 1. The maximum training epoch of the training process was set as 1500, and the learning rate was 0.2. The unit number in each middle layer was determined by an empirical formula which was set as 6 in the current model.

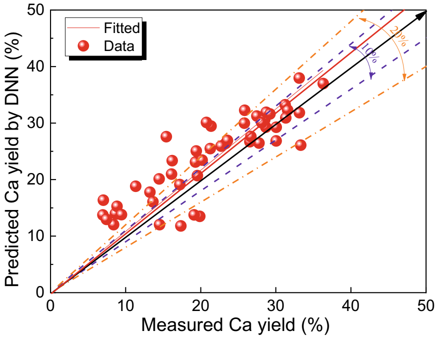

Fig. 3 Comparison between predicted calcium yields using neural network model and the detected yields in industrial trials [14]

Development of the Software for the Online Control of Precise Calcium Treatment

For thermodynamic equilibrium calculation of multicomponent and multiphase systems, two methods were contained, one was the minimizing Gibbs free energy method and the other was the classical thermodynamic calculations based on chemical reaction equilibrium between different elements in the molten steel. In the current thermodynamic model, the minimizing Gibbs free energy method was adopted to calculate the thermodynamic equilibrium in the steel-inclusions system. Three types of phase were contained in the steel-inclusion system, including the molten steel phase, the liquid inclusions phase, and the solid inclusions phase. The Wanger model was applied to calculated activities of elements in the molten steel [17, 18]. Reported interaction parameters were evaluated and used to improve the accuracy of thermodynamic calculation results. The coexistence theory was applied to calculate activities of Al_2O_3 and CaO in liquid inclusions. The calculated effects of T.Ca content on the composition of inclusions in the molten steel is shown in Fig. 4. Inclusions could be controlled in liquid state when the T.Ca content is 12–18 ppm.

Combined the established thermodynamic model and calcium yield prediction model, the software for the online control of precise calcium treatment was developed.

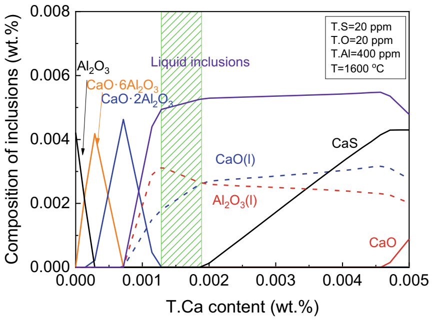

Fig. 4 Effect of T.Ca content on the composition of inclusions

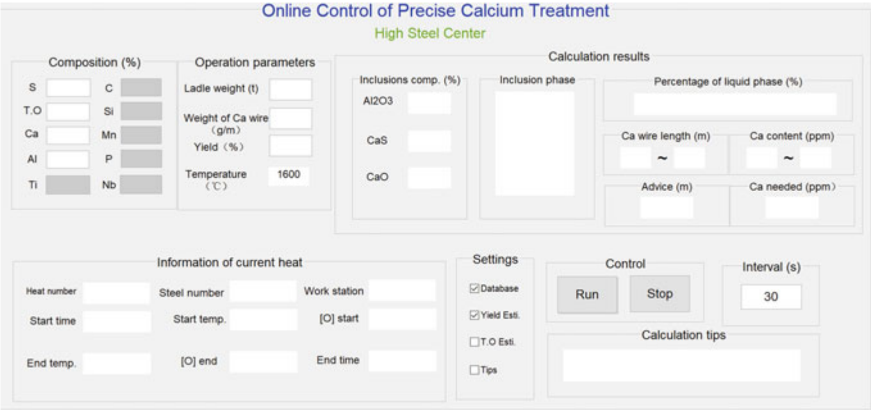

Temperature (℃) 1600

☑ Database
☑ Yield Esti.
☐ T.O Esti.
☐ Tips

Interval (s) 30

Fig. 5 Operation interface of the software

The operation interface of which is shown in Fig. 5. After connecting the industrial database, the information on the composition and temperature of the molten can be acquired so that the appropriate T.Ca content could be calculated through the established thermodynamic model. Then, the calcium yield could be predicted based on the reported deep neural network model according to the information of steel composition, temperature, and other operation parameters during calcium treatment process. Then, the optimal additional length of the calcium wire can be calculated based on the prediction of calcium yield on the basis of Eq. (2).

$$L = \frac{W \times (n[\mathrm{Ca}]_{\mathrm{T}} - n[\mathrm{Ca}]_{\mathrm{O}})}{\eta \times \beta \times \mu} \tag{2}$$

where L is the appropriate addition length of calcium wire, m; W is the mass of molten steel, t; $n[\mathrm{Ca}]_{\mathrm{T}}$ is the target calcium content in the molten steel calculated by the established model, ppm; $n[\mathrm{Ca}]_{\mathrm{O}}$ is the initial calcium content before calcium treatment process, ppm; η is the calcium yield calculated by the prediction model, %; β is the calcium content of calcium wire, %; μ is the mass of calcium wire per meter, g/m.

Conclusions

A calcium yield prediction model was established based on the neural network technology. After the composition, temperature of the molten steel and other operation parameters was read, the calcium yield can be predicted to guide the industrial calcium treatment process. Based on the minimizing Gibbs free energy method, a thermodynamic model was established to predict the composition of inclusions after calcium addition during the refining process. Combing the calcium yield prediction model, a software for the online control of precise calcium treatment was developed, in which the optimal calcium wire feeding length can be reported so that the precisely and timely guidance of calcium treatment operation can be realized.

Acknowledgements The authors are grateful for support from the National Science Foundation China (Grant No. 52004025 and No. 51704018, No. 51725402), Fundamental Research Funds for the Central Universities (Grant No.FRF-TP-17-001C2 and FRF-TP-19-037A2Z), the High Steel Center (HSC) at North China University of Technology, Yanshan University and University of Science and Technology Beijing, China.

References

1. Choudhary SK, Ghosh A (2008) Thermodynamic evaluation of formation of oxide—sulfide duplex inclusions in steel. ISIJ Int 48(11):1552–1559
2. Zhang L, Thomas BG, Associate R (2002) Alumina inclusion behavior during steel deoxidation. In: 7th European electric steelmaking conference, Venice, Italy, pp 77–86
3. Zhang L, Thomas BG (2006) State of the art in the control of inclusions during steel ingot casting. Metall and Mater Trans B 37(5):733–761
4. Wang QY, Bathias C, Kawagoishi N, Chen Q (2002) Effect of inclusion on subsurface crack initiation and gigacycle fatigue strength. Int J Fatigue 24(12):1269–1274
5. Larsson M, Melander A, Nordgren A (1993) Effect of inclusions on fatigue behaviour of hardened spring steel. Mater Sci Technol 9(3):235–245
6. Lamut J, Falkus J, Jurjevec B, Knap M (2012) Influence of inclusions modification on nozzle clogging. Arch Metall Mater 57(1):319–324
7. Ren Q, Yang W, Cheng L, Hu Z, Zhang L (2020) Effect of calcium treatment on magnetic properties of non-oriented electrical steels. J Magnetism and Magnetic Mater 494
8. Li M, Liu Y, Zhang L (2019) Effect of reoxidation on inclusions in steel during calcium treatment. Metallurgical Res Technol 116(2):206–214
9. Zhang L, Liu Y, Zhang Y, Yang W, Chen W (2018) Transient evolution of nonmetallic inclusions during calcium treatment of molten steel. Metall and Mater Trans B 49(4):1841–1859
10. Liu Y, Zhang L (2018) Relationship between dissolved calcium and total calcium in Al-killed steels after calcium treatment. Metall and Mater Trans B 49(4):1624–1631
11. Yang W, Zhang L, Wang X, Ren Y, Liu X, Shan Q (2013) Characteristics of inclusions in low carbon al-killed steel during ladle furnace refining and calcium treatment. ISIJ Int 53(8):1401–1410
12. Zhang L (2019) Non-metallic inclusions in steels: fundamentals (in Chinese). Metallurgical Industry Press, Beijing
13. Zhang L (2019) Non-metallic inclusions in steels: industrial practice (in Chinese). Metallurgical Industry Press, Beijing
14. Wang W, Zhang L, Ren Y, Luo Y, Sun X, Yang W (2021) Prediction of calcium yield during calcium treatment process performed in steelmaking using neural network. Metall and Mater Trans B 53(1):1–7
15. Wang W, Luo Y, Sun X, Zhang L (2019) Study on effect of calcium treatment on inclusions evolution mechanism and Ca yield. In: Ladle refining 2019 annual meeting proceedings. Suzhou, China, pp 416−420
16. Sun X, Wang W, Luo Y, Zhang J, Ren Y, Zhang L (2019) Evolution of inclusions in high-sulfur and low-oxygen steels after calcium treatment. In: AISTech 2019-proceedings of the iron and steel technology conference Pittsburgh, Pa., USA, pp 1233–1247

17. Suito H, Inoue R (1996) Thermodynamics on control of inclusions composition in ultra-clean steels. ISIJ Int 36(3):528–536
18. Wan Y, Chen W, Zhang S (2014) Thermodynamic analysis and experimental research of 50W600 non-oriented silicon steel after calcium treatment. Shanghai Metals 36(1):37–41

Part IV
New Processes and Insights

Reductant Formation Enthalpy in DC Ferrochrome Smelting: Merely Academic or Fundamental to Operation?

H. J. Oterdoom, M. A. Reuter, and J. H. Zietsman

Abstract The start-up and operation of DC furnaces for ferrochrome and titania slag but also ferronickel and ferrocobalt have proven again and again to be more challenging than anticipated. A combination of few furnaces in operation, a limitation on shared operational experience, quick response times between operational decisions and consequences, and a limited fundamental understanding of process mechanisms is a part of the causes for the results. Understanding the process chemistry, energy balance, and interactions between them is fundamental to investigating the mechanisms taking place in a DC furnace. As part of a PhD investigation of process mechanisms and behaviour of DC ferrochrome furnaces, this paper will describe the potential operational consequences of ignoring something as basic as the formation enthalpy of reductants. Only one of many pitfalls, reductant is used as an example to demonstrate that fundamental understanding of process chemistry is required for designing, operating, and studying DC furnaces. Only with at least an understanding of process chemistry it can be possible to connect operational experiences to process mechanisms. The paper will conclude with a brief discussion of the presented results, and how these relate to the PhD study.

Keywords DC furnace · Operation · Feed-to-power · Ferrochrome · Dynamic simulation · Digital twin · Reductant

---

H. J. Oterdoom (✉)
University of Pretoria, Dusseldorf, Germany
e-mail: u18195530@tuks.co.za

M. A. Reuter
SMS Group, Dusseldorf, Germany
e-mail: markusandreas.reuter@sms-group.com

J. H. Zietsman
University of Pretoria, Pretoria, South Africa
e-mail: johan.zietsman@up.ac.za

Ex Mente Technologies, Pretoria, South Africa

S. Wagstaff et al. (eds.), *Materials Processing Fundamentals 2023*, The Minerals, Metals & Materials Series, https://doi.org/10.1007/978-3-031-22657-1_13

Introduction

In multiple projects, the start-up and operation of DC furnaces has been problematic. There is no clear singular cause for the experienced delays in reaching design capacity. The main issues -in hindsight- appear again and again to be unrealistic expectations, underestimation of challenges, and a lack of preparation. Merrow and McNulty are only two of many that have written about project failure [1, 2]. There are at least the following two topics that reoccur in analyses of project disappointments:

- Equipment design: the equipment initially installed was not fit for the task.
- Raw materials to be processed: something unexpected happened in the processing or handling.

Both are closely related. Only when the process is fully understood, then the optimal design can be developed, but only when the equipment has been installed, then the process can be observed and optimized. Especially new processes in larger-than-known equipment have proven to be a risky business.

On a global level, the climate change is pushing the metallurgical industry into looking at ways to reduce greenhouse gas emissions. Power to these furnaces can be green, but reductants will be needed, also in a green future. Replacing reductants from fossil origin by alternative reductants can contribute to greener metal production. A better fundamental understanding of the behaviour of reductants in production and their role in the energy balance is important to support a transition towards alternative reductants.

Two papers had a significant impact on this paper: one by Barcza et al. [3] and the other by Theron [4]. These papers and personal industrial experiences, as well as an interest in digital twinning, environment, risk reduction, process fundamentals and mechanisms, and the availability of increased computer capabilities led to this investigation.

Physics and Furnaces

The bigger furnaces get, the more physics affect the operation. This is not only true for the mechanical aspects like refractory expansion, but also in heat and mass transfer mechanisms. Thermodynamics remain the same, but distances and volumes change, and that means time and temperature (differences) become increasingly important, as these affect kinetics and therefore the operation.

Small-scale testwork may therefore be more misleading than thought, especially when such work is done to tick off boxes for management instead of having actual targets relevant to the large-scale operation. Risks can remain high if an intermediate step between small-scale and large-scale industrial furnace is ignored, and an upscaling factor of 10 should be seen as a maximum [5, 6].

Because physics becomes more important, it is up to the metallurgists to better connect thermochemistry and physics and investigate what happens over time and space. Single black-box calculations will probably not be capable to describe those phenomena that are relevant for an optimal mechanical design.

Feed materials will not all follow the same pathway through the reactor until the products leave the furnace via gas duct or tapholes. It is therefore that a dynamic multizone model is being developed to be able to investigate heat and mass transfer as well as process pathways and kinetics in a DC furnace. As a test for a basic version of this model, it was decided to investigate the possible effect of (ignoring) the reductant formation enthalpy (RFE) in the production of ferrochrome (FeCr) in an open bath DC furnace.

DC Furnace and Ferrochrome Production

An open bath furnace, like a DC furnace for FeCr, relies heavily on a strictly maintained balance between power input, feedrate, feed composition, reactions, and heat losses. A change in any of these factors will require other factors to be adjusted. Reactions can be considered constant if both feed composition and the furnace power input are constant. Changes in heat losses are relatively slow for most furnaces and considered constant in this investigation.

Ferrochrome is made by reducing chromite ore with a reductant. The required amount of reductant is calculated to achieve a certain recovery of chrome, and fluxes are added to achieve a targeted slag composition. The mass and energy balances are calculated, and then a furnace is designed including the compensation for heat losses.

The premixed feed is charged continuously into the open bath and smelted to form alloy, slag, and process gas. The balance between power input and feedrate, known as feed-to-power ratio (FtP), is in modern furnaces carefully controlled by using an automated loss-in-weight system. Alloy and slag are tapped intermittently. An incorrect FtP will lead to overheating of the bath, unwanted side reactions, or freezing of the bath. The FtP usually has to be adjusted if there is a change in composition, temperature or behaviour of raw materials. This can be caused by a change in, for example,

- used raw material,
- preheating,
- prereduction,
- particle size distribution,
- weather,
- supplier, or
- source of raw material.

Feed Materials for Ferrochrome

Ore and reductant are the main raw materials of interest for mass and energy balances. In published calculations, and probably in many industrial situations too, compounds are used instead of minerals for ores, fluxes, and reductants. For example, in ferrochrome calculations, the ore is commonly described by a combination of Cr_2O_3, MgO, SiO_2, Al_2O_3, CaO and, when lucky, both FeO and Fe_2O_3 as main components [7–9]. Mineralogical compositions like $FeCr_2O_4$, $MgAl_2O_4$, or $MgSiO_3$ are hardly used, let alone an accurate composition like $Mg_{0.56}Ti_{0.01}Cr_{1.33}Fe_{0.51}Al_{0.59}O_4$ [10].

As demonstrated by for example Sweeten [9], mineralogy can affect the mass and energy balances of a smelting operation because of the role of the formation enthalpy. Barcza [3] showed that a 0.5% deviation between feedrate and power input, already creates problems:

> The control over the feed rate and power level to within about 0.5 percent accuracy appears to be necessary, particularly at power levels greater than 20 MW, so that the unwanted increase in energy consumption caused by increased bath temperature and the favouring of undesirable side reactions can be avoided. Having a model that can investigate effect of formation enthalpy on actual DC ferrochrome operation therefore seemed a useful investigation.

An accuracy of 0.5% equals 200 kW on a 40 MW furnace. With such a furnace having heat losses in the range of 4−8 MW, the 200 kW is 2.5−5.0% on the heat losses, and only 0.56−0.63% on the metallurgical energy consumption of 32−36 MW. Both percentage ranges are at best within the range where heat loss measurements or thermochemical calculations are accurate.

Reductant

Reductants are important in metal production. Nowadays even more so, because fossil-fuel-based reductants contribute to climate change, and their use should be minimised. A better understanding of the behaviour of reductants in smelting operations can support the change to, for example, alternative reductants like biochar or end-of-life plastics.

For reductants often the proximate analysis is used:

- moisture,
- C-fix,
- volatile matter, and
- ash.

A detailed ash analysis is usually known and applied in the mass and energy balances. The exact composition of the volatile matter, typically given by VM or volatiles, is sometimes either assumed, or recalculated based on the ultimate analyses (C, H, N, O, S) in combination with assumptions [4].

One factor not often used in calculations with reductants is the gross calorific value (GCV). This can give information on the RFE of complex substances like coal, anthracite, or coke.

This paper will focus on the effect of ignoring the RFE on DC FeCr operation.

Challenges with Using Reductants in Calculations

A reductant is a highly complex "mineral" of mainly C-H–O connections with other elements connected (for example S, N, Na), and locked in materials, like pyrite or clay.

It is important to understand that volatile matter in the cold reductant is not present in the gaseous state, but only released as gas from the solid during heating. The relative quantities of fixed carbon and gases and the composition of the volatiles depend strongly on variables like particle size distribution and process conditions. Especially, heating rate and final temperature are important [4, 11–13].

Reductants therefore are a tricky substance to do calculations with. Some issues are:

- When and where how many volatile products are released remains uncertain.
- There is a wide range of non-organic and organic compounds possible (clay, pyrite, sulfates, alkalis loose or as organic compound, etc.) that can affect the behaviour of the reductant, catalyse reactions, or obstruct them.
- Getting reliable values for proximate and ultimate analyses, and determination of the GCV are a problem because accurate sampling and analysing of reductants is extremely hard, and even with utmost care results may not be consistent [14].

To make things harder, one should be extremely careful to make sure if the values are based on analyses as received (AR), air dried (AD), dry basis (DB), or dry ash free (DAF). Even with support literature [15, 16] errors are easily made. For example, there is a difference between the GCV values when given based on analyses "as received" or "dry ash free".

Reductant Enthalpy of Formation and GCV

Reductants have an enthalpy of formation, just like chromite ore, bauxite, or methane (CH_4), but the RFE is harder to determine. Reductants with identical chemical compositions can be structured completely different on an atomic level, and thus have very different enthalpies of formation and GCV values. Theron showed the effect on formation enthalpy by using different compositions for the volatiles based on the same ultimate analyses [4]. Reductants as a bulk commodity do have a (quite) constant GCV.

Table 1 Example based on methane to show the effect of enthalpy of formation on an energy balance, calculated with HSC

		1 kg CH_4	1 kg ($C + 2H_2$)
Comment		All gas	Solid graphite + gas
Enthalpy at 25° before combustion	kWh/kg	−1.3	0
Enthalpy at 25° after combustion	kWh/kg	−16.7	−16.7
Theoretical GCV as calculated	kWh/kg	15.4	16.7
Measured GCV of CH_4 [26]	kWh/kg	15.4	15,4
Difference theoretical to measured GCV	kWh/kg	0,0	−1,3
Stoichiometric combustion temperature	°C	1677	1804

To explain the effect of the formation enthalpy, the GCV determination of methane is given in Table 1. Pure methane has no issues with solids, clay minerals, or sulphur. Methane has a GCV of 15.4 kWh/kg, measured by calorimeter [26]. The calculated GCV can be based on combustion of CH_4 or $C+2H_2$. The difference is the enthalpy of formation: the energy that was required to form the CH_4 from the elements. That cost causes a lower final combustion temperature because less energy is available from CH_4 in reality than from $C+2H_2$ in theory.

A similar approach is applicable to reductants like anthracite or coke. These reductants have measured GCV values, but only the elemental composition can be used in thermodynamic calculations. It is possible to calculate a theoretical GCV based on the ultimate analysis and consider the difference to the actual GCV as a correction factor [4] or RFE [27]. Note that enthalpy is given as a negative value, whereas GCV is a positive value.

$$\mathrm{RFE} = \mathrm{GCV} - \text{theoretical GCV}$$

If RFE > 0, then more chemical energy is available than calculated based on the ultimate analysis. In a DC furnace this means that more feed should be smelted per hour than calculated or else the bath heats up.

If RFE < 0, then less chemical energy is available than calculated based on the ultimate analysis. In a DC furnace this means that less feed should be smelted per hour or else the bath will freeze in.

Kleynhans [18] provided an excellent dataset that is used in this paper. Table 2 shows a selection from that dataset with the theoretical GCV and RFE added. Anthracites and cokes are given by An and Co, respectively.

Note that these anthracites have a positive deviation, while all cokes have a negative one. Secondly, most anthracites are in the same range, meaning that changing from one anthracite to another mostly has less impact than changing from anthracite to coke or vice versa, but not in all cases.

Table 2 Selection of data from Kleynhans [18] and theoretical GCV values based on Zietsman [27]. The ultimate analysis is "air dried"

		An1	An2	An3	An4	An5	An10	Co1	Co2	Co5
Inh. mois	%	3.8	1.9	2.9	2.1	1.4	3.2	1.2	0.2	0.4
Ash	%	15.7	20.3	11.8	12.1	15.5	16.3	20.4	7.7	12.4
VM-volatiles	%	5.0	9.7	4.9	4.5	6.5	5.0	1.6	0.6	0.9
Fixed C	%	75.5	68.1	80.4	81.3	67.6	75.5	76.8	91.5	86.3
C	%	74.1	70.6	78.2	79.8	76.0	73.6	75.5	89.1	84.7
H	%	1.62	2.60	2.12	2.01	2.49	1.69	0.20	0.03	0.01
N	%	1.63	1.69	1.77	1.44	1.55	1.64	0.87	1.33	1.19
O	%	2.01	2.14	2.05	1.80	2.15	2.12	1.04	0.80	0.48
S	%	1.14	0.74	1.07	0.70	0.84	1.42	0.78	0.80	0.78
GCV	kWh/t	7558	7567	8192	8197	8153	7606	6481	8125	7508
Th. GCV[1]	kWh/t	7411	7468	7979	8,072	7919	7400	6970	8141	7733
RFE	kWh/t	147	98	212	125	234	205	−90	−16	−224

[1] Theoretical GCV determined by calculation in HSC of combustion of the ultimate analysis of the air dried reductant at 25 °C with H_2O as liquid product

On GCV Formulas

Several GCV formulas exist to approximate the real GCV as determined by official guidelines. Reviews are included in [14, 17]. Care must be taken to use a consistent calculation method with the correct analyses as explained. Be consistent with the units kWh, MJ, btu per kg, t, lb.

Considering the assumptions in theoretical GCV calculations, it may be more appropriate to talk about an enthalpy correction based on a certain method, than claiming to have "the" method to determine the RFE.

Applying the method for calculating the RFE as described by Zietsman on data from Kleynhans gave results ranging from around +250 to −1000 kWh/t of reductant. Using Theron's slightly different calculation for a correction value gave values in the same order of magnitude.

Calculation in HSC

A dynamic calculation was set up using the software HSC [19]. This software allows for dynamic changes in operation, parameters, and compositions. The effect of such a change can then be visualised.

The HSC dynamic simulation software allows, i.e.,

- Inclusion of multiple reaction zones within a reactor.

- Changes in operating conditions while the simulation is running.
- Varying temperatures of output streams.
- Simulate events like tapping or process disruptions.
- Monitoring the involved energy flows between the different zones.

The aim of this investigation is limited to demonstrating how ignoring the RFE affects the bath temperature and chemical reactions.

If these effects lead to operational problems and how fast what will happen depends partially on the process itself. In open bath smelting, this can be very different for FeCr, titania slag, or smelting of direct reduced iron. Secondly, the furnace design, for example bath volumes, plays a role: large slag volumes will respond slower than small slag volumes.

Simplifications—Conditions

When changing from one reductant to another, the main calculation parameter is the carbon to ore ratio. This is because most carbon is used for the reduction of Cr_2O_3 and formation of chromium carbides. Assuming the ore does not change, then the same amount of C-fix will be required to achieve the same reduction of the ore. If the reductant has a different fixed carbon content, then the quantity of reductant per ton of ore is adjusted accordingly.

Slag, alloy, and off-gas should remain the same. However, the difference in moisture, ash quantity, and ash composition may affect the required quantity of fluxes. A change in the quantity of fluxes may then affect the required C-fix if the quantity of especially iron oxides changes. Moisture and reactions between carbon and water will affect the required reductant quantity too. An interpolation loop is thus formed where a new balance must be found. The overall effect may be a different energy consumption, requiring a change in FtP setpoint, even without considering the RFE.

Such loops, and they appear when changing for example ore or reductant composition, moisture content, furnace load, and type or source of fluxes, are the main challenge for metallurgists in the highly sensible open bath operations.

Because too many variables would cloud the purpose of this paper, i.e., to show how the use of RFE and GCV by themselves alone are significant, some simplifications have been made.

- The ore was taken as compounds and included a selection of only the most important ones.
- The same ore was used in all calculations.
- S from the reductant is neglected in the mass balance.
- No dust losses are in the simulation because these are not relevant to show the effect of the RFE.
- Formed process gas leaves the furnace instantly.
- Temperatures for all exit streams are fixed at 1,800 °C in the calculations. This is to prevent confusion by having internal energy streams.

- In this model, raw materials enter the calculations at the same point of energy input: the electrode tip

Input Data

Table 3 shows the analyses for the raw materials that were used in the calculations. Data were taken from the literature and simplified to not unnecessarily complicate the calculations. An anthracite and a coke were deliberately selected to create a bigger difference.

Table 3 Raw materials used in the calculations

		Ore[1]	Bauxite	Quartz		Co1[2]	An1[2]
Feedrate	tph	20		As required by the calculations			
Moisture	%	2.0	2.0	2.0		1.2	3.8
GCV	kWh/t					6,480	7,560
Theoretical GCV	kWh/t					6,970[3]	7,411[3]
RFE	kWh/t					−490[4]	+ 147[4]
Solid part (Dry Basis)							
Cr_2O_3	%	51.00					
FeO	%	12.50					
Fe_2O_3	%	0.00				2.82	4.08
SiO_2	%	7.00	10.50	100		13.30	7.86
MgO	%	20.50	0.00			0.45	0.64
Al_2O_3	%	8.50	0.00			4.03	4.40
CaO	%	0.50	0.00			0.39	0.24
C	%		0.00			79.01	82.79
$Al(OH)_3$	%		76.00				
$Fe(OH)_3$	%		12.00				
TiO_2	%		1.50				
Sum	%	100	100	100		100	100

[1] Based on [8, 20, 21] and simplified
[2] From Kleynhans unless specified differently; ash adjusted to have less components, normalised, and dry basis; moisture is calculated in separately
[3] Based on [27] as described in Table 2
[4] RFE = GCV—theoretical GCV

Results

Step 1 Model Test Base Case Ignoring RFE for Both Reductants

The dynamic calculation was tested by first doing a "batch" calculation of one hour to verify if the results compare to industrial data.

Two calculations were done with different reductants. From Kleynhans, an anthracite and a coke, An1 and Co1, were selected. The target slag composition was based on literature [22]. The calculated required energy, quantities of reductant and fluxes, and some other results are given in Table 4.

Some values in Table 4 are not the same as industrial values. The calculated alloy is not high carbon ferrochrome as produced industrially: that has C in the range 8−9.5% [24, 25]. As in other simulations, for example with FactSage in [23], C in FeCr and FeO in slag are too low. These are indications the approach to add more reaction zones could be meaningful: by allowing more reaction zones and pathways, a better approximation of industrial values could probably be achieved.

The chrome recovery is very high. This should be corrected for mechanical furnace dust losses. Taking these in the order of 2−4% leaves 91−94% recovery, which is in line with values as found in the literature for high carbon FeCr [24].

Changing reductant from coke-1 to anthracite-1 has multiple effects. For one, the moisture content already affects carbon consumption and energy requirement. Secondly, the different ash requires a change in charged fluxes if the slag is to be

Table 4 Results from HSC calculations with 20 tph of chromite and the fluxes and reductants needed to achieve the given target slag composition at 1800 °C

		Coke-1	Anthracite-1
Cr_2O_3	%	4.5	4.5
Al_2O_3	%	27.7	27.8
SiO_2	%	22.9	22.9
MgO	%	43.4	43.3
FeO	%	0.1	0.1
Cr	%	71.2	71.0
C	%	5.4	5.3
Si	%	0.6	0.6
Load	MW	**40.26**	**41.99**
Ore	tph	20	20
Reductant	tph	5.14	5.24
Bauxite	tph	**1.08**	**1.04**
Quartz	tph	**0.02**	**0.32**
Feed-to-power	kg/MW	**652**	**634**
Chrome recovery	%	96.1	96.1

kept the same. As a result, a different furnace power is required to smelt the same quantity of ore.

Thirdly, the FtP has changed because of the different reductant. The change of 18 kg/MW may seem small but is about 3%. A similar change can be seen in the MW required: 1.7 MW is about 4%. This is well above the 0.5% accuracy limit given by Barcza [3]. This change requires that the previously applied FtP must be adjusted to prevent overheating when changing from coke-1 to anthracite-1. To conclude, already a change in reductant without consideration of the RFE can be a reason to adjust any preprogrammed FtP relationship in the control software.

Step 2 Application of Different RFE's on the Previous Calculation

The aim was to see if the ignoring the RFE could be a cause for problems in DC FeCr smelting. Changing the reductant without considering the RFE is already a reason to adjust the FtP ratio as shown under step 1. If no calculations are done to investigate the effects of a reductant change, then any possible effects of the RFE could simply be taken as part of the adjustment, without understanding where part of the required change came from.

A different approach was needed to isolate the RFE effects.

Based on the RFE's, changing from anthracite-1 to coke-1 during production would lead to an energy shortage and thus freezing of the bath. By changing from coke-1 to anthracite-1, the overheating of the bath could be investigated.

Assume the operation with coke-1 has been running stable and in equilibrium for days at 40.26 MW without consideration for the RFE. That means feedrate, energy balance, and assumptions for heat losses are all in equilibrium, irrespective of how accurate these are individually. Assuming the feedrate and analyses of raw material analyses are stable and highly accurate, then more detailed calculations on the RFE become possible.

In step 1 with coke-1, the total required load was 40.26 MW, of which 88% (35.43 MW) was assumed to cover metallurgy excluding RFE. The rest, 4.83 MW, are considered to be heat losses, but actually cover both real heat losses and all metallurgical issues ignored or not known, like the RFE.

$$\text{Assumed energy balance} = 40.26\,\text{MW} = 35.43\,\text{MW} + 4.83\,\text{MW}$$

The calculated RFE for coke-1 = -490 kWh/t. This means that 490 kWh/t reductant have been used in the calculation to produce FeCr but were not available in reality. This means that the initially calculated heat loss of 4.83 MW was smaller, because part of this energy was needed to compensate for the ignored RFE.

The energy balance including RFE is thus

$$40.26\,\text{MW} = (35.43 + 5.14 * 0.490) + (4.83 - 5.14 * 0.490) = 37.95 + 2.31$$

The new heat loss is 2.31 MW and assumed to be also the actual heat loss for the case with the new reductant, anthracite-1.

In the case with anthracite-1 as a reductant, Table 4 shows the required anthracite, fluxes, and energy to have a similar process. The furnace load of 41.99 MW is, however, calculated without considering the RFE correction for anthracite-1. The 41.99 MW included 12% of heat losses, 5.04 MW, "Because with 12% heat losses the furnace operated stable with coke-1 and the given feedrate".

The real furnace heat losses are only 2.31 MW. The difference of 2.73 MW must be kept in mind, because this by itself would already upset the process and raise the bath temperature.

The anthracite-1 calculation without RFE or heat loss correction has 36.95 MW for the metallurgical reactions (41.99−5.04). The RFE correction is 5.24t anthracite*(147) kWh/t = 0.77 MW.

The actual required energy with anthracite-1 is therefore: 36.95 + 2.31−0.77 = 38.49 MW. Relative to the actually required energy of 38.49 MW, the 41.99 MW is 9.1 percent too much energy input. These 3.50 MW surplus are available in the reaction zone and should not be written away as thermal losses: it is at the electrode tip where the feed is processed and where the surplus energy will overheat the bath and make side reactions happen.

A solution is to set the 2.31 MW as heat losses, being 5.5% of the furnace load. This directs 2.73 MW from heat losses to the reaction zone. Then to compensate for the RFE, 0.77 MW is added as a stream of energy directly into the reaction zone operation. This method seems appropriate as it compensates for the real thermal losses whilst having identical bath conditions and compensate for the energy "released" from the coke.

Note that the difference in RFE between anthracite-1 and coke-1 is relatively big. Changing from anthracite-1 to most other anthracites would not be so drastic regarding the RFE.

Secondly, in industry, the feedrate would be adjusted to the power, whereas in this calculation the power has been adjusted to a fixed rate of charging ore and the required additions. This was done to show clearer the effect raw materials have on the energy consumption.

Step 3 Run the Continuous Model with the New Values and See What Happens

The continuous model was tested once the batch mass and energy balances were validated. The principle of the continuous model is as shown in Fig. 1. Feed materials and power enter the reaction zone. Reactions happen based on temperature and the equilibrium calculation that HSC provides. The model allows for collecting products

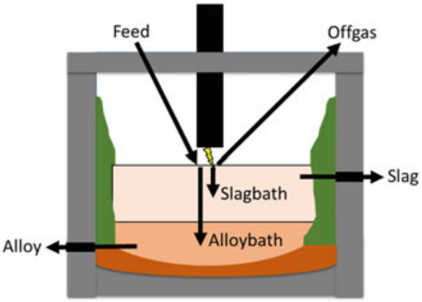

Fig. 1 Representation of the model with input of raw materials and energy input at a single point used as reaction zone. From the reaction zone, alloy and slag collect in the alloy and slag bath, respectively, to be tapped intermittently

in the furnace in a slag and alloy bath (called "tanks" in HSC) and tapping from these tanks once certain bath levels have been reached. By assigning volumes to the tanks, it is possible to simulate how a furnace acts over time. Following bath volumes were used:

- Slag bath volume approximately 55 m^3
- Alloy bath volume approximately 70 m^3

First, the operation was run with coke-1 to verify the energy balance was stable. Next, anthracite-1 was used together with the values for power, reductant and fluxes as given in Table 4 without considering the RFE. To then simulate over time the effect of the corrected heat loss and the RFE, the following values were used:

- Power input: 41.99 MW.
- Heat loss: 2.31 MW = 5.5%➔this already adds 2.73 MW to the reaction zone.
- Energy input into the reaction zone due to RFE: 0.77 MW.

The results of a 24-h simulation run are shown in Fig. 2. Reaction zone and slag and alloy baths all start at 1800 °C. Slag and alloy go 100% to the slag and alloy baths, and both are tapped when certain levels are exceeded. This is visible in the upper left graph of Fig. 2. Process gas leaves the furnace continuously and instantly. The first five hours are with the original settings with heat losses of 12% and no RFE correction.

At t = 5 h, the RFE and heat loss correction as given above are activated. The excess of available energy causes the temperature of the reaction zone to instantly increase as can be seen in the lower left image of Fig. 2. Because the reaction zone has not been assigned a volume, it instantly jumps to the new equilibrium value of 1.885 °C. The formed slag and alloy mix with the slag and alloy baths and the temperatures of both slowly rise. Compositions of alloy bath and slag bath are shown in the graphs on the right.

With the higher temperature, the carbon content in the alloy drops while the Cr_2O_3 and Al_2O_3 contents in slag increase. At the same time, both MgO and SiO_2 in slag decrease. Note that Barcza et al. [3] came to similar graphs, where C and Cr from alloy were consumed and the MgO content in the slag was reduced due to the formation of Mg-gas.

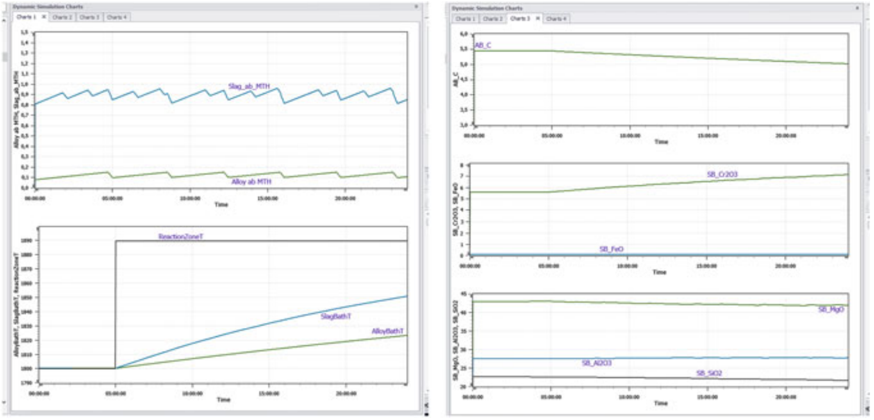

Fig. 2 Screenshots from HSC SIM results. Tapping (top left) ensures the bath levels remain within certain limits. Applying the corrections based on ERF's show a strong increase in reaction zone temperature (bottom left). As the temperature increases, the alloy bath (AB) is losing C (top right), while the slag bath (SB) gets richer in Cr_2O_3 (middle right) but is losing MgO and SiO_2 due to Mg and SiO gas formation

Summary and Conclusions

Aiming for an accuracy of 0.5% for the feed-to-power is an admirable target but may be very hard in reality due to the lack in accuracy in heat loss measurements and limitations in thermochemical calculations.

By isolating the effects of the enthalpy of formation of reductants on a FeCr DC smelting operation in a dynamic simulation, it could be shown this can have a significant impact on the operation. A check of the formation enthalpy of available reductants on site by comparing the actual GCV with the theoretical GCV should be done to see what the impact of a reductant change can be. The information can be used as an extra warning and to calculate a pre-emptive FtP correction.

Single step black-box models have worked well for many years in many processes. The modern open bath furnaces may have been proof that this approach does not sufficiently address the importance of heat and mass transfer. The presented model got close to industrial values but requires more accuracy.

A dynamic model to investigate and visualize the effects of changes in raw materials or operational parameters has been demonstrated to lead to increased understanding and insight.

Better understanding of the behaviour of carbonaceous reductants in a furnace will support a transition to using recycled reductants, like (pyrolyzed) plastics or biowaste.

The advice remains to stick to one reductant and if change is needed, to do so gradually. Not only because of the RFE but also because in reality multiple variables can change simultaneously. Therefore, paying attention carefully to the operation, like tapping temperatures and compositions, remains an important tool to keep the process controlled.

The basic functionality of the dynamic model has been demonstrated, so next is to include more zones for more accurate process simulation. With the improvements made, ideas about the mechanisms inside a DC FeCr furnace will be further investigated as part of the PhD.

References

1. Merrow EW, Phillips KE, Myers CW (1981) Understanding cost growth and performance shortfalls in pioneer process plants. Rand Corporation for Department of Energy
2. McNulty T (1998) Developing innovative technology. Min Eng 50(19):50–55
3. Barcza NA, Curr TR, Jones RT (1990) Metallurgy of open-bath processes. Pure Appl Chem 62(9):1761–1772
4. Theron JA, Le Roux E (2015) Representation of coal and coal derivatives in modelling. J South Afr Inst Min Metall 115(5):339–348
5. Barnes A, Mackey P, Alvear G (2009) Process development and growth of non-ferrous metals production: the role of pilot plants. Plenary address, European Metallurgical Conference, Innsbruck, Austria, 28 June−1 July 2009
6. Barnes RA, Jones RT (2011) Cobalt from slag—lessons in transition from laboratory to industry. In: Paper presented at Conference of Metallurgists, Montreal, Canada, 2–5 October 2011
7. Pan X (2013) Effect of South Africa reductants on ferrochrome production. Paper presented at the 16th IFAC Symposium on Automation in Mining, Mineral and Metal Processing, San Diego, California, USA, 25–28 August 2013
8. Geldenhuys IJ (2013) Aspects of DC chromite smelting at Mintek—an overview. In: Paper presented at Infacon XIII, Almaty, Kazakhstan, 9–13 June 2013
9. Sweeten NJ et al. (2018) Chrome ore mineralogy and the furnace mass and energy balance. In: Paper presented at Infacon XV, Cape Town, South Africa, 25–28 February 2018
10. Sommerfeld M, Friedrich B (2022) Proposition of a thermogravimetric method to measure the ferrous iron content in metallurgical grade chromite. Minerals. https://doi.org/10.3390/min12020109
11. Merrick D (1983) Mathematical models of the thermal decomposition of coal. Fuel 62:534–539
12. Sampaio RS, Fruehan RJ, Ozturk B (1991) Rate of coal devolatilization in iron and steelmaking processes. In: Paper presented at 1991 Ironmaking conference proceedings, Washington, USA
13. Wei Q, Qiang X, Yuyi H, Jiatao D, Kaidi S, Qian Y, Jincao W (2012) Combustion characteristics of semicokes derived from pyrolysis of low rank bituminous coal. Int J Min Sci Technol 22:645–650. https://doi.org/10.1016/j.ijmst.2012.08.009
14. Neavel RC, Hippo EJ, Smith SE, Miller RN (1986) Coal characterization research: sample selection, preparation, and analyses. Preprints of papers. American Chemical Society. Div Fuel Chem 25(3):246–257
15. WCI World Coal Institute (2009) Coal conversion facts: basis of analysis. https://drummondco.com/wp-content/uploads/coalconversionfacts200704_06_2009.pdf. Accessed 6 September 2022
16. SGS (2022) Coal calculations. https://www.sgs.com/en-au/services/coal-calculations. Accessed 6 September 2022
17. Mason DM, Gandhi KN (1983) Formulas for calculating the calorific value of coal and coal chars: development, tests, and uses. Fuel Process Technol 7:11–22
18. Kleynhans ELJ, Beukes JP, Van Zyl PG, Bunt JR, Nkosi NSB, Venter M (2017) The effect of carbonaceous reductant selection on chromite pre-reduction. Metall Mater Trans B 48b:827–840

19. HSC chemistry 10, HSC SIM Flowsheet Module, version 10.0.8.5
20. Strakhov VM, Medyanik VS, Malinovskaya LI, Tsernikel AA, Veselovsky IA (2016) Production of high-carbon ferrochrome from dry-quenched semicoke. Coke and chemistry 59(7):254–259
21. McCullough S, Hockaday S, Johnson C, Barcza NA (2010) Pre-reduction and smelting characteristics of Kazakhstan ore samples. In: Paper presented at Infacon XII, Helsinki, Finland
22. Oterdoom HJ et al (2018) (2018) High carbon ferrochrome smelting in a DC furnace: smelt small stuff and stop sintering. Paper presented at Infacon XV, Cape Town, South Africa
23. Lu J (unknown) Ferrochrome production. in-ho-group.snu.ac.kr/wp-content/uploads/Ferrochrome-Production.pdf Accessed 28 July 2022
24. Yessenzhulov AB (2020) New and reconstructed JSC “TNC “Kazchrome” facilities. In: Paper presented at 2nd conference on The best available technologies for steel and ferroalloys production, Moscow, Russia
25. Jones RT, Erwee MW (2016) Simulation of ferro-alloy smelting in DC arc furnaces using Pyrosim and Factsage. CALPHAD: Comput Coupling of Phase Diagrams and Thermochem 55:20–25
26. Dale A, Lythall C, Aucott J, Sayer C (2002) High precision calorimetry to determine the enthalpy of combustion of methane. Thermochim Acta 382:47–54
27. Zietsman J (2022) Essential theory of thermochemistry—mass and energy balances: organic feed materials. Lecture notes on mass and energy balances

Measuring and Processing of Electrical Parameters in a Submerged Arc Furnace

Hákon Valur Haraldsson, Halldór Traustason, Yonatan A. Tesfahunegn, Merete Tangstad, and Gurún Sævarsdóttir

Abstract Electric arcs are necessary for high Si yield in submerged arc furnaces (SAFs) for Si/FeSi production, and a certain fraction of heat dissipation in the arc enables optimal operating conditions. Direct measurement of the arc characteristics is impossible due to hostile conditions inside the SAF, so controlling the heat dissipation is both a science and an art. The arcs exhibit non-linear electrical characteristics and behave in a complex manner. Hence, implementing a data acquisition (DAQ) system to collect current and voltage waveforms typically on the electrodes or transformer connections combined with appropriate signal processing offers an estimate of the actual arc parameters, enabling improved understanding of the arcing in the furnace, and improving furnace operation. In this paper, a DAQ system gathering data from a FeSi SAF will be discussed, and the data is processed and used to determine various furnace conditions including arc and charge current as well as harmonics.

Keywords Submerged arc furnace · Arc footprint · Arc harmonics · Electric arc

---

H. V. Haraldsson · H. Traustason · Y. A. Tesfahunegn · G. Sævarsdóttir
Department of Engineering, Reykjavík University, Reykjavík, Iceland
e-mail: halldor.traustason@pcc.is

Y. A. Tesfahunegn
e-mail: yonatant@ru.is

G. Sævarsdóttir
e-mail: gudrunsa@ru.is

H. V. Haraldsson (✉) · M. Tangstad · G. Sævarsdóttir
Department of Materials Science and Engineering, Norwegian University of Science and Technology, Trondheim, Norway
e-mail: hakonh12@ru.is

M. Tangstad
e-mail: merete.tangstad@ntnu.no

S. Wagstaff et al. (eds.), *Materials Processing Fundamentals 2023*, The Minerals, Metals & Materials Series, https://doi.org/10.1007/978-3-031-22657-1_14

Introduction

The furnace used to produce silicon is called a submerged arc furnaces (SAF) because the electrodes that carry the electric current are submerged in the raw materials used in the production process. In some processes operated in submerged arc furnaces such as in ferromanganese production, there is actually no arc in the furnace and all the heat is dissipated as the current passes through the materials in the furnace, such as the coke bed below the electrodes. For silicon and ferrosilicon production, however, the presence of an arc is essential. In this case, much of the current will pass through an electric arc, which burns in a cavity or crater which is filled with gas not solid materials, this is thought to be due to the high viscosity of the SiO_2 and the formation of a SiC crust around the cavity. Liquid silicon forms in a pool below the arcs and is tapped into ladles using tap holes. The extremely hostile environment inside SAFs makes any direct observation of the arc impossible.

A submerged arc furnace is a fairly large machine usually spanning a few floors in the building it is situated in. In simple terms, the furnace converts electricity and internal energy of carbon materials to heat which melts the raw materials, thus creating usable metals. The furnace itself is circular and varies from approximately 5–11 m in diameter and from 3–5 m in height. Raw materials are added from the top and will descend slowly in the furnace while they are heated. A diagram of a SAF can be seen in Fig. 1.

Since the arc cannot be measured directly, estimating its parameters can be difficult. In an operating furnace, we can only measure the voltage and current going into each electrode, but by creating a complete electric circuit model of the furnace and knowing its parameters, either by simulation or measurements, we can use the measured voltage and current waveforms in each electrode to indirectly estimate the arc. There are not many published studies on measuring arc parameters but previous work on this has been done in [1] and [2]; in [3], measurements are used to model the

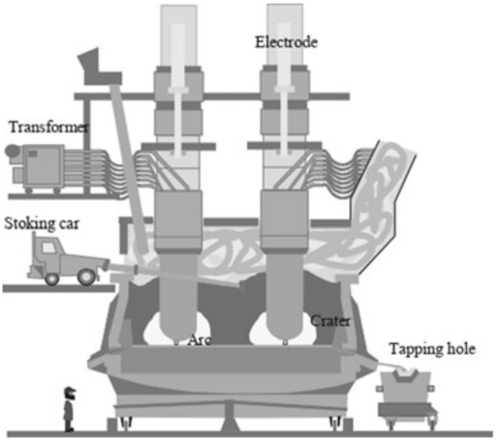

Fig. 1 A schematic drawing of a SAF in operation

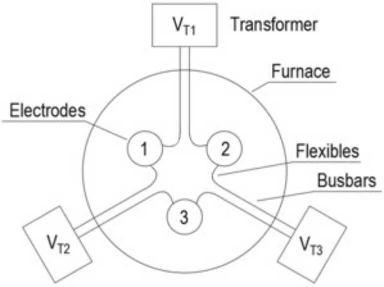

Fig. 2 A SAF in knapsack configuration

effects of electrode height on arc currents. All measurements on any type of furnace require some sort of data acquisition (DAQ) system to collect and process the data. For industrial applications, reliable and accurate equipment is essential, so selecting the correct equipment can be a challenge. Lorenzo et al. [4] detail this for a Spanish ferroalloy company, and Gerritsen et al. [5] describe some of the methods used and impact of error in the measurements. These should not be confused with direct arc modeling, which is a different approach [6].

In this paper, we will describe the DAQ system that was implemented on a FeSi SAF in Elkem Iceland. We will discuss the SAF properties required for data processing to estimate actual SAF parameters. Finally, we will describe how the data is processed from raw measurements to actual useful parameters that are used to estimate current distribution, arc footprint, and arc harmonics in the furnace.

Inside the furnace, the electrodes are submerged in the raw materials, below each electrode there is a cavity where the arc is burning. This cavity or crater is filled with gas not solid materials, and this is thought to be due to the high viscosity of the SiO_2 and the formation of a SiC crust around the cavity. Liquid silicon forms in a pool below the arcs and is tapped into ladles using tap holes.

Electric Circuit Description of a SAF

A 3-phase SAF generally consists of 3 transformers placed concentrically around the furnace with 120° between them, and this is done to minimize mutual inductance between them. The transformers are connected to 3 electrodes that conduct electric power to the furnace through bus bars and flexibles. This setup is called a knapsack configuration and is shown on Fig. 2.

When discussing a SAF from an electrical standpoint, the main focus is on the currents present in the electrode, and what electrical parameters affect them. The electrode current is the total current that travels down the electrode from the delta connection connecting the transformers, before it diverges to different paths. To understand what is happening, we must see what the total electrical characteristics of the SAF are. Industrial high current arcs are generally present within the electric

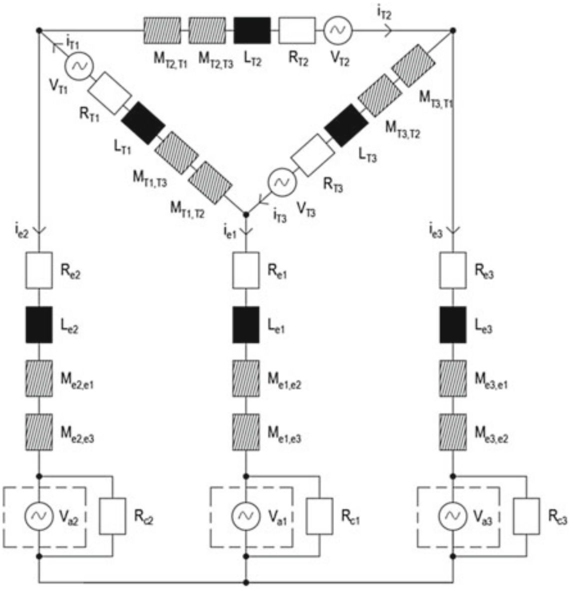

Fig. 3 The electric circuit used to describe a SAF [7]

arc furnaces, and to determine the behaviour of the furnace and the arc itself, a complete electric circuit must be implemented.

The circuit should include most of the actual components present, transformer resistances R_{Ti}, impedances L_{Ti}, and mutual inductance between them ($M_{Ti,Ti+1}$ and $M_{Ti,Ti+2}$), as well as the resistances of the electrodes (R_e) and the phase inductance including the mutual inductance (L_e and $M_{ei,ei+1}$ and $M_{ei,ei+2}$). Mutual inductance due to currents in the bus bars and flexibles are normally lumped into the phase inductance, which is accurate if the furnace is reasonably symmetrical.

We consider the electrode current to split up into two parts, the current going into the arc and then the current in the charge material. R_c represents the charge resistance and V_a the arc voltage drop. This is a simplification but gives a reasonable estimate since other components are rather small in a well-operating furnace. The physical properties of the charge materials differ with location in the furnace, as intermediate reactions change their composition and temperature changes with depth both of Fig. 3 shows the electric circuit of a three-phase SAF and where each component is located in it.

Estimating SAF Parameters

The DAQ System

The data acquisition system for SAF samples both the voltage and current in each electrode as well as a few of the higher harmonics that are present in the signal. Here,

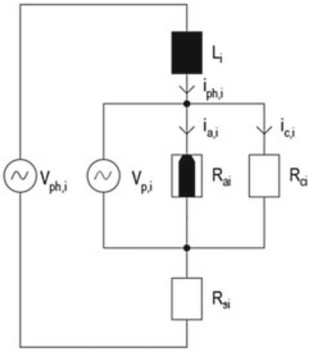

Fig. 4 The simplified circuit model used to estimate arc characteristics from the measurements

the measurement frequency f_S is 3000 Hz which gives about 60 samples per period. This sampling rate allows for the estimation of harmonics up to 1500 Hz which is the 30th harmonic 50 Hz.

The DAQ system consists of three voltage sensors that measure the electrode voltage through step-down modules since it is too high to measure directly, the current sensors measure the current in each electrode using the hall effect. A detailed description can be found in [8] where the DAQ system design and implementation are described in detail.

Data Processing

A method has been developed to estimate the current that passes through the arc and charge material. The simplified circuit presented in Fig. 4 shows the model used to process the measured current and voltage waveforms. The model is similar to the section surrounding the arc in Fig. 3 but most circuit elements have been combined and the furnace resistance is included. Current and voltage measurements for each electrode are defined as i_{phi} and V_{phi}. Here, the subscript i denotes the electrode numbering. The total phase voltage V_{phi} is a combination of the voltage induced in the furnace V_{Li}, the voltage over the arc V_{pi} (which is over the time varying arc resistance R_{ai} and the assumed constant charge resistance R_{ci} connected in parallel), and finally, the voltage over the furnace short-circuit resistance R_{si}, the liquid metal resistance, and the base resistance in the furnace. V_{pi} can be considered as the power producing voltage or load voltage that contributes to the actual silicon production.

Now, the equivalent phase resistance R_{ph}, the arc resistance R_{a}, and the charge resistance R_{c} can be defined using Ohms law as:

$$R_{\mathrm{ph}} = \frac{1}{\frac{1}{R_{\mathrm{a}}} + \frac{1}{R_{\mathrm{c}}}} + R_{\mathrm{s}} \tag{1}$$

$$R_{\mathrm{a}} = \frac{R_{\mathrm{c}}(R_{\mathrm{ph}} - R_{\mathrm{s}})}{R_{\mathrm{s}} + R_{\mathrm{c}} - R_{\mathrm{ph}}} \tag{2}$$

$$R_{\mathrm{c}} = \frac{R_{\mathrm{a}}(R_{\mathrm{ph}} - R_{\mathrm{s}})}{R_{\mathrm{s}} + R_{\mathrm{a}} - R_{\mathrm{ph}}} \tag{3}$$

The induced voltage present in the phase voltage causes a phase shift in the current, and this results in the current lagging behind the voltage by 30° to 45°. The magnitude of the phase shift varies with the size of the furnace but also with electrode movement withing the furnace. The induced voltage V_{Li} must therefore be removed from the total phase voltage V_{phi} before the resistances can be calculated. This is done by a simple time-dependent differentiation of the current signal to estimate the induced voltage:

$$V_{\mathrm{pi}} = V_{\mathrm{phi}} - Li\frac{\mathrm{d}i_{\mathrm{phi}}}{\mathrm{d}t} \tag{4}$$

Here, L_i is the total inductance present in the electrode, and this value is found by iteration until the phase shift is negligible. With the phase shift removed, the total phase resistance for each electrode R_{phi} can be determined. The phase resistance or zero crossing resistance is the resistance when both the phase current and the power producing voltage cross the zero point simultaneously. R_{phi} is found by plotting the Lissajous curve for i_{phi} and V_{pi}, and then, the slope is estimated as the curve passes zero. To find R_c, we need both R_s and R_a, and the short-circuit resistance is either known from the modeling, such as in [9], or can be assumed to be around 5% of the phase resistance similar to what is done in [8]. Determining the arc resistance R_a can be difficult since you ideally need measurements from when the furnace being measured when only an arc is present without any charge materials present, this is important since different furnaces will have different parameters. Previous measurements carried out in the same furnace when a pure arc was present were used and determined the arc resistance to be around 2.5–4 mΩ [2]. This will give an upper and lower limit for the charge resistance R_{c}, and consequently, both the arc resistance R_{a} and the arc current i_{a} will have similar limits; here, we will show the upper limit only for simplicity of the graphs. Now, all that is needed to determine the range for the arc current i_a which is the voltage over the arc V_a given as:

$$V_{\mathrm{ai}} = V_{\mathrm{pi}} - i_{\mathrm{phi}}R_{\mathrm{s}} \quad \Rightarrow \quad i_{\mathrm{ai}} = \frac{V_{\mathrm{ai}}}{R_{\mathrm{ai}}} \tag{5}$$

Results

The ability to estimate furnace parameters both after or preferably during operation will allow for better control of the overall operation of a furnace. The data used in this

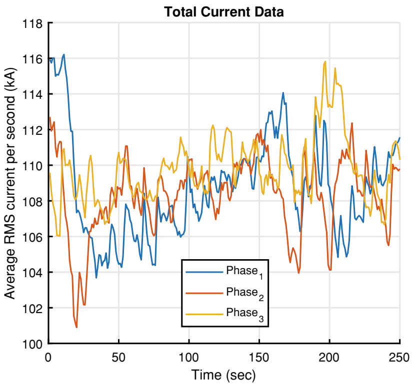

Fig. 5 Total RMS electrode current and voltage data averaged over one second periods

Fig. 6 To find the zero crossing phase resistance, we do a linear fit around the center of the voltage versus current curve

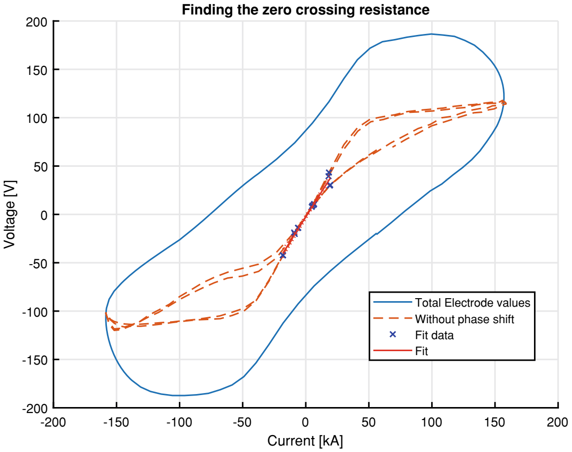

paper for all three electrodes can be seen in Fig. 5 where the RMS values for current and voltage have been averaged over one second periods. From these figures, we can easily observe the intensely variable nature of the furnace's electric properties.

Now, we can pick a piece of the data to investigate in more detail. First, we need to remove the induced voltage in the electrodes; Fig. 6 shows the voltage vs. current profile before and after the induced voltage is removed and the fit used to estimate the zero passage resistance using Eq. 4.

Now, we can find out the charge resistance R_c using Eq. 3, and since it is assumed constant over each period, the change in the phase resistance must be due to the arc resistance R_a. We can now divide the electrode current into charge and arc currents, and in Fig. 7, we can see all three current for two periods. Here, a large part is going into the arc so we estimate that it is probably rather short and that this will increase the harmonic distortions in the furnace as a result.

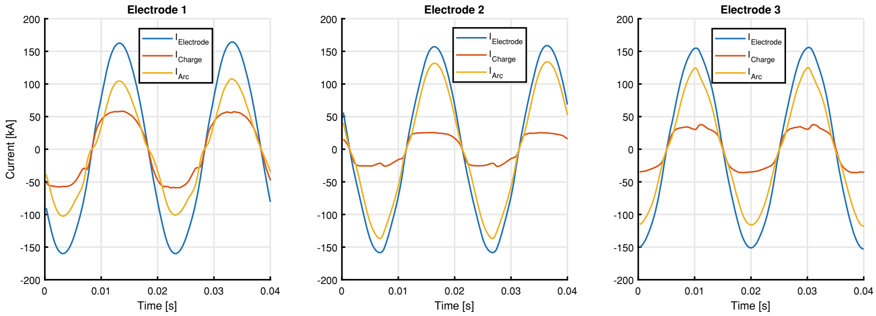

Fig. 7 Current distribution for all three electrodes. The arc and charge currents vary somewhat between them

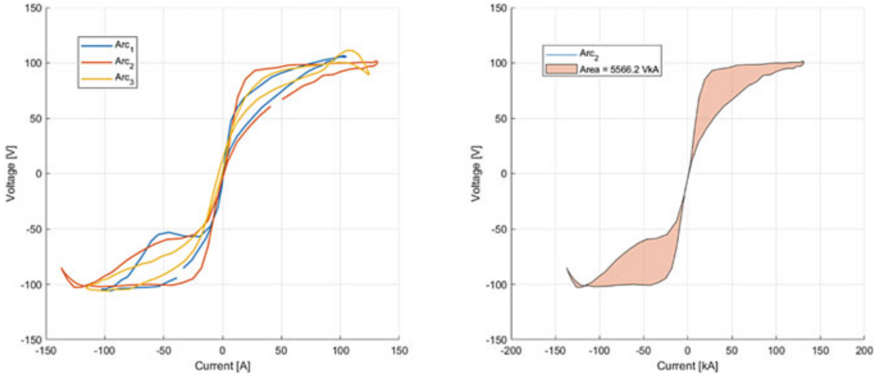

Fig. 8 The arc footprints for all three arcs and the footprint area for arc 2

Another factor of interest is the arc footprint or the voltage and current graph area. This area has the units kVA so it tells us how much power is present in the arc over a whole period but the shape of the curve can also be connected to furnace operations. Theses can be tapping, how the charge material is distributed and so forth. Figure 8 shows all three arc footprints, and the area for arc 2 is 5566.2 kVA.

More data during various furnace operations is needed to connect these footprints to what is actually happening in the furnace, and ideas would be to properly observe during tapping, charge refilling, and electrode operation and to catalog the arc footprints to get a better understanding of the electric behaviour during these events.

The final thing looked into in this paper are the harmonics. These are very important to consider since they can be used along with the rest of the parameters help give a better image of what is going on as well as being important on their own. Minimizing the total electrode harmonics is important so that the total harmonic distortion (THD) does not go over the limit allowed by the electric utility supplying power to the furnace. Seeing what frequency components are present in which current can also

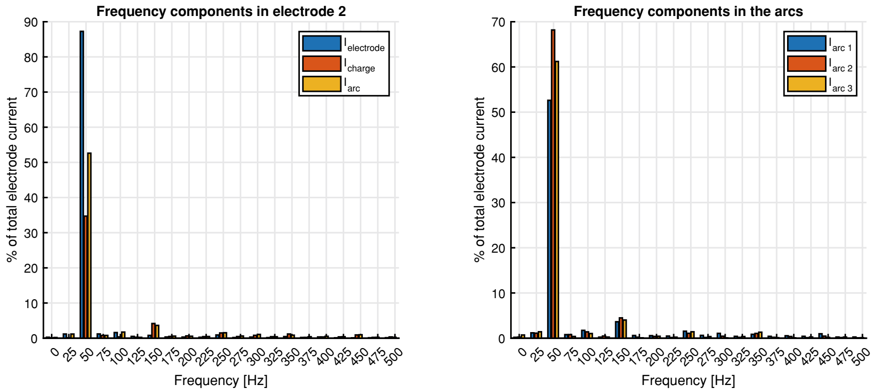

Fig. 9 The frequency components present in electrode 2 and in all three arcs as a percentage of total current in each electrode

give an idea of the situation at each electrode and in the charge material. This can be arc length and material properties in the charge and metal bath below the electrodes. Figure 9 shows the current harmonics in the furnace for electrode 2 and all the arcs, and we can see which frequency components are present in the furnace currents in the given period.

Conclusion

We have used data gathered using a DAQ system implemented in Elkems FeSi plant in Iceland to estimate various furnace parameters. The data is initially a set of voltage measurements that must be converted to actual voltage and current values based on the selected furnace, and measurement equipment. Using this data and previous measurements done on the furnace, we have devised a method of estimating the furnace current distribution profile for arc and charge currents.

The method described allows us to estimate all electrode current and voltage parameters for each time period. Using reference data for a pure arc, we can find the constant charge resistance based on each electrode's slope of the Lissajous curve. This, in turn, allows us to estimate the arc resistance, which is very variable during each period.

By having a better idea of what is going on inside the furnace in relation to the arc and charge currents should allow for smother furnace operation, which should improve silicon yield and lower the specific energy consumption. More measurements are however needed during operations to collect more data on current behaviour, preferably during tapping, filling, and general electrode operation.

Acknowledgements The Icelandic Research Fund is greatly acknowledged for their funding of this work.

References

1. Saevarsdottir G, Magnusson T, Bakken JA (2007) Electric arc on a coke bed in a submerged arc furnace
2. Saevarsdottir G (2012) Bakken: Current distribution in submerged arc furnaces for silicon metal/ferrosilicon production, international ferroalloys congress; 12th, INFACON 12. In: INFACON 12, INFACON, International Ferroalloys Congress; 12th, INFACON 12. Norwegian Ferroalloy Research Organization;. Backup Publisher: Norwegian Ferroalloy Industry, pp 717–728. https://www.pyro.co.za/InfaconXII/717-Saevarsdottir.pdf
3. Hauksdottir AS, Soderstrom T, Thorfinnsson YP, Gestsson A (1995) System identification of a three-phase submerged-arc ferrosilicon furnace. IEEE Trans Control Syst Technol 3(4):377–387
4. Lorenzo A, Lage M, Bullon J, Rivas J, Fondado A, Torres A, Farina J, Rodriguez-Andina JJ (2007) Measurement of electrical parameters in high-current arc furnaces. In: 2007 IEEE international symposium on industrial electronics, pp 1565–1568 (2007). https://doi.org/10.1109/ISIE.2007.4374836
5. Gerritsen T, Tracy PE, Saber FNM (2015) Electrode voltage measurement in electric furnaces: analysis of error in measurement and calculation
6. Haraldsson H, Tesfahunegn YA, Tangstad M, Sævarsdottir G (2021) Modelling of electric arcs for industrial applications, a Review. SSRN J
7. Saevarsdottir G, Larsen H, Bakken J. Modelling of industrial AC-arcs 3:1–15. https://doi.org/10.1615/HighTempMatProc.v3.i1.10
8. Traustason HG. Data acquisition of electrical parameters and interpretation of SAF data
9. Tesfahunegn YA, Magnusson T, Tangstad M, Saevarsdottir G (2018) Effect of carbide configuration on the current distribution in submerged arc furnaces for silicon production-a modelling approach. In: Nastac L, Pericleous K, Sabau AS, Zhang L, Thomas BG (eds) CFD modeling and simulation in materials processing 2018. The Minerals, Metals & Materials Series. Springer, Heidelberg, pp 175–185 https://doi.org/10.1007/978-3-319-72059-3_17

Volatilization Behavior of Arsenic from a Hematite Ore During Non-isothermal Heating in Argon Atmosphere: An Overview

E. K. Chiwandika and S.-M. Jung

Abstract The high grade iron ore has depleted necessitating the need to investigate the use of low grade ores that may include arsenic-containing iron ores. Arsenic (As) is volatile increasing the possibility of its removal from the ore by roasting or sintering. As volatilization from iron ore is limited by many chemical interactions with other metallic elements and oxides within the ore. The possibility of the volatilization of As from a hematite ore was investigated using the thermogravimetric-differential scanning calorimetry (TG-DSC) and the vertical tube furnace by raising the temperature at a rate of 10 K/min in the temperature range of 298 to 1623 K. Predictions of the most stable As compound formed in the sintering temperature range were done first using basic thermodynamics, then X-ray diffraction (XRD) measurements were done on the cooled and crushed samples to identify the change in phases after heating to temperatures above 1273 K. Electron probe microanalysis (EPMA) verified the possibility of the existence of some of the phases identified by XRD. Results showed that the percentage weight loss of the pellet and As loss from the pellet increased with temperature. Metallic element distribution above 1273 K showed that As was highly concentrated in the same area as Ca, Si, and Al in agreement with the XRD results and the thermodynamic predictions that showed that $3CaO{\cdot}2As_2O_5(s)$ and the $AlAsO_4(s)$ as the most stable As-containing phases even after heating to temperatures of about 1623 K.

Keywords Arsenic · Volatilization · Percentage weight loss · Volatilization rate · Sintering · Non-isothermal heating

---

E. K. Chiwandika (✉)
Department of Materials Technology and Engineering, Harare Institute of Technology, P. O. Box BE 277, Belvedere, Harare, Zimbabwe
e-mail: chiwandikae@gmail.com

S.-M. Jung
Graduate Institute of Ferrous Technology, Pohang University of Science and Technology, Pohang 37673, Korea

S. Wagstaff et al. (eds.), *Materials Processing Fundamentals 2023*, The Minerals, Metals & Materials Series, https://doi.org/10.1007/978-3-031-22657-1_15

Introduction

The global annual steel production is growing, increasing the demand for raw material. The available high grade iron ore has depleted necessitating the utilization of low grade ores. The use of such ores has some economic advantages since prices of such resources are still low due to little or no competition in demand of such ores. Arsenic (As) containing iron ores are an example of such underutilized resource. Arsenic exists in a wide range of arsenates and associated minerals and also shows some polymorphic behavior. $As_2O_3(s)$ that can exist as arsenolite, claudetite or a glassy form [1]. This makes it difficult to understand the mode of existence of As in the ores. The oxidation state of As in some of the compounds of As may form ranges from + 2, + 3, and + 5. Examples of such compounds include but not limited to arsenopyrite ($Fe_xAs_yS_z(s)$), oxides ($As_2O_5(s)$ or $As_2O_3(s)$) or sulfides ($As_2S_3(s)$) in ores [2, 3]. Iron ores may contain As as high as 0.5 weight percent [4] and when such ores are directly charged into the blast furnace, As readily dissolves into the molten iron rendering its removal very difficult. The As in steel negatively impacts the mechanical properties of steel products such that engineers demands that steels for special purposes like those used in petroleum bars, large dynamo rotor, and in nuke industries contain no As [5]. As removal methods prior to the blast furnace process should be developed for the effective utilization of this resource.

Some researchers have tried to remove As by roasting or sintering, but these methods are not effective enough as 50–75% of the As was retained inside the ore [6]. Contreras et al. [7] used the HSC chemistry 5.0 software to predict the distribution of trace element between gas, liquid, and solid phases as a function of temperature in coal combustion. Their results showed that $3CaO \cdot As_2O_5(s)$ was the most stable phase, and remains non-volatile even at temperatures above 1573 K in addition, the water solubility of this compound was found to be low [7]. As volatilization was strongly related to the chemical bonds holding As in coal at 873 to 1773 K [4].

The behavior of As in iron ores during sintering is yet to be cleared due to the complexity of As existence. The standard gas for calibrating state-of-the-art equipment like the quadrupole mass spectrometer (QMS) is not easily available for online gas analysis during As volatilization. Furthermore, development of the pollution prevention method caused by the treatment of such an ore demands great attention. This investigation is aimed at providing the basic understanding of some of the phases that might develop during sintering of the hematite ore containing As and finding the most suitable temperature to remove As which might also help in the development of the pollution prevention methods caused by As.

Thermodynamic of As Volatilization

The generation of calcium ferrite is of great importance in the sintering of iron ores due to better strength and reducibility caused by the presence of derivatives of calcium ferrites in sinter [8]. Volatilization of As from iron ore during sintering or roasting can be complicated by interactions with other metal components in the ore. The possible compounds formed by these interactions includes $FeAsO_4(s)$, $AlAsO_4(s)$, $KAs_3O_4(s)$, $NaAs_3O_8(s)$, $3MgO{\cdot}As_2O_5(s)$, and $CaO{\cdot}As_2O_5(s)$ [2, 4, 7, 9]. A thermodynamic analysis of some the compounds that may be formed in the sinter in the presence of As was done by the plot of ΔG^o vs temperature, Fig. 1, using the thermodynamic data from the equations below [10]

$$CaO(s) + Fe_2O_3(s) = CaO \cdot Fe_2O_3(s) \tag{1}$$

$$\Delta G^\circ = -30,000 - 4.8T\ (973 - 1489\ \text{K})\text{J/mol} \tag{2}$$

$$2CaO(s) + Fe_2O_3(s) = 2CaO \cdot Fe_2O_3(s) \tag{3}$$

$$\Delta G^\circ = -53,100 - 2.5T(973 - 1723\text{K})\text{J/mol} \tag{4}$$

$$2CaO(s) + SiO_2(s) = 2CaO \cdot SiO_2(s) \tag{5}$$

$$\Delta G^\circ = -120,000 - 11.3T(298 - 2403\ \text{K})\text{J/mol} \tag{6}$$

$$Al_2O_3(s) + As_2O_3(g) + O_2(g) = 2AlAsO_4(s) \tag{7}$$

$$\Delta G^\circ = -536,068 + 93.49T(1373 - 1673\text{K})\ \text{J/mol} \tag{8}$$

$$3CaO(s) + As_2O_3(g) + O_2(g) = 3CaO \cdot 2As_2O_5(s) \tag{9}$$

$$\Delta G^\circ = -775,454 + 268.8T(1373 - 1678\ \text{K})\ \text{J/mol} \tag{10}$$

The ΔG^o for Eqs. (7) and (9) was calculated using FactSage 6.2 software.

It can be concluded that the $3CaO{\cdot}2As_2O_5(s)$ and $2AlAsO_4(s)$ are the more stable compounds at the selected temperature range than the calcium ferrite and the $2CaO{\cdot}SiO_2(s)$.

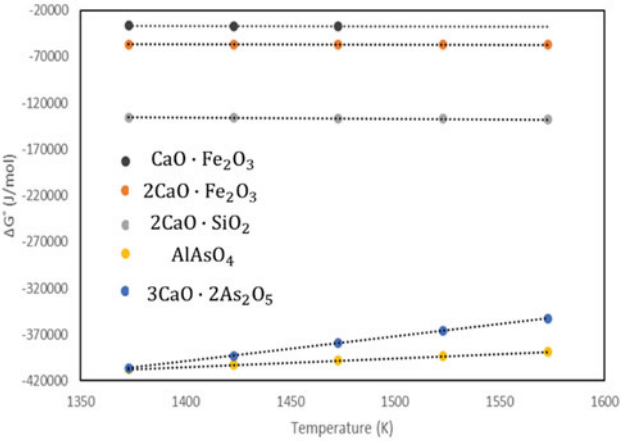

Fig. 1 Plot of ΔG^{o} versus temperature for some of the possible reactions that can occur during sintering

Experimental

Materials

To a hematite ore with As content of 0.035 wt%, loss on ignition (LOI) of 7.10 wt% and an average particle size of under 1 mm, about 1 wt% reagent grade $As_2O_3(s)$ was added targeting an As content above 0.5 wt% in the blend. The mixture was blended at 34 revolutions per minute (rpm) for 1 h using the Turbula Mixer (T_2F Nr. 120,942 Switzerland) to make a blend of chemical composition shown in Table 1.

The As content in the blend was then measured using the inductively coupled plasma atomic emission spectroscopy (ICP-AES) and found to be 0.74 wt%. X-ray fluorescence (XRF) analysis was done on the ore to have a general understanding of the other components in the ore. The other components in the ore were found to be $TiO_2(s)$, $Cr_2O_3(s)$, $NiO(s)$, $P_2O_5(s)$, and $Na_2O(s)$. The phases in the hematite ore-As_2O_3 blend were identified by X-ray diffraction (XRD) (Bruker AXS) with a Cu tube at a scan angle of 20° to 80°, scanning rate of 2°/min, a voltage of 40 kV, and a current of 40 mA. The results were as shown in Fig. 2.

The Fe-containing phase identified in the hematite ore-As_2O_3 blend was the $Fe_2O_3(s)$. As existed as a As_2O_3 dimer, $As_4O_6(s)$ in the blend. The gangue existed in the ore as the $SiO_2(s)$, $MgO{\cdot}SiO_2(s)$, and the $Al_2O_3{\cdot}SiO_2(s)$.

Table 1 Chemical composition of hematite ore-As_2O_3 blend (wt%)

Analyte	Total Fe	FeO	Fe_2O_3	SiO_2	Al_2O_3	CaO	S	K	MgO	MnO	As	LOI	Others
Fe_2O_3 ore- As_2O_3 blend	54.36	0.25	77.45	6.08	1.59	0.36	0.07	0.01	0.09	0.42	0.74	9.49	12.94

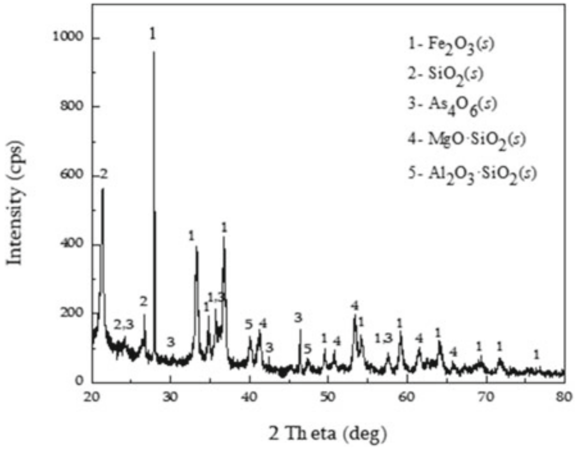

Fig. 2 XRD pattern of the hematite ore-As_2O_3 blend

Experimental Procedure

Loss of Mass Profile Based on the TG-DSC

The loss of mass profile in the ores was determined by the TG-DSC (TGA/DSC 1 Star system Mettler Toledo). About 100 mg of the hematite ore only and hematite ore-As_2O_3 blend were placed in an aluminium oxide crucible and placed inside the TG-DSC furnace, and the temperature was raised from room temperature to 1573 K at a rate of 10 K/min in argon atmosphere. An Ar atmosphere at a flow rate of 70 mL/min was used during this procedure. The loss of mass profile was also investigated using the vertical tube furnace where both the ore and the ore-As_2O_3 blend were pressed at 20 MPa into cylindrical disc pellets weighing 1 g. Two pellets with total mass of 2 g were placed into a platinum crucible (basket) and suspended in the vertical tube furnace using a platinum wire, and temperature was raised at 10 K/min to target temperature in an Ar atmosphere at 1 L/min. When the target temperature ranging from 298 to 1623 K was reached, the crucible was pulled to the cold end of the furnace and cooled to room temperature in Ar atmosphere. After cooling the final mass of the pellets was measured. Pellets heated to temperatures above 1273 K were crushed to fine powder and supplied for ICP analyses to determine the amount of As remaining. XRD analyses were also performed on these heated samples, and some of the pellets were prepared for electron probe microanalysis (EPMA; (Joel (Japan)/JXA-8530F) analyses for verification of the existence of phases identified by XRD. Elemental mapping by EPMA analyses were done using a voltage of 20 keV and a beam current of 50 nA at a magnification of 400X. Arsenic volatilized was the evaluated using data obtained from ICP using Eq. (11)

$$\%\Delta \text{ As volatilized} = \frac{\left(\frac{\text{As}_i}{W_i}\right) - \left(\frac{\text{As}_f}{W_f}\right)}{\left(\frac{\text{As}_i}{W_i}\right)} \times 100 \qquad (11)$$

where As_i is the initial As content in the sample, As_f is the final As content in the sample, W_i is the initial weight of the sample, and W_f is the final sample weight.

Results and Discussion

Mass Loss as a Function of Temperature

The mass loss profile from the hematite ore and from the hematite-As_2O_3 blend were investigated using the TG-DSC where the weight loss form the hematite ore only was used as the reference. The results were as shown in Fig. 3a and b.

The mass loss profiles from both the ore and from the blend showed a similar trend. This mass loss was from the volatilization of all the volatile matter in the ores. Comparison between Fig. 3a and b showed that the mass loss from the ore-As_2O_3 blend was higher than that from the ore alone. This led to the conclusion that part of the difference in mass loss curve between that shown in Fig. 3a and b might be attributed to the presence of the As_2O_3 since the mass loss curve of the hematite ore alone was used as the baseline. In addition, the loss on ignition (LOI) of the hematite ore was 7.10 wt% while that of hematite-As_2O_3 was 9.49 wt%. The difference was about 2.39 wt% and part of this might be from the volatilized As_2O_3. However, more research should be done after calibrating the QMS by nebulizing a solution of known As concentration for online analyses. This will enable the quantification of the exact amount of As volatilized since a natural ore with other diverse volatile materials was used. The mass loss profiles based on the vertical tube furnace shown

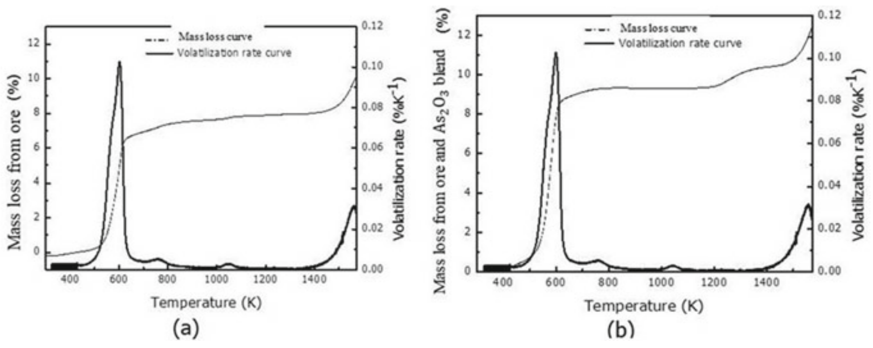

Fig. 3 Plot of mass loss and volatilization rate with increasing temperature-using data from TG-DSC of: **a** hematite ore only and **b** hematite ore-As_2O_3 blend [11]

Fig. 4 Plot of mass loss with increasing temperature-using data based on the vertical tube furnace [11]

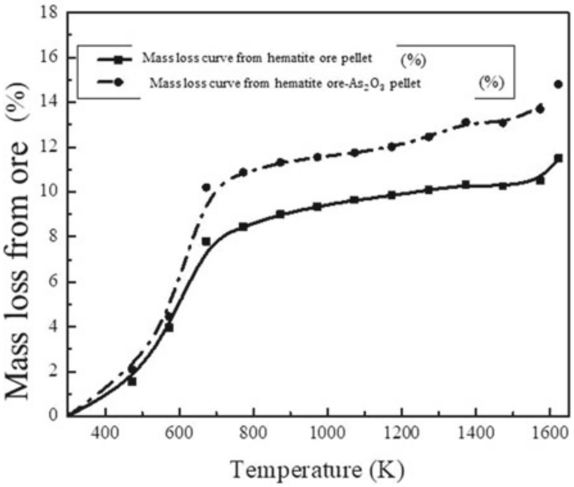

in Fig. 4 showed some similar trend with that obtained from the TG-DSC data in Fig. 3. Thus, the change in phases were therefore investigated using samples heated non-isothermally in the vertical tube furnace.

The mass loss profile shown in Fig. 3a and b must be related to the volatilization rate and the bonding strength holding the volatile material in the pellet. The volatilization rate curve was plotted by taking the derivative of the mass loss profile shown in Fig. 3a and b. A closer inspection of the volatilization rate curves shown in Fig. 3a and b showed some specific peaks at 473 to 673 K, 700 to 800 K, 1000 to 1100 K, and above 1400 K on the volatilization rate curves of both the hematite ore and the hematite ore-As_2O_3 blend. This led to the conclusion that the volatilization of the volatile matter from the ore depends on the chemical bonds holding them in the ore [4].

The peak at 473 to 673 K in Fig. 3a might be due to dehydration of the ore while that in Fig. 3b might be due to dehydration along with the As lost from the phase transformation of $As_2O_3(s)$. The phase transformation of $As_2O_3(s)$ from the arsenolite to the claudetite was predicted to occur at around 503 K thermodynamically. This phase transformation temperature is expected to occur at 453 K in the presence of water vapor [1]. Furthermore, the sublimation of $As_2O_3(s)$ occurs at around 588 K [12]. The TG-DSC analysis of the $As_2O_3(s)$ reagent grade was done to provide more evidence as shown in Fig. 5.

Figure 5 shows that the mass loss started at around 503 K corresponding to the phase change of the $As_2O_3(s)$ and increased rapidly up to temperatures of just above 600 K. This acceleration might have been caused by the sublimation of $As_2O_3(s)$ that was reported to occur at around 588 K [12].

Part of the mass loss of the hematite ore-As_2O_3 blend at 700 to 800 K in Fig. 3b was from the evaporation of the remaining $As_2O_3(s)$ among other reactions, the boiling temperature of $As_2O_3(s)$ was reported to be around 703 K [12] Fig. 5 shows

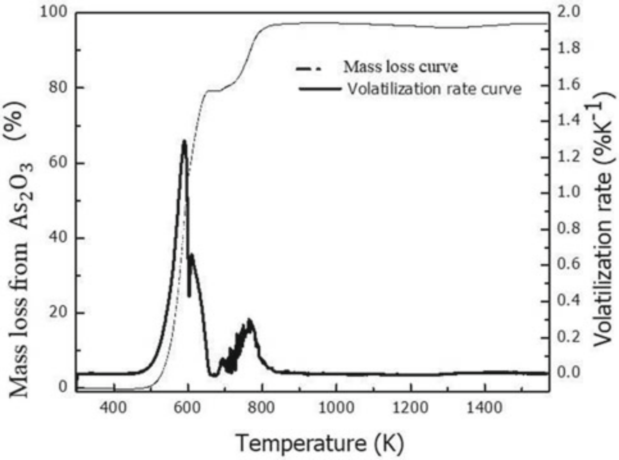

Fig. 5 Plot of mass loss and volatilization rate with increasing temperature-using data from TG-DSC of As_2O_3 [11]

a characteristic peak between 700 to 800 K corresponding to the evaporation of the $As_2O_3(s)$. The increase in volatilization rate observed above 1400 K shown in Fig. 3a and b might be due to the loss of $O_2(g)$ from the thermal decomposition of hematite that occurs above 1473 K [13]. Volatilization of As from the decomposition of arsenates other than $3CaO{\cdot}As_2O_5(s)$, $2CaO{\cdot}As_2O_5(s)$, and $AlAsO_4(s)$ above 1 373 K is also expected. It is believed that these were the cause for the increase in mass loss observed above 1400 K in Fig. 3b.

Temperature range of 1373–1673 K is of great importance in iron ore sintering, sample non-isothermally heated to this temperature range were crushed and the As content analyzed using the ICP-AES to determine the amount of As lost from the samples. Figure 6 shows the As volatilization trend from the ore.

Fig. 6 Arsenic volatilized from the sample with increasing temperature

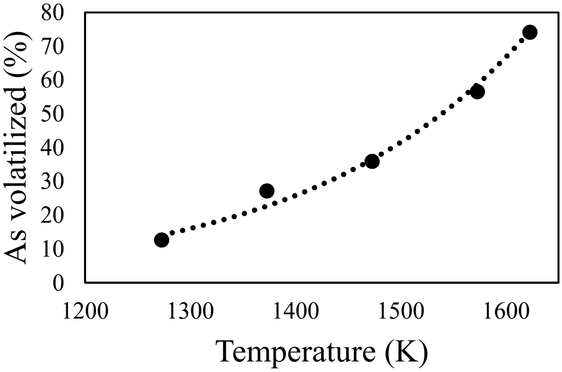

The loss of As from the blend increased with increasing temperature and complete removal of As from the ore was not accomplished even at 1623 K, Fig. 6. Part of the As might have remained trapped inside the ore due to the interactions with other metal oxide in the ore.

Phase Development with Increasing Temperature

In the sintering of iron ores, phases developed at temperatures higher than 1373 K are of great importance. Figure 7a–d shows the XRD results of the hematite blend after heating at 1373 K and above.

The phases identified at 1373 K and 1473 K were the $Fe_2O_3(s)$, $SiO_2(s)$, $MnAsO_4(s)$, $2CaO{\cdot}As_2O_5(s)$, and $AlAsO_4(s)$, at 1573 K, $MnAsO_4(s)$ decomposed and the $Fe_2O_3(s)$, $Fe_3O_4(s)$, $SiO_2(s)$, $3CaO{\cdot}As_2O_5(s)$, and $AlAsO_4(s)$ were also phases identified while the $3CaO{\cdot}As_2O_5(s)$, $2CaO{\cdot}As_2O_5(s)$, and $AlAsO_4(s)$ phases were the most stable As-containing phases at 1623 K. Figure 7c–d provided the evidence of the thermal decomposition of hematite shown by the presence of $Fe_3O_4(s)$ peaks at 1573 K and 1623 K. The complete escape of the As from the ore was complicated by the presence of other metallic oxides in the ore in agreement with the thermodynamic prediction in Fig. 1.

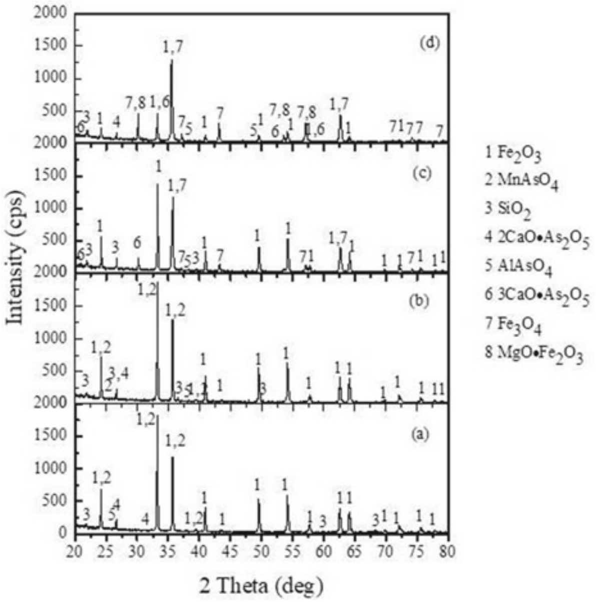

Fig. 7 XRD analysis of the hematite ore-As_2O_3 pellet after non-isothermal heating to: **a** 1373 K, **b** 1473 K, **c** 1573 K, and **d** 1623 K [11]

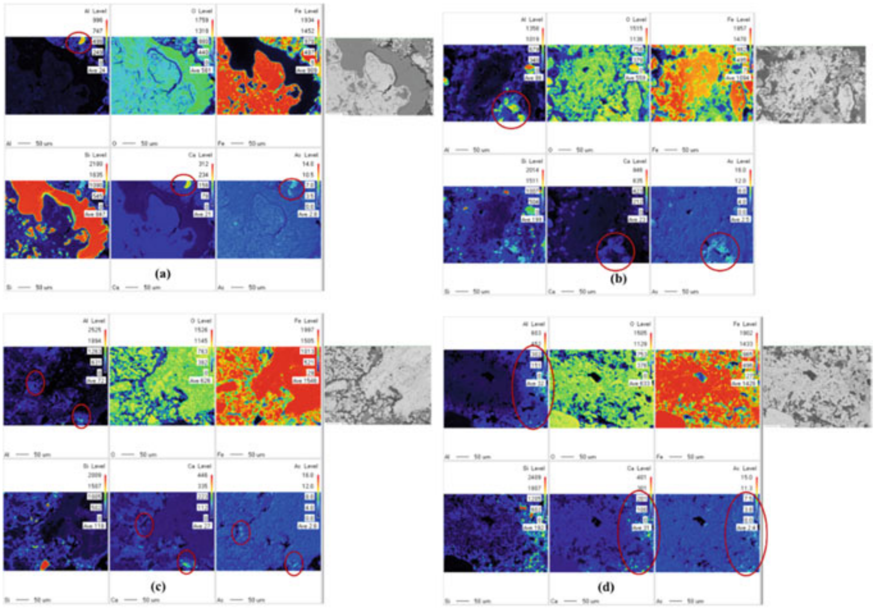

Fig. 8 Elemental mapping of the pellet non-isothermally heated to: **a** 1373 K, **b** 1473 K, **c** 1573 K, and **d** 1623 K [11]

Elements Distribution in the Sintered Pellets with Increasing Temperature

The EPMA (Joel JXA-8530F) mappings were performed to provide more evidence that As remained trapped inside the sintered ore even after heating to temperatures above 1273 K, Fig. 8a–d

It can be clearly shown in Fig. 8a–d that As was highly concentrated in the same area as Ca, and Al shown by the points marked in red on the EPMA mappings in agreement with the thermodynamic predictions in Fig. 1. It can be safely concluded that $2CaO{\cdot}As_2O_5(s)$, $3CaO{\cdot}As_2O_5(s)$, and the $AlAsO_4(s)$ were likely to be the most stable As-containing phase basing on the XRD, EPMA, and thermodynamic predictions.

The results of this research only provide the basic understanding of the behavior of As during non-isothermal heating in an Ar atmosphere but in actual iron ore sintering process, $CaO(s)$ is intentionally added to produce fluxed and semi-fluxed sinters in a gaseous atmosphere that varies from reducing during the burning of the coal to oxidizing during cooling. Further, research should be done in reducing and oxidizing conditions and on the kinetics of As volatilization to fully understand arsenic volatilization during sintering. The production of acidic sinters should be investigated since lower amount of As is expected to be trapped inside the sinter in the form of $2CaO{\cdot}As_2O_5(s)$ or $3CaO{\cdot}As_2O_5(s)$. Some preliminary results on the

Fig. 9 Plot of $\ln[(1-(1-\alpha)^{1/3})^2/T^2]$ versus $1/T$ based on non-isothermal As volatilization

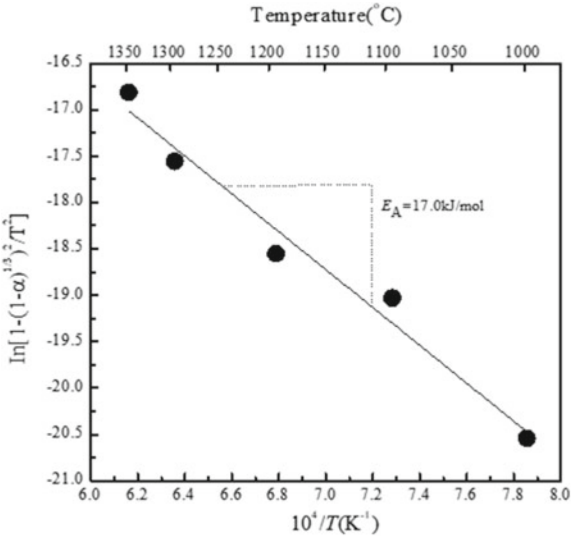

kinetics of non-isothermal As volatilization [14] based on results shown in Fig. 7 are shown in Fig. 9.

The activation energy, E_A, and the pre-exponential factor, A, were calculated to be 17.0 kJ/mol and 246.6 min^{-1}, respectively. The evaluated activation energy value falls within the range of the diffusion-controlled mechanism, 8.37–20.93 kJ/mol, reported in the literature [15]. However, more results are needed were the heating rate is changed to fully validate the kinetics results. Further investigation, especially in gold production on the use of CaO(s) or Al_2O_3(s) to hold As from the off gas in the form of 2CaO·As_2O_5(s), 3CaO·As_2O_5(s), or $AlAsO_4$(s) to prevent pollution, must be done since these arsenates can thermodynamically form and also appears to be stable even at 1623 K.

Conclusions

(1) The volatilization of As and other volatile components in the ore increased with temperature. The rate of volatilization may depend on the chemical bonds holding the volatile materials in the ore.

(2) The presence of metal oxide like CaO or Al_2O_3 have potential of preventing the complete volatilization of As by the formation of the stable 2CaO·As_2O_5(s), 3CaO·As_2O_5(s), and $AlAsO_4$(s). These interactions with different metal oxide components in the ore limited the complete escape of As from the pellet during the non-isothermal heating process even at temperatures as high as 1623 K.

(3) Further, investigations on the formation of the $2CaO \cdot As_2O_5(s)$ or $3CaO \cdot As_2O_5(s)$ in developing technologies for As pollution prevention by using $CaO(s)$ to trap gaseous arsenic compounds in the off gas are highly encouraged.

(4) Preliminary kinetic results showed the evaluated activation energy, E_A, and the pre-exponential factor, A, were 17.0 kJ/mol and 246.6 min^{-1}, respectively. The evaluated activation energy value falls within the range of the diffusion-controlled mechanism, however, more results are required for validation.

References

1. Safarzadeh MS, Miller JD, Haung HH (2014) The behavior of arsenic trioxide in non-ferrous extractive metallurgical processing. Metallurgical Res Technol 111:95–105
2. Cheng R, Ni H, Zhang H, Zhang X, Bai S (2017) Mechanism research on arsenic removal from arsenopyrite ore during a sintering process. Int J Miner Metall Mater 24(4):353–359
3. Grund SC, Hanusch K, Wolf HU (2005) Arsenic and arsenic compounds. Wiley-VCH Verlag GmbH & Co. 4:1–43
4. Lui H, Pan W, Wang C, Zhang Y (2016) Volatilization of As during coal combustion based on isothermal thermogravimetric analysis at 600–1500°C. Energy Fuels 30:6790–6798
5. Lu Q, Zhang S, Hu X (2011) Study on removal arsenic from iron ore with arsenic in sintering process. Trans Tech Publication 284:238–241
6. Chakraborti N, Lynch DC (1983) Thermodynamics of roasting arsenopyrite. Metall Trans B 14:239–251
7. Contreras ML, Arostegui JM, Armesto L (2009) Arsenic interactions during co-combustion process based on thermodynamic and equilibrium calculations. Fuel 88:539–549
8. Harvey T, Pownceby MI, Chen J, Webster NAS, Nguyen TBT, Matthews L, O'Dea D, Honeyands T (2021) Effects of temperature, time, and cooling rate on the mineralogy, morphology and reduction of iron ore sinter analogues. JOM 78:345–355
9. Mikhail SA, Turcotte AM (1992) Thermal decomposition of arsenopyrite in the presence of calcium oxide. Thermochim Acta 212:27–37
10. Lee H (1999) Chemical thermodynamics for metals and materials. Imperial College Press, London, p 287
11. Chiwandika EK, Jung SM (2022) Volatilization behavior of arsenic from a hematite ore during non-isothermal heating in argon atmosphere. J Sustain Metallurgy 8:458–467
12. Helsen L, Bulck EV, Bael MKV, Vanhoyland G, Mullens J (2004) The behavior of arsenic oxide (AS_2O_5 and As_2O_3) and the influence of reducing agents (glucose and activated carbon). Thermochim Acta 414:145–153
13. Kim BS, Xing L, Qu Y, Wang C, Shao L, Zou Z, Song W (2020) Kinetic study on thermal decomposition behavior of hematite ore fines at high temperature. Metall and Mater Trans B 51:395–406
14. Kim BS, Kim EY, Kim CK, Lee HI, Sohn JS (2008) Kinetics of oxidative roasting of complex copper concentrate. Minerals Trans 49(5):192–1198
15. Biswas AK (1981) Principles of blast furnace ironmaking. Cootha Publishing House, Brisbane, Australia, pp 34–39

Comprehensive Recovery of Elemental Sulfur and Sulfide Minerals from Pressure Acid Leaching Residue of Zinc Sulfide Concentrate with an Integrated Flocculation Flotation-Hot Filtration Process

Guiqing Liu, Bangsheng Zhang, Zhonglin Dong, Fan Zhang, Fang Wang, Tao Jiang, and Bin Xu

Abstract An efficient flocculation flotation-hot filtration process was developed to recover elemental sulfur and sulfide minerals from a pressure acid leaching residue of zinc sulfide concentrate. The particle size distribution of the residue indicated that the portion of thin particle with the size of -37 um reached 67.65 and 36.27% of sulfur in the residue was distributed in this size fraction, necessitating the flocculation flotation for recovering the elemental sulfur and sulfide minerals. 94.59% of the sulfur was recovered with the flotation process of one-time blank rougher, two-time agent-added roughers, and two-time blank cleaners with Z-200 as the collector and polyacrylamide as the flocculant. After hot filtration for the flotation concentrate at 145 °C for 2 h, 85.32% of the elemental sulfur in the concentrate was recovered, and its product purity reached 98.64%. The filter cake of sulfide minerals can be returned to the leaching stage for zinc recovery.

Keywords Pressure acid leaching residue of zinc sulfide concentrate · Elemental sulfur · Sulfide minerals · Flocculation flotation · Hot filtration

---

G. Liu
School of Metallurgy, Northeastern University, Shenyang 110819, Liaoning, China

G. Liu · B. Zhang · F. Zhang · F. Wang
Jiangsu BGRIMM Metal Recycling Science and Technology Co. Ltd, Xuzhou 221121, Jiangsu, China

Z. Dong · T. Jiang · B. Xu (✉)
School of Minerals Processing and Bioengineering, Central South University, Changsha 410000, Hunan, China
e-mail: xubincsu@csu.edu.cn

B. Xu
Peace Building, School of Minerals Processing and Bioengineering, Central South University, Changsha 410083, Hunan, China

S. Wagstaff et al. (eds.), *Materials Processing Fundamentals 2023*, The Minerals, Metals & Materials Series, https://doi.org/10.1007/978-3-031-22657-1_16

Introduction

Zinc is an important non-ferrous metal and has been widely applied in many fields such as automobile, battery, and construction [1]. Traditionally, zinc is extracted by pyro-hydrometallurgical process from sphalerite (i.e., zinc sulfide) [2, 3]. However, high operation cost is required because the process is conducted at high temperatures [4–7]. In addition, hazardous gas containing SO_2 and some heavy metals (e.g., Hg and Pb) will be generated, which causes a great threat to the environment and human beings [8–12].

In order to avoid the disadvantages of pyro-hydrometallurgical processes, hydrometallurgical processes have been developed. Among the alternatives, oxygen pressure acid leaching process has attracted the most attention [13], and the related reaction is shown in Eq. (1). It can be seen that apart from $ZnSO_4$, part of sulfur in zinc sulfide is converted into elemental sulfur [14–16]. Thus, the residue from oxygen pressure acid leaching of sphalerite can be regarded as a resource for recovering elemental sulfur [17].

$$2ZnS + 2H_2SO_4 + O_2 = 2ZnSO_4 + 2H_2O + 2S \tag{1}$$

It should be noted that some undissolved sulfides in the sphalerite during leaching also enter into the residue. Thus, the separation and recovery of elemental sulfur and sulfides have become a vital issue. Froth flotation is a predominant beneficiation technique that can selectively separate target minerals from gangue minerals by making use of their difference in natural hydrophobicity [18]. However, two problems needed to be solved when froth flotation was adopted. First, oxygen pressure acid leaching residue generally possesses a very small particle size, and thus, it is difficult to recover it by conventional froth flotation. Second, the elemental sulfur and sulfides have very close hydrophobicity, and thus, their selective flotation separation is difficult.

In this study, an efficient flocculation flotation-hot filtration process was developed to recover elemental sulfur and sulfide minerals from a pressure acid leaching residue of zinc sulfide concentrate. One-time agent-added rougher flotation was first conducted to ascertain the optimal floatation condition. Then, open-circuit and closed-circuit flocculation flotation experiments were successively performed to ascertain flotation flow sheet and corresponding test indexes. Finally, hot filtration was adopted to separate elemental sulfur from sulfide minerals. High-purity elemental sulfur product was recovered, and sulfide minerals can be returned to the leaching stage for zinc recovery, and thus, the comprehensive recovery of the pressure acid leaching residue was realized.

Materials and Methods

Materials and Reagents

The raw material in this study was oxygen pressure leaching residue of zinc sulfide concentrate from a metallurgical plant in Qinghai Province. The residue was mixed adequately with wet sampler for the next tests and experiments. The chemical composition of leaching residue in Table 1 showed that sulfur was the most abundant element whose content achieved 44.41%. The phase analysis of sulfur in Table 2 indicated that 37.73% of the sulfur in the residue existed in the form of elemental sulfur. The mineral composition of the residue was detected by X-ray diffraction (XRD), and the result is shown in Fig. 1. The main minerals are elemental sulfur, jarosite, pyrite, and quartz.

The particle size distribution of the residue is shown in Table 3. The sulfur distribution ratio in the size fraction of -37 μm was the highest (36.27%), and the sulfur grade in the size fraction of −74 + 44 μm was the highest (89.38%), and the sulfur distribution ratio in this fraction also achieved 32.71%. Thus, sulfur was mainly distributed in the two fractions. The result indicated that the particle size of leaching residue was very fine, and flocculation flotation may be a feasible method to recover the sulfur in the residue.

All the reagents used in this study such as O-isopropyl-N-ethyl thionocarbamate (Z-200), ammonium dibutyl dithiophosphate (ADDTP), and ethyl xanthate (EX) were of analytical grade, and tap water was used in all experiments.

Table 1 Chemical composition of the oxygen pressure leaching residue (%)

Element	Cu	Pb	Zn	S	Fe	SiO_2	MgO
Content	0.055	2.24	2.28	44.41	21.23	14.34	0.33
Element	Al_2O_3	CaO	As	Mn	Cd	Ag*	
Content	2.01	3.40	0.12	0.11	0.016	96.5	

Note "*" unit is g/t

Table 2 Sulfur phase distribution of the oxygen pressure leaching residue (%)

Sulfur phase	Elemental sulfur	Sulfide	Sulfate	Total
Content	37.73	1.94	2.91	42.58
Distribution	81.97	12.03	6.00	100

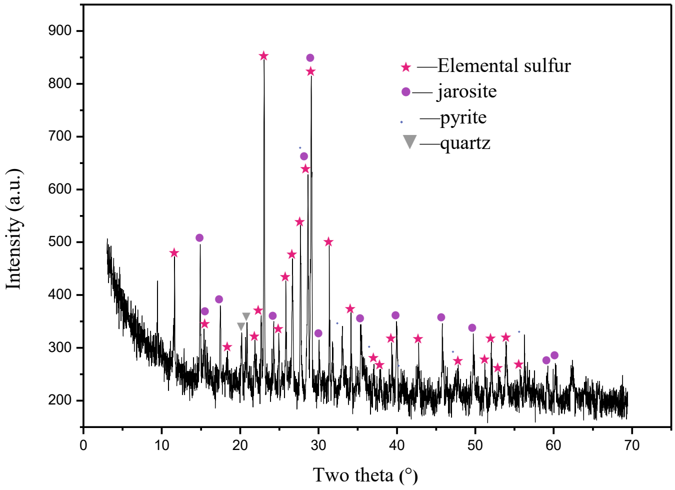

Fig. 1 XRD spectrogram of the oxygen pressure leaching residue

Table 3 Particle size distribution of the oxygen pressure leaching residue

Size fraction (mesh)	Weight (g)	Yield (%)	Grade (%)	Distribution ratio (%)
+100	1.8	0.35	67.94	0.53
−100+200	47.2	9.07	85.79	17.39
−200+325	85.2	16.37	89.38	32.71
−325+400	34.2	6.57	89.19	13.10
−400	352.2	67.65	23.97	36.27
Total	520.6	100.00	44.72	100.00

Flotation Experiment

The flotation experiments of oxygen pressure acid leaching residue were carried out in an XFD-63 flotation machine. First, the tap water and residue were put into the cell, and the pH value of formed pulp was regulated to around 8.0 with HCl or NaOH solution. After that, the collector and flocculant polyacrylamide (if used) were successively added into the pulp which was separately agitated at 1650 rpm for 2 min. The aeration flotation was performed for 5 min, and the concentrate and tailing were dried for sulfur content analysis.

Fig. 2 Flow sheet of one-time rougher flotation

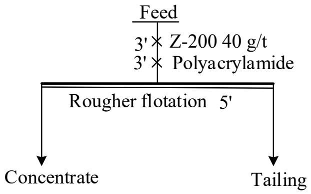

Analytical Methods

The elemental composition of the oxygen pressure leaching residue was analyzed with inductively coupled plasma-atomic emission spectrometer (ICP-AES). The sulfur phase composition was detected with a chemical selective dissolution method on the basis of the different dissolution behavior of different sulfur phase in various solvents. The particle size distribution was ascertained by a wet screen analysis. The mineralogical composition was determined by X-ray diffractometer.

Results and Discussion

One-Time Rougher Flocculation Flotation

Effect of Flocculant Dosage

Polyacrylamide was used as the flocculant, and the effect of its dosage on the grade and recovery of sulfur in flotation concentrate was first investigated at pulp concentration 35%. The used flow sheet is shown in Fig. 2, and the results are indicated in Fig. 3.

With the increase of polyacrylamide dosage, the sulfur grade of the concentrate first increased and achieved its maximum 73.93% with 50 g/t polyacrylamide. However, when polyacrylamide dosage was over this value, the sulfur started to decline. The sulfur recovery rose with increased polyacrylamide dosage, but as the dosage was beyond 50 g/t, no obvious increase of the sulfur recovery was obtained. Therefore, the optimal polyacrylamide dosage was 50 g/t.

Effect of Type of Collector

The effect of collector type on the grade and recovery of sulfur in flotation concentrate was also studied at a pulp concentration 35%. The used flow sheet is presented in Fig. 4, and the results are shown in Fig. 5.

From the figure, when EX was adopted, the sulfur grade arrived at 75.26%, but its recovery was only 80.02%. As for ADDTP, the sulfur recovery was enhanced to

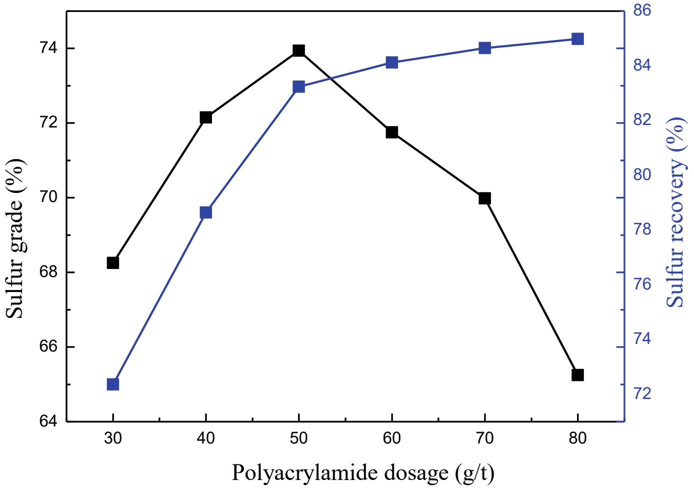

Fig. 3 Effect of polyacrylamide dosage on the sulfur grade and recovery of flotation concentrate

Fig. 4 Flow sheet of one-time rougher flotation

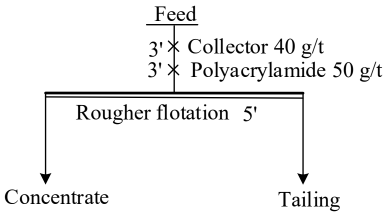

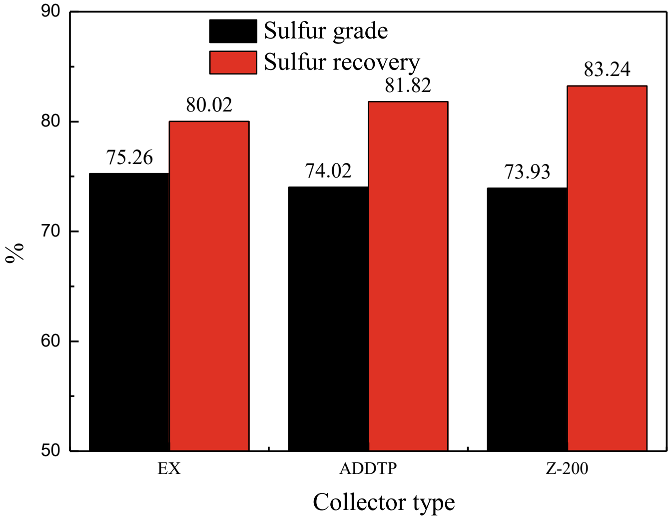

Fig. 5 Effect of collector type on the sulfur grade and recovery of flotation concentrate

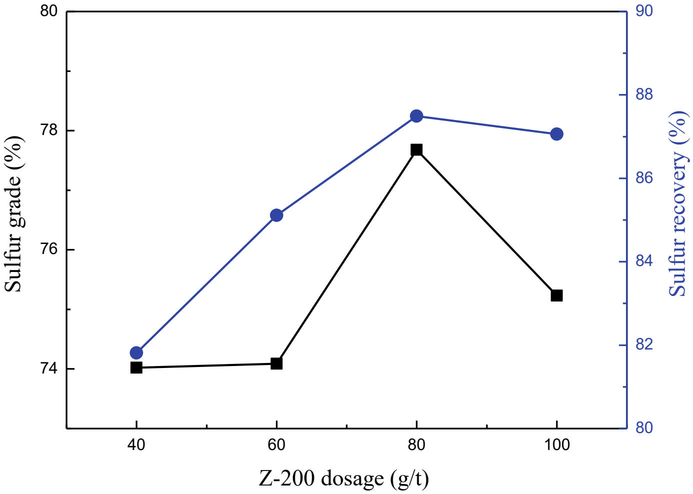

Fig. 6 Effect of Z-200 dosage on the sulfur grade and recovery of flotation concentrate

81.82%, but its sulfur grade was lower than that of EX. In comparison, 83.24% of the sulfur was recovered, and the sulfur grade of the concentrate achieved 73.93% when Z-200 was used. Thus, Z-200 exhibited the optimal flotation performance on the sulfur in the oxygen pressure leaching residue. Therefore, Z-200 was selected as the flotation collector.

Effect of Collector Dosage

The effect of Z-200 dosage on the grade and recovery of sulfur in flotation concentrate was investigated at a pulp concentration 35% and polyacrylamide dosage of 50 g/t, and the results are indicated in Fig. 6.

With the increase of Z-200 dosage, the sulfur grade and recovery of the concentrate first increased and achieved their maximums 77.68 and 87.49% at 80 g/t. However, when Z-200 dosage was beyond this value, both the sulfur grade and recovery began to decline. This is because Z-200 also adsorbed on the surfaces of gangue minerals when its dosage was too high. As a result of this, these gangue minerals were also floated with elemental sulfur and sulfide minerals, leading to a decrease of sulfur grade and recovery. Thus, the optimal Z-200 dosage was 80 g/t.

Effect of Pulp Concentration

The effect of pulp concentration on the grade and recovery of sulfur in flotation concentrate was investigated at Z-200 dosage 80 g/t and polyacrylamide dosage of 50 g/t, and the results are displayed in Fig. 7.

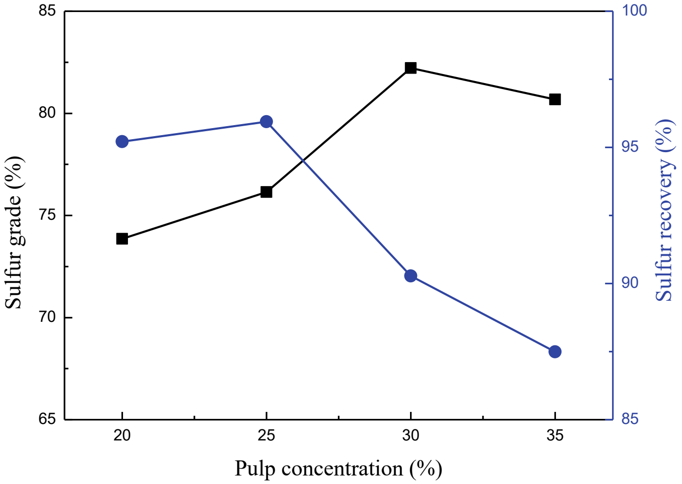

Fig. 7 Effect of pulp concentration on the sulfur grade and recovery of flotation concentrate

Clearly, pulp concentration had a significant influence on the grade and recovery of sulfur. With the increase of pulp concentration from 20 to 25%, both the grade and recovery of sulfur increased. Nevertheless, when the pulp concentration was over 25%, the sulfur recovery started to decrease although the sulfur grade continued to increase. Thus, the optimal pulp concentration was 25%.

Open-Circuit Flocculation Flotation

Based on the above conditional tests and further flotation flowchart experiments, the flow sheet of open-circuit flocculation flotation was ascertained, as is shown in Fig. 8, and the results are shown in Table 4. Here, the purpose of adding one-time blank rougher before agent-added rougher was to allow the easily floatable elemental sulfur and sulfide to adhere to the surface of the foam by virtue of their hydrophobicity. As a result, part of the elemental sulfur and sulfide could be recovered, which was beneficial to save the reagent dosage in the subsequent flotation as well as improve the product purity. It can be seen that the open-circuit flocculation flotation process consisted of one-time blank rougher, two-time agent-added roughers, and two-time blank cleaners. Under the optimal conditions, the sulfur grade of the concentrate reached 90.16%. However, the sulfur recovery was only 58.01%.

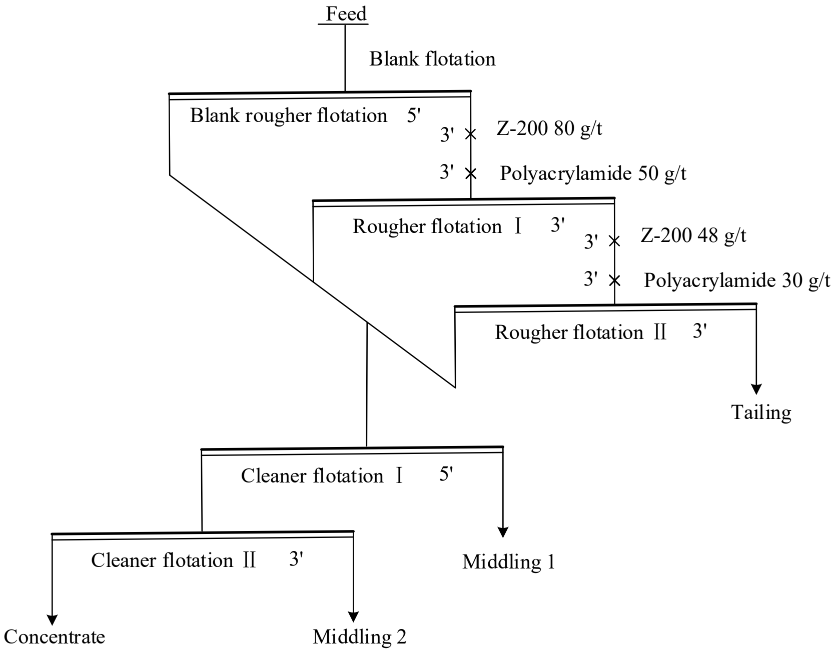

Fig. 8 Flow sheet of open-circuit flocculation flotation

Table 4 Test results of open-circuit flocculation flotation of the leaching residue

Product	Yield (%)	Grade (%)	Recovery (%)
Concentrate	35.60	90.16	58.01
Middling 1	13.81	59.69	14.90
Middling 2	24.97	51.82	23.38
Tailing	25.62	8.02	3.71
Feed residue	100.00	55.33	100.00

Closed-Circuit Flotation Experiment

To investigate the effect of middling return on sulfur flotation, a closed-circuit flotation experiment was carried out. The flowchart is shown in Fig. 9, where the tailing of the 1st cleaner (middling 1) was returned to the blank rougher, and the tailing of the 2nd cleaner (middling 2) went back to the 1st cleaner. The results of closed-circuit flotation in Table 5 indicated that the sulfur recovery was increased to 94.59%, and its grade also arrived at 87.92%. Therefore, after closed-circuit flocculation flotation, most of the sulfur in the leaching residue was recovered, and the sulfur grade was also high.

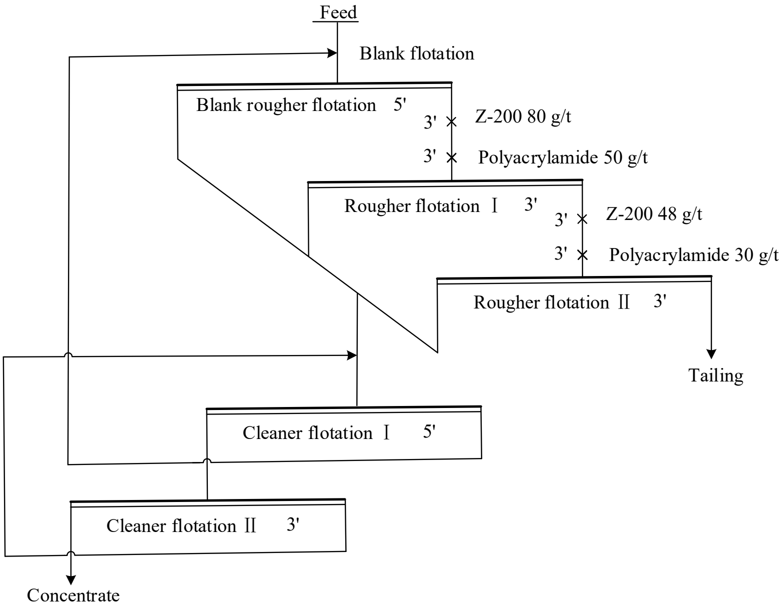

Fig. 9 Flow sheet of closed-circuit flocculation flotation of the leaching residue

Table 5 Test results of closed-circuit flocculation flotation of the leaching residue

Product	Yield (%)	Grade (%)	Recovery (%)
Concentrate	60.98	87.92	94.59
Tailing	39.02	7.86	5.41
Feed residue	100.00	56.68	100.00

Hot Filtration of Flotation Concentrate

The result of sulfur phase analysis for the concentrate is displayed in Table 6. 81.16% of the sulfur in the concentrate existed as elemental sulfur, i.e., the purity of elemental sulfur concentrate product achieved 81.16%. However, the sulfide content also arrived at 6.37%, which decreased the elemental sulfur grade. In order to obtain the elemental sulfur with higher purity, hot filtration process was conducted for the concentrate in a home-made equipment.

Table 6 Sulfur phase distribution of the elemental sulfur concentrate product (%)

Sulfur phase	Elemental sulfur	Sulfide	Sulfate	Total
Content	81.16	6.37	0.39	87.92
Distribution	92.31	7.25	0.44	100

Table 7 Sulfur phase distribution of the elemental sulfur product from the hot filtration of flotation concentrate (%)

Sulfur phase	Elemental sulfur	Sulfide	Sulfate	Total
Content	98.64	0.76	0.32	99.72
Distribution	98.92	0.76	0.32	100

After repeated conditional test, the optimal hot filtration temperature and time were separately 145 °C and 2 h, under which 85.32% of the elemental sulfur in the concentrate was recovered in the form of hot filtrate. The result of sulfur phase analysis for the elemental sulfur product in Table 7 indicated that the elemental sulfur purity reached 98.64%. Therefore, after hot filtration, a high-purity elemental sulfur product could be obtained. The filter cake contained abundant sulfide minerals that can be returned to the leaching stage for zinc recovery.

Conclusions

The present work put forward an efficient flocculation flotation-hot filtration process for recovering elemental sulfur and sulfide minerals from a pressure acid leaching residue of zinc sulfide concentrate. The chemical composition and phase analyses showed that the sulfur content achieved 44.41 and 37.73% of the sulfur existed as elemental sulfur. The mineral composition analysis showed that the main minerals are elemental sulfur, jarosite, pyrite, and quartz. The particle size distribution analysis indicated that the portion of thin particle with the size of -37 um reached 67.65%. When Z-200 was used as the collector and polyacrylamide as the flocculant, after closed-circuit flocculation flotation consisting of one-time blank rougher, two-time agent-added roughers, and two-time blank cleaners, 94.59% of the sulfur in the residue was recovered hot filtrate, and the sulfur grade arrived at 87.92%. The flotation concentrate was subjected to hot filtration; 85.32% of the elemental sulfur in the concentrate was recovered at temperature 145 °C and time 2 h, and the purity of obtained elemental sulfur product reached 98.64%. The filter cake containing sulfide minerals was returned to the leaching stage for zinc recovery. Thus, after the process of flocculation flotation-hot filtration of flotation concentrate, the elemental sulfur and sulfide minerals in the pressure acid leaching residue of zinc sulfide concentrate were comprehensively recovered.

Acknowledgements This research was funded by National Key Research and Development Program of China (Nos. 2018YFC1902005 and 2018YFC1902006).

References

1. Halfyard JE, Hawboldt K (2011) Separation of elemental sulfur from hydrometallurgical residue: a review. Hydrometallurgy 109:80–89
2. Wang ZY, Cai XL, Zhang ZB, Zhang LB, Wang SX, Peng JH (2015) Separation and enrichment of elemental sulfur and mercury from hydrometallurgical zinc residue using sodium sulfide. T. Nonferr Metal Soc 25:640–646
3. Pacyna EG, Pacyna JM, Sundseth K, Munthe J, Kindbom K, Wilson S, Steenhuisen F, Maxson P (2010) Global emission of mercury to the atmosphere from anthropogenic sources in 2005 and projections to 2020. Atmos Environ 44:2487–2499
4. Nriagu JO, Pacyna JM (1988) Quantitative assessment of worldwide contamination of air, water and soil by trace metals. Nature 333:134–139
5. Li GH, Feng XB, Li ZG, Qiu GL, Shang LH, Liang P, Wang DY, Yang YK (2010) Mercury emission to atmosphere from primary Zn production in China. Sci Tot Environ 408:4607–4612
6. Li GH, Feng XB, Qiu GL (2008) Environmental mercury contamination of an artisanal zinc smelting area in Weining County, Guizhou, China. Environ Pollut 154:0–31
7. Xu ZF, Qiu DF, Lu HM, Wang HB (2005) Review on research of oxidic-acidic pressure of zinc concentrates. Nonferr. Metal. 57:101–105 (in Chinese)
8. Liu SP, Wang HB, Jiang KX, Zhang BS (2009) New development of zinc hydrometallurgical in China. Min Metall 18:25–279
9. Dong ZL, Jiang T, Xu B, Yang YB, Li Q (2019) An eco-friendly and efficient process of low potential thiosulfate leaching-resin adsorption recovery for extracting gold from a roasted gold concentrate. J Clean Prod 229:387–398
10. Li HL, Wu XY, Wang MX, Wang J, Wu SK, Yao XL, Li LQ (2014) Separation of elemental sulfur from zinc concentrate direct leaching residue by vacuum distillation. Sep Purif Technol 138:41–46
11. Gu Y, Zhang TA, Liu Y, Mu WZ, Zhang WG, Dou ZH, Jiang XL (2010) Pressure acid leaching of zinc sulfide concentrate. Trans Nonferrous Met Soc China 20:s136–s140
12. Dong ZL, Jiang T, Xu B, Yang J.K, Chen Y.Z, Yang YB, Li Q (2020) Comprehensive recoveries of selenium, copper, gold, silver and lead from a copper anode slime with a clean and economical hydrometallurgical process. Chem Eng J 393
13. Padilla R, Vega D, Ruiz MC (2010) Pressure leaching of sulfidized chalcopyrite in sulfuric acid–oxygen media. Hydrometallurgy 86:80–88
14. Xu B, Chen YZ, Dong ZL, Jiang T, Zhang BS, Liu GQ, Yang JK, Li Q, Yang YB (2021) Eco-friendly and efficient extraction of valuable elements from copper anode mud using an integrated pyro-hydrometallurgical process. Resour Conserv Recycl 164
15. Liu FP, Wang JL, Peng C, Liu ZH, Wilson BP, Lundström M (2019) Recovery and separation of silver and mercury from hazardous zinc refinery residues produced by zinc oxygen pressure leaching. Hydrometallurgy 185:38–45
16. Fan YY, Liu Y, Niu LP, Jing TL, Zhang TA (2019) Separation and purification of elemental sulfur from sphalerite concentrate direct leaching residue by liquid paraffin. Hydrometallurgy 186:162–169
17. Rao S, Wang DX, Liu ZQ, Zhang KF, Cao HY, Tao JZ (2019) Selective extraction of zinc, gallium, and germanium from zinc refinery residue using two stage acid and alkaline leaching. Hydrometallurgy 183:38–44
18. Qin SC, Jiang KX, Wang HB, Zhang BS, Wang YF, Zhang XD (2020) Research on behavior of iron in the zinc sulfide pressure leaching process. Minerals 10:224–239

Part V

Additive Manufacturing and Materials First Principles

Automatic Process Mapping for Ti64 Single Tracks in Laser Powder Bed Fusion

Toby Wilkinson, Massimiliano Casata, and Daniel Barba

Abstract Using an unsupervised convolutional neural network classifier, an automated workflow to generate the process map for printing Ti-6Al-4 V with laser powder bed fusion with minimal human supervision is proposed. Single scan vectors using a range of laser powers and scan speeds were printed on a bare Ti-6Al-4 V baseplate, which were then imaged using optical microscopy without further material preparation steps. After resizing and thresholding, the resulting dataset was used to train the neural network into automatically differentiating the tracks into categories. Post-analysis reveals that the model can differentiate between commonly observed track morphologies and map out the viable processing window automatically for the alloy.

Keywords Additive manufacturing · Titanium alloy · Machine learning · Laser powder bed fusion (LPBF)

Introduction

Metal additive manufacturing (AM) has become a subject of immense academic and commercial interest in recent years due to its ability to process a wide range of alloys for use in many different sectors and with high geometric complexity. The material feedstock is in powder form and is melted by a laser in a layer-by-layer fashion, gradually forming a 3D object. While conceptually simple, the process involves many different physical phenomena including the multi-phase flow of the melt pool, residual stresses from high thermal gradients, and the resulting microstructure of the material. All these factors, plus many more uncited, play a key role in determining the quality and mechanical properties of the final part.

Of all the possible variables involved in the laser powder bed fusion (LPBF) process, the laser power (P) and scan speed (v) are two of the most important, having a significant impact on the resulting part quality. LPBF is a hierarchical process

---

T. Wilkinson (✉) · M. Casata · D. Barba
E.T.S de Ingeniería Aeronáutica y del Espacio, Universidad Politécnica de Madrid, Madrid, Spain
e-mail: tb.wilkinson@upm.es

S. Wagstaff et al. (eds.), *Materials Processing Fundamentals 2023*, The Minerals, Metals & Materials Series, https://doi.org/10.1007/978-3-031-22657-1_17

where individual scan vectors are the fundamental unit of construction, and defects caused by inappropriately chosen processing parameters will propagate through the hierarchy and affect the 3D part performance. Such defects include keyhole and lack of fusion porosity and spatter [1–3]. As a result, optimisation of the processing parameters should begin at the fundamental scan vector level.

The traditional optimisation process is expensive in terms of time, labour, and materials costs, requiring the printing of many 3D samples and their subsequent metallurgical analysis to determine reasonable parameters. These density values of these sample cubes are usually used to then select the "optimal" printing parameters. Other methods that focus on the single-track morphology using experimental [4] or computational [5] results use a *P*–v plot to investigate the effect of these parameters on the melt pool dimensions or defects. These results are then used to determine the printing parameters. This work will also use a *P*–*v* plot to investigate the track morphologies but using machine learning (ML) instead of manual methods.

ML is a type of artificial intelligence (AI) that uses large quantities of data to train a computer model to accomplish a complex task that it may not have been explicitly written for. Depending on the problem to be solved and the availability of training data, algorithms can learn in three different ways: supervised, unsupervised, or with reinforcement. AM is a manufacturing method that lends itself well for use in combination with ML, given the digital nature of many processing steps within the AM manufacturing chain. In fact, there is a rich history of ML being used to solve various problems within AM, including process parameter optimisation [6–8] and part design [9].

Methods

Computational Methodology

Invariant Information Clustering

The chosen paradigm for the unsupervised clustering of the images was taken from [10] and is called Invariant Information Clustering (IIC). This method aims to train a neural network (NN) to learn representations of the input dataset that are invariant under image transformations. The full mathematical description of the method can be found in the corresponding article but will be summarised briefly here.

IIC clustering uses contrastive learning, which means a pair of images forms the input, and the loss is calculated by comparing the outputs of the NN for each image in the pair in some way. This version uses positive image pairs as training data, i.e., images that should be classified as the same object by the neural network. Since we are performing unsupervised clustering, this kind of image pairing is rarely available, so the authors propose the use of synthetic augmentation to modify the original image in such a way that it remains recognisable, but to the neural network is a different image. Acceptable transformations include rotation, translation, and cropping. Colour corrections, such as changing the brightness and contrast, are also acceptable.

The output layer of the NN creates a discrete probability distribution across the number of chosen categories for the input image using a SoftMax activation function. This is the traditional activation function used by classification NNs. The loss function used by this network uses the concept of mutual information. In simple terms, the mutual information between two variables is a way of measuring the dependence of these variables on each other. What this means in this case, is that the mutual information of two completely different images should be 0. As stated in [10], maximising mutual information has the effect of making the representations of each image in a pair the same, hence assigning them the same cluster label.

Neural Network Architecture

As described above, the chosen ML paradigm was an unsupervised convolutional neural network (CNN). This is widely regarded as the industry standard network type for machine vision applications, due to its efficient sharing of weights within the convolutional layers. Famous convolutional architectures include AlexNet [11] and the VGG configurations [12] which have shown impressive accuracies in large-scale image classification tasks and continue to inspire the construction of models today.

For this work, a custom CNN model was implemented using TensorFlow [13] and Python 3.7, with various design choices inspired by models in literature and common practice. The model architecture is shown in Fig. 1. As is standard practice when using classifying images, the architecture has two main parts: the convolutional network and a fully connected prediction head. Between the two, a global average pooling layer [14] is used to vectorise the resulting feature maps before the fully connected layers. This results in fewer parameters in the network and is considered more "convolutional" in nature than the traditional flatten layers, since each feature map then resembles a categorical variable.

The network begins with a rescaling layer, which simply normalises all pixel values to between 0 and 1. This is standard practice when preparing data for various ML methods since it ensures all inputs are distributed across the same range. For neural networks, this may improve training performance, but it is important if using pretrained networks whose training data was in this standard range.

In total, there are 12 convolution layers, each with a ReLU activation function [11] and followed by a batch normalisation (BatchNorm) [15]. The convolution layers all have a filter size of 3 × 3, with a stride of 1 and are padded, such that the output shape matches the input shape. There are a total of three max pooling layers that reduce the height and width of the feature maps by a factor of 2, and after each max pooling layer, the number of filters in each convolution layer is increased by a factor of two, starting at 32 and finishing at 256.

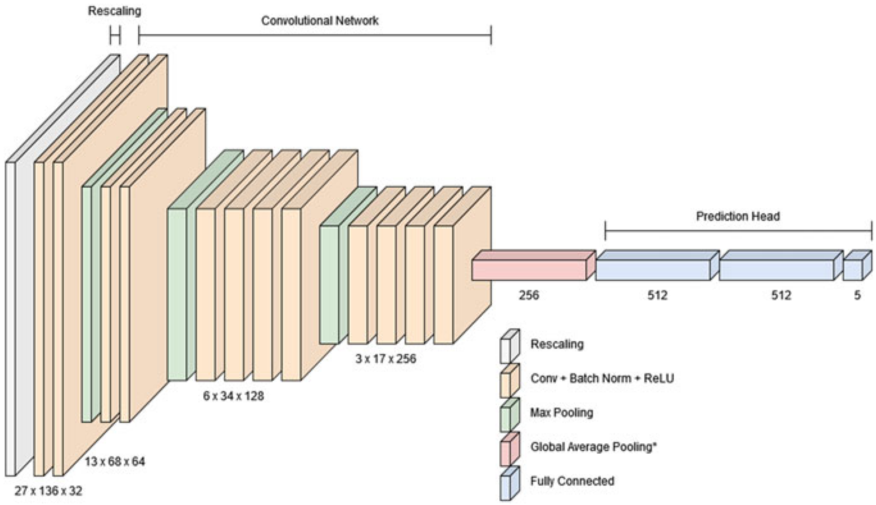

Fig. 1 Custom CNN architecture. Layer types are identified by the colours shown in the key. For conciseness, the BatchNorm layers are not shown

For the prediction head, this has two hidden, fully connected layers, each with 512 neurons and ReLU nonlinearity, followed by BatchNorm layers. The final, output layer has the same number of neurons as the desired number of categories, in this case, 5, and has a SoftMax activation function to provide a probability distribution.

The following augmentations were chosen:

- Random rotation
- Random horizontal translation
- Random horizontal mirroring
- Random brightness
- Random contrast

To utilise the power of GPU acceleration available within TensorFlow [13], batches of 512 images were passed through the network simultaneously. With each new epoch, a new augmentation is randomly generated for each input image. With each training step, the original and augmented image passes through the network in the same state, so with the same weights and biases for each layer. Then, the value of the loss is calculated, and the parameters updated.

The model was trained for 500 epochs using the Adam optimiser [16] on a PC with an Nvidia RTX A4000 GPU with 8 GB dedicated memory and an Intel i9 CPU.

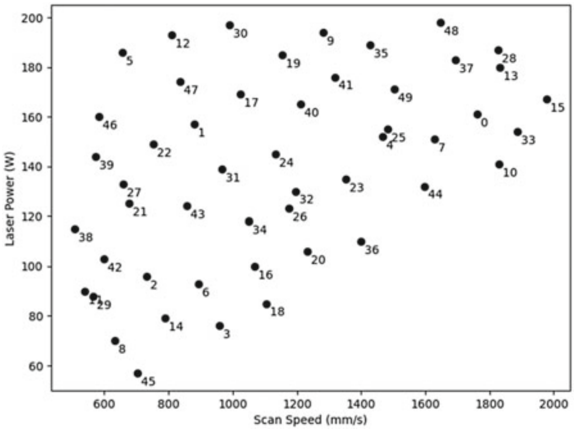

Fig. 2 The chosen combinations of laser power and scan speed plotted in a scatter graph with the track ID annotated

Experimental Methodology

LPBF Equipment

For these experiments, the LBPF equipment was an Aconity Mini (Aconity GmBH, Germany) system equipped with a 400 W IR single-mode laser with a spot size of 80 µm. No substrate heating was used. Argon gas was used to create the inert gas atmosphere, and the oxygen concentration was kept below 200 ppm for the duration of the laser irradiation. The substrate plates used were solid Ti-6Al-4 V with equal diameters of 25 mm and thickness of 15 mm. Before laser irradiation, the upper surface of the substrates was ground using 180-grit sandpaper.

50 combinations of P and v were chosen using a Latin hypercube sampling scheme within a restricted range, based on commonly observed values for Ti-6Al-4 V in literature [4, 8, 17]. The data points with very low calculated energy densities were removed from the study to ensure visible melt tracks were printed.

The final parameter set is shown in Fig. 2.

Track Printing and Processing

A custom Python script was used to generate the build file for the LPBF machine, using the chosen parameter set. A total of 50 single scan vectors 10 mm in length, spaced 800 µm apart, were printed on two identical substrate plates across two builds. The lines were not sorted in any particular order on the substrates. A diagram of the substrate plate with the placement of the single tracks is shown in Fig. 3. The upper surface of each substrate plate was aligned with the machine bed level to ensure accurate spot size.

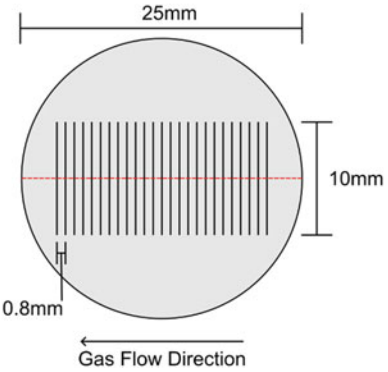

Fig. 3 Geometry of the substrate plates with the position of the single tracks indicated. The red dashed line shows where the sample plate is cut post-print to measure the track widths and depths

Data Collection and Image Processing

The printed samples were directly imaged using an optical microscope. Between 15 and 20, 8-bit grayscale images with pixel dimensions of 2168 × 2168 were captured for each track. The pixel resolution used was 2.0290 pixels/μm.

A similar image processing method to [6] was followed to generate a significantly large dataset for training the NN. A custom Python script was written to scale down each image by a factor of 4, and then slice them into smaller samples with dimensions of 136 × 27 pixels. These images were then segmented using the WEKA segmentation tool [18] available within Fiji [19], removing the background. An overview of the process is given in Fig. 4. Images that did not contain a track, or only, a small fraction of a track were removed from the dataset, leaving a total of 16,231 images. A training split of 0.15 was used to separate the training and testing datasets, so 13,797 images were used to train the network, with the remaining 2434 used to test.

To view the cross-sections of the tracks, the substrate plates were cut perpendicular to the track direction, embedded in resin, polished, and then etched. An optical microscope was then used to capture images of the cross-sections, which were then

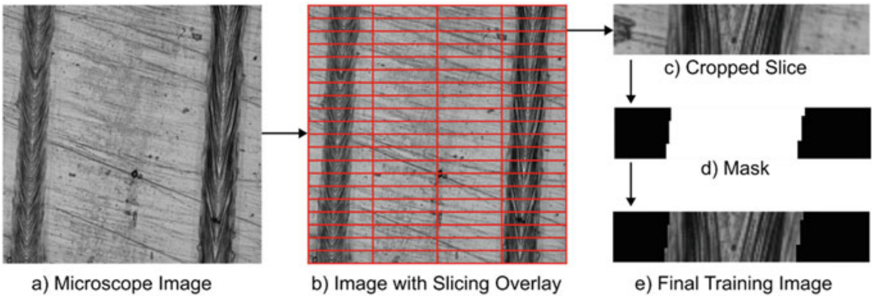

Fig. 4 An overview of the image preparation workflow. **a** shows the original image, which is then sliced as shown in (**b**), resulting in slices as shown in (**c**). WEKA segmentation is used to create a mask **d** which finally creates the image for training (**e**)

measured using image processing software. Only, a single cross-section per track was measured. Note, the cross-sectional images are not used to train the CNN. These are only used for measurements of the track dimensions.

Results

The results of the clustering are summarised in Fig. 5, with different colours separating the cluster assignments.

The 5 categories are identified as categories 0–4. After visually assessing the different images within each category, a representative track for each was selected and is displayed in Fig. 6. The tracks exhibit different morphologies, depending on where they lie on the process map.

Fig. 5 Parameter set studied in this work, clustered according to the output of the CNN

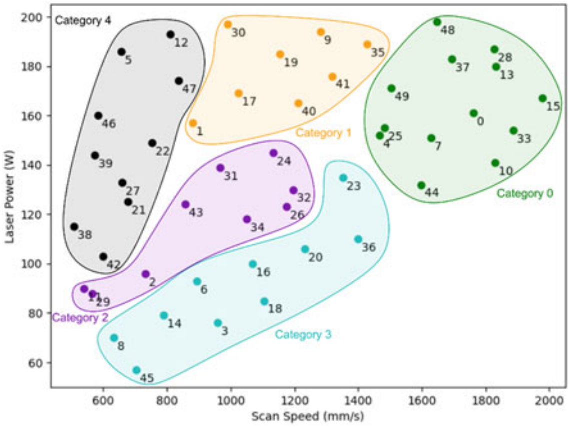

Fig. 6 Representative tracks from each of the 5 categories. Each image is labelled with the track ID and then the category

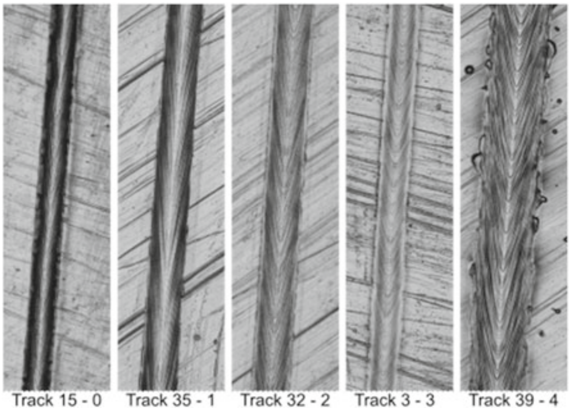

For each of the identified groups, the number of members, as well as the mean laser power and scan speed with standard deviation, is shown in Table 1.

Within the range of parameters selected, category 0 covers the largest number of tracks in this study and has the highest mean scan speed compared to the other groups. In fact, the entire group of tracks have scan speeds exceeding 1450 mm/s, suggesting that there is a well-defined threshold at which this track morphology exists. Given that the mean track width of the group is higher than the mean depth, this group is unlikely to result in keyhole mode melt pools. Track 15 is an example track in category 0 and lies at the top right of the process map, with high power and scan speed. It has a much darker colour in general with a light central section, evidence of a convex upper surface. There are no visible discontinuities or spatter particles in the image.

The category 1 tracks have the highest mean laser power and a small standard deviation, meaning this morphology only covers a small range of powers. Since the mean track depth is greater than the mean track width for this group, it is likely that printing in this parameter range would result in keyhole mode melt pools and cause porosity in a 3D part. Track 35 is labelled as category 1 and lies at the top of the process map, having a higher power compared to track 32. The upper surface of track 35 is more convex compared to that of track 32, which can be determined by the difference in colour between the centre and external edges of the track.

Category 2 covers the central region of the process map, and, looking at the group statistics, does not appear to produce keyhole mode melt pools on average. Track 32 is category 2 and lies centrally on the process map. The image shows a consistent track, with minor variation of the width and flat top. There are no obvious defects visible seen for this track in Fig. 6.

Category 3 is located to the left of the process map, with a low mean laser power. On average, this group produces tracks with the lowest depth and joint lowest width. If the layer thickness chosen for printing a part was 60 μm or greater (common in LPBF), lack of fusion defects may appear between the layers. Track 3 is an example of a category 3 track. The upper surface is flat, and the width appears consistent along the length. Compared to the other 4 tracks, it is lighter in colour on average.

Category 4 lies in the upper left part of the process map, with the lowest mean scan speed of all the categories while covering a large range of scanning speeds. The

Table 1 Calculated mean and standard deviation of the laser power, scan speed width and depth for the tracks assigned to each of the 5 groups by the ML model

Category number	Track count	Mean laser power (W)	Mean scan speed (mm/s)	Mean track width (μm)	Mean track depth (μm)
0	13	164.00 ± 18.43	1703.15 ± 157.80	92.38 ± 11.59	78.05 ± 23.38
1	8	179.00 ± 13.57	1161.38 ± 173.17	114.20 ± 8.01	125.78 ± 18.02
2	9	117.00 ± 19.82	912.44 ± 239.94	121.08 ± 8.41	92.89 ± 15.86
3	10	91.10 ± 21.47	1013.10 ± 251.72	92.88 ± 9.97	54.99 ± 12.03
4	10	148.20 ± 28.59	665.50 ± 101.14	157.21 ± 16.21	180.77 ± 33.79

mean depth and width of these tracks are greater than those in the other categories, and on average, the tracks are in keyhole mode since the depth is greater than the width. Track 39 is an example of category 4. This track shows more inconsistency compared to the other 4, with spatter and high variation in the width along the length.

In summary, given the images and data presented, the tracks in categories 0 and 2 are consistent and the least likely to result in keyhole or lack of fusion defects, or to suffer from excessive spattering.

Discussion

The results presented in the previous section will now be compared to examples from the literature to determine the success of the proposed method and place the results in context.

Several studies present a processing window for Ti-6Al-4 V based on computational or physical experimentation [3, 4, 20]. They provide thresholds for the different melting regimes of single tracks in terms of the applied energy density. Comparing the process map in that work (Fig. 13 of [20]) with Fig. 5 in this work, there are numerous similarities. In their paper, Promoppatum et al. identify 4 key regions: over melting, incomplete melting, balling effects, and continuous melting. The regions are represented clearly in the process map given in this work:

- Category 0 matches with "Balling Effects". While no balling of the tracks is observed in the data presented here, there is a distinct morphology change, and with higher laser speeds or powers, this may be seen to occur.
- Category 2 exhibits no visible defects and is unlikely to exhibit keyhole defects. This matches the "continuous melting" zone highlighted in [20].
- Category 3 closely matches the "incomplete melting" zone since the track depths are the lowest.
- Category 4 corresponds to the "over melting" zone, and this is clearly observed in the data presented in this paper, since there are defects visible in the upper surface photo in Fig. 6, and the dimensions given in Table 1 are evidence of keyhole mode melt tracks.
- Category 1 is not represented in [20], but could be thought of a transition region between "complete melting" and "over melting", since the upper surface appears consistent, but the tracks measurements suggest keyhole mode melt tracks.

Note, the exact numerical representations of these regions do not exactly match with those from Promoppatum et al. but the general location is clearly visible. The same arguments can also be made if the work presented here is compared to the process map seen in [4], and the same trends and general locations of the groups are seen. This variation is likely explained by the use of powder in that paper, whereas in this work, bare substrate plates are used. This variation can be observed in 316L stainless steel single tracks [21], where the varying powder thickness varies where these regions sit on the process map. Interestingly however, similar groups are also observed in the 316L samples, suggesting that the general group layout may be consistent across multiple materials. Hence, this CNN could be used to characterise other alloys, besides Ti-6Al-4 V, for automatically generating process maps.

Conclusion

In this study, we have demonstrated how unsupervised image clustering can be used to automatically generate a process map for the printing of LPBF single tracks. A CNN was used to create 5 distinct groups of single tracks, based on the upper surface morphology. These five groups showed key differences in their measured widths and depths. The results from this clustering could be used to better refine a processing window for the printing of 3D test samples, such as cubes.

The data presented in this work alone is not sufficient to fully determine the processing parameters for high-quality 3D objects, since there are many other variables at play, such as the hatch spacing and layer thickness. However, it has been shown that this technique can offer a good starting point for the development of optimal printing parameters without the high material and time cost of traditional methods.

Acknowledgements This project has received funding from the European Union's Horizon 2020 Marie Skłodowska-Curie Actions—Innovative European Training Networks under grant agreement No 956401.

References

1. Yang T et al. (2020) Laser powder bed fusion of AlSi10Mg: influence of energy intensities on spatter and porosity evolution, microstructure and mechanical properties. J Alloys Compd 849. https://doi.org/10.1016/j.jallcom.2020.156300
2. Li Z et al. (2022) A review of spatter in laser powder bed fusion additive manufacturing: in situ detection, generation, effects, and countermeasures. Micromachines (Basel) 13(8):1366. https://doi.org/10.3390/mi13081366
3. Luo Q, Yin L, Simpson TW, Beese AM (2022) Effect of processing parameters on pore structures, grain features, and mechanical properties in Ti-6Al-4V by laser powder bed fusion. Addit Manuf 56. https://doi.org/10.1016/j.addma.2022.102915
4. Soylemez E (2018) Modelling the melt pool of the laser sintered Ti6Al4V layers with Goldak's double-ellipsoidal heat source process mapping and transient melt pool geometry analysis of Ti-6Al-4V in direct metal laser sintering view project. 2018. [Online]. Available: https://www.researchgate.net/publication/328792215
5. Tapia G, Khairallah S, Matthews M, King WE, Elwany A (2018) Gaussian process-based surrogate modeling framework for process planning in laser powder-bed fusion additive manufacturing of 316L stainless steel. Int J Adv Manuf Technol 94(9–12):3591–3603. https://doi.org/10.1007/s00170-017-1045-z

6. Silbernagel C, Aremu A, Ashcroft I (2019) Using machine learning to aid in the parameter optimisation process for metal-based additive manufacturing. Rapid Prototyp J 26(4):625–637. https://doi.org/10.1108/RPJ-08-2019-0213
7. Liu Q et al (2020) Machine-learning assisted laser powder bed fusion process optimization for AlSi10Mg: new microstructure description indices and fracture mechanisms. Acta Mater 201:316–328. https://doi.org/10.1016/j.actamat.2020.10.010
8. Liu S, Stebner AP, Kappes BB, Zhang X (2021) Machine learning for knowledge transfer across multiple metals additive manufacturing printers. Addit Manuf 39. https://doi.org/10.1016/j.addma.2021.101877
9. Yao X, Moon SK, Bi G (2017) A hybrid machine learning approach for additive manufacturing design feature recommendation. Rapid Prototyp J 23(6):983–997. https://doi.org/10.1108/RPJ-03-2016-0041
10. Ji X, Henriques JF, Vedaldi A (2018) Invariant information clustering for unsupervised image classification and segmentation, July 2018. [Online]. Available: http://arxiv.org/abs/1807.06653
11. Krizhevsky A, Sutskever I, Hinton GE (2012) ImageNet classification with deep convolutional neural networks. In: Proceedings of the 25th international conference on neural information processing systems, vol 1. pp 1097–1105
12. Simonyan K, Zisserman A (2014) Very deep convolutional networks for large-scale image recognition, Sep. 2014, [Online]. Available: http://arxiv.org/abs/1409.1556
13. Abadi M et al. (2016) TensorFlow: a system for large-scale machine learning. May 2016, pp 44. [Online]. Available: http://arxiv.org/abs/1605.08695
14. Lin M, Chen Q, Yan S (2013) Network in network, Dec. 2013. [Online]. Available: http://arxiv.org/abs/1312.4400
15. Ioffe S, Szegedy C (2015) Batch normalization: accelerating deep network training by reducing internal covariate shift, Feb. [Online]. Available: http://arxiv.org/abs/1502.03167
16. Kingma DP, Ba J (2014) Adam: a method for stochastic optimization. Dec. 2014, [Online]. Available: http://arxiv.org/abs/1412.6980
17. Barba D, Alabort C, Tang YT, Viscasillas MJ, Reed RC, Alabort E (2020) On the size and orientation effect in additive manufactured Ti-6Al-4V. Mater Des 186. https://doi.org/10.1016/j.matdes.2019.108235
18. Arganda-Carreras I et al (2017) Trainable Weka segmentation: a machine learning tool for microscopy pixel classification. Bioinformatics 33(15):2424–2426. https://doi.org/10.1093/bioinformatics/btx180
19. Schindelin J et al (2012) Fiji: an open-source platform for biological-image analysis. Nat Methods 9(7):676–682. https://doi.org/10.1038/nmeth.2019
20. Promoppatum P, Onler R, Yao SC (2017) Numerical and experimental investigations of micro and macro characteristics of direct metal laser sintered Ti-6Al-4V products. J Mater Process Technol 240:262–273. https://doi.org/10.1016/j.jmatprotec.2016.10.005
21. Tran HC, Lo YL (2019) Systematic approach for determining optimal processing parameters to produce parts with high density in selective laser melting process. Int J Adv Manuf Technol 105(10):4443–4460. https://doi.org/10.1007/s00170-019-04517-0

Part VI
Poster Session

Simulation of Ferroalloy Casting in Copper Moulds

Haifei An, Weijian Tian, Hao Chen, Shaojun Chu, Lihong Li, and Hao Bai

Abstract In China, for the production of ferroalloys such as ferrosilicon and ferroaluminium, the mould casting is usually used, and the material of casting mould is usually cast iron. However, in the process of periodic heating and cooling, cracks appear at the edge of mould. This severely affects the service life, thus increasing the casting cost, which has become a bottleneck of the development of ferroalloy industry. In the casting process, the lower thermal conductivity of the cast iron causes greater alternating thermal stresses, which are the reason for damages of cast iron moulds. In this study, the copper which has excellent heat transfer properties was used as the mould material to develop a new type of ferroalloy mould. In order to study the service performance of copper mould, the casting process of ferroalloy in copper mould and the temperature field of copper mould under different water cooling intensities were simulated by using ANSYS Workbench 17.0 software. The results show that under water cooling conditions, the maximum temperature of the mould cannot reach 1083°C in the casting process, so the molten ferroalloy would not destroy the copper mould, which has low melting point, proofing the feasibility of copper as the mould material. In addition, the water cooling intensity of the mould has great influence on the cooling rate of the mould. And the optimized water cooling intensity is important for proper operation of the copper moulds.

Keywords Ferroalloy · Mould · Copper · Temperature field · Cooling

---

H. An · W. Tian · H. Chen · S. Chu · H. Bai (✉)
State Key Laboratory of Advanced Metallurgy, University of Science and Technology Beijing, Beijing 100083, China
e-mail: baihao@metall.ustb.edu.cn

School of Metallurgical and Ecological Engineering, University of Science and Technology Beijing, Beijing 100083, China

L. Li
Shantou Huaxing Metallurgical Equipment Co., Ltd., Shantou 515063, China

S. Wagstaff et al. (eds.), *Materials Processing Fundamentals 2023*, The Minerals, Metals & Materials Series, https://doi.org/10.1007/978-3-031-22657-1_18

Introduction

Ferroalloy is one of the important basic raw materials in the iron and steel industry, which plays a key role in improving the quality of steel [1, 2]. With the rapid development of the modern steel industry, the demand for ferroalloys is increasing. At present, China's ferroalloy production accounts for about 40% of the world's output, and it has become the world's largest ferroalloy producer and consumer [3]. According to the database of China Commercial Industry Research Institute, the national ferroalloy output in 2018 was increased by 4.5% to 31.23 million tons [4]. In the ferroalloy production, casting is the key process to ensure the production efficiency and quality of ferroalloy. In general, there are three casting methods for the solidification of ferroalloy: ingot mould casting, pit-layered casting, and machine casting [5–8]. The technological process of all the methods is generally composed of pouring, slag removal, primary crushing, and secondary processing. In this process, the cast needs to be crushed further manually or mechanically in order to meet the requirement of the users for product size. After the crushing process, the powdering loss of products reaches 8–10%, and especially, the powdering loss of high carbon ferromanganese even reaches 16–17%, resulting in a declination in yield and product quality [9].

In recent years, some technologies of continuous mould casting granulation for ferroalloy have been proposed in order to decrease powdering loss [10] by eliminating the crushing process. In this technology, the molten ferroalloy is continuously poured into the drainage device, and then dispersed and injected into the circulating mould. The ferroalloy solidifies in the cavities, demoulds, and the granulated ferroalloy products are obtained without further processing. This process reduces the product loss and improves the environment. For this technology, the mould plays a key role in solidification and forming of the ferroalloy. At present, cast iron is widely used as the mould material [11]. Although the cast iron has the advantages of high strength, easy processing, and so on, its disadvantages are also obvious. For example, after a period of thermal shocks, the mould will crack locally, thus reducing the service life. Many researches have been carried out to improve the quality and service life of the moulds [5]. In terms of moulds materials, several kinds of cast iron, such as normal gray iron, medium manganese gray iron, ductile iron, compacted graphite cast iron, rare earth gray iron, and vanadium titanium cast iron, have been tried. However, the service life of the mould is still not ideal.

The casting mould is not only the shaping equipment, but it is also a heat exchanger [12]. In the casting process, due to the repeated scouring at the mould cavities surface by the high temperature molten ferroalloy, the periodic temperature changes cause expansion and contraction alternately, so that the mould experiences non-isothermal temperature field and nonuniform stress field. The maximum thermal stress occurs on the surface of the mould cavities, which exceeds the yield strength of the mould material, causing plastic deformation. In addition, the heat dissipation capacity of the mould is insufficient during the process of cyclic use, which lead to demould of casts if the cooling intensity is not enough. Therefore, the alternating thermal stress and thermal load are the main factors affecting the use of mould.

Consider that copper has excellent heat transfer performance, it was used as the mould material to develop a new type of ferroalloy mould in this study. As is known, the thermal conductivity of pure copper (CW004A) can reach 400 W/(m K), and it is 10 times that of gray iron, which will make the temperature distribution more uniform. Therefore, pure copper has lower alternating thermal stress and lower overall temperature than cast iron in the same environmental conditions. In order to study the service performance of the copper mould, the casting process of ferroalloy in copper mould and the temperature field of copper mould under different cooling intensity were simulated by using ANSYS Workbench 17.0 software. This study would provide a theoretical reference for further research and development of ferroalloy casting system with copper mould.

Model Description

The development ferroalloy granulation casting system developed, as shown in Fig. 1, is composed of the pouring device, moulds, and circulating rotating device. The motors drive the moulds to move counter-clockwise at a constant speed while the molten ferroalloy is poured into the moulds by the pouring equipment. Then, the ferroalloy is solidified in the moulds and demoulded. The moulds enter the next cycle after water cooling.

In order to study the service performance of copper moulds, the temperature field change of a single mould in a cycle was simulated numerically, which involves the analysis on solidification of the ferroalloy and transient heat transfer of the mould. The complete casting cycle is divided into two stages according to the different initial and boundary conditions before and after demoulding, and the demoulding time is ignored. The temperature field of the mould from pouring to demoulding is simulated at stage 1, and the mould temperature field of natural cooling or forced water cooling after demoulding is simulated at stage 2.

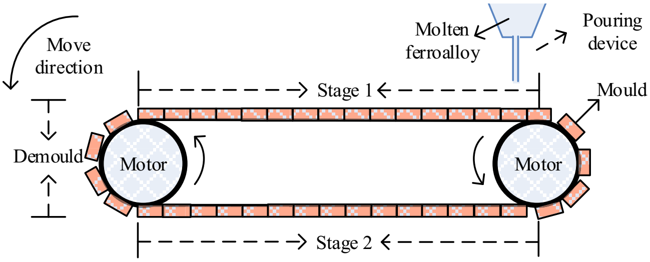

Fig. 1 Schematic diagram of ferroalloy granulation casting system

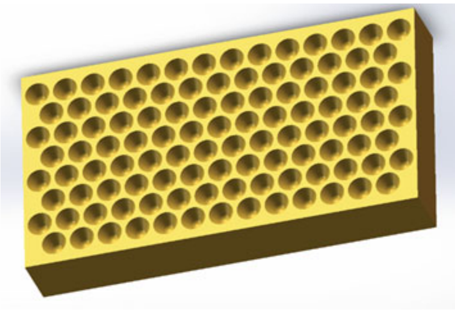

Fig. 2 Three-dimensional model of copper mould

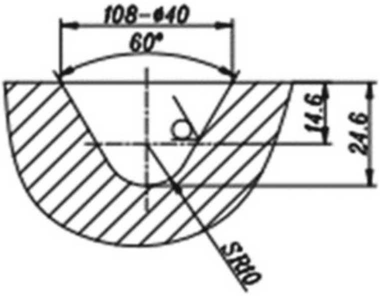

Fig. 3 Single cavity size

Physical Model

The mould can be set as a copper cuboid of 650 mm × 349 mm × 97 mm, with 108 cavities on its upper surface. The three-dimensional model of copper mould is built by SolidWorks software, as shown in Fig. 2. The size of each cavity is shown in Fig. 3. The mass of a single copper mould is 183 kg, and the cavity can hold 4.8-kg ferrosilicon alloy, so the copper-metal ratio of mould is 38.1.

Mathematical Model

Governing Equations

The release of latent heat during the solidification of ferroalloys is a major feature of the casting forming process. The latent heat of metal solidification accounts for about 50% of the heat transferred from the casting to the mould, so it has a great influence on the temperature field of the casting and must be considered. The relationship between temperature, time, and space can be described by Fourier partial differential equations for heat conduction, which actually becomes an unsteady-state conduction process with internal heat source [13]:

$$\frac{\partial \boldsymbol{T}}{\partial \boldsymbol{t}} = \frac{\boldsymbol{\lambda}}{\boldsymbol{C\rho}}\left(\frac{\partial^2 \boldsymbol{T}}{\partial \boldsymbol{x}^2} + \frac{\partial^2 \boldsymbol{T}}{\partial \boldsymbol{y}^2} + \frac{\partial^2 \boldsymbol{T}}{\partial \boldsymbol{z}^2}\right) + \frac{\boldsymbol{Q}}{\boldsymbol{C\rho}} \tag{1}$$

where T is the temperature (°C); C is the specific heat capacity (J/(kg K)); ρ is the average density of the liquid and solid phases (kg/m^3); Q is the amount of latent heat released, which is the internal heat source (J); λ is the thermal conductivity (W/(m K)).

How to deal with the latent heat of crystallization is key to the success of casting solidification simulation. The enthalpy method is usually used for alloys with a wide crystallization temperature range [14]. Enthalpy method introduces an enthalpy function into Fourier partial differential equation, which specifies the relationship between enthalpy and temperature. When solving the equation, the enthalpy value of a certain temperature node is obtained as a known value, and then, the node temperature is obtained through the solution of the equation.

When the solidification phase transition is considered, the enthalpy function of the metal is as follows:

$$H = H_0 + \int_{T_0}^{T} C_P \mathrm{d}T + (1 - f_s)L \tag{2}$$

where T_0 is the reference temperature or reference temperature (°C); H_0 is the enthalpy at the reference temperature (J); f_s is the solid fraction.

Derive the time from the above formula:

$$\frac{\partial H}{\partial t} = \left(c_P - L\frac{\partial f_s}{\partial T}\right)\frac{\partial T}{\partial t} \tag{3}$$

Substitute formula (3) into formula (1):

$$\rho\frac{\partial H}{\partial t} = \lambda\left(\frac{\partial^2 T}{\partial x^2} + \frac{\partial^2 T}{\partial y^2} + \frac{\partial^2 T}{\partial z^2}\right) \tag{4}$$

The enthalpy and temperature of the next node can be obtained according to the initial enthalpy and the relationship of enthalpy and temperature.

Thermophysical Parameters

According to Neumann Kopp law [15], when the temperature of composition is above Debye temperature, the heat capacity can be obtained by the following formula:

$$C_m = \sum_i x_i c_{im} \tag{5}$$

Table 1 Specific heat capacity of 75 ferrosilicon

Temperature (°C)	300	600	900	1100	1207	1340	1500
Specific heat capacity J/(kg K)	796	946	1000	985	980	975	965

Table 2 Thermophysical parameters of pure copper (CW004A)

Temperature (°C)	Density (kg/m^3)	Thermal conductivity (W/(m K))	Specific heat capacity (J/(kg K))
20	8920	405.5	385
100	8920	404.1	388
300	8920	390.5	396
500	8920	367.7	404
700	8920	342.4	414
900	8920	322.9	427
1000	8920	312.7	445
1600	8920	290.0	470

where x is the mole fraction of the component. The difference between the specific heat capacity calculated by the law and the experimental results is not more than 4%. The specific heat capacity of 75 ferrosilicon varying with temperature was calculated, as shown in Table 1. The copper mould is made of pure copper (CW004A), and the thermophysical parameters are shown in Table 2.

The phase diagram of ferrosilicon shows that $T_s = 1207$ °C and $T_l = 1340$ °C, the phase transition interval between fluid and solid is defined as 133°C. The thermal conductivity of ferrosilicon is set to 25 W/(m K). The relationship between enthalpy and temperature of 75 ferrosilicon is calculated by enthalpy method, as shown in formula (6).

$$H = \begin{cases} 2.12 \times 10^6 T & T \le 1207\,°\mathrm{C} \\ 3.42 \times 10^7 T - 3.87 \times 10^{10} & 1207\,°\mathrm{C} < T \le 1340\,°\mathrm{C} \\ 2.12 \times 10^6 T - 2.13 \times 10^{10} & 1340\,°\mathrm{C} < T \le 1600\,°\mathrm{C} \end{cases} \tag{6}$$

Initial and Boundary Conditions

At stage 1, the mould temperature field from pouring to demoulding was simulated. The initial temperature of molten iron is 1550 °C; the initial temperature of mould is 40 °C, and the ambient temperature is 30 °C.

According to the literature [12, 16], the interfacial heat transfer coefficient increases linearly with the increase of temperature, which means that the higher the temperature of the casting itself, the greater the interfacial heat transfer coefficient between the casting and air. In order to simplify the calculation, the convective heat transfer coefficient between casting and air was set as 100 W/(m^2 K), and the convective heat transfer coefficient between mould and air was set as free convection heat transfer coefficient of 10 W/(m^2 K).

At Stage 2, the mould temperature field of natural cooling or forced water cooling after demoulding of castings is simulated. The temperature load at the end of the previous stage was taken as the initial condition of the cooling process in the next stage. The convective heat transfer coefficient of natural cooling was set to be free convection heat transfer coefficient of 10 W/(m^2 K), and the convective heat transfer coefficient of forced water cooling was set to 500 W/(m^2 K), 1000 W/ W/(m^2 K), 2000 W/(m^2 K), 5000 W/(m^2 K), and 8000 W/(m^2 K), respectively, corresponding to different water cooling intensity.

Mesh Generation

The pre-processing software MESH was used to generate structured hexahedral meshes for the mould and the casting, respectively, and the boundary layer encryption was performed on the contact area between the casting and the mould. Considering the accuracy and the speed of calculation, it is determined after the mesh independence test that the minimum size of the mesh was 2 mm, divided into 1.43 million grids, and the average quality of the grid was 0.8495. The physical model meshing was generated as shown in Fig. 4.

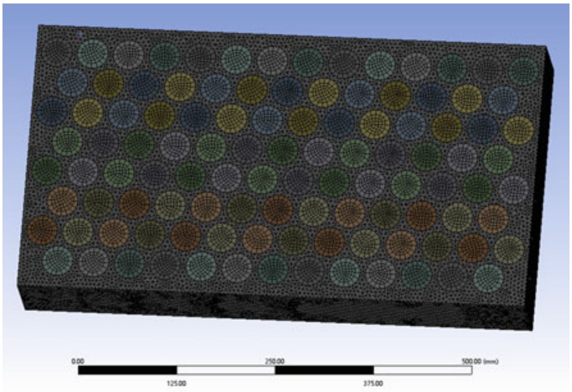

Fig. 4 Mesh generation of physical model

Results and Discussion

Solidification Process of Ferroalloy

The boundary conditions of the mould change before and after demoulding, and the demoulding time affects the temperature field of the mould, so the demoulding time should be determined first. Therefore, the solidification process of the ferroalloy was studied. After pouring molten iron, the temperature changes of the mould and molten iron under the cooling intensity of 10 W/(m^2 K) (natural cooling) were simulated and analyzed to determine the appropriate demoulding time.

Seven temperature monitoring probes were set at the central axis of the mould cavity to monitor the temperature change during the casting process. The probe 1 is in the molten iron, and the probes 2–7 are in the mould, as shown in Fig. 5. The temperature changes at seven probes were collected for further studies. Also, the maximum and minimum temperature in the solidification process were monitored, respectively. The results are shown in Fig. 6.

Fig. 5 Distribution of temperature monitoring probes

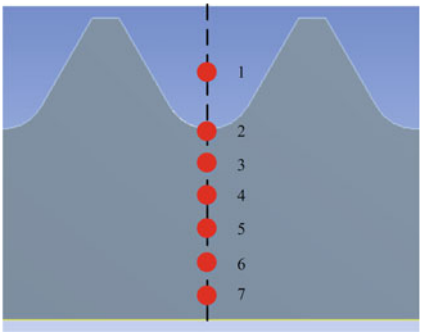

Fig. 6 Temperature change diagram of mould and molten iron under different water cooling intensity

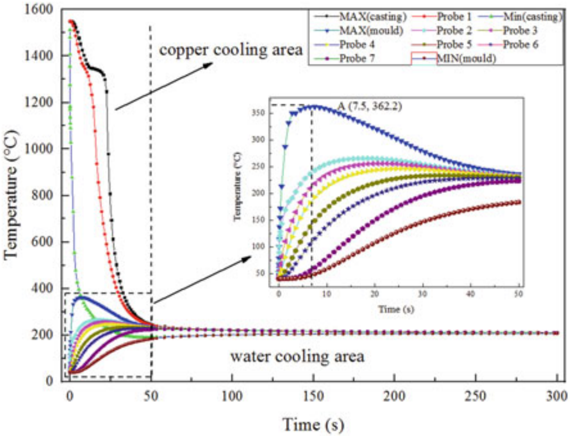

Due to the excellent heat transfer performance of the copper mould, the temperature of molten iron decreases rapidly after pouring, and the corresponding temperature of copper mould increases rapidly. The mould temperature rose to the highest at 362.2 °C in 7.5 s, and then, the temperature dropped slowly, indicating that the copper mould can fully bear the thermal shock of molten iron under this copper-iron ratio and will not have destructive influence on the mould. Ignoring the minimum temperature curve, it was found that the temperature of all probes of the mould is about 220°C in 50 s, and the overall temperature difference is within 50°C, which is very close to the temperature of hot metal, indicating that the mould has fully absorbed the heat of molten iron, and extending the time is not conducive to the cooling of the mould. Therefore, it was suggested that the longest demoulding time is 50 s after pouring.

Temperature Field Before Demoulding

The casting demoulding time was determined to be 50 s, and the data of the first 50 s were analyzed, as shown in Fig. 7. It can be found that the maximum temperature curve of molten iron has a plateau area, which is due to the release of a large amount of solidification latent heat during the cooling process of ferrosilicon that slows down the temperature drop. The temperature plateau area of the probe near the mould was not obvious. This was because the excellent heat transfer performance of the copper mould offsets the effect of latent heat release, which makes the cooling rate of the molten iron faster. The latent heat of solidification is basically released at 22.5 s, and the molten iron is completely solidified without any liquid core. Regardless of other factors, it can be used as the minimum time point for demoulding. When the time exceeds 22.5 s, the maximum temperature of the casting decreased rapidly. The heat flux of molten iron between the starting point and point B was much greater than the heat flux of the copper mould, so the mould temperature rose sharply and can reach 350.4 °C in 2.7 s. Between point B and point C, that is, within 2.7–7.5 s, the output heat flux of molten iron was slightly larger than the heat dissipation flux in the copper mould, so the mould temperature slowly rose to a maximum of 362.2 °C. The highest temperature was within the safe use range of copper metal, which shows that the copper mould meets the production requirements. After 7.5 s, the molten iron output heat flux was less than the heat dissipation flux in the copper mould, so the mould temperature was slowly reduced. Among the common ferroalloys, the sum of sensible heat and latent heat of ferrosilicon is the highest, which verifies the feasibility of copper as the mould material for common ferroalloys (Fig. 8).

Fig. 7 Temperature change curve of mould and molten iron before demoulding

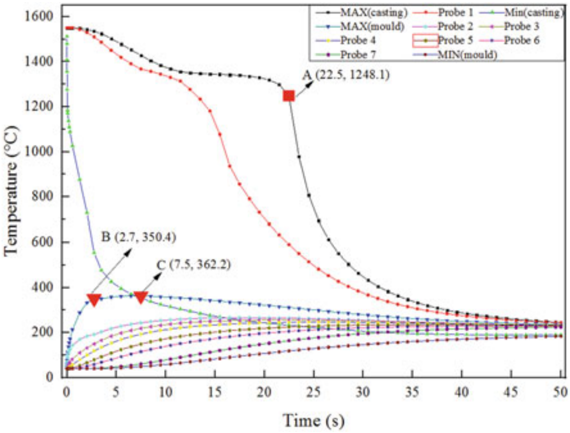

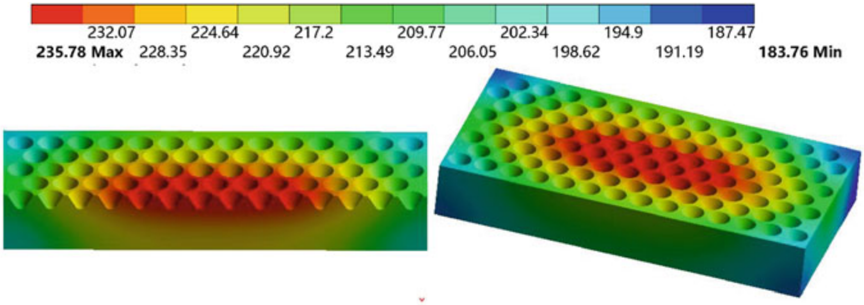

（a）Section view （b）Oblique view

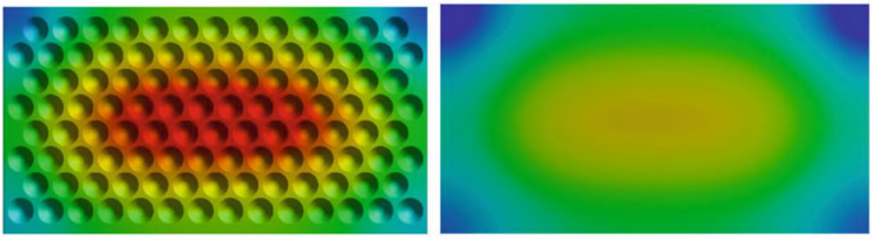

（c）Front view （d）Bottom view

Fig. 8 Temperature field of the mould at 50 s before demoulding

Temperature Change of the Mould After Demoulding Under Different Cooling Conditions

At stage 2, the mould temperature changes due to natural convection cooling or forced water cooling after demoulding of castings was simulated. The temperature load at the end of the previous stage was taken as the initial condition of the cooling process in the next stage. The convective heat transfer coefficient of natural convection cooling in air was 10 W/(m^2 K), and the intensity of forced water cooling was set to 500, 1000, 2000, 5000, and 8000 W/(m^2 K), respectively. The temperature changes at seven temperature probes were collected according to Fig. 5, and the result was shown in Fig. 9. The cooling process was divided into two areas. Before demoulding, the heat of molten iron was mainly absorbed by the copper mould, and the heat lost by natural convection with air accounted for a small part, which was referred to as the copper cooling area. After demoulding, forced water cooling was used for copper mould, which was referred to as the water cooling area.

In order to keep the stability of the copper mould and reduce the heat accumulation, the mould temperature was cooled to below 100 °C. The greater the water

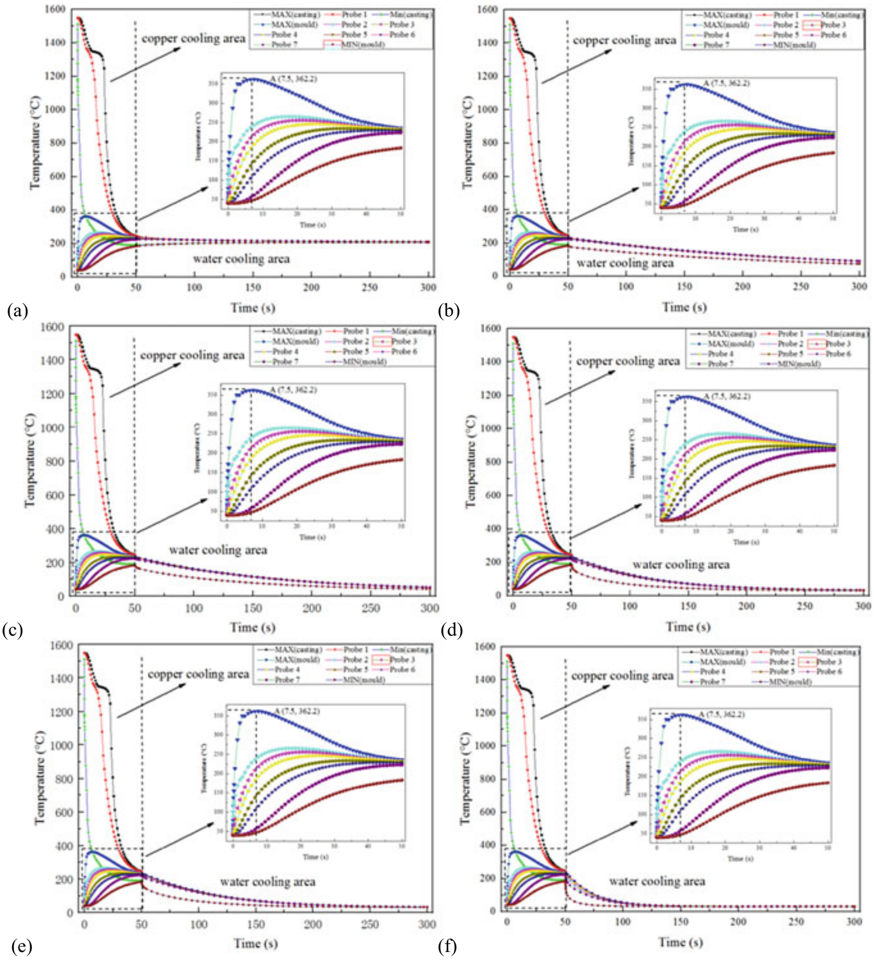

Fig. 9 Temperature change diagram of mould and molten iron under **a** natural convection and different water cooling of: **b** 500, **c** 1000, **d** 2000, **e** 4000, and **f** 8000 W/(m^2 K), respectively

cooling intensity, the shorter time the mould cooling to 100 °C. Figures 10 and 11, respectively, show the variation curves of the highest temperature and the lowest temperature of copper mould under different water cooling intensities. The results show that when the water cooling intensity is doubled, the temperature of copper mould can be reduced by about 30 °C after 50 s of cooling; when the water cooling intensity exceeds 4000 W/(m^2 K), the cooling enhancement effect becomes slower. In order to ensure the safe use of copper mould, the cooling time is calculated according to the maximum temperature change. At 4000 W/(m^2 K) water cooling intensity, it takes 49.2 s to cool to 100 °C and 111.0 s to cool to 40 °C. At 8000 W/(m^2 K) water cooling intensity, it takes 26.3 s to cool to 100 °C and 76.8 s to cool to 40 °C. The water cooling intensity of the mould has great influence on the cooling rate of the mould. Considering the pouring cycle and cooling effect comprehensively, the cooling intensity should be set at 8000 W/(m^2 K), and the corresponding cooling time is only 26.3 s, which can ensure the continuous and stabilized work of the copper mould.

Fig. 10 Maximum temperature change of copper mould under different water cooling strength

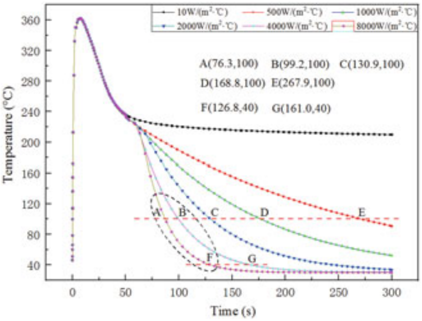

Fig. 11 Minimum temperature change of copper mould under different water cooling intensity

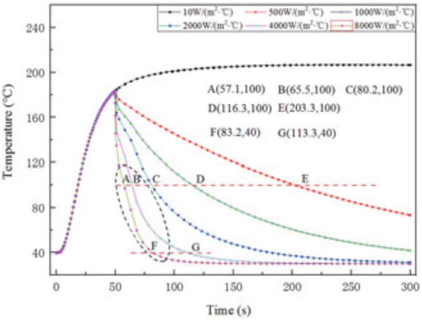

Conclusions

When the copper-iron ratio of mould is 37.8, the highest temperature of the copper mould during the casting process of the ferrosilicon rise to 362.2 °C, and the residence time of the peak temperature was short, so the molten ferroalloy would not destroy the copper mould which has low melting point. Among the common ferroalloys, the sum of sensible heat and latent heat of ferrosilicon is the highest, which proofs the feasibility of copper as the mould material for common ferroalloys.

At 50 s after pouring, the mould has fully absorbed the heat of molten ferroalloy, indicating that an appropriate demoulding time can be 50 s.

The water cooling intensity of the mould has great influence on the cooling rate of the mould. The results show that when the water cooling intensity is doubled, the temperature of copper mould can be reduced by about 30 °C after 50 s of cooling. On the other hand, when the water cooling intensity exceeds 4000 W/(m^2 K), the cooling enhancement effect becomes slower.

Finally, the optimized water cooling intensity is important for proper operation of the copper moulds. Considering the pouring cycle and cooling effect comprehensively, the cooling intensity should be set at 8000 W/(m^2 K) for a corresponding cooling water flow of 5 m/s. It takes 26.3 s to cool to 100 °C at its intensity, which can ensure the continuous and stable condition of the copper mould.

References

1. Xiwang M, Bai Zhitao L, Guanghua. (2020) Review of comprehensive utilization of typical ferroalloy slags. Chin J Eng 42(6):663–679
2. Surup GR, Trubetskaya A, Tangstad M (2020) Charcoal as an alternative reductant in ferroalloy production: a review. Processes 11(8):1432
3. Xiao L, Jinyan L, Yuanyuan Z (2020) Prospects of resource utilization techniques of solid waste in China’s ferroalloy industry. Ferro-Alloys 51(01):44–48
4. Website: https://baijiahao.baidu.com/s?id=1623908174446883124&wfr=spider&for=pc
5. Zhao LJ, Le J, Dejian Z (2014) Current situation and trends of research on the ingot mould design. Mech Res Appl 27(06):189–191
6. Hongyi Y (2020) SA brief discussion on application of combined ingot mould in ferroalloy production. J Jisco Technol 02:44–46
7. Dongsheng D, Yanlin X, Yanyou Z (2009) Application of water cool ingot mould in ferroalloy production. Ferro-Alloys 40(05):24–26
8. Curcio P, Kerezsi B, Brown P (2004) Failure investigation of lime coated grey cast iron moulds at TEMCO ferroalloy smelter. Eng Fail Anal 11(6):925–933
9. Jalkanen H, Gasik M (2013) Chapter 3—Theory of ferroalloys processing. In: Handbook of Ferroalloys. Elsevier Ltd
10. Wenchao H, Xuewei L, Feifei P et al (2019) Granulation of ferrosilicon alloy by rotary multi-nozzles cup atomizer: granulation behavior and model formation. Adv Powder Technol 30(5):895–902
11. Kaila VN, Dave IB (2020) The influence of coating sand materials on shell mould properties of investment casting process. Mater Today Proc

12. Stieven GDM, Soares DDR, Oliveira EP et al (2021) Interfacial heat transfer coefficient in unidirectional permanent mould casting: modeling and inverse estimation. Int J Heat Mass Transf 166(1):120765
13. Cuesta FJ, Lamúa M (2009) Fourier series solution to the heat conduction equation with an internal heat source linearly dependent on temperature. J Food Eng 90(2):291–299
14. Knig-Haagen A, Franquet E, Faden M et al (2020) Influence of the convective energy formulation for melting problems with enthalpy methods. Int J Therm Sci 2020:106477
15. Leitner J, Voňka P, Sedmidubský D et al (2010) Application of Neumann–Kopp rule for the estimation of heat capacity of mixed oxides. Thermochimica Acta 497(1):7–13
16. Liu X, Fakir OE, Cai Z et al (2019) Development of an interfacial heat transfer coefficient model for the hot and warm aluminium stamping processes under different initial blank temperature conditions. J Mater Process Technol 273

Effects of Temperature and Density on Transition Slab Length During Steel Grade Transition

Sicheng Song, Yanhui Sun, Yaoguang Li, and Chao Zhuo

Abstract The length of the transition slab may be decreased by manipulating differences in temperatures or densities of new and old grade steels. The molten steel liquidus temperature and density are related to the composition. For most elements in steel, both the liquidus temperature and density of the molten steel decrease with an increase in their mass fraction. Therefore, the temperature and density of molten steel cannot simultaneously shorten the transition slab. This study compared the effect of temperature and density on the length of the transition slab using numerical simulation methods based on flow, heat transfer, and mass transfer. The model was verified using a physical simulation and an industrial experiment. Finally, the effects of temperature and density on the transition slab length were elucidated.

Keywords Steel grade transition · Transition slab · Intermix · Tundish · Simulation · Continuous casting

Introduction

Compared with die casting, continuous casting offers higher yield and higher quality of slabs; for this reason, continuous casting has become a common method for molten steel solidification. As steel products become more refined, steel mills are often required to produce steel in small batches. To further improve the production efficiency, steel grade transition is increasingly becoming a common method in steel production. However, steel grade transition inevitably results in transition slabs. Therefore, studies on continuous casting have long been focused on reducing the length of the transition slab [1–5].

Thomas [2] developed a series of measures to shorten the length of the transition slab by considering the tundish furniture, minimum tundish weight at the opened ladle, cross-sectional area of the mold, size of the tundish, and casting order of steel grades. Kant et al. [6] mainly considered the effect of the location of the dam in the

---

S. Song · Y. Sun (✉) · Y. Li · C. Zhuo
School of Collaborative Innovation Center of Steel Technology, University of Science and Technology Beijing (USTB), Beijing 100083, China
e-mail: sunyanhui_ustb@163.com

S. Wagstaff et al. (eds.), *Materials Processing Fundamentals 2023*, The Minerals, Metals & Materials Series, https://doi.org/10.1007/978-3-031-22657-1_19

six-strand caster on the length of the transition billet, and their study concluded that placing the dam at the outlet close to the inlet can significantly reduce the length of the transition billet. Siddiqui and Jha [7] used the volume of fluid method for numerical simulations, which considered the effect of the turbulence inhibitor on the length of the transition slab. They concluded that the turbulence inhibitor increases the length of the transition slab. Amorim et al. [4] established a steel grade transition model for a six-strand billet continuous caster. Huang and Thomas [8] suggested that during the steel grade transition, argon injection has a slight effect on the surface composition of the slab but has no effect on the mixing inside the slab. Li and Tsukihashi [9] developed a mathematical model to analyze the mass transfer during steel grade transition using a static magnetic field. The model reduces the length of the transition slab by approximately 50% by applying a 0.5 T magnetic field. Ahn et al. [10] found that an electromagnetic field suppressed the lower vortex in the mold and formed a plug flow zone, which reduced the mixing of two different grades of steel and shortened the length of the transition slab. Chattopadhyay et al. [11] considered the effect of a turbulence inhibitor on steel grade transition under non-isothermal conditions. Alizadeh et al. and Damle and Sahal [3, 12] found that the weight of mixed-grade steels is influenced by the new molten steel volume, slab size, casting rate, and non-isothermal effects.

To ensure the quality of the slab during actual production, low-superheat casting is generally required. The liquidus temperature and density of the molten steel are both related to its composition. To determine a more suitable casting sequence, we calculated the steel grade transition at different temperatures and densities via numerical simulation. This helped to further shorten the length of the transition slab.

Simulation Model

Model Assumptions

(1) The molten steel in the model is considered to be an incompressible Newtonian fluid under turbulent conditions.
(2) The model ignores chemical reactions in molten steel.
(3) The variation in the molten steel element mass fraction in the model is mainly caused by the flow, and diffusion has little effect on it.
(4) The model ignores the rise and fall in the molten steel level in the tundish during ladle replacement.
(5) The shear stress at the steel–slag interface in the model was set to 0.
(6) The model considers the area below 2 m of the meniscus of the mold to have laminar flow, and it is assumed that the composition of the molten steel in the laminar flow area does not change.

Governing Equations

The continuity and Navier–Stokes equations can be written as follows:

$$\frac{\partial \rho}{\partial t} + \nabla \cdot (\rho \vec{v}) = 0 \tag{1}$$

$$\frac{\partial (\rho \vec{v})}{\partial t} + \nabla \cdot (\rho \vec{v} \vec{v}) = -\nabla p + \mu \nabla \cdot \left(\nabla \vec{v} + \nabla \vec{v}^{T} \right) + \rho \vec{g} \tag{2}$$

where ρ is the density, t is the time, $\vec{v}$ is the velocity, p is the static pressure, μ is the laminar viscosity, and $\vec{g}$ is the gravity.

The turbulence kinetic energy k, and its rate of dissipation ε, are employed as follows:

$$\frac{\partial (\rho k)}{\partial t} + \rho k \frac{\partial (v_i)}{\partial x_i} = \frac{\partial}{\partial x_j}\left[\left(\mu + \frac{\mu_t}{\sigma_k} \right) \frac{\partial k}{\partial x_j} \right] + \mu_t \left(\frac{\partial v_i}{\partial x_j} + \frac{\partial v_j}{\partial x_i} \right) \frac{\partial v_i}{\partial x_j} - \rho \varepsilon \tag{3}$$

$$\begin{aligned} \frac{\partial}{\partial t}(\rho \varepsilon) + \frac{\partial}{\partial x_i}(\rho \varepsilon v_i) &= \frac{\partial}{\partial x_j}\left[\left(\mu + \frac{\mu_t}{\sigma_\varepsilon} \right) \frac{\partial \varepsilon}{\partial x_j} \right] \\ &+ C_{1\varepsilon} \frac{\varepsilon}{k} \mu_t \left(\frac{\partial v_i}{\partial x_j} + \frac{\partial v_j}{\partial x_i} \right) \frac{\partial v_i}{\partial x_j} - C_{2\varepsilon} \rho \frac{\varepsilon^2}{k} \end{aligned} \tag{4}$$

The turbulent viscosity, μ_t, is expressed as:

$$\mu_t = \rho C_\mu \frac{k^2}{\varepsilon} \tag{5}$$

where $C_{1\varepsilon}$ (1.44), $C_{2\varepsilon}$ (1.92), and C_μ (0.09) are constants, σ_k (1.00) and σ_ε (1.30) are the turbulent Prandtl numbers for k and ε, respectively.

The conservation equation for species transfer is expressed as follows:

$$\frac{\partial}{\partial t}\left(\rho C_{spe} \right) + \nabla \cdot \left(\rho \vec{v} C_{spe} \right) = -\nabla \cdot \left[-\left(\rho D_{spe,liq} + \frac{\mu_t}{Sc_t} \right) \nabla C_{spe} \right] \tag{6}$$

where C_{spe} is the local mass fraction of the spe^{th} species, $D_{spe,liq}$ is the liquid-phase diffusion coefficient, and Sc_t (0.70) is the turbulent Schmidt number.

The energy conservation equation is expressed as follows:

$$\frac{\partial \left(\rho C_p T \right)}{\partial t} + \frac{\partial \left(\rho C_p T u_i \right)}{\partial x_i} = \frac{\partial}{\partial x_i}\left[\left(\lambda + \frac{c_p \mu_t}{Pr_t} \right) \frac{\partial T}{\partial x_i} \right] \tag{7}$$

where C_p is the specific heat capacity, T is the temperature, λ is the thermal conductivity, and Pr_t (0.85) is the turbulent Prandtl number.

Boundary Conditions and Properties

The computational domain of this model includes the tundish, mold, and part of the secondary cooling area. The three-dimensional model and the mesh are shown in Fig. 1. The remaining calculation parameters are listed in Table 1. Owing to the long mixing time of molten steel, we imported the data on the submerged entry nozzle (SEN) in the tundish area into the SEN in the mold area and calculated the tundish and mold parts separately, thereby improving the calculation efficiency.

To bring the model closer to the actual situation, the boundary conditions of this model were set as follows:

(1) The ladle nozzle in the tundish area and SEN in the mold area were both set as velocity inlets, (the inlet conditions are listed in Table 1).
(2) The outlet at the bottom of the mold and the SEN in the tundish area were both set as outflows.

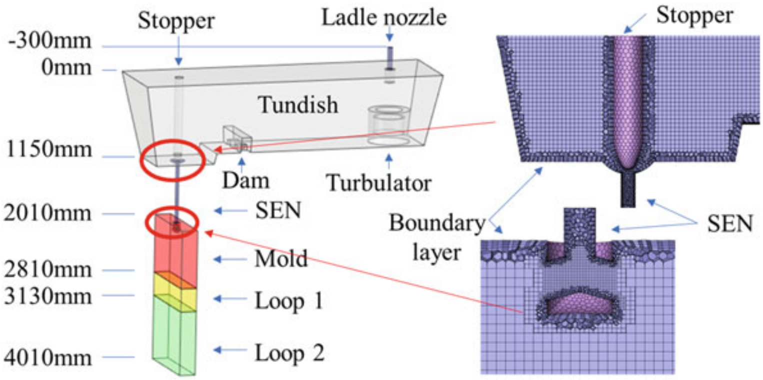

Fig. 1 Graph and grid of the computational domain

Table 1 Calculated parameters in the model

Parameter	Value	Parameter	Value
Ladle nozzle inner diameter	75 mm	SEN inner diameter	56 mm
Ladle nozzle outer diameter	140 mm	SEN outer diameter	116 mm
Tundish length	4214 mm	Billet cross-section	1260 mm × 220 mm
Tundish width	1181 mm	Casting speed	1.5 m/min
Ladle nozzle velocity	1.569 m/s	SEN velocity	2.802
Ladle nozzle turbulence intensity	3.668%	SEN turbulence intensity	3.531%

Table 2 Temperature parameters

Parameter	Value	Parameter	Value
Tundish wide wall	3200 W/m^2	Tundish narrow wall	3800 W/m^2
Tundish free surface	15,000 W/m^2	Tundish bottom wall	1400 W/m^2
Mold wide face	2,420,000 W/m^2	Mold narrow face	2,230,000 W/m^2
Loop 1 wide face	1520 W/ (m^2 K)	Loop 1 narrow face	1320 W/ (m^2 K)
Loop 2 wide face	847 W/ (m^2 K)	Loop 2 narrow face	685 W/ (m^2 K)
Mold free surface	15,000 W/m^2		

Table 3 Material parameters

Parameter	Value	Parameter	Value
Specific Heat	650 J/(kg K)	Viscosity	0.0062 kg/ (m s)
Thermal Conductivity	45 W/(m K)	Liquid-phase diffusivity [13]	2.0e−09 m^2/s

(3) The rest of the boundaries were set as walls. The shear forces at the steel–slag interface in the tundish part and the steel–slag interface in the mold part were both set to zero. The heat-dissipation parameters of the walls are listed in Table 2.

The molten steel density was calculated in real time using the volume-weighted mixing law. In addition, because the same density or the same liquidus temperature can correspond to multiple steel grades, the molten steel parameters were all set as constants (Table 3).

Experimental and Numerical Procedure

In this study, the temperature difference was obtained by subtracting the temperature of the new grade from that of the old grade. The density difference was obtained by subtracting the density of the new grade from that of the old grade. Four temperature and four density differences were used to study the effects of temperature and density on the length of the transition slab. The 16 numerical simulation schemes are listed in Table 4.

In this study, the flow field and temperature field of the tundish and mold areas during normal production were obtained first. The mixing process in the tundish was then calculated, and the residence time distribution (RTD) data at the outlet of the tundish were obtained. Finally, the profile method was used to import the mold, and the molten steel compositions on the surface and center of the slab at the exit of the mold were calculated.

Table 4 Numerical simulation experiment scheme

No	New grade temperature (K)	Old grade temperature (K)	Temperature difference (K)	New grade density (kg/m^3)	Old grade density (kg/m^3)	Density Difference (kg/m^3)
1	1670.0	1820.0	−150.0	7100	6800	300
2	1770.0	1820.0	−50.0	7100	6800	300
3	1820.0	1770.0	50.0	7100	6800	300
4	1820.0	1670.0	150.0	7100	6800	300
5	1670.0	1820.0	−150.0	7100	7000	100
6	1770.0	1820.0	−50.0	7100	7000	100
7	1820.0	1770.0	50.0	7100	7000	100
8	1820.0	1670.0	150.0	7100	7000	100
9	1670.0	1820.0	−150.0	7000	7100	−100
10	1770.0	1820.0	−50.0	7000	7100	−100
11	1820.0	1770.0	50.0	7000	7100	−100
12	1820.0	1670.0	150.0	7000	7100	−100
13	1670.0	1820.0	−150.0	6800	7100	−300
14	1770.0	1820.0	−50.0	6800	7100	−300
15	1820.0	1770.0	50.0	6800	7100	−300
16	1820.0	1670.0	150.0	6800	7100	−300

Results and Discussion

Validation Experiments

We used physical simulations and industrial experiments to verify the model. The ratio of the tundish model to the actual tundish used in the physical simulation was 1:3. In the physical simulation, water and brine represent different steel grades, and a schematic of the water model experiment is shown in Fig. 2a. The physically simulated ink distribution is shown in Fig. 3. During the industrial test, samples were taken every 1 min at two positions: the center and the surface, as shown in Fig. 2b. The steel grades used in the industrial test are presented in Table 5.

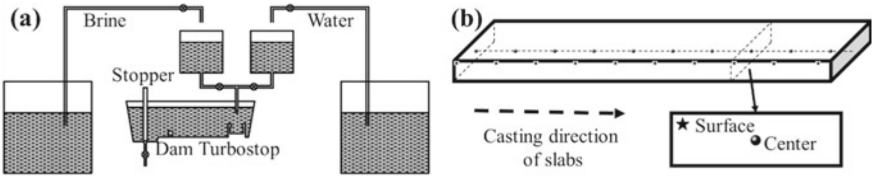

Fig. 2 Schematic of verification experiments: **a** physical simulation, **b** industrial test

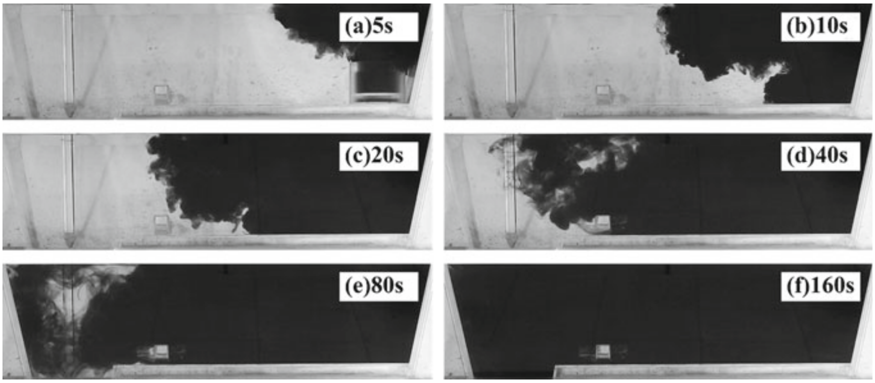

Fig. 3 Black ink dispersion photo in the water model

Table 5 Composition and physical parameters of the experimental steels

Steel grade	Weight (%)					Density (kg/m^3)	Liquidus temperature (K)
	C	Si	Mn	P	S		
DC01 (New)	0.011	0.024	0.174	0.012	0.006	7134.95	1806.47
SPHC (Old)	0.058	0.032	0.188	0.015	0.008	7124.49	1802.49

We transformed the RTD data from water model experiments using the following equation.

$$F = \frac{C_t - C_o}{C_n - C_o} \tag{8}$$

where C_t is the fraction of a given element at time t; C_o and C_n are the fractions of that element measured in the old and new grades, respectively. Additionally, we compared the results of the field experiments and model predictions. The results showed good agreement, as shown in Fig. 4.

Flow Field

This study found that the mixing process in the tundish may be roughly divided into two types. We chose schemes 6 and 11 to represent these two cases, as shown in Fig. 5. The temperature difference in scheme 6 is − 50 K, and the density difference is 100 kg/m^3. In scheme 11, the temperature difference is 50 K, and the density difference is − 100 kg/m^3.

The new grade in scheme 6 enters the turbostop from the ladle nozzle and sinks to the bottom of the tundish along the outside of the turbostop after the speed is

Fig. 4 Comparison of predicted and measured slab compositions

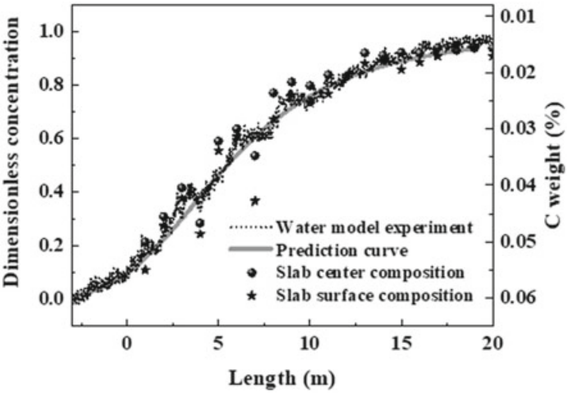

reduced, and soon reaches the SEN. The old grade residing in the upper part of the tundish needs to flow and mix for a long time before it can gradually flow out of the tundish to complete the steel grade transition. At the same time, the new grade in scheme 11 enters the turbostop from the ladle nozzle and returns to the upper part of the tundish after deceleration. The new grade then flows to the stopper rod along the steel–slag interface. In the early stage of mixing, it does not affect the flow of the old grade out of the tundish, causing a rapid decrease in the proportion of the old grade in the tundish, thereby effectively shortening the length of the transition slab. The dam in the tundish prevents the last part of the old grade from flowing out of the tundish to a certain extent, and this part of the old grade can only flow out by mixing with the new grade or through two holes in the dam.

In scheme 6, the new grade reaches the SEN earlier, and the old grade completely flows out of the tundish later than those in scheme 11. Therefore, we adopted a scheme similar to scheme 11 rather than scheme 6 to shorten the transition slab.

After the molten steel is mixed in the tundish, the composition of the molten steel flowing from the SEN to the mold is relatively uniform; therefore, the variation in the molten steel composition in the mold is smaller than that in the tundish. As shown in Fig. 6, after the molten steel flows from the SEN into the mold, it first reaches the narrow face of the mold. Subsequently, part of the molten steel flows down the mold, so that the new grade mass fraction on the surface of the slab is slightly higher than that in the center of the slab. Similarly, the new grade in scheme 6 enters the mold earlier than in scheme 11, and the old grade in scheme 6 completes the mixed casting process later than in scheme 11.

As shown in Fig. 7, although the center and surface compositions of the slab differ, the difference is small. Compared with the RTD curve at the SEN, the center and surface components of the slab have a certain hysteresis, but the change trends in the three are consistent. In scheme 6, the new grade reaches the SEN earlier than in scheme 11, and the old grade in scheme 6 flows out of the tundish completely later than in scheme 11. The RTD curves of schemes 6 and 11 are consistent with the molten steel flow laws shown in Figs. 5 and 6. The research results show that the

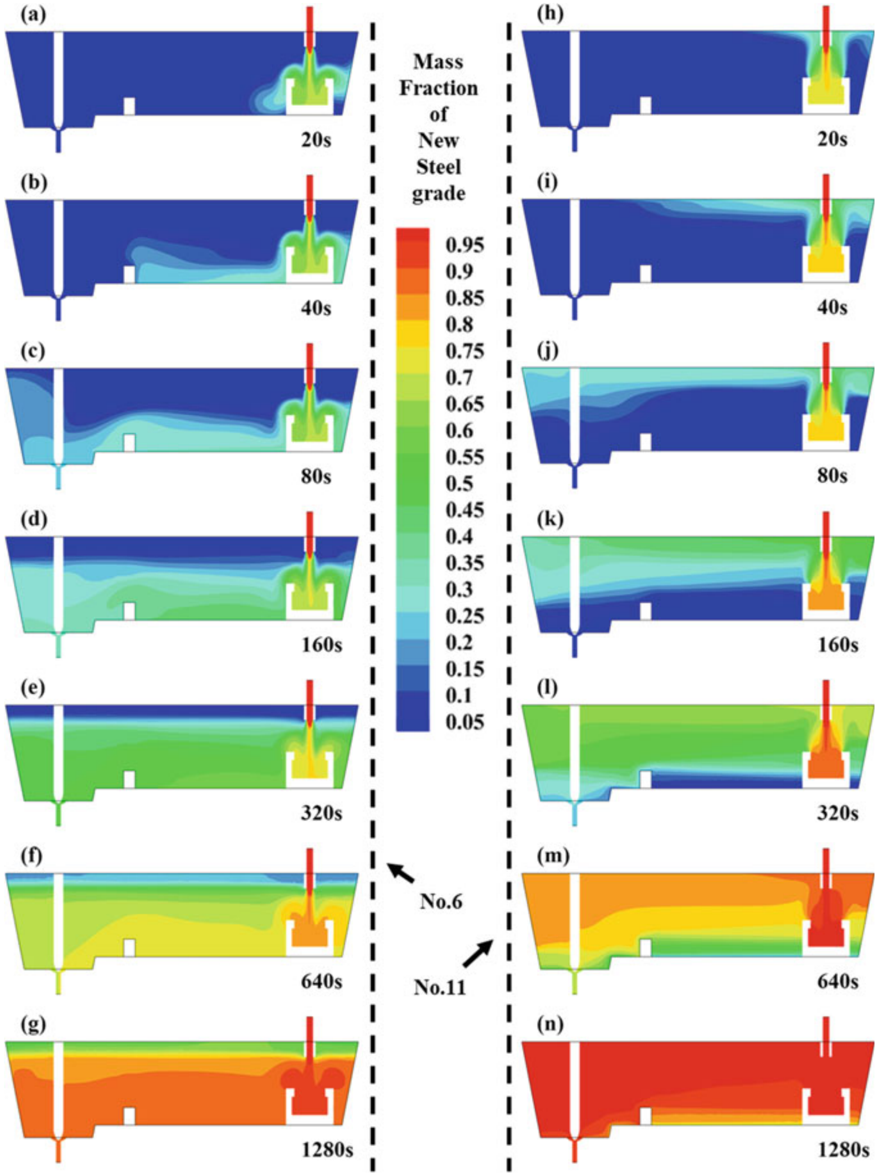

Fig. 5 Numerical simulation results for the mass fraction of new grade in the tundish as a function of time (**a**–**g**) steel grade transition in scheme 6, (**h**–**n**) steel grade transition in scheme 11

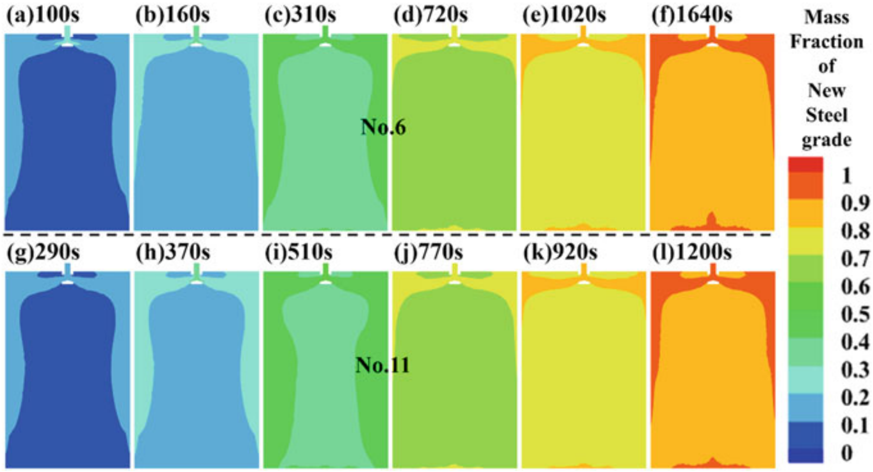

Fig. 6 Numerical simulation results for the mass fraction of new grade in the mold as a function of time: (**a**–**f**) steel grade transition in scheme 6, (**g**–**l**) steel grade transition in scheme 11

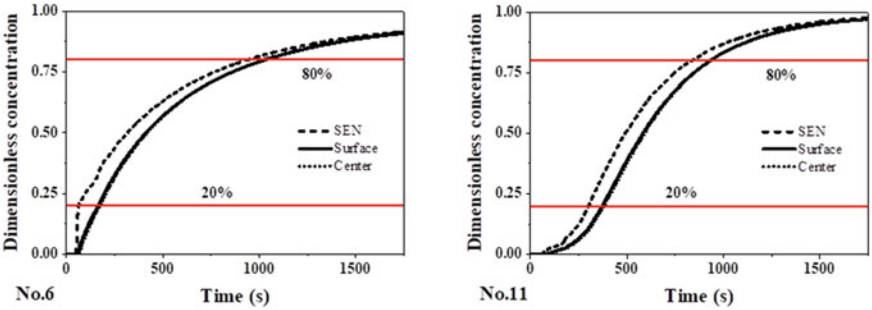

Fig. 7 Mass fraction of the new grade at the tundish outlet and the steel stream outlet in the model

molten steel flow in the mold has little effect on the composition distribution in the slab; therefore, only, the mixing process in the tundish needs to be investigated to obtain the change rule for the length of the transition slab.

RTD Curves

The RTD curves of the 16 groups of tundish experiments at SEN are shown in Fig. 8. We assumed that the molten steel with the mass fraction of the new grade below 20% met the requirements of the old grade, above 80%—the new grade, and between 20 and 80%—the transition slab.

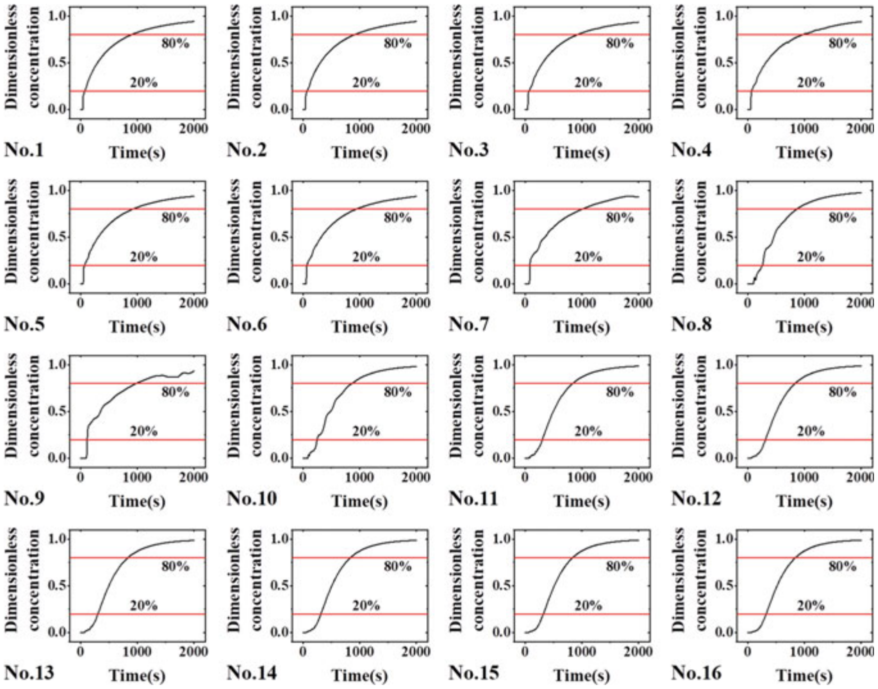

Fig. 8 RTD curves of 16 experiments (corresponding to Table 4)

By analyzing the RTD curves of the 16 groups of experiments, we determined the time at which the mass fraction of the new grade reached 20%, reached 80%, and the time for producing the transition slab (Table 6). A contour map was drawn based on the data in Table 6, as shown in Fig. 9.

Table 6 Critical moment at SEN during the steel grade transition

No	New grade 20% (s)	New grade 80% (s)	Transition slab duration (s)	No	New grade 20% (s)	New grade 80% (s)	Transition slab duration (s)
1	1070.1	1892.3	822.2	9	1114.5	1976.8	862.3
2	1069.9	1902.0	832.1	10	1244.5	1859.2	614.7
3	1069.4	1914.6	845.2	11	1300.6	1836.9	536.3
4	1063.3	1964.0	900.7	12	1310.1	1830.0	519.9
5	1068.6	1918.9	850.3	13	1303.2	1833.1	529.9
6	1063.5	1937.7	874.2	14	1310.6	1831.4	520.8
7	1082.4	2005.6	923.2	15	1317.7	1833.1	515.4
8	1255.2	1862.3	607.1	16	1324.0	1835.6	511.6

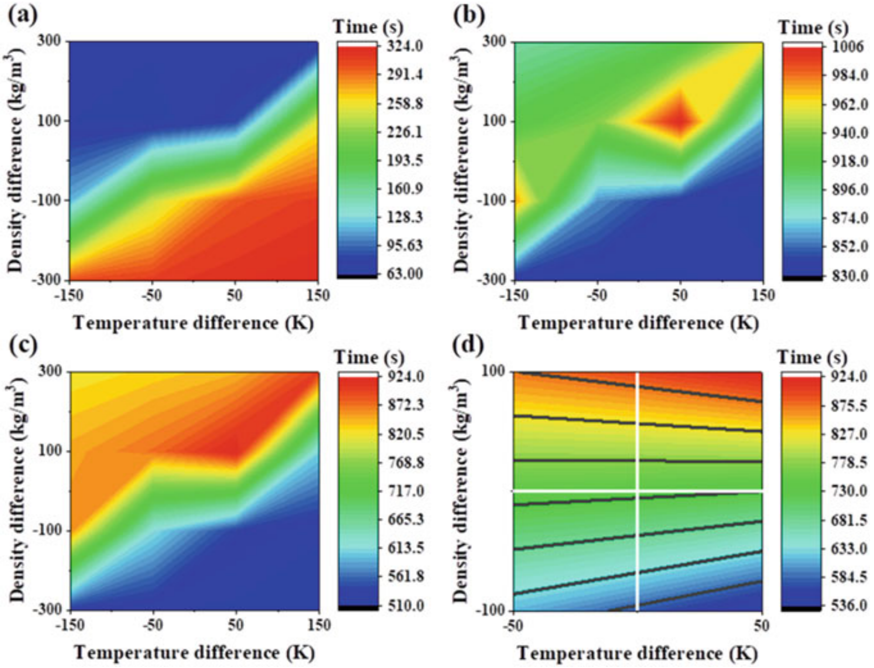

Fig. 9 Contour plot drawn from critical moments at SEN during steel grade transition: **a** new grade 20%, **b** new grade 80%, **c** transition slab duration, **d** the duration of the transition slab for the usual range of temperature and density differences during steel grade transition

As shown in Fig. 9a, the smaller the density difference and the greater the temperature difference, the later the mass fraction of the new grade reaches 20%. At the same time, the greater the density difference and the smaller the temperature difference, the earlier the mass fraction of the new grade reaches 20%.

As shown in Fig. 9b, the lower the density difference and the greater the temperature difference, the earlier the mass fraction of the new grade reaches 80%. However, with the increase in density difference and decrease in temperature difference, the time when the mass fraction of the new grade reached 80% did not monotonously increase.

As shown in Fig. 9c, a decrease in density difference and an increase in temperature difference result in shorter transition slab production time. In this study, the transition slab took the longest to be produced at a temperature difference of 50 K and density difference of 100 kg/m^3. Notably, at greater density differences and lower temperature differences, the time for producing the transition slab decreases. This result is attributed to the combined flow and temperature fields of the molten steel in the tundish.

At present, in most steel companies, the old and new grades involved in the steel grade transition process have small differences in composition, meaning that the temperature and density differences are also small. Thus, the casting sequence of steel grades needs to be arranged in such a way that the mixed casting is conducted under the conditions in the lower half of Fig. 9d, and conditions in the upper half of Fig. 9d are avoided. The length of the transition slab could be changed by changing the casting sequence of the old and new grades. At the same time, the effect of density on the length of the transition plate cannot be ignored. When the composition difference between the old and new grades is small, the effect of a 1 kg/m^3 change in density on the length of the transition slab is equivalent to that of a temperature change of 3 K.

Conclusions

In this study, the effects of the density and temperature of the old and new grades on the length of the transition slab were studied using numerical simulation. We verified the model using physical simulations and industrial experiments to ensure its accuracy. From the above analysis, the following conclusions can be drawn.

(1) The density of the new grade is lower than that of the old grade; therefore, the tundish can preferentially discharge the old grade accumulated at the bottom of the tundish, quickly reducing the proportion of the old grade in the tundish and shortening the transition slab.
(2) During the steel grade transition, after the new and old grades are mixed in the tundish, the composition of the molten steel entering the mold does not change drastically. The simulation results show that the difference between the compositions at the surface and center of the slab is small, indicating that the flow field has little effect on the compositions at the surface and center of the slab.
(3) With the decrease in density difference and increase in the temperature difference, the time required to produce the transition slab decreases. However, after the generation time of the transition slab reaches the maximum, further increase in the density difference and decrease in the temperature difference reduce the time to produce the transition slab. This was attributed to the combined action of the molten steel flow and temperature fields.
(4) If the composition difference between the old and new grades is small, the effect of a 1 kg/m^3 change in density on the length of the transition slab is equivalent to that of a 3 K temperature change. Therefore, the effect of molten steel density on the length of the transition slab cannot be ignored.

References

1. Huang X, Thomas BG (1993) Modeling of steel grade transition in continuous slab casting processes. Metall Mater Trans B 24:379–393. https://doi.org/10.1007/BF02659140
2. Thomas BG (1997) Modelling study of intermixing in Tundish and strand during a continuous-casting grade transition. Iron and Steelmaker 24:83–96
3. Alizadeh M, Edris H, Pishevar AR (2008) Behavior of mixed grade during the grade transition for different conditions in the slab continuous casting. ISIJ Int 48:28–37. https://doi.org/10.2355/isijinternational.48.28
4. Amorim LLC, Silva CA, Resende AD, Silva IA, Oliveira MJM (2018) A study of intermix in a six-strand billet caster. Metall Mater Trans A 49:6308–6324. https://doi.org/10.1007/s11663-018-1177-z
5. Siddiqui MIH, Kim M (2019) Two-phase numerical modeling of grade intermixing in a steelmaking Tundish. Metals 9:40. https://doi.org/10.3390/met9010040
6. Kant S, Jha PK, Kumar P (2011) Investigation of effect of dam on intermixing during ladle changeover in six strand billet caster tundish. Ironmaking Steelmaking 38:391–397. https://doi.org/10.1179/1743281211Y.0000000007
7. Siddiqui MIH, Jha PK (2014) Assessment of turbulence models for prediction of intermixed amount with free surface variation using coupled level-set volume of fluid method. ISIJ Int 54:2578–2587. https://doi.org/10.2355/isijinternational.54.2578
8. Thomas BG, Huang X, Sussman RC (1994) Simulation of argon gas flow effects in a continuous slab caster. Metall Mater Trans B 25:527–548. https://doi.org/10.1007/BF02650074
9. Li B, Tsukihashi F (2001) Effect of static magnetic field application on the mass transfer in sequence slab continuous casting process. ISIJ Int 41:844–849. https://doi.org/10.2355/isijinternational.41.844
10. Ahn JH, Yoon JK, lee JE (2002) Analysis of mixed grade transition in continuous thin slab casting with EMBR. Met Mater Int 8:271.https://doi.org/10.1007/BF03186096
11. Chattopadhyay K, Isac M, Guthrie RIL (2012) Modelling of non-isothermal melt flows in a four strand delta shaped billet caster tundish validated by water model experiments. ISIJ Int 52:2026–2035. https://doi.org/10.2355/isijinternational.52.2026
12. Damle C, Sahal Y (1996) A Criterion for Water Modeling of Non-isothermal Melt Flows in Continuous Casting Tundishes. ISIJ Int 36:681–689. https://doi.org/10.2355/isijinternational.36.681
13. Li YG, Sun YH, Bai XS (2012) Numerical simulation of the flow, solidification, and solute transport in a billet mold under electromagnetic stirring. Metall Res Technol 118:221. https://doi.org/10.1051/metal/2021015

Mathematical Simulation Study on the Effect of Nozzle Side Hole Structure Parameters on the Behavior of Molten Steel in Stainless Steel Mold

Si-kun Peng, Ming-mei Zhu, Kun-chi Jiang, and Cheng-hong Li

Abstract In this paper, the influence of structural parameters such as the area and shape of the side hole of the submerged nozzle on the flow behavior of steel and the distribution of liquid slag layer in the mold of large section stainless steel continuous casting slab at high casting speed is studied by combining physical model with mathematical simulation. The results show that with the increase of side hole area, the fluctuation of molten steel level in the mold decreases; the impact depth increases; the flow rate of molten steel decreases; the distribution of liquid slag layer is gradually uniform, and the number of slag entrainment decreases. Compared with the rectangular side hole shape, when the side hole shape is oval, the fluctuation of molten steel level in the mold is reduced; the distribution of liquid slag layer is more uniform, and the number of slag entrainment is reduced. The research results can provide a theoretical basis for designing a reasonable submerged nozzle.

Keywords Stainless steel · Mold · Submerged nozzle · High efficiency continuous casting

Introduction

Stainless steel has the characteristics of low solidification temperature, small thermal conductivity, large thermal expansion coefficient, large shell shrinkage, long solidification time, etc. Therefore, unlike other steels, the side holes of the submerged nozzle of the mold are usually inclined upward to generate an upward reflux to promote slagging. However, this nozzle design is also easy to cause excessive upflow in the mold and large disturbance to the steel slag interface, leading to slag entrapment and secondary oxidation of molten steel [1]. This is also often an important reason for defects such as warping and sagging on the surface of stainless steel billet and leads to surface defects of subsequent plates and strips. Therefore, it is very important to design a reasonable nozzle structure to optimize the flow field of the mold to reduce

---

S. Peng · M. Zhu (✉) · K. Jiang · C. Li
College of Materials Science and Engineering, Chongqing University, Chongqing 400044, China
e-mail: zhumingmei@cqu.edu.cn

S. Wagstaff et al. (eds.), *Materials Processing Fundamentals 2023*, The Minerals, Metals & Materials Series, https://doi.org/10.1007/978-3-031-22657-1_20

the occurrence rate of slag or inclusion defects in the hot rolling plate of a specific section slab [2–4].

Using the methods of physical simulation and mathematical simulation, many metallurgical workers have studied the influence of submerged nozzle structure on the flow behavior of molten steel in slab mold. Deng Xiaoxuan [5] and other scholars have conducted corresponding experiments on different shapes of the side holes of the nozzle. It is concluded that the velocity of square nozzle is the highest. The flow stream of elliptical nozzle and rectangular nozzle is more dispersed, and the velocity distribution at the outlet is uniform, while the flow stream of square nozzle is concentrated at the lower part of the side hole. Zhang et al. [6] studied the fluid flow in the mold in combination with industrial test, water model, and numerical simulation, and found that increasing the inner diameter of the nozzle and the area of the side hole can slow down the liquid level fluctuation. Bai et al. [7] studied the influence of nozzle structure on turbulence, and proposed that the vertical injection angle and the area of the return flow area of the molten steel stream at the outlet of the nozzle increase with the length of the side hole. Wu et al. [8] used numerical simulation to study the influence of nozzle structural parameters on the liquid level fluctuation, and found that increasing the height and width of the side hole of the nozzle has little effect on reducing the jet exit velocity, but will reduce the effective area fraction of the side hole. Najjar et al. [9] studied the influence of nozzle structure parameters on the jet by means of finite element model, and found that reducing the height of the side hole can increase the average jet velocity and turbulence intensity, improve the effective area fraction of the side hole, which is conducive to reducing the accumulation of alumina inclusions at the bottom of the nozzle and easing the blockage of the nozzle.

In this paper, the large section stainless steel continuous casting rectangular slab mold under high drawing speed is taken as the research object. The numerical simulation and physical simulation experiments are carried out, and the influence of nozzle structure parameters on the flow of molten steel is obtained. Finally, the theoretical basis is provided for the design of reasonable mold nozzle.

Numerical Simulation and Physical Simulation

Physical Simulation and Research Methods

Physical Model

The hydraulic model is established based on the similarity principle. The geometric similarity ratio of 0.6:1 was selected. The mold and submerged nozzle model are made of transparent plexiglass, and the normal temperature water is used to simulate the molten steel. The water model test device is shown in Fig. 1.

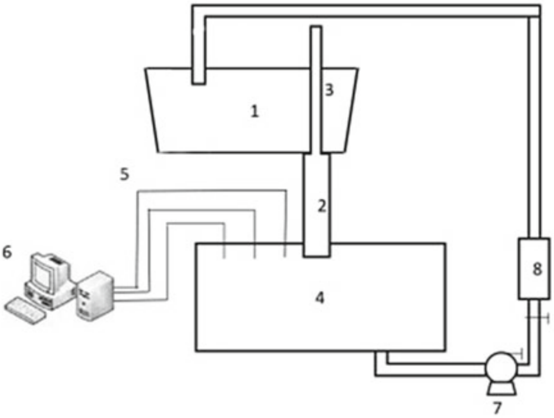

Fig. 1 Schematic diagram of experimental device. 1. Tundish, 2. Nozzle, 3. Stopper, 4. Mold, 5. Wave height meter, 6. Computer, 7. Water pump, 8. Flowmeter

Research Method

(1) The wave height meter is used to measure the fluctuation of each point in Fig. 2. The X measuring point is at the narrow side; the Y measuring point is at 1/4 of the mold, and the Z measuring point is near the water inlet. The data acquisition time of each measuring point is 600 s, and the average wave height is obtained by arithmetic mean. At the same time, blue ink is used as a tracer to find the impact point position of the stream and record its impact depth through flow field observation.

(2) In the experiment, the liquid slag layer distribution at different times under each scheme was photographed with a camera. The maximum and minimum liquid slag thickness on both sides of the crystallizer in each picture was obtained through picture processing, and the maximum liquid slag thickness at different times was averaged. Finally, the average value of liquid slag thickness difference at different times is used to characterize the uniformity of liquid slag distribution. At the same time, observe the liquid level of the crystallizer within 5 min, and record the average number of slag inclusions per minute.

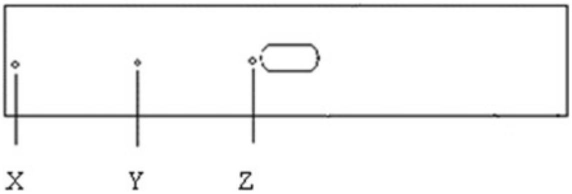

Fig. 2 Wave height measurement points

Numerical Simulation

Basic Assumptions

In order to facilitate the mathematical simulation, the assumptions for the calculated model are as follows:

(1) The solid, liquid phase metal and liquid slag in the mold are all regarded as Newtonian fluids, that is, incompressible viscous fluids, and they are all stable, that is, the fluid density is constant;
(2) The influence of metal phase transformation on the temperature distribution in the mold and the influence of solidified shell on the flow of molten steel in the mold are ignored;
(3) The influence of billet shrinkage and mold vibration on the flow field of molten steel during solidification is not considered;
(4) The liquid level of the crystallizer is free.

Basic Equation

The flow of molten steel in the mold is a turbulent three-dimensional unsteady flow. The governing equations describing the flow of molten steel in the mold include continuity equation, momentum equation, energy equation, and standard k-ε equation; the governing equation is as follows:

$$\frac{\partial(\rho u_i)}{\partial x_i} = 0 \tag{1}$$

$$\rho\frac{\partial\left(u_i u_j\right)}{\partial x_f} = \mu_{\text{eff}}\left(\frac{\partial^2 u_i}{\partial x_j^2}\right) - \frac{\partial P}{\partial x_i} + \rho g_i \tag{2}$$

$$\frac{\partial\left(\rho\mu_j H\right)}{x_j} = \frac{\partial}{\partial x_j}\left(k_{\text{eff}}\frac{\partial T}{\partial x_j}\right) \tag{3}$$

$$\rho v_i\frac{\partial k}{\partial x_i} = \frac{\partial}{\partial x_j}\left(\frac{\mu_{\text{eff}}}{\sigma_k}\frac{\partial k}{\partial x_i}\right) + \mu_t\frac{\partial v_i}{\partial x_j}\left(\frac{\partial v_i}{\partial x_j} + \frac{\partial v_j}{\partial x_i}\right) - \rho\varepsilon \tag{4}$$

$$\rho v_j\frac{\partial \varepsilon}{\partial x_j} = \frac{\partial}{\partial x_j}\left(\frac{\mu_{\text{eff}}}{\sigma_\varepsilon}\frac{\partial \varepsilon}{\partial x_j}\right) + C_1\mu_t\frac{\varepsilon}{K}\frac{\partial v_j}{\partial x_i}\left(\frac{\partial v_i}{\partial x_j} + \frac{\partial v_j}{\partial x_i}\right) - C_2\frac{\varepsilon}{K}\rho\varepsilon \tag{5}$$

wherein ρ is the fluid density, kg m^{-3}; μ_i is the velocity component, m s^{-1}; x_i is directional component; p is pressure, Pa; g_i is gravitational acceleration, m s^{-2}; T is temperature, K; k_{eff} is the effective thermal conductivity W m^{-1} K^{-1}; k is the turbulent kinetic energy, m^2 s^2; μ_{eff} is the effective viscosity coefficient, Pa s; ε is the energy dissipation rate of turbulent flow, m^2 s^3; σ_k, σ_ε, C_1, and C_2 are empirical constants with values of 1.0, 1.3, 1.44, and 1.92, respectively.

Model Parameters and Boundary Conditions

Based on the consideration of symmetry, this paper takes 1/2 of the mold area as the research object, and the calculation area of the mold is divided by hexahedral non-uniform grid. The inlet of the model nozzle is defined as the velocity inlet, whose velocity can be calculated by the billet drawing speed according to the flow balance principle, and its temperature is the sum of the liquidus temperature and superheat of the molten steel. The outlet of the calculation domain is defined as the velocity outlet. The non-slip boundary condition is used for the wall surface, and the standard wall function is used for the calculation of the flow field near the wall surface. The normal derivatives of the boundary velocity and other variables on the symmetry plane are zero. Table 1 shows process parameters required for numerical simulation.

Simulation Scheme

The cross-section size of the prototype mold studied in this paper is 200 mm × 1530 mm, and the immersion depth of the long nozzle in the simulation process is 120 mm. In this paper, four types of nozzles with different geometries are considered. As shown in Table 2 for structural parameters.

Table 1 Numerical simulation parameters of mold

Parameters	Density of molten steel	Viscosity of molten steel	Inlet vertical speed	Inlet turbulent kinetic energy	Turbulent dissipation rate at inlet
Data	6908 kg m^{-3}	0.00807 $\text{kg m}^{-1}\ \text{s}^{-1}$	1.16 m/s	$0.01\ \mu_{\text{in}}^2\ \text{m}^2/\text{s}^2$	$k_{\text{in}}^{1.5}/(0.5d_0)\ \text{m}^2/\text{s}^3$

Table 2 Structural parameters of water inlet

Nozzle number	Side hole inclination/°	Mesopore diameter/mm	Side hole shape	Side hole size/mm^2
1	15	60	Rectangle	50 × 56
2	15	60	Rectangle	52 × 58
3	15	60	Rectangle	56 × 60
4	15	60	Oval like	56 × 16

Table 3 Liquid level fluctuation

Nozzle number	Wave height at narrow edge (mm)	Wave height at 1/4 of mold (mm)	Wave height at 1/2 of mold (mm)
1	4.74	4.12	3.76
2	4.53	3.93	3.55
3	3.51	3.40	3.26
4	4.16	3.83	3.68

Table 4 Impact depth

Nozzle number	Impact depth (mm)
1	138.3
2	141.0
3	148.0
4	145.3

Results and Analysis

Physical Simulation Experiment Results and Analysis

Liquid Level Fluctuation and Impact Depth

Table 3 shows the experimental results of the liquid level fluctuation of the crystallizer under nozzles 1–4 and Table 4 shows the experimental results of the impact depth. It can be seen from the analysis of the experimental data that with the increase of the side hole area of the nozzle, the fluctuation of the liquid steel level in the mold decreases, and the impact depth of the liquid steel increases. Under the same side hole area, changing the shape of the side hole from rectangular to oval will increase the liquid level fluctuation of molten steel in the mold and reduce the impact depth.

Uniformity of Liquid Slag and Number of Slag Curling

As shown in Table 5 for the experimental results of the uniformity of liquid slag distribution in the crystallizer under No. 1 to No. 4 nozzles, and as shown in Table 6 for the experimental results of the number of slag entrapment. According to the analysis of the experimental data, when No. 1 and No. 2 nozzles are used, there is no liquid slag layer at the narrow side of the mold, and the exposed length is 7.3 mm and 2.3 mm, respectively, and there is slag entrapment, which will lead to no flux inflow at the meniscus, which will easily lead to cohesive breakout, thus affecting the smooth progress of continuous casting. However, when No. 3 and No. 4 nozzles are used, the liquid slag layer is evenly distributed, and there is no slag entrapment. With the increase of the side hole area of the nozzle, the uniformity of the liquid

Table 5 Uniformity of liquid slag distribution

Nozzle number	Maximum thickness of liquid slag layer/mm	Minimum thickness of liquid slag layer/mm	Thickness difference/mm	Length of exposed part/mm
1	19.3	0	19.3	7.3
2	18.7	0	18.7	2.3
3	18.3	3.3	15.0	0
4	16.7	6.3	10.3	0

Table 6 Times of slag curling per minute

Nozzle number	Slag curling times
1	0.7
2	0.3
3	0
4	0

slag layer becomes better. When the area of side holes is the same, the shape of side holes changes from rectangular to oval, which will further improve the uniformity of liquid slag layer.

Numerical Simulation Results and Analysis

The velocity distribution in the central section of the mold, the velocity distribution at the outlet of the two side holes and the liquid surface velocity distribution are shown in Figs. 3 and 4. Table 7 shows the maximum, minimum, and average velocities of the crystallizer liquid level. It can be seen from Figs. 3 and 4 that the flow field of the crystallizer using these four kinds of nozzles has formed an obvious upper loop, and the upward stream forms a small reflux area in the upper part of the crystallizer, which has a certain impact on the removal of inclusions. In this area, if the flow rate of molten steel moving upward along the mold wall is too large, turbulence will be generated, and the mold flux will be drawn into the molten steel. It can be seen from Table 7 that with the increase of the side hole area, the maximum speed, minimum speed, and average speed of the liquid steel decrease, while changing the shape of the side hole from rectangular to oval like will reduce the maximum speed and minimum speed of the liquid surface of the mold, while the average speed of the liquid surface increases.

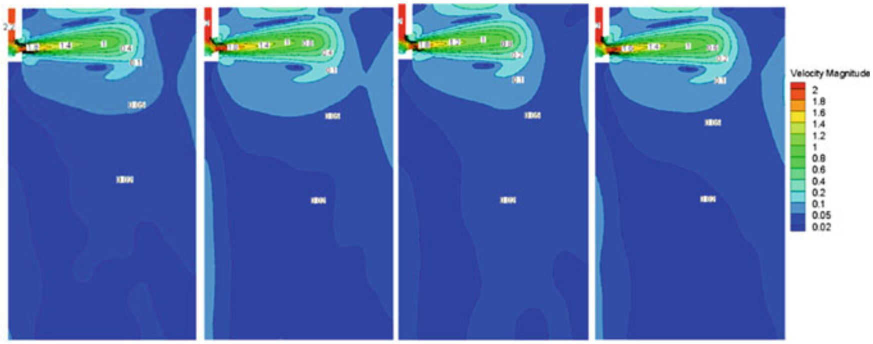

(a)1# (b)2# (c)3# (d)4#

Fig. 3 Velocity distribution in central section

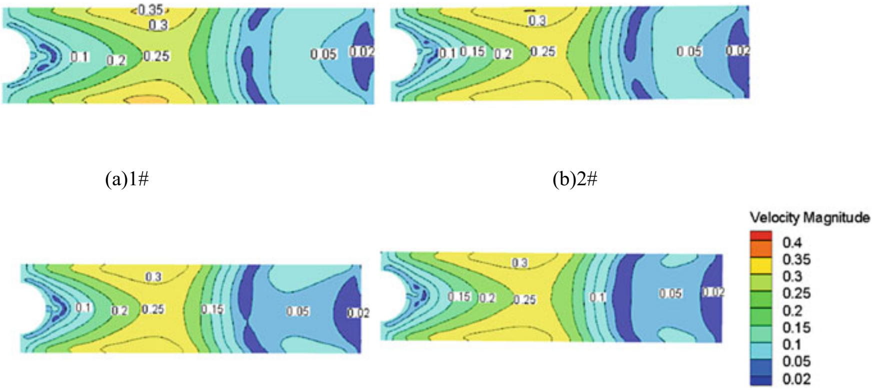

(a)1# (b)2#

(c)3# (d)4#

Fig. 4 Liquid surface velocity distribution

Table 7 Velocity value of liquid level

Nozzle number	Maximum velocity (m/s)	Minimum velocity (m/s)	Average velocity (m/s)
1	0.365387	0.000803	0.150020
2	0.354292	0.001503	0.149764
3	0.351240	0.001046	0.140803
4	0.341723	0.000162	0.145382

Conclusion

The effects of the structural parameters such as the area and shape of the side hole of the submerged nozzle on the steel flow behavior and the distribution of liquid slag layer in the mold of large section stainless steel continuous casting slab at high drawing speed were studied by combining physical model with mathematical simulation. The results show that:

(1) The liquid level fluctuation of molten steel in the mold decreases with the increase of the side hole area, and the liquid level wave heights at the narrow side 1/4 and 1/2 of the mold decrease from 4.74 mm, 4.12 mm, and 3.76 mm to 3.51 mm, 3.40 mm, and 3.26 mm, respectively; the liquid level fluctuation increases as the shape of the side hole changes from rectangular to oval like, and the liquid level wave heights at the narrow side 1/4 and 1/2 of the mold increase from 3.51 mm, 3.40 mm, and 3.26 mm to 4.16 mm, 3.83 mm, and 3.68 mm, respectively.
(2) The impact depth of molten steel in the mold increases with the increase of the side hole area, from 138.3 mm to 148.0 mm; as the shape of the side hole changes from rectangular to oval like, it decreases from 148.0 mm to 145.3 mm.
(3) The uniformity of liquid slag in the mold becomes better with the increase of the area of the side hole, and when the area of the side hole is too small, there will be no liquid slag layer at the narrow edge of the molten steel, and there will be slag curling, which will lead to no inflow of protective slag at the meniscus, resulting in cohesive steel leakage. Changing the shape of side hole from rectangle to ellipse will further improve the uniformity of liquid slag.
(4) With the increase of the area of the side hole of the nozzle, the flow pattern of molten steel in the mold has no obvious change, and the flow rate has decreased. The maximum velocity of the free surface has decreased from 0.36539 to 0.35124 m/s, and the average velocity of the free surface has decreased from 0.15002 to 0.14080 m/s. The shape of the side hole changed from rectangle to ellipse; the flow pattern of molten steel in the mold did not change significantly; the maximum velocity of free liquid surface decreased from 0.35124 to 0.34172 m/s, and the average velocity of free liquid surface increased from 0.14080 to 0.14538 m/s.

Acknowledgements This research was funded by the Natural Science Foundation of Chongqing, China, grant number cstc2019jcyj-msxmX0526.

References

1. Youlin J, Yanping B, Jianhua L et al (2009) Simulation of steel/slag interface behavior and analysis of slag entrapment in stainless steel slab continuous casting mold. J Eng Sci 31(005):618–624

2. Jingfeng C Control and optimization of wide width stainless steel continuous casting process. Wuhan University of Science and Technology
3. Yingdong W, Zhongqiu L, Mingjie Q et al (2020) Experimental study on steel/slag interface fluctuation and slag entrainment behavior in continuous casting mold. J Mater Metall 19(1):8
4. Gang L, Yong G, Chong L et al (2020) Research on the improvement and control of edge warping defects of ultra low carbon if steel. Continuous Casting 45(2):6
5. Xiaoxuan D, Xiao X, Xinhua W et al (2014) Effect of nozzle outlet shape on flow field characteristics in slab continuous casting mold with high drawing speed. J Iron Steel Res 26(7):35–40
6. Zhang LF, Yang SB, Cai KK et al (2007) Investigation of fluid flow and steel cleanliness in the continuous casting strand. Metall Mater Trans B 38(1):63–83
7. Bai H, Thomas BG (2001) Turbulent flow of liquid steel and argon bubbles in slide-gate tundish nozzles: part 2 effect of operation conditions and nozzle design. Metall Mater Trans B 32(2):269–284
8. Wu DF, Cheng SS (2008) Effect of SEN design on surface fluctuation and solidifying shell in slab mold and its optimization. Acta Metall 21(5):341–350
9. Najjar FM, Thomas BG, Hershey DE (1995) Numerical study of steady turbulent flow through bifurcated nozzles in continuous casting. Metall Mater Trans B 26(4):749–765

Author Index

S. Wagstaff et al. (eds.), *Materials Processing Fundamentals 2023*, The Minerals, Metals & Materials Series, https://doi.org/10.1007/978-3-031-22657-1

Subject Index

S. Wagstaff et al. (eds.), *Materials Processing Fundamentals 2023*, The Minerals, Metals & Materials Series, https://doi.org/10.1007/978-3-031-22657-1